The wake of an unsteady actuator disc

Yu, Wei

DOI
10.4233/uuid:0e3a2402-585c-41b1-81cf-a35753076dfc

Publication date
2018

Document Version
Final published version

Citation (APA)
Yu, W. (2018). *The wake of an unsteady actuator disc*. [Dissertation (TU Delft), Delft University of Technology]. https://doi.org/10.4233/uuid:0e3a2402-585c-41b1-81cf-a35753076dfc

THE WAKE OF AN UNSTEADY ACTUATOR DISC

THE WAKE OF AN UNSTEADY ACTUATOR DISC

Proefschrift

ter verkrijging van de graad van doctor
aan de Technische Universiteit Delft,
op gezag van de Rector Magnificus prof. dr. ir. T. H. J. J. van der Hagen,
voorzitter van het College voor Promoties,
in het openbaar te verdedigen op dinsdag 3 april 2018 om 15:00 uur

door

Wei YU

Master of Science in Power Engineering and Engineering Thermophysics
University of Chinese Academy of Science, Beijing, China
geboren te Hubei, China.

Dit proefschrift is goedgekeurd door de
promotor: Prof. dr. ir. G. A. M. van Kuik
copromotor: Dr. ir. C. J. Simão Ferreira

Samenstelling promotiecommissie:

Rector Magnificus,	voorzitter
Prof. dr. ir. G. A. M. van Kuik,	Technische Universiteit Delft, promotor
Dr. ir. C. J. Simão Ferreira,	Technische Universiteit Delft, copromotor

onafhankelijke leden:

Prof. dr. G. J. W. van Bussel	Technische Universiteit Delft
Prof. dr. ir. L. L. M. Veldhuis	Technische Universiteit Delft
Prof. dr. S. Aubrun	École Centrale de Nantes
Dr. M. Gaunaa	Technical University of Denmark
Prof. dr. S. J. Watson,	Technische Universiteit Delft, reservelid

overig lid:

Dr. ir. J. G. Schepers	Energy Research Centre of the Netherlands

Keywords: Dynamic inflow, actuator disc, free wake vortex ring, unsteady load, engineering model

Printed by: ProefschriftMaken

ISBN 978-94-6366-020-4

An electronic version of this dissertation is available at
`http://repository.tudelft.nl/`.

To my parents

SUMMARY

Blade Element Momentum (BEM) is the most important aerodynamic analysis method for wind turbines. BEM is derived assuming stationary conditions, which limits its ability to model the unsteady aerodynamic effects. This becomes increasingly relevant for the flexible blades of current large-scale turbines, and the employment of passive and active aerodynamic control strategies, such as yaw, pitch control and smart rotor control. Currently, sub-models are included to consider the unsteady aerodynamic effects for wind turbine design. Previous research developed several dynamic-inflow engineering models to be integrated into BEM, to account for the unsteady flow acceleration. However, their applicability for unsteady load and the relative performance between the models are not fully known. The development of the dynamic wake of an actuator disc under unsteady load needs further understanding, to improve the engineering prediction of dynamic-inflow effect.

This research aims to evaluate the accuracy of BEM with current dynamic-inflow engineering models; to further understand the dynamic wake flow-field of an actuator disc undergoing unsteady load; to improve current dynamic-inflow engineering models for wind turbine design using numerical and experimental approaches.

A free wake vortex ring (FWVR) model is firstly developed. The accuracy of BEM with current dynamic-inflow engineering models of Pitt-Peters, Øye and ECN in predicting the induction of an actuator disc with unsteady load is verified using the developed FWVR model.

The wake flow response of an actuator disc undergoing unsteady loads is studied experimentally by using a disc model with variable porosity. The unsteady load is generated by a ramp type variation of porosity of the disc, at several reduced times of the ramp motion. The wake development of an actuator disc undergoing the same unsteady load tested in the experiments is further studied using the FWVR model.

The steady actuator-disc model is extended to unsteady load. Results from this linear actuator-disc model are compared with those from the FWVR model.

Finally, a new engineering model is developed using the differential form of the Duhamel's integrals of indicial response of the actuator-disc type vortex-models. The time constants of the indicial functions are obtained by the indicial responses of a linear and a nonlinear actuator-disc model, respectively.

The work provides more insights into the wake development of an unsteady actuator disc. The experimental results create a database for validation of unsteady numerical models, in prediction of the dynamic induction in the near wake of an actuator disc or a rotor. The limitation of current dynamic-inflow engineering models are evaluated and discussed. The new engineering model, which is developed based on the indicial response of the nonlinear actuator-disc model, can better predict the dynamic-inflow effects, especially for the radial distribution of the dynamic-inflow effect.

SAMENVATTING

Blade Element-Momentum-theorie (BEM) is de belangrijkste aerodynamische analyse methode voor windturbines. BEM is afgeleid met de aanname van stationaire condities, waarmee het modelleren van niet-stationaire aerodynamische effecten maar beperkt mogelijk is. Deze beperking is bijzonder relevant voor de huidige grootschalige windturbines die uitgerust zijn met flexibele bladen, maar ook bij toepassing van passieve en actieve regel strategieën, zoals 'jaw control', 'pitch control' en 'smart rotor control'. Momenteel worden in de ontwerpfase van windturbines sub-modellen toegepast voor het meenemen van niet-stationaire aerodynamische effecten. Eerder onderzoek heeft enkele ingenieursmodellen opgeleverd voor BEM met een dynamische instroming (dynamic inflow). De mate van toepasbaarheid van deze modellen voor niet-stationaire belasting en de onderlinge verschillen in prestaties worden echter nog niet volledig begrepen. Een beter begrip is vereist van de ontwikkeling van het dynamische zog achter een niet-stationair belaste remmende schijf (actuator disc), om tot een verbeterde voorspelling te komen van het dynamische instromingseffect. Met het huidige onderzoek wordt ernaar gestreefd om de nauwkeurigheid van BEM te evalueren tegen in omloop zijnde dynamische-instromingsmodellen, om meer te weten van het stromingsveld van een dynamisch zog achter een remmende schrijf onder niet-stationaire belasting en om huidige dynamische instromingsmodellen te verbeteren gebruikmakende van een numerieke en experimentele aanpak.

Als eerste is een "Free Wake Vortex Ring-model (FWVR) ontwikkeld. Met het FWVR model is een verificatie uitgevoerd van de nauwkeurigheid in het voorspellen van de inductie van een remmende schijf onder niet-stationaire belasting, gebruikmakende van BEM aangevuld met de dynamische instromingsmodellen van Pitt-Peters, Øye en ECN.

De respons van de stroming in het zog achter een remmende schijf onder niet-stationaire belasting is experimenteel onderzocht, middels een schijfmodel met variabele porositeit. De niet-stationaire belasting is opgewekt met een stapsgewijze variatie in porositeit van de schijf. Deze stap in porositeit is toegepast met verscheidene gereduceerde tijdsschalen. Daarnaast zijn dezelfde testcases toegepast in het FWVR-model in de bestudering van de zog ontwikkeling van een remmende schijf.

Het stationaire remmende schijfmodel is uitgebreid voor niet-stationaire belasting. Resultaten van dit lineaire remmende-schijfmodel zijn vergeleken met die van het FWVR model. Als laatste is een nieuw ingenieursmodel ontwikkeld gebaseerd op de wervel modellen voor een remmende schijf, gebruikmakend van de differentiaalvorm van de Duhamel-integralen voor een indiciële respons. De tijdsconstanten van de indiciële functies zijn verkregen op basis van het lineaire en niet-lineaire remmende schijf model.

Dit werk verschaft meer inzichten in de zog ontwikkeling van een niet-stationaire remmende schijf. De experimentele resultaten vormen een database voor de validatie van niet-stationaire numerieke modellen in het voorspellen van de dynamische inductie

in het nabije zog van een remmende schijf of rotor. De beperkingen van huidige dynamische instroming modellen zijn geëvalueerd en bediscussieerd. Het nieuwe ingenieursmodel dat is gebaseerd op de indiciële respons van het niet-lineaire remmende schijf model, kan de dynamische-instromingseffecten beter voorspellen, in het bijzonder de verdeling hiervan langs de straal van de schijf.

NOMENCLATURE

Acronyms

BEM Blade Element Momentum Method

ECN The ECN model

FWVR Free Wake Vortex Ring

MT Momentum Theory

MT+Øye Momentum theory integrated with the Øye model

MT+P-P Momentum theory integrated with the Pitt-Peters model

TUD-VR The new model based on the indicial response of the nonlinear actuator disc model

TUD-VT The new model based on the indicial response of the linear actuator disc model

Symbols

$\bar{v}_z$ Averaged axial velocity at the actuator disc plane [ms^{-1}]

δt^* Reduced ramp time ($\delta t^* = \frac{\delta t}{D/V_0}$) [-]

Γ Strength of vortex ring [$m^2\ s^{-1}$]

γ Strength of semi-infinite vortex tube [ms^{-1}]

Ω Solid angle [steradian]

ρ Fluid density [$kg\ m^{-3}$]

τ^* Time constant of velocity decay in the wake [s]

τ_0 Time scale of dynamic inflow ($\frac{D}{V_0}$)[s]

τ_1 Time constant in the Øye model [s]

τ_2 Time constant in the Øye model [s]

$\vec{f}$ The force density on the flow [Nm^{-3}]

A Area of the disc [m^2]

a Axial induction factor [-]

A_w	Area of streamtube section in the wake [m^2]
C_t	Thrust coefficient [-]
D	Diameter of the disc [m]
d	Displacement of the moving disc [m]
k	Reduced frequency ($k = \frac{\omega D}{2V_0}$) [-]
p_0	Pressure at the far upstream [N/m^2]
p_w	Pressure in the wake [N/m^2]
R	Radius of the actuator disc [m]
r	Radial coordinate [m]
R_i	Radius of i^{th} vortex ring [m]
R_{tube}	Radius of the semi-infinite vortex tube [m]
T	Thrust [N]
t	Time [s]
V_0	Free stream velocity [ms^{-1}]
V_d	Velocity at the disc [ms^{-1}]
v_r	Radial velocity [ms^{-1}]
v_r^{ind}	Radial induced velocity [ms^{-1}]
V_w	Velocity in the wake [ms^{-1}]
V_z	Axial velocity [ms^{-1}]
v_z^{ind}	Axial induced velocity [ms^{-1}]
v_{int}	Intermediate induced velocity [ms^{-1}]
v_{qs}	Quasi-steady induced velocity [ms^{-1}]
z	Axial coordinate [m]

CONTENTS

1

INTRODUCTION

1

This chapter introduces the motivation of the research and the main research questions, the approach and the outline of the thesis.

1.1. RESEARCH MOTIVATION

A wind turbine is a device for extracting kinetic energy from the wind. Wind is an unsteady flow of air, resulting in time-varying interactions and load on the wind turbines. This becomes increasingly relevant for the flexible blade of current large-scale turbines, and the employment of passive and active aerodynamic control strategies, such as yaw, pitch control and smart rotor control.

The main unsteady aerodynamic phenomena occur at three main scales: airfoil scale, blade scale and rotor scale. The latter is the so-called 'Dynamic inflow' or 'Dynamic wake' or 'Dynamic induction' problem, on which this thesis focuses.

Currently, the most popular design method for wind turbines is Blade Element Momentum (BEM) theory. BEM is derived assuming stationary conditions, which limits its ability to model the unsteady aerodynamic effects. Additionally, sub-models are required to be included to consider the unsteady aerodynamic effects for wind turbine design. Previous research developed several dynamic-inflow engineering models to be integrated into BEM, to account for the unsteady flow acceleration.

However, the relative performance between the models and their limitations are unknown. For the load cases of a primary study of this thesis (chapter 3), the current dynamic inflow models are found to underestimate the dynamic inflow effect. Because some of the current dynamic-inflow engineering models have parameters tuned based on limited load cases or using simplified vortex models, none of the existing models is considered as generic.

Furthermore, most of the previous research only focuses on the actuator plane. The understanding of the dynamic response of the entire flow field of an unsteady rotor is still limited.

This research aims :

- To evaluate the accuracy of BEM with current dynamic-inflow engineering models to account for the dynamic inflow effect.
- To further understand the dynamic wake flow field of an actuator disc undergoing unsteady load.
- To improve current dynamic-inflow engineering model for wind turbine design.

1.2. RESEARCH QUESTIONS

The research in this thesis focuses on understanding the unsteady wake development of an actuator disc, and its effect on the prediction of the dynamic induction at the actuator disc plane. The main research questions which evoke the study are :

- How accurate is BEM with current engineering models to account for dynamic inflow?
- How does the wake flow field of an unsteady actuator disc develop?
- How to improve the engineering models for dynamic inflow?

Each research question is analyzed in detail as follows:

1.2.1. HOW ACCURATE IS BEM WITH CURRENT ENGINEERING MODELS TO ACCOUNT FOR DYNAMIC INFLOW?

Although BEM was derived assuming steady conditions, it is used at dynamic inflow conditions by introducing dynamic-inflow engineering models.

BEM is based on the momentum theory and the blade element theory. There are two key intrinsic assumptions in BEM model. One is the equilibrium state assumption of momentum theory. The accuracy of BEM with engineering add-ons in unsteady load cases is unknown. The other assumption is the radial independence of flow passing through each adjacent annulus. The current dynamic-inflow engineering models are developed based on uniformly loaded rotor. However, they are integrated into BEM for radially-varying unsteady load assuming independent annuli. Its applicability in these cases is not yet fully verified.

1.2.2. HOW DOES THE WAKE FLOW FIELD OF AN UNSTEADY ACTUATOR DISC DEVELOP?

The unsteady load variation on the rotor affects the flow field in front of the rotor plane, at the rotor plane and aft the rotor.

The induced flow in front of and at the rotor plane is of the most interest for the dynamic inflow problem as it defines the inflow conditions, which determine the unsteady blade aerodynamic load and the rotor performance.

The flow field aft of the rotor is also of interest, as it can influence the process of turbulent mixing and re-energising in the wake. The unsteady wake development of front turbines determines the inflow conditions for the turbines downstream in a wind farm.

Previous studies mainly focused on the measurement of dynamic load during the unsteady load cases. However, there is limited measurement data of the unsteady wake flow response of a wind turbine.

Furthermore, previous research focused on the operational events of wind turbine, e.g. during a pitch angle transient, yaw and wind speed change etc. In these operational cases, the problem of dynamic inflow and the problem of unsteady airfoil aerodynamics are intertwined. There is no experimental work using an actuator disc to investigate the unsteady flow field of an open rotor. The use of an actuator disc to numerically and experimentally investigate the dynamic inflow effects is of interest for three reasons; firstly,

it is the basis of the design theory of an open rotor - BEM; secondly, it lends a fundamental perspective to many existing engineering models, which are also derived from the actuator disc theory; thirdly, the use of actuator disc model can help the study of dynamic inflow problem by eliminating the effect of blade geometry, rotational momentum, tip vortices etc.

1.2.3. HOW TO IMPROVE THE ENGINEERING MODEL FOR DYNAMIC INFLOW?

The existing dynamic-inflow engineering models are found to underestimate the dynamic inflow effects in chapter 3. This may result from the simplification of the vortex models and the limited load cases when these models are developed. A few steps are carried out to improve the performance of current engineering models using the more physically representative free wake vortex models.

The first step is to investigate the performance of a linearized free wake vortex model by extending the actuator disc model from steady to unsteady load. The second step is to develop a new engineering model directly based on the free wake vortex-models. The time constants of the flow decay functions are obtained based on a systematic study using both the linear and nonlinear actuator-disc based vortex-models. The strength of the thrust also affects the flow decay. The effect of different baseline thrusts are also investigated when developing the new engineering models.

1.3. APPROACH

In order to answer the research questions, both numerical and experimental methods are used.

The vortex model introduced by Joukowsky (1912, 1914, 1915, 1918) consists of blade bound vortices, a root vortex and a vortex at the tip of each blade. It is a basic vortex model which gives detailed information of a rotor flow field. The time-dependent free wake model can handle unsteady load intrinsically. Although tracking the discrete vortex element can be computationally expensive, it is still considerably less expensive than computational fluid dynamics (CFD) methods. This type of vortex model is chosen for this study.

In this thesis, a free wake vortex ring (FWVR) model is firstly developed to verify BEM with current dynamic-inflow engineering models for unsteady rotor aerodynamics (chapter 3). Radially varied load is also considered in this model.

The FWVR model is the foremost model used through out the thesis. It is used to verify BEM in chapter 3, to study the dynamic wake of an unsteady actuator disc undergoing transient load in chapter 5, to serve as a benchmark for comparison of the improved vortex tube model in chapter 6, and to obtain the time constants of the engineering model and serve as benchmark for comparison of all the engineering models in chapter 7.

The vortex model of Joukowsky results in a tubular vortex surface with uniform circulation based on the assumption of infinite number of blades. The tubular vortex becomes a circular cylinder vortex surface when the wake expansion is neglected. However, this type of fixed wake vortex model can only account for the steady flow field. In this thesis, the classical steady actuator disc vortex model is extended to unsteady and

radially varied flow for the unsteady rotor aerodynamic (chapter 6).

The dynamic inflow problem can be also studied using experimental techniques. In order to gain fundamental understanding of the impact of an unsteady actuator disc on the flow field, a novel experiment is designed to investigate the basic problem of wake flow response of an actuator disc undergoing unsteady load by using a disc model with variable porosity (chapter 4). The unsteady wake field of the actuator disc model is further analyzed using the experimental data and numerical results from the FWVR model in chapter 5.

A new dynamic-inflow engineering model is proposed in chapter 7. It is developed based on a linearized actuator disc model and a nonlinear actuator disc model for the flow decay at the actuator disc plane. The models are validated against the numerical results from the FWVR model and current dynamic inflow models of Pitt-Peters, Øye and ECN.

1.4. ORGANIZATION OF DISSERTATION

Chapter 1 Introduction

This chapter introduces the motivation, the main research questions, the approach and the organization of this thesis.

Chapter 2 State of the art of unsteady rotor aerodynamics

This chapter provides the context of this research by introducing the problem of unsteady rotor aerodynamics and the state of the art numerical and experimental studies on the dynamic inflow.

Chapter 3 Verifying BEM for unsteady load using a free wake vortex ring model

A FWVR model is firstly developed and verified in this chapter. The accuracy of BEM with current dynamic-inflow engineering models in predicting the induction of an actuator disc with unsteady load is investigated using the developed FWVR model. The results suggest that current engineering models need to be improved.

Chapter 4 Experimental study of an actuator disc undergoing unsteady load

In order to improve the current engineering models, the dynamic inflow problem needs better understanding. In this chapter, an experiment is designed to study the dynamic wake development of an actuator disc undergoing transient load.

Chapter 5 Numerical study of an actuator disc undergoing unsteady load

This chapter further investigates the wake development of an actuator disc undergoing transient load computationally by the FWVR model developed in chapter 3. The numerical results complement the experimental work in chapter 4 by providing information such as the vorticity field and contributions from different vortex elements, which allows the disclosure of the physics behind the observed wake development.

Chapter 6 Semi-analytical actuator disc solution for unsteady load

The FWVR model is demonstrated to be sufficient to predict the steady and unsteady wake of an actuator disc in chapter 3 and 5. This chapter investigates the unsteady wake of an actuator disc using semi-analytical actuator disc solutions. The classical steady actuator disc model is extended to unsteady conditions for this purpose. The improved actuator disc model is an intermediate model between an engineering model and a high fidelity free wake model, in terms of accuracy and computational time.

1

Chapter 7 A new dynamic-inflow engineering model based on linear and nonlinear actuator-disc vortex-models

A new engineering model is developed in this chapter. The time constants of the engineering models are obtained both from the linear actuator disc model developed in chapter 6 and the nonlinear actuator disc model developed in chapter 3. The performance of the new developed engineering model is compared to the current widely used engineering models and the direct numerical results from the FWVR model.

Figure 1.1 shows the structure of the thesis and the connection between chapters.

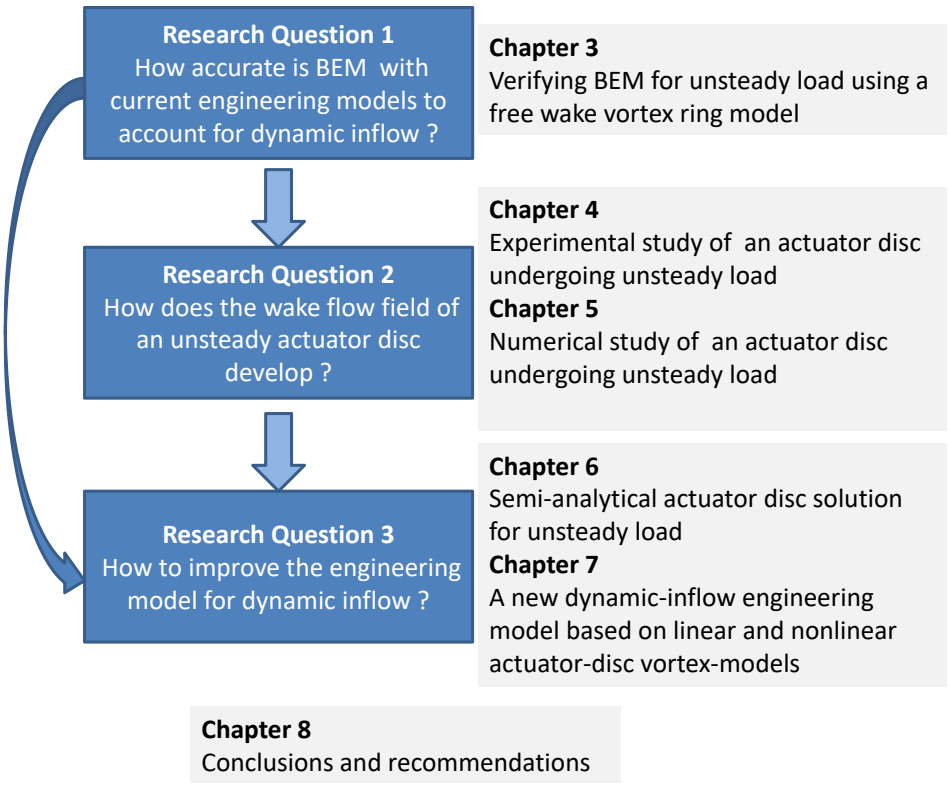

Figure 1.1: Graphic outline of the thesis.

2

STATE OF THE ART OF UNSTEADY ROTOR AERODYNAMICS

Research is what I'm doing when I don't know what I'm doing.

Wernher von Braun (1912-1977)

This chapter briefly introduces unsteady rotor aerodynamics and the history of dynamic inflow. The state of the art of research on dynamic inflow is presented separately for aspects of modelling and experimental work. This chapter introduces the following models: Blade Element Momentum and the actuator-disc wake model for steady rotor aerodynamics, the advanced vortex model and computational fluid dynamics (CFD) for unsteady rotor aerodynamics. The state of the art of dynamic-inflow engineering models used in the wind energy field is also introduced: the Pitt-Peters model (Pitt and Peters, 1981), the Øye model (Øye, 1986, 1990) and the ECN model (Schepers, 2012). These models are validated and benchmarked against experimental and numerical results later in this thesis. Finally, the experimental work on dynamic-inflow problem in the wind energy field are presented.

2.1. INTRODUCTION TO UNSTEADY AERODYNAMICS

Understanding aerodynamics is essential for the design of efficient and reliable wind turbines. According to Huyer et al. (1996), underestimating power output and load leads to the failure of generators, gear-boxes, and even turbine blades. This in turn increases operational and maintenance costs.

Furthermore, wind turbines are subjected to non-stationary environment. Turbulence, wind shear, the flexible blade structure of wind turbines, and the passive and active aerodynamic control strategies, such as yaw, pitch control and smart rotor control, leads to a wind turbine operating in a highly dynamic state. All these factors enhance the complexity of the flow field of a wind turbine. To accurately predict the unsteady flow field of a wind turbine is challenging.

The various aerodynamic sources which contribute to the unsteady aerodynamic load on a wind turbine are summarized in Figure 2.1, including the variation of wind speed or direction, turbulence, blade deformation, pitch, yaw, wake dynamic, etc. Only the effect of change due to change in load, not change in inflow is the subject of this thesis, which can be caused by a rotor-thrust change resulting from a pitch action, rotor speed variation, etc.

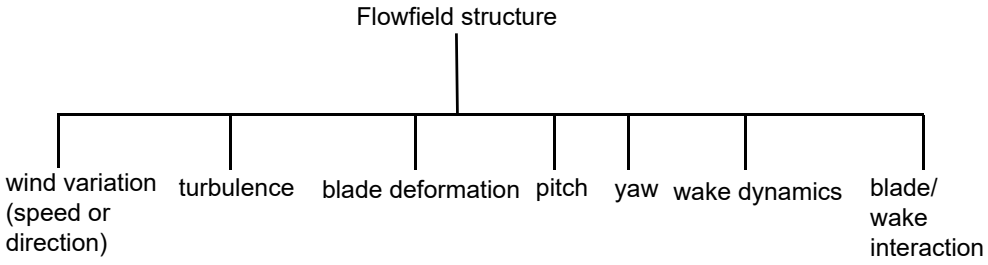

Figure 2.1: Summary of the various aerodynamic sources that contribute to the unsteady airloads on a wind turbine (modified from Leishman (2002)).

According to the length scale, the unsteady aerodynamics of a wind turbine can be divided into three main scales: airfoil scale, blade scale and rotor scale. This thesis focuses on the rotor scale, the phenomenon is also called 'Dynamic inflow' or 'Dynamic

wake' or 'Dynamic induction' in the literature.

Dynamic inflow refers to the time lagging in the response of the induced velocity field of a rotor following rapid changes in the rotor operating state (Hansen and Butterfield, 1993). The characteristic time scale for dynamic inflow is the ratio of the rotor diameter and the speed of incoming flow, represented by D/V_0 (Snel and Schepers, 1995). The wake can not reach a new equilibrium state instantaneously to a change in rotor loading because of the inertia of the air in the wake. This can be observed after a change in blade pitch angle or change in rotor thrust.

2.2. HISTORY OF DYNAMIC INFLOW RESEARCH

Dynamic inflow has gained much attention in rotary-wing analysis, relevant to the design and analysis of both rotorcraft and wind turbine.

2.2.1. DYNAMIC INFLOW IN ROTORCRAFT

Dynamic-inflow phenomena influence the unsteady rotor load. It has maintained a dominant position in the real-time flight simulation, stability computations, and flight mechanics and control (Peters, 2009). The history of dynamic-inflow development in rotorcraft application was summarized in Pitt (1980), Gaonkar and Peters (1986) and Peters (2009).

The dynamic-inflow studies in rotorcraft flight dynamics started in the 1950's. Amer (1950) developed a theory to predict the pitch and roll damping of a rotor. The response of a hovering rotor to rapid changes in collective pitch was measured by Carpenter and Fridovich (1953), and they addressed the time lag of inflow by introducing the 'apparent mass' concept. They assumed that the uniform induced velocity of the initial flow field is analogous to the flow field produced by an impermeable disc moved normal to its plane. Sissingh (1952) derived the inflow formulas for both hover and forward flight. It is the first prototype of a dynamic-inflow model, albeit quasi-steady, Peters (2009) thought that it includes enough physics to explain the effects.

The research boomed in the 1970's and 1980's. The unsteady dynamic rotor hovering wake was modeled as an approximate steady-state wake with a time lag by Crews and Hohenemser (1973). Crews' unsteady inflow theory (Crews and Hohenemser, 1973) was extended by Peters (1974) to encompass more general inflow models. Pitt and Peters (1981) used the potential functions of Mangler and Squire (Mangler and Squire, 1950) to develop a closed-form representation of the induced flow matrix [L] and the rotor response matrix [M]. This was the development of the Pitt-Peters dynamic inflow model, which became one of the most important models in flight simulations and rotor response analysis of rotorcraft.

2.2.2. DYNAMIC INFLOW IN WIND TURBINE

Snel and Schepers (1995) pointed out that the wind turbine operational conditions are different from the conditions experienced by helicopters. Helicopters are designed for high thrust with minimum power consumption at low induction factors, while wind turbines are designed for maximum power extraction at high induction factors close to 1/3. The dynamic-inflow effects enhance with higher induction factors, due to the interrela-

tionship between the dynamic-inflow problem and the induction field. Therefore, some of the assumptions and simplifications used in the helicopter related models may not be applicable for wind turbine aerodynamics, which needs further justification.

The importance of dynamic inflow in wind energy applications has been realized since the 1990's, and subsequently it became one of the most interesting topics of wind turbine research.

A joint investigation of dynamic-inflow effect supported by six European organizations was initiated in the 1990's, the JOULE project I (Snel and Schepers, 1995) and II (Schepers and Snel, 1995). Several dynamic-inflow models were proposed and tested in these research. The Pitt-Peters dynamic-inflow model (Pitt and Peters, 1981) for rotorcraft was modified to annular sections to apply to wind turbines by Suzuki (2000). Detailed measurements on dynamic-inflow characteristics under a series of unsteady operational conditions were conducted during the NREL/NASA Ames wind tunnel tests (Hand et al., 2001) on a 10m rotor. Dynamic inflow measurements are also part of the goal of ongoing EU FP5 projects on the MEXICO rotor in phase I (Schepers and Snel, 2009) and phase II (Schepers et al., 2014).

The importance of including a dynamic-inflow model when estimating the free mean wind speed and the induced velocities in aero-servo-elastic modelling was demonstrated by Henriksen et al. (2013). To consider dynamic-inflow effects for designing a controller of wind turbines was also found important by van Engelen and van der Hooft (2004) and Hansen et al. (2005).

2.3. DYNAMIC INFLOW MODELLING

The most rigorous way of calculating the unsteady flow field of a rotor is to solve the time-dependent incompressible Navier-Stokes equations (Snel, 1998). However, due to the computational cost of CFD, it is used more often as an analysis method rather than a design method presently.

Vortex modelling by using the Euler equations instead of the Navier-Stokes equations is an intermediate method between the CFD and BEM method, in terms of the computational cost, complexity and accuracy. Free wake vortex models can intrinsically handle the unsteady aerodynamic problem. Even though the computational cost of the vortex models is considerably less than that of CFD, it is still much higher than Blade Element Momentum method.

The current widely used design and analysis tool for rotor aerodynamics is still BEM method. However, due to the quasi-steady wake assumption, BEM can only account for the steady rotor aerodynamics. A practical solution is to integrate BEM with dynamic-inflow engineering models.

BEM method and the state of the art dynamic-inflow engineering models of Pitt-Peters, Øye and ECN are introduced in the following first two subsections. The basic actuator-disc model for steady wake and more advanced models for dynamic wake of a rotor are introduced in the last two subsections, respectively.

2.3.1. BLADE ELEMENT MOMENTUM THEORY

Since the first introduction of BEM method to wind turbine design (Wilson and Lissaman, 1974) four decades ago, it has remained the main tool for wind turbine rotor aerodynamic design and aero-servo-elastic load simulation. The major reasons behind the predominance can be summarized as

- It is computationally cheap and easily integrated with a servo-elastic model.
- This approach allows fundamental understanding of the effects of varying geometrical and aerodynamic parameters on the performance of a wind turbine (Leishman, 2002), by taking into account the sectional aerodynamics of airfoil.
- In spite of the assumptions and oversimplifications made in BEM theory, the method often predicts rotor performance with acceptable accuracy (Hansen and Butterfield, 1993).

The blade element momentum theory applied for wind turbine analysis is reported in ample literature, e.g. the textbooks by Burton et al. (2001) and Leishman (2006). The basic ideas of momentum theory and blade element theory and their main assumptions which challenge the application to dynamic inflow study are introduced concisely below.

AXIAL MOMENTUM THEORY

The momentum theory is the most basic way to analyze a wind turbine, which is also called "actuator-disc theory" or "one-dimensional slip-stream theory". It was first developed by Rankine (1865) and Froude (1889). The history of the development of momentum theory can be found in van Kuik et al. (2015). Sørensen (2016) summarized the recent development of momentum theory on application to HAWT.

In the axi-symmetric axial flow, a 1-D model of the control volume of a wind turbine is shown in Figure 2.2. The rotor is represented by a hypothetical permeable actuator disc, which exerts a force on the flow. The boundary surface which separates the affected flow from undisturbed flow is extended upstream and downstream to form a streamtube. The flow within the streamtube slows down, the cross-sectional area of the streamtube must expand to accommodate it. The undisturbed wind speed is V_0, the axial induced velocity at the plane of the turbine is denoted as v_i, with the axial induced velocity in the far wake being v_w. The axial induced velocity is the velocity reduction resulting from the energy extracting of the turbine. Therefore, the net velocity at the plane of the turbine is $V_0 - v_i$, the net velocity in the far wake is $V_0 - v_w$.

- `Mass conservation`

  By applying the principle of the conservation of mass, the fluid mass flow rate, $\dot{m}$, through the disc is

$$\dot{m} = \rho A(V_0 - v_i). \tag{2.1}$$

- `Momentum conservation`

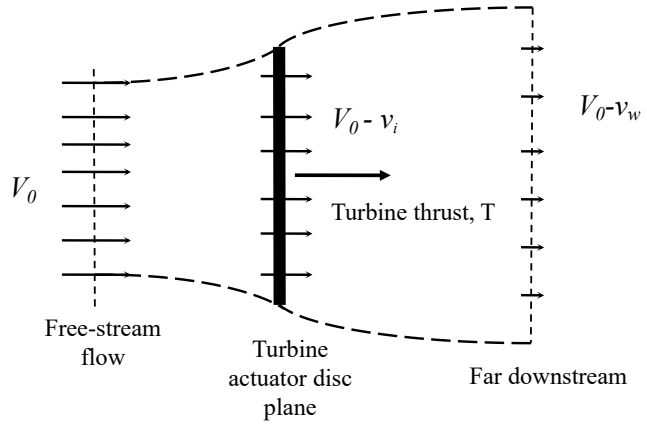

Figure 2.2: Flow model used for the momentum theory analysis of a wind turbine.

The thrust on the disc can be represented by the change of momentum of the flow across the disc

$$T = \dot{m}V_0 - \dot{m}(V_0 - v_w). \tag{2.2}$$

After expanding the above equation, a relationship between the thrust on the turbine and the velocity deficit in the far downstream can be obtained,

$$T = \dot{m}V_0 - \dot{m}V_0 + \dot{m}v_w = \dot{m}v_w. \tag{2.3}$$

- `Energy conservation`

  By applying the law of the conservation of energy, the power extracted from the flow is

$$P = \frac{1}{2}\dot{m}V_0^2 - \frac{1}{2}\dot{m}(V_0 - v_w)^2 = \dot{m}v_w(V_0 - \frac{1}{2}v_w). \tag{2.4}$$

  The energy absorbed by the disc can also be obtained by

$$P = T(V_0 - v_i). \tag{2.5}$$

  Substituting Equation 2.3 into Equation 2.5 yields

$$P = \dot{m}v_w(V_0 - v_i). \tag{2.6}$$

  Under the assumption of no viscosity and no other loss, the kinetic energy absorbed by the disc should equal to the power extracted from the flow (ie. Equation 2.4 equals to Equation 2.6), which gives $v_i = v_w/2$.

  In the analysis of a wind turbine, it is usual to define an independent parameter, the induction factor $a = v_i/V_0$. Accordingly, $v_i = aV_0$, $v_w = 2aV_0$.

Combining Equation 2.3 and 2.1, the thrust is

$$T = \rho A(V_0 - v_i)\, v_w. \tag{2.7}$$

Substituting $v_i = aV_0$, $v_w = 2aV_0$ into Equation 2.7 gives

$$T = \rho A(V_0 - V_0 a)2V_0 a = 2\rho AV_0^2(1-a)a. \tag{2.8}$$

The thrust coefficient is defined by

$$C_t = \frac{T}{\frac{1}{2}\rho AV_0^2}. \tag{2.9}$$

Consequently,

$$C_t = \frac{2\rho AV_0^2(1-a)a}{\frac{1}{2}\rho AV_0^2} = 4a(1-a). \tag{2.10}$$

Combining Equation 2.6 and 2.1 gives

$$P = \dot{m}v_w(V_0 - v_i) = \rho A(V_0 - v_i)v_w(V_0 - v_i) = \rho A(V_0 - v_i)^2 v_w. \tag{2.11}$$

Substituting $v_i = aV_0$, $v_w = 2aV_0$ into Equation 2.11 results in

$$P = \rho A(V_0 - aV_0)^2 2aV_0 = 2\rho AV_0^3(1-a)^2 a. \tag{2.12}$$

The power coefficient is defined as

$$C_p = \frac{P}{\frac{1}{2}\rho AV_0^3}. \tag{2.13}$$

Hence

$$C_p = \frac{2\rho AV_0^3(1-a)^2 a}{\frac{1}{2}\rho AV_0^3} = 4(1-a)^2 a. \tag{2.14}$$

The momentum theory itself only gives the averaged velocity of the actuator disc, but not the velocity distribution at the disc. It is valid for inviscid, incompressible, steady flow.

STEADY ASSUMPTION OF THE AXIAL MOMENTUM THEORY

The momentum theory is only applicable when the flow field reaches an equilibrium state. It assumes that the velocity and pressure field follows the load changes instantaneously. However, during the operation of a wind turbine, the load on the disc varies frequently due to the sources in Figure 2.1.

Figure 2.3 shows the change of the streamtube and the velocity when the load on the disc changes from a low thrust to a higher one. The flow will be decelerated due to the increased load. It takes a certain time for the flow to accomplish the change due to the inertia of the streamtube flow volume. To understand the time delay of the development of the new induction flow field is essential to model the dynamic inflow effect correctly by adding it into the steady BEM simulation.

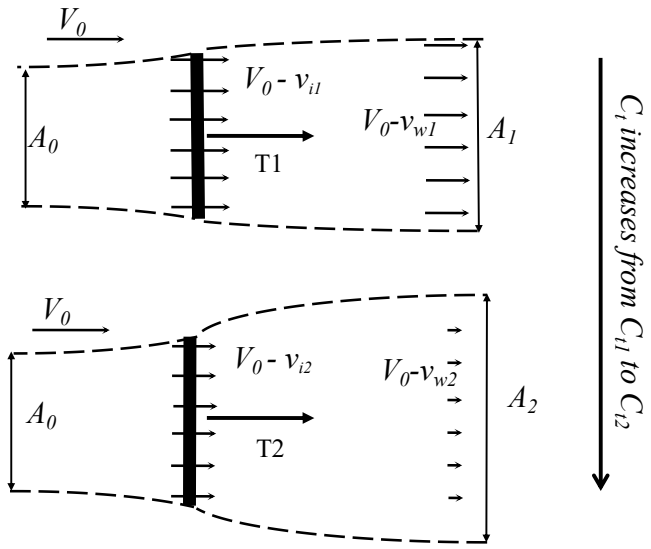

Figure 2.3: Change of the streamtube and velocity when the load change on the rotor.

BLADE ELEMENT THEORY

The momentum theory considers the averaged force and velocity at the actuator disc plane. In practice, the equations are applied to annuli, which is swept by an independent element of the blade. The induced velocity at each element is attained by performing a momentum balance for an annular control volume containing the blade element and the air bounded by the stream surfaces extending upwind and downwind of the element. The aerodynamic forces on the element are calculated using two-dimensional lift and drag coefficients at the local angle of attack.

ASSUMPTION OF THE BLADE ELEMENT THEORY

The main assumption of the blade element theory is that they are independent from each other. This is challenged when applying it to the analysis of the blade with abrupt changes of load in radial direction. According to Sørensen and Kock (1995), this assumption is acceptable, except for regions where load changes abruptly, for example, at the root and the tip regions. The annuli were shown to be not independent and the pressure at the boundary of the annuli was suggested by van Kuik and Lignarolo (2016) to be included in the momentum theory to remedy the effect of annuli independent assumption. Another situation where this assumption might not be applicable is when distributed aerodynamic control is applied. For instance, the application of trailing edge flaps or micro-tabs can create a non-uniform distributed loading along the blade span.

2.3.2. DYNAMIC-INFLOW ENGINEERING MODELS

Various dynamic-inflow engineering models have been proposed and applied in the wind energy field. The widely used ones are the models of Pitt-Peters (Pitt and Peters,

1981), Øye (1986, 1990), and ECN (Schepers, 2012), which are introduced in the following in detail. All the models describe the distribution of the inflow in the form of ordinary equations, with time constants representing the dynamic lag in the build-up of the inflow. The theory behind the models are different. The model of Pitt and Peters (1981) is based on the 'apparent mass ' theory. The latter two are developed based on vortex models.

THE PITT-PETERS DYNAMIC INFLOW MODEL

THE Pitt-Peters dynamic inflow model (Pitt and Peters, 1981) was developed for an actuator disc with an assumed inflow distribution across the disc. Based on the assumption that the equation of Pitt-Peters can be applied to a blade element or actuator annulus level, the dynamic inflow equation for each annular ring becomes

$$\frac{1}{\rho A_j V_0^2/2}\left[\frac{8}{3\pi}\rho A_j r_j \frac{dv_j}{dt} + 2\rho A_j v_j (V_0 + v_j)\right] = C_{tj}. \tag{2.15}$$

where j indicates the j^{th} annular ring, A_j and C_{tj} are the area and thrust coefficient of the j^{th} annulus and v_j is its azimuthal averaged induced velocity. The first term inside the outer bracket of Equation 2.15 represents the additional force on the rotor disc resulting from the accelerating or decelerating inflow (Leishman, 2002), while the second term results from the static pressure difference across the actuator disc.

THE ØYE DYNAMIC INFLOW MODEL

IN the dynamic inflow model of Øye (1986, 1990), the induced velocity is estimated by filtering the quasi-steady values through two first-order differential equations

$$v_{int} + \tau_1 \frac{dv_{int}}{dt} = v_{qs} + b\tau_1 \frac{dv_{qs}}{dt}. \tag{2.16}$$

$$v_z + \tau_2 \frac{dv_z}{dt} = v_{int}. \tag{2.17}$$

where v_{qs} is the quasi-steady value from BEM, v_{int} is an intermediate value and the final filtered value v_z is treated as the induced velocity. After calibration using a vortex ring model (Øye, 1990), the two time constants are recommended as follows (Snel and Schepers, 1995)

$$\tau_1 = \frac{1.1}{(1-1.3a)}\frac{R}{V_0}. \tag{2.18}$$

$$\tau_2 = (0.39 - 0.26(\frac{r_j}{R})^2)\tau_1. \tag{2.19}$$

where a is the axial induction factor, R is the rotor radius, r_j is the radius of j^{th} annulus, and b is a constant value of 0.6.

THE ECN DYNAMIC INFLOW MODEL

THE dynamic inflow model developed by Schepers (2012), was derived from an integral relation of the streamtube model (see more details of the streamtube model in subsection 2.3.3). For the condition of constant wind speed, the equation is

$$\frac{R}{V_w} f_a \frac{da}{dt} + a(1-a) = C_{tj}/4. \tag{2.20}$$

where C_{tj} is the axial force coefficient on the rotor annulus j. The term f_a is a function of the radial position, defined as

$$f_a = 2\pi / \int_0^{2\pi} \frac{[1-(r/R)cos\Phi_r]}{[1+(r/R)^2-2(r/R)cos\Phi_r]^{3/2}} d\Phi_r. \tag{2.21}$$

These models have been applied to different aero-elastic codes. The Pitt-Peters model has been applied in the open source code from NREL — Aerodyn (Laino and Hansen, 2002), the Øye's model has been applied to DTU's code HAWC2 (Larsen and Hansen, 2007), the ECN's model has been applied to the code PHATAS (Lindenburg, 2005). The improvements over quasi-steady models was reported. However, to what extent they can reflect the real dynamic inflow problem is unknown, and their comparative performance is not fully evaluated.

The use of BEM with engineering add-ons has become popular in the design frame of a wind turbine, due to its favorable implementation within an aero-servo-elastic program and the modest computational time. In addition to the engineering models, more advanced models, which can account for more physics, are introduced in the following sections.

2.3.3. ACTUATOR-DISC MODEL FOR STEADY WAKE

The vortex model was introduced by Joukowsky (1912, 1914, 1915, 1918), consisting of blade bound vortices, a root vortex and a vortex at the tip of each blade. The application of the actuator disc with infinite number of blades leads to a simple wake model, which is illustrated in Figure 2.4. Details of a rotor flow field can be calculated from such a vortex model.

It results in a linear actuator-disc model representation as shown in Figure 2.5, when the wake expansion is neglected. Analytical formulae of the velocity induced by a right cylinder were independently obtained by Callaghan and Maslen (1960), Gibson (1974), van Kuik and Lignarolo (2016), and Branlard and Gaunaa (2014) using different approaches. Callaghan and Maslen (1960) derived the magnetic field of a finite solenoid based on vector potential, which is applicable to velocity field calculation of a right vortex cylinder with tangential vorticity in rotor aerodynamics. Gibson (1974) obtained all three components of the velocity field induced by a semi-infinite vortex cylinder based on a lemma and integration by parts and proved the feasibility of applying the semi-infinite vortex cylinder to actuator disc flow. van Kuik and Lignarolo (2016) obtained the analytical axial velocity of a semi-infinite vortex tube using the gradient of the solid angle. Branlard and Gaunaa (2014) obtained the analytical equations of the velocity field induced by a finite or semi-infinite vortex tube using direct integration of the Biot-Savart law.

Using a superposition of a system of coaxial vortex cylinders to calculate the induced velocity field of non-uniform disc loading was applied by Heyson and Katzoff (1956) and Branlard and Gaunaa (2014).

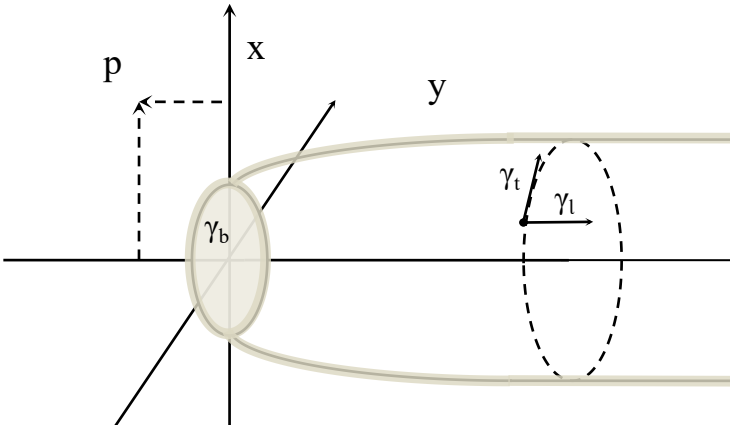

Figure 2.4: A nonlinear actuator disc model, representing the wake of a wind turbine.

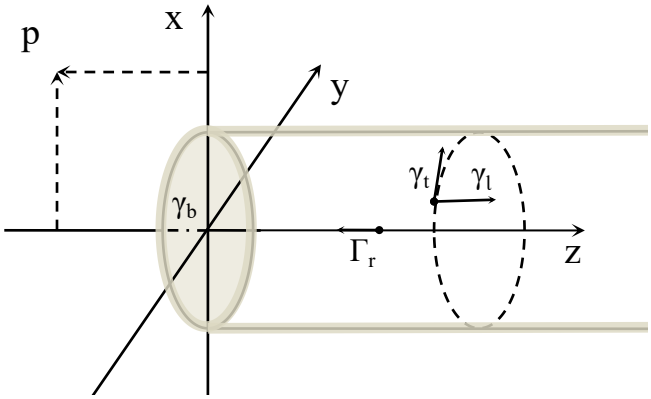

Figure 2.5: A linear actuator disc model, representing the wake of a wind turbine.

2.3.4. ADVANCED MODELS FOR DYNAMIC WAKE

The free tracking vortex-based model and CFD models inherently can account for the unsteady aerodynamic effects of a rotor. These advanced models are more physically representative than the dynamic-inflow engineering models, at the cost of more computational time.

VORTEX MODELLING

Vortex models have become popular in the analysis of a wide range of aerodynamic problems (Cottet and Koumoutsakos, 2000; Lewis, 1991). The historical and recent de-

velopments of the vorticity-based methods for the study of wind turbine aerodynamics are detailed in Branlard (2017). The vortex models applied to rotor wake problems can be divided into two categories : the "prescribed" and "free" vortex techniques (Leishman, 2002).

In the prescribed vortex models, positions of the vortical elements are specified beforehand based on semi-empirical rules. The prescribed vortex model in wind turbine application is constrained by the limited documented wake vortices positions, which has to be obtained by experiments encompassing a wide range of rotor geometric (e.g., blade shape and twist) and operating states (wind speed, yaw angle, etc.) (Leishman, 2002).

In the free vortex models, the vortex elements are convected and deformed freely under the action of the local velocity field to force-free locations, which are pertinent for the dynamic inflow study. The free vortex model has been applied to the helicopter analysis since 1970s (Clark D.R., 1970). The application has been transmitted to wind turbines later on. The theoretical development of a method for prediction of the aerodynamic performance of horizontal axis wind turbines was presented by Jeng and Keith (1982). Various vortex tools were applied in the JOULE projects (Snel and Schepers, 1995; Schepers and Snel, 1995). Among them, the AWSM code (van Garrel, 2003) is a free wake lifting line model developed in ECN; the ROVLM (Bareiss and Wagner, 1993) is a free/hybrid wake code, in which the flow field around a solid lift producing surface is modelled by superposition of the singularities of a source and a doublet on the panel with the free stream velocity. This is also called panel method or panel model. The code GENUVP (Voutsinas, 2006) is also a free wake panel code based on a vortex particles (vortex blobs) approximation of the wake. Time constants in the Øye 's dynamic-inflow engineering model (Snel and Schepers, 1995) was also tuned using a hybrid wake model represented by discretized vortex rings (Øye, 1990).

A 3D unsteady free wake panel model was applied to a vertical axis wind turbine (VAWT) by Ferreira (2009) to understand the dynamics of the 3D near wake. A 3D unsteady, potential flow panel model was also used by Micallef (2012) to study the 3D flow field near a horizontal axis wind turbine (HAWT) rotor under yawing. Recently, a free wake lifting line model was developed and applied to HAWT under yawing and pitching conditions. A good agreement with experiments of three different turbine models in terms of blade load, the rotor torque and the locations of the tip vortex cores in the wake was obtained (Qiu et al., 2014).

The needed memory and computational time increases exponentially with the increase of number of discrete elements per vortex filament, which makes the technique of free wake vortex modelling very expensive. However, it is still considerably less expensive than using CFD methods. Due to the artificial viscosity, CFD tends to cause concentrated vorticity to decay (Peters, 2009). This explains why the free wake models are more suitable for induced field calculation than CFD. The artificial viscosity is needed for numerical stability in CFD.

The application of the GPU technique makes it practical to run the simulations in this thesis using free wake modelling on a personal computer.

COMPUTATIONAL FLUID DYNAMICS

In the application of CFD to rotor aerodynamics, the continuous flow domain of the wake of a wind turbine is governed by the RANS or LES equations. The equations are solved in a discrete manner. It is divided into two categories based on the different representation of the blades — the generalized actuator disc approach and the direct approach (Sanderse et al., 2011). In the former, the blades are represented by a body force; in the latter, the actual blades are directly discretized on a computational mesh.

Depending on the different ways of representing the blades, the generalized actuator disc approaches are divided into actuator disc, actuator line and actuator surface. Rajagopalan and Rickerl (1990) were one of the first to apply the actuator-type approach in a CFD code. Although the actuator disc methods are only for steady load conditions, Sørensen and Myken (1992) made it suitable for unsteady computations by representing the axisymmetric Euler equations in a vorticity-stream function formulation. Sørensen and Kock (1995) employed this model to calculate the unsteady flow past the 2 MW Tjæreborg wind turbine. As an extension of the actuator disc approach, the actuator line approach, where the force term is represented by a actuator line for the wake calculation of a rotor , was introduced by Sørensen and Shen (2002). The method was implemented in the CFD code of EllipSys3D by Mikkelsen (2003), which has been applied in various subsequent researches. The actuator line was further extended to actuator surface approach by Shen et al. (2007, 2009).

The CFD methods are increasingly applied to wind turbine aerodynamics and wind farm aerodynamics. However, the demanding computational requirements limit it for analysis tool rather than design tool at current stage.

2.4. EXPERIMENTS ON DYNAMIC INFLOW

Most of the experimental research on dynamic inflow of wind turbines were conducted in the projects mentioned in subsection 2.2.2. Some more details are given in this section.

Øye (1986) observed the delay of response of flapwise moment and power from change of pitch angle on Nibe B HAWT. In the project JOULE I (Snel and Schepers, 1995), both axisymmetric and yawed cases were tested. Two turbines were utilized for the test. The measurement on the full scale turbine of Tjæreborg focused on pitching transient and yawed flow conditions (Øye, 1991a,b). However, only the blade bending moments were successfully measured. The measurement on a wind turbine model tested in the TUDelft open jet wind tunnel focused on the wind gust and yawed flow. The velocity at three fixed positions just downstream the rotor plane was measured by a hot wire for some specific test cases (Snel and Schepers, 1995). The wind gust was not simulated successfully, because the generation of gust was slower than the dynamic inflow time scale. The velocity measured at downstream planes was not representative as the azimuthal position relative to the rotating blade also changed in this set-up where the measurement positions were fixed. In the project JOULE II (Schepers and Snel, 1995), a big supplement to the project JOULE I was that partial pitch transient load cases were tested.

In the NREL/NASA Ames wind tunnel test (Hand et al., 2001), a series of operational conditions ranging from upwind axial operation, down wind operation, pitch step, yaw

operation and variation in angle of attack were tested. An important improvement of this test was that the instantaneous pressure at five radial positions instead of only blade bending moment as in previous projects was measured. This provides the information for studying the radial dependency of the time constant along the blade (Schepers, 2007).

In the MEXICO project phase I (Schepers et al., 2012), pitching transient and variation of incoming flow were tested on a 3 bladed turbine with 4.5m diameter in the Large Low-speed Facility (LLF) of DNW in the Netherlands. However, the dynamic inflow effects were too small to be used for validation due to a slow change in pitch and flow (Schepers et al., 2014). Therefore, in the second phase (Schepers et al., 2014), the test cases in phase I were reconducted, and also yawed conditions were tested.

Full scale turbines operating in real atmospheric flow conditions were further tested in DANAERO experiment (Madsen et al., 2010; Troldborg et al., 2013). Measurements were performed on a 2MW NM80 turbine with an 80m rotor undergoing pitch transient at the Tjæreborg Enge site (Madsen et al., 2010) . However, Schepers et al. (2014) thought that it was not sufficient for analysis of dynamic inflow effects due to the atmospheric turbulence effect, because only 10 min data was acquired. Consequently, a new campaign was performed on a Siemens 3.6MW turbine at the Høvsøre test site in Denmark (Madsen et al., 2010). The blade bending moment and flow at five radial locations along the blade were obtained under pitch transient with a pitch rate of 1 degree per second.

The above mentioned experiments were performed with different size of turbine models, ranging from wind tunnel models to full-scale wind turbines. Basically, two different operational cases were tested: the axi-symmetric case, including step pitch and variation in incoming flow; the axi-asymmetric case, yawed conditions. The blade bending moment was the focus for most cases. The distributed pressure and inflow velocity at different radial locations along the blade were measured at some specific tasks. The velocity in the wake was only measured once in the test case of wind gust during project JOULE I (Snel and Schepers, 1995). As mentioned, the first problem of this test was that the generation of gust was too slow. The second problem was that the velocity was measured at fixed location in the wake of the rotor while the blade rotates.

In summary, the previous experimental work on dynamic inflow can be improved at the following two aspects.

- The unsteady airfoil aerodynamics is intertwined in the dynamic inflow problem in the past tested cases, where the blades of a full-scale wind turbine or a wind turbine model are pitching. New experimental set-ups should be designed to decouple the effects.

- Previous research mainly focused on the load and velocity measurement at the rotor plane, not in the wake. The wake determines the induction on the rotor and it also determines the inflow conditions for the downstream rotors, but the wake development under unsteady load is unknown and requires new research.

3

VERIFYING BEM FOR UNSTEADY LOAD USING A FREE WAKE VORTEX RING MODEL

You can avoid reality, but you cannot avoid the consequences of avoiding reality.

Ayn Rand (1905-1982)

The main content of this chapter has been published in

Yu, W., Ferreira, C. S., van Kuik, G., and Baldacchino, D. (2016) Verifying the Blade Element Momentum Method in unsteady, radially varied, axisymmetric loading using a vortex ring model. Wind Energ., doi: 10.1002/we.2005.

Although BEM method was derived for steady conditions, it is used for unsteady conditions by using corrections of dynamic-inflow engineering models. Its applicability in these cases is not yet fully verified. In this chapter, the validity of the assumptions of quasi-steady state and annuli independence of the blade element momentum theory for unsteady, radially varied, axisymmetric load cases is investigated. Firstly, a free wake model which combines a vortex ring model with a semi-infinite cylindrical vortex tube is developed, and applied to an actuator disc in three load cases: (I) steady uniform and radially varied, (II) two types of unsteady uniform load, and (III) unsteady radially-varying load. Results from the three cases are compared with Momentum Theory, and also with the dynamic-inflow engineering models of Pitt-Peters, Øye model and ECN model for the unsteady load cases. For unsteady load, the free wake vortex ring model predicts different hysteresis loops of the velocity at the disc or local annuli, and different aerodynamic work from the dynamic-inflow engineering models. Given that the free wake vortex ring model is more physically representative, the results indicate that the dynamic-inflow engineering models should be improved for unsteady loaded rotor, especially for radially-varying unsteady loads.

3.1. INTRODUCTION

As introduced in chapter 2, the mostly used BEM method is challenged by two main intrinsic assumptions. One is the equilibrium state assumption of Momentum Theory. Another is the assumption of radial independence of flow passing through each adjacent annulus.

A few works were tried to improve these limitations of BEM. Sørensen and Myken (1992) obtained a nonlinear and unsteady actuator-disc model using a time-dependent vorticity-stream function formulation, but Chattot (2014) pointed out that errors will be introduced with this method because vorticity diffuses from the slip line unphysically. Chattot (2014) tried to extend the steady actuator disc theory to unsteady flow based on conservation laws, but his numerical results showed the formulae can not correctly account for unsteady effects. Conway (1995) obtained a linear solution for an actuator disc with steady heavy loads, which was extended to a semi-analytical non-linear method to consider certain distributions of radially-varying load (Conway, 1998).

The current approach to overcome the limitation of BEM to steady conditions is to apply dynamic-inflow engineering models. The dynamic-inflow engineering models of Pitt-Peters, Øye and ECN, which are introduced in chapter 2, are integrated with Momentum Theory for verification in this chapter.

The unsteady load on wind turbines is determined by the non-stationary environment. The limits of the effectiveness of velocity prediction of BEM in unsteady load cases are unknown. Furthermore, some dynamic-inflow models are based on the same independent annuli assumption of BEM. To date, only specific radially-varying load and unsteady load of an actuator disc were discussed separately in previous studies (Conway, 1998; Madsen and Rasmussen, 2004).

In this chapter, the validity of BEM with dynamic-inflow engineering models in predicting the induction of an actuator disc with unsteady, radially-varying load is investigated using a free wake vortex ring (FWVR) model. The time-dependent modelling can handle unsteady load intrinsically. The vortex rings are expanding or contracting freely

due to the radial velocity induced by all the vortex rings and the semi-infinite cylindrical vortex tubes. Local pressure gradients caused by locally varied load can be considered in this model.

In section 3.2, the approach and the development of the FWVR model are detailed. Subsequently, a convergence study and the validity of the FWVR model are addressed in section 3.3. Results are presented in section 3.4 for three load cases: (I) steady uniform and radially-varying load, (II) two types of unsteady uniform load, (III) unsteady radially-varying load. Additionally, the effect of dynamic induction on aerodynamic work is also discussed. Conclusions are drawn in section 3.5.

3.2. APPROACHES AND MODEL DEVELOPMENT

3.2.1. THE DEVELOPMENT OF THE FWVR MODEL

The development of the FWVR model will be presented in this section. The three dynamic-inflow models of Pitt-Peters, Øye and ECN will be applied to Momentum Theory on the entire actuator disc for Case II, and applied to each annulus for Case III, for comparison with the FWVR model.

For an incompressible, inviscid fluid, the motion of the fluid particles is governed by the Euler equation

$$\rho \frac{D\vec{v}}{Dt} = -\nabla p + \vec{f} \tag{3.1}$$

and the continuity equation

$$\nabla \cdot \vec{v} = 0 \tag{3.2}$$

where $\vec{v}$ is the velocity vector, $\vec{f}$ is the force density distribution which the body acts on the flow, ρ is the fluid density and p is the static pressure. When wake rotation can be neglected, the vortex tube of an actuator disc can be treated as distributed ring vortices along the tube surface shed from the edge of the actuator disc and extended to the infinite downstream (Conway, 1995).

The vortex surface is modelled as discrete vortex rings, which are shed from any radial location of the disc's surface where the local pressure gradient is non-zero. In axial and axi-symmetric flow, $\vec{f} = \vec{e}_z f$. Integrating it across the thickness dz of the disc yields a pressure jump $\Delta p = \int f dz$. van Kuik (2003) obtained a relationship between vortex strength and pressure jump, given by

$$\frac{D\Gamma_{edge}}{Dt} = \frac{\Delta p}{\rho}. \tag{3.3}$$

The wake model is segregated into the near wake and the far wake, similar to the work from Øye (1990), van Kuik and Lignarolo (2016) for a steady load case. In this chapter, the near wake is modelled by dynamic surfaces, consisting of free vortex rings shed from the edge of the actuator disc or other radial locations of the disc's surface where the local pressure gradient is non-zero; the far wake is represented by semi-infinite cylindrical vortex tubes with constant strength and radius. The vortex rings are considered as thin, axi-symmetric and uniform. Axi-symmetric rings means that rings may expand or contract, their central axis always coinciding with the axis of the actuator disc. Figure 3.1 illustrates the vortex model schematically. The wake consists of numerous vortex rings

for the near wake and semi-infinite vortex tubes for the far wake. The vortex rings are shed at the edge and at positions where there is a pressure jump.

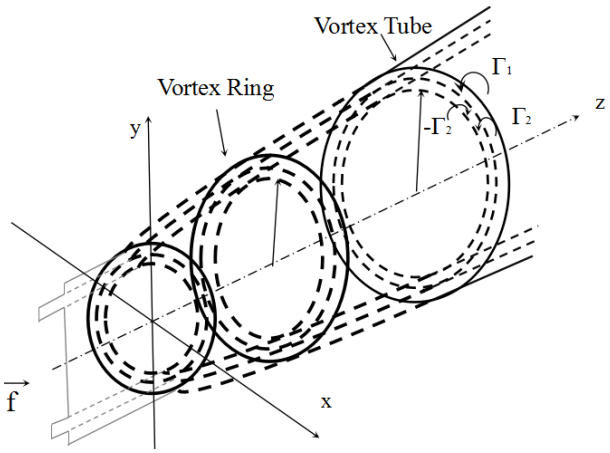

Figure 3.1: Scheme of the vortex model. The wake consists of vortex rings for the near wake and semi-infinite vortex tubes for the far wake. Vortex rings are shed at the edge and positions where there is a pressure jump.

NEAR WAKE MODEL

As shown in Equation 3.3, the strength of the unsteady vortex surface grows in time. The gain in circulation of the newly generated vortex ring as it passes through the edge of an annulus with a constant load Δp is

$$\frac{\Delta\Gamma}{\Delta t} = \frac{\Delta p}{\rho}. \tag{3.4}$$

From the definition of thrust coefficient, it follows that

$$C_t = \frac{T}{\rho A V_0^2/2} = \frac{A\Delta p}{\rho A V_0^2/2} \tag{3.5}$$

where T is thrust on the disc or disc-annulus having an area A, and V_0 is the undisturbed wind speed. Combining Equation 3.4 with Equation 3.5, the relationship between the strength of the new vortex ring produced in time Δt and thrust coefficient is given by

$$\Delta\Gamma = C_t(V_0^2/2)\Delta t. \tag{3.6}$$

The analytical formulas for the velocity field induced by an infinitely thin axi-symmetric vortex ring are given by Yoon and Heister (2004). Their expressions are modified with the cut-off radius δ here, the effect of δ is discussed in the subsection 3.3.1.. Figure 3.2 shows the cartesian coordinate system used in this chapter for velocity field calculation. When the actuator disc is located at the z=0 plane with the centreline along

z axis, the axial and radial velocities at an arbitrary point P in the field induced by the i^{th} vortex ring are given by

$$v_z^{ind} = \frac{\Gamma_i}{2\pi\sqrt{(z_p - z_i)^2 + (r_p + R_i)^2 + \delta}}[K(m^2) + \frac{R_i^2 - r_p^2 - (z_p - z_i)^2}{(z_p - z_i)^2 + (r_p - R_i)^2 + \delta}E(m^2)] \quad (3.7)$$

$$v_r^{ind} = -\frac{(z_p - z_i)\Gamma_i}{2\pi r_p\sqrt{(z_p - z_i)^2 + (r_p + R_i)^2 + \delta}}[K(m^2) - \frac{R_i^2 + r_p^2 + (z_p - z_i)^2}{(z_p - z_i)^2 + (r_p - R_i)^2 + \delta}E(m^2)] \quad (3.8)$$

where $< z_p, r_p >$ are the field coordinates of point P where the velocity is to be calculated, z_i is the axial coordinate and R_i is the radius of i^{th} vortex ring. $K(m)$ and $E(m)$ are the complete elliptic integrals of the first and second kind, where m is given by

$$m^2 = \frac{4r_pR_i}{(z_p - z_i)^2 + (r_p + R_i)^2 + \delta}. \quad (3.9)$$

The method from Abramowitz and Stegun (1972) is used for evaluating the first and second kind integrals. When the evaluation point P is too close to the vortex ring, there is an unphysically large induced velocity at that point. There are two commonly used methods to remove the singularity, one is to use a cut-off, the other is to apply a viscous vortex model with a finite core size (Leishman et al., 2002). A third option to avoid the singularity is using the scheme of merging vortex elements when they are getting close to each other. The cut-off radius is used in this model.

A vortex ring will induce a velocity in the entire flow field and on itself. The self-induced velocity is not negligible, but it can not be calculated directly from Equation 3.7 and Equation 3.8 because of the singularity. There are different ways compared by Baldacchino (2012) to solve this problem. Although the self-induced velocity represented by the induced velocity evaluated at the ring centroid is not theoretically correct, Baldacchino (2012) showed the difference tends to zero when the ratio between the core radius and ring radius tends to zero. Infinitely thin vortex rings are assumed in this model, and it is acceptable to use the induced velocity at the center of each ring. The self-induced axial velocity v_z^s and radial velocity v_r^s are given by

$$v_z^s = \frac{\Gamma}{2R_i}, \quad (3.10)$$

$$v_r^s = 0. \quad (3.11)$$

The radial and axial positions of the vortex rings are updated using a second order Euler method as follows

$$z_i^n = z_i^{n-1} + ({v_{z(i)}}^{n-1} + V_0)\Delta t + \frac{1}{2}\frac{({v_{z(i)}}^{n-1} + V_0) - ({v_{z(i)}}^{n-2} + V_0)}{\Delta t}(\Delta t)^2 \quad (3.12)$$

$$R_i^n = R_i^{n-1} + {v_{r(i)}}^{n-1}\Delta t + \frac{1}{2}\frac{{v_{r(i)}}^{n-1} - {v_{r(i)}}^{n-2}}{\Delta t}(\Delta t)^2 \tag{3.13}$$

where $< z_i^n, R_i^n >$ represent axial and radial position of i^{th} vortex ring at time step n, and $z_i^0 = 0$,$R_i^0 = R$. $< v_{z(i)}^n, v_{r(i)}^n >$ are the axial and radial velocity of the i^{th} vortex ring induced by all vortex rings and the semi-infinite vortex tubes in the field at time step n. The influence of time step is discussed in subsection 3.3.1.

3

Theoretically, the shed vortex rings need an infinite long time to transport infinitely far, which is impractical. To make it more practical while keeping the model physically correct, the far wake is replaced by a semi-infinite cylindrical vortex tube. The replacement happens after a sufficiently large time, when the shedding and transporting vortex ring system approach a steady state.

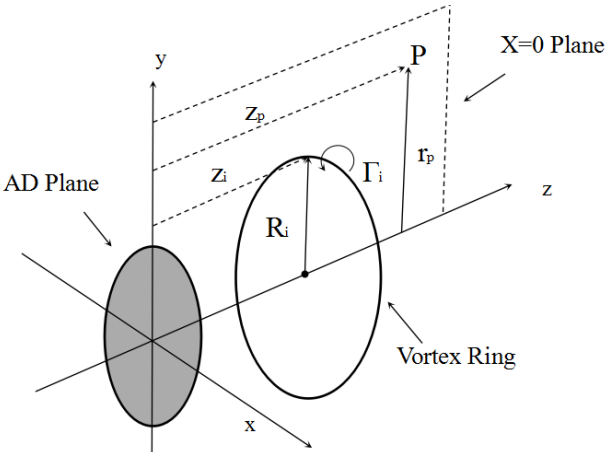

Figure 3.2: A schematic of the coordinate system for computing the induced velocity at an arbitrary point.

FAR WAKE MODEL

The far wake part is represented by a semi-infinite cylindrical vortex tube, for which the vortex strength density, should match that of the near wake part; the vortex strength density is given by

$$\gamma = \frac{\Gamma}{\Delta s} \tag{3.14}$$

where Δs should be the distance of adjacent rings in the ideal situation when the rings are uniformly spaced. Due to vortex dynamics, the distance between adjacent rings are not the same (see Figure 3.6). Alternatively, the averaged value of the distance of rings in the fully developed wake excluding the expansion part is used. Taking the case of C_t=8/9 in Figure 3.6 as an example, the far wake is replaced at 11R, the near wake fully expands at 4R, $\Delta s = \frac{11R-4R}{N}$, N is the number of rings between 4R-11R.

The axial velocity induced by the semi-infinite cylindrical vortex tube can be calculated from the analytical solution from van Kuik and Lignarolo (2016)

$$v_z^{ind} = \frac{\gamma}{4\pi}\Omega(z_0) \tag{3.15}$$

where Ω (defined in (Paxton, 1959)) is the solid angle that the tube opening subtends to the position (z_p, r_p), where the velocity field is to be evaluated. The radial velocity is calculated using the following analytical equation from Branlard and Gaunaa (2014)

$$v_r^{ind} = -\frac{\gamma}{2\pi}\sqrt{\frac{R_{tube}}{r_p}}\left[\frac{2-m^2}{m}K(m^2) - \frac{2}{m}E(m^2)\right] \tag{3.16}$$

where $K(m^2)$ and $E(m^2)$ are the complete elliptic integrals of the first and second kind, and m is given in Equation 3.9 by replacing (z_i, R_i) with (z_{tube}, R_{tube}).

The FWVR model is validated against wind tunnel measurements of a steady actuator disc model, which is presented in subsection 3.3.2.

3.2.2. LOAD CASES

A variety of load cases are performed in the FWVR model to evaluate the dynamic induction of an actuator disc with different types of load. Velocities calculated from the FWVR model are compared with those from Momentum Theory, and also with the dynamic-inflow engineering models of Pitt-Peters, Øye and ECN for the unsteady load cases. The three load cases categories are listed in Table 3.1.

The load of C_t=7/9 is treated as a baseline load case, the temporally-varying and radially-varying load are defined based on it. For Case I (a) and (b), a local radially-varying load is prescribed at the annulus of 0.6R-0.8R, a uniform steady load Case I (0) is given as reference. In Case II (1), a step uniform time-varying load is considered, while Case II (2) prescribes a harmonically time-varying uniform load. Lastly, a combination of the parameters in Case I and II is prescribed as III, where a harmonically time-varying radially-varying load is applied at 0.6R-0.8R.

In Case II and III, the unsteady load occurs at τ=50 when the velocity is converged for C_t = 7/9. The amplitude of harmonic load is ΔC_t=1/9. The harmonic reduced frequencies in Case II (2) and III are 0.05, 0.2, 0.5, 1, when non-dimensionalizing normalizing using $k = \frac{\omega D}{2V_0}$. The time and velocity presented in the results are non-dimensionalizing using $\tau = \frac{V_0 t}{R}$ and the incoming wind speed V_0, respectively.

In order to quantify the hysteretic response of all these models, the amplitude and phase delay from the Lissajous figure (Al-Khazali and Askari, 2012) are discussed. An example of Lissajous figure is shown in Figure 3.3, where the vertical height A represents the velocity amplitude, width of the hysteresis loop represents the phase lag.

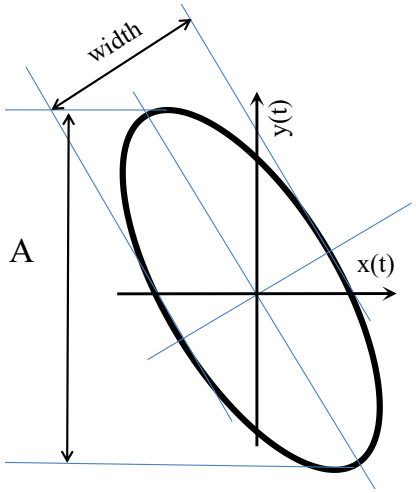

Figure 3.3: Lissajous figure, A – the velocity amplitude, width – the phase lag.

Table 3.1: Load cases.

Load cases	uniform	radially-varying
steady	I. 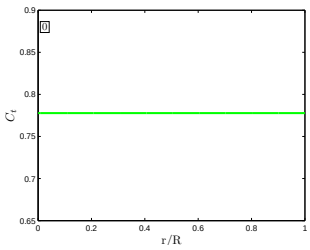	I. 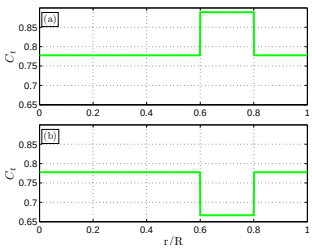
unsteady step	II.(1). 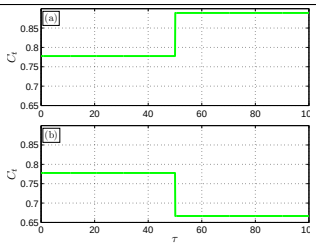	
unsteady harmonic	II.(2). 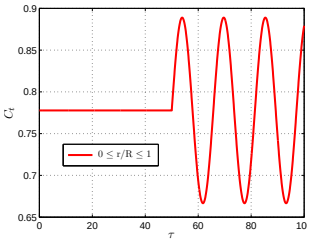	III. 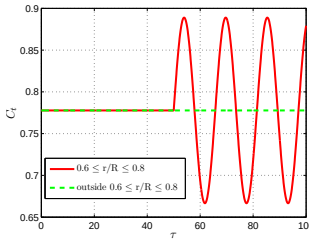

3.3. MODEL CONVERGENCE STUDY AND VALIDATION

3.3.1. A CONVERGENCE STUDY

This section addresses the two convergence issues of the FWVR model. The first one is the effect of parameters used in the model, mainly the time step and cut-off radius. The second one is the extension of the shed vortex rings.

Results show $\bar{v}_z$ at the actuator disc to decrease monotonically with time. At time τ=50, the difference from Momentum Theory in $\bar{v}_z$ at actuator disc for C_t=7/9 is less than 0.5%, and the decreasing rate $\frac{d(\bar{v}_z(50))}{d\tau}$ is at 9×10^{-6}. Therefore, $\bar{v}_z(50)$ at actuator disc for C_t= 7/9 for these verification cases are checked. Figure 3.4 shows $\bar{v}_z(50)$ at the actuator disc using five different cut-off radii $\delta = 1\times10^{-3}, 1\times10^{-4}, 1\times10^{-5}, 1\times10^{-6}, 1\times10^{-7}$, and six different time steps $\Delta\tau$=0.05, 0.04, 0.03, 0.02, 0.01, 0.005. When the cut-off is smaller than $\delta = 1\times10^{-5}$, the difference of $\bar{v}_z(50)$ from that of Momentum Theory is within 0.2% percent. The difference in $\bar{v}_z(50)$ is less than 0.1% for time steps smaller than $\Delta\tau$=0.02, which give confidence in using $\Delta\tau \le 0.02$ and $\delta \le 1\times10^{-5}$ for all the simulations. Therefore, results at τ =50 are acquired for steady load cases, results at τ=50 after load change are acquired for unsteady load cases.

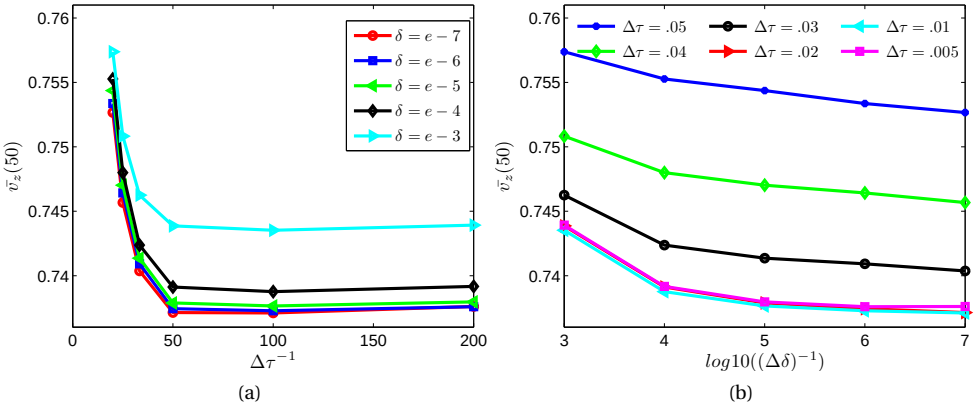

Figure 3.4: Convergence of the averaged velocity at the actuator disc at τ=50 inverse (a) time step, versus (b) cut-off radius, for C_t=7/9 (The curve for $\Delta\tau$=0.02 almost coincides with that for $\Delta\tau$=0.01).

The influence of the extension of the shed vortex rings on the convergence of the averaged axial induced velocity $\bar{v}_z$ at the disc is shown in Figure 3.5. It shows the contribution from the semi-infinite vortex tube, from the vortex rings and from both of them to $\bar{v}_z$ at the actuator disc for different extensions of the shed vortex rings, for C_t= 4/9, 6/9, 7/9, 8/9. A larger extension of the vortex rings increases its contribution to the total induction, as the contribution from the semi-infinite vortex tube become less significant. However, the total induction from both vortex rings and the semi-infinite vortex tube converges after certain extensions of vortex rings. Although a longer extension is needed for a larger thrust to converge, the total induction $\bar{v}_z$ converges at 10R for all considered thrust coefficients. Therefore, it is reasonable to replace the far wake with a semi-infinite

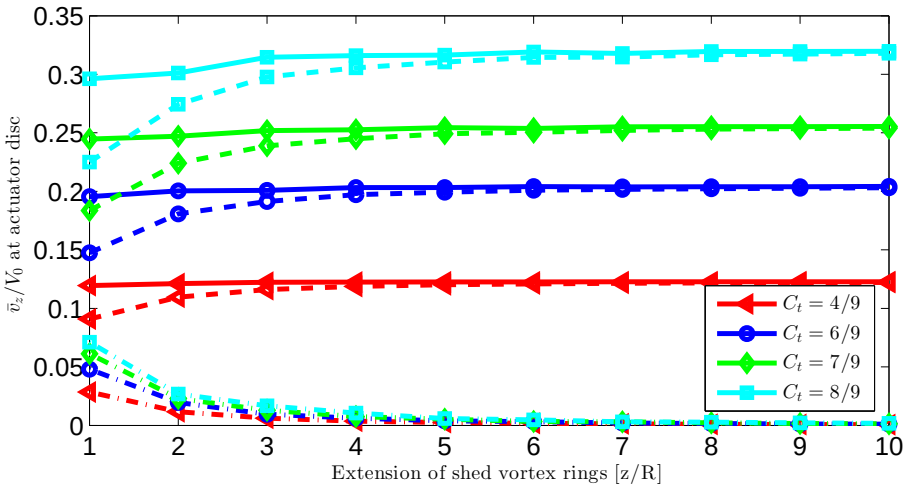

Figure 3.5: Averaged induced velocity at the actuator disc from the vortex rings (dash line), the semi-infinite vortex tube (dash dot line) and the total (solid line) for different extensions of vortex rings, for C_t=4/9, 6/9, 7/9, 8/9.

vortex tube after 10R.

Figure 3.6 shows the location of the vortex rings of the fully developed near wake for C_t= 4/9, 6/9, 7/9, 8/9, where instability can be seen downstream. The larger the thrust, the longer the distance is for a complete wake expansion. The dot line shows the ideal radius in the infinite far wake from Momentum Theory. Taking into account the convergence of the total $\bar{v}_z$ in Figure 3.5 and the locations of the core of the vortices, the semi-infinite vortex tube starts from around 11R (shown in Figure 3.6) for all these thrust coefficients. At these places, the FWVR model has a converged $\bar{v}_z$ and the ideal wake radius can be used as radius of the semi-infinite vortex tube.

3.3.2. THE FWVR MODEL VALIDATION

The validity of the FWVR model is addressed in this section. The velocity field of an actuator disc represented by a porous mesh was measured by Lignarolo et al. (2016b). The experiments were conducted in the ⌀3m Open Jet Facility (OJF) at Delft University of Technology, more details about the wind tunnel are given in chapter 4. The wind speed was 4.7 m/s, the corresponding Reynolds number to the disc diameter of 0.6m is 188000. The porosity of the disc made by three layers of metal mesh is 60%, the thrust measured by a force balance is C_t = 0.93. The three-component velocity field of the disc was obtained with a stereoscopic particle image velocimetry (SPIV). The experiment was also used to benchmark four large eddy simulation (LES) codes and a vortex model for the flow field of the near wake of an actuator disc (Lignarolo et al., 2016a). The measured time averaged axial velocity field is shown in Figure 3.7, the intersections of the vortex rings with the symmetry plane from the FWVR model are represented by black points. The blank region immediately aft the disc was not covered by the measurements. The expansion from the FWVR model matches with the tunnel measurement well. Notably,

the C_t=0.93 is high, which leads to earlier start of the instability from the FWVR model. The vortex rings start to roll up at around z/R=1.0, while still remaining within the shear layer of the measured wake of the actuator disc model.

Figure 3.8 compares the velocity at planes of z/R=-0.5, 0.2, 1.5, 3.0, 4.5 between the FWVR model and the measurements for C_t=0.93. The FWVR model captures the velocity profile generally well. Due to the lack of turbulence dissipation in the FWVR model, the experimental velocity distribution at the edge of the wake is smoother. As the same as the four LES codes and the vortex model in (Lignarolo et al., 2016a), the velocity values outside the wake from the FWVR model are relatively lower than experimental results.

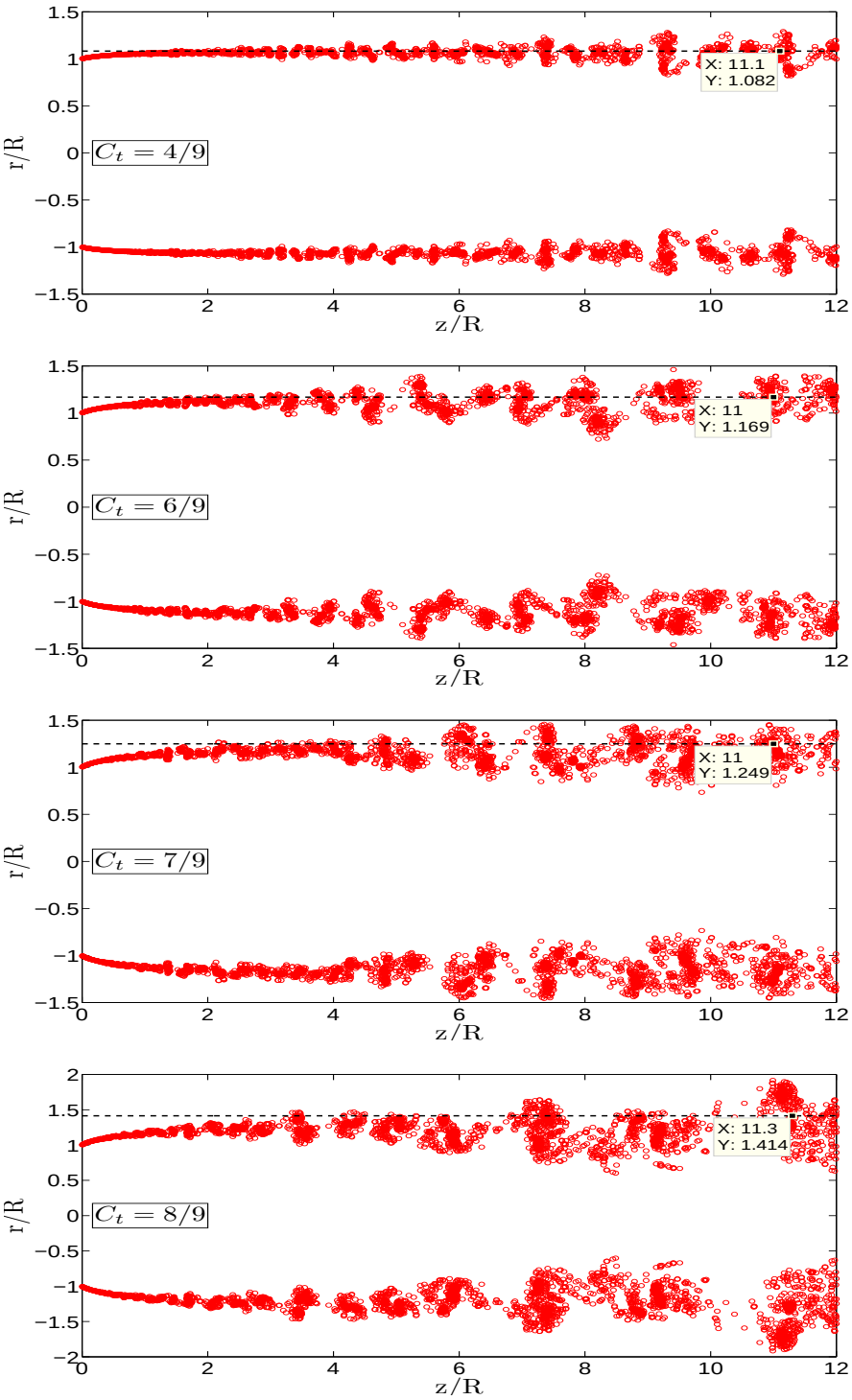

Figure 3.6: Location of vortex rings in the fully developed near wake for C_t=4/9, 6/9, 7/9, 8/9. Points represent intersections of the rings with the symmetry plane. Dotted lines show the ideal radius in infinite far wake from Momentum Theory.

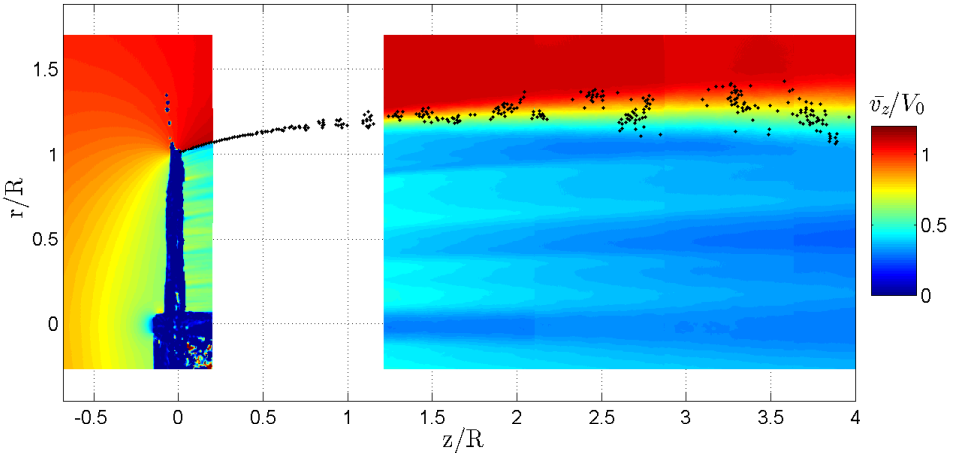

Figure 3.7: Comparison between positions of vortex rings from the FWVR model and time averaged velocity field from the wind tunnel measurements of an actuator disc for C_t=0.93. Black points represent intersections of the rings with the symmetry plane.

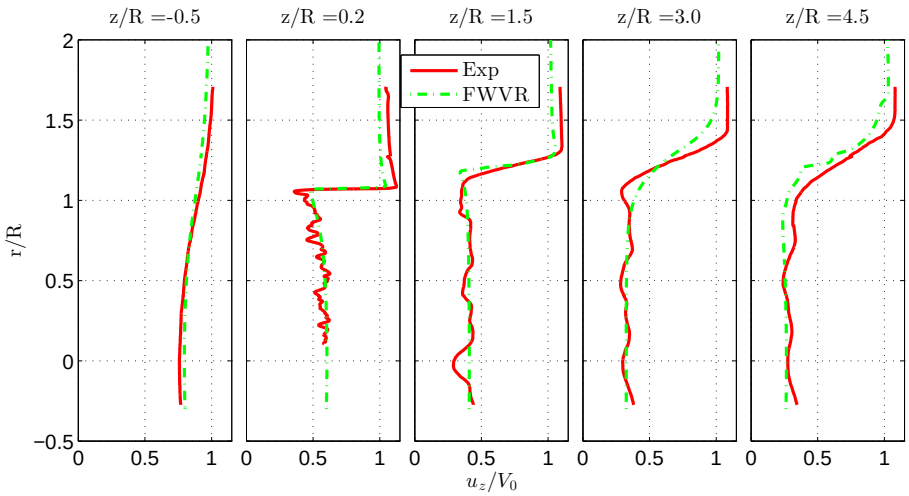

Figure 3.8: Velocity comparison between the FWVR model and wind tunnel measurements at planes of z/R=-0.5, 0.2, 1.5, 3.0, 4.5 for C_t=0.93.

3.4. RESULTS AND ANALYSIS

This section focuses on the analysis of the velocity field obtained from the FWVR model for the load cases in Table 3.1, the results will be compared with Momentum Theory for all three cases, and also compared with the dynamic-inflow engineering models of the Pitt-Peters, Øye and ECN for Cases II and III.

3.4.1. STEADY UNIFORM AND RADIALLY-VARYING LOAD

The results for Case I are discussed in this section. All data for figures 3.9 - 3.11 are obtained at τ=50.

Figure 3.9 compares the distribution of axial velocity v_z at the actuator disc plane calculated from the FWVR model and Momentum Theory for the uniform load (Case I (0)), radially increased load (Case I (a)) and radially decreased load (Case I (b)). For Case I (0), v_z calculated from the FWVR model matches with that from Momentum Theory, but it is not as uniform as Momentum Theory assumes, especially at the edge of actuator disc, which was also found by Sørensen and Kock (1995); Sørensen and Mikkelsen (2001); van Kuik and Lignarolo (2016). For Case I(a) and (b), the locally changed v_z captured by the FWVR model matches generally well with that from Momentum Theory.

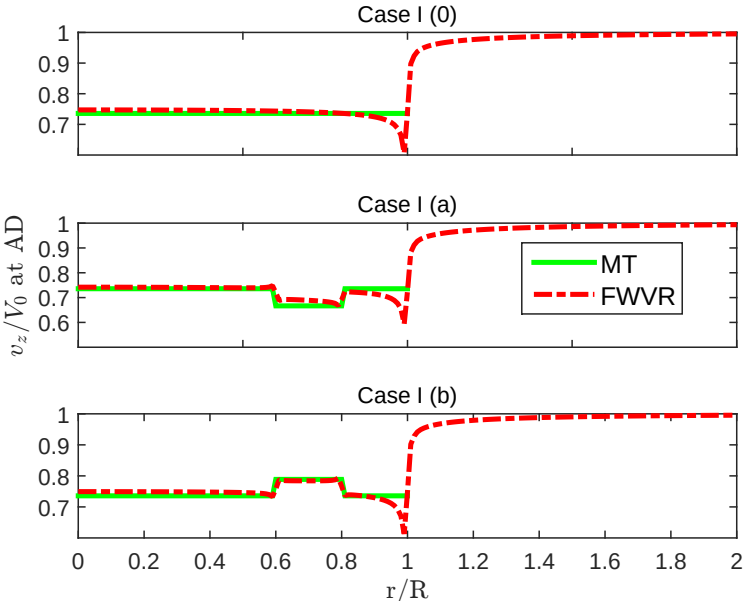

Figure 3.9: Comparison of the distribution of the axial velocity at the actuator disc plane between the FWVR model and Momentum Theory for load Case I (0),(a),(b).

Figure 3.10 shows the axial velocity v_z and radial velocity v_r obtained from the FWVR model at the actuator disc plane for Case I(0),(a),(b). As seen v_z and v_r change dramatically at the region 0.6R-0.8R where load locally varied. Outside the local annulus, v_z and v_r change slightly compared to Case I (0). The slight change in velocity at other annuli shows that although the assumption of independent annuli is incorrect, its effect here is

not significant. Another phenomenon is that v_z and v_r decrease sharply at the actuator disc edge, both of which keep decaying as the locations move outside from the center of the disc.

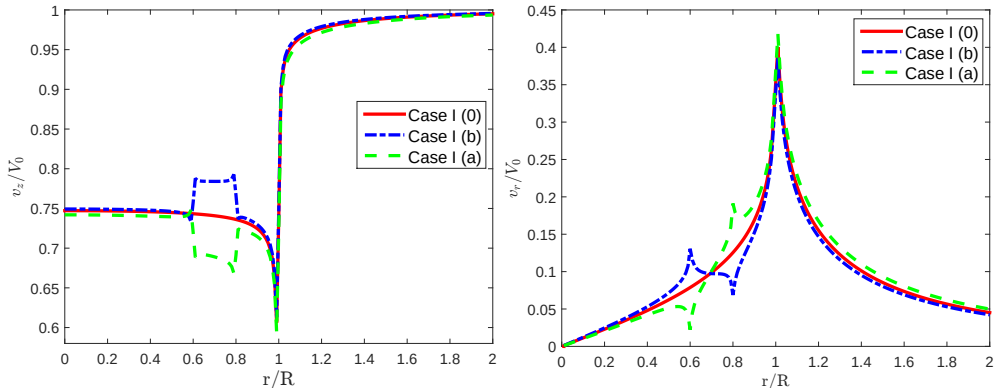

Figure 3.10: Comparison of the distribution of the axial (left) and the radial (right) velocity at the actuator disc plane from the FWVR model for load Case I (0),(a),(b).

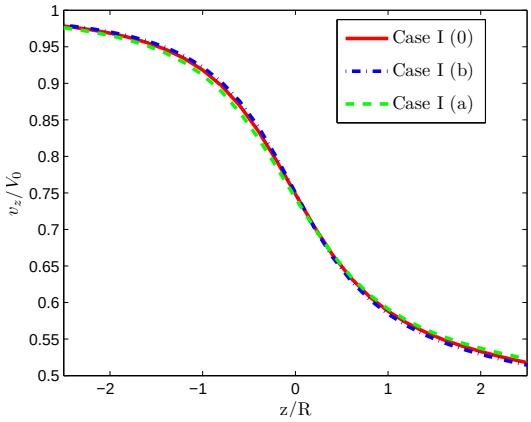

Figure 3.11: Comparison of the axial velocity along the centreline from the FWVR model for load Case I (0),(a),(b).

The analysis of the steady radially-varying load shows that the main effect of the local load variation is largely confined to the same local region; slight differences outside the local load variation region are present, but they are not significant.

3.4.2. UNSTEADY UNIFORM LOAD

In this section, the load Case II, two types of unsteady uniform load : (1) step time-varying load and (2) harmonically time-varying load are investigated.

STEP TIME-VARYING LOAD

Figure 3.12 shows the averaged axial velocity $\bar{v}_z$ at the actuator disc predicted by the FWVR model, Pitt-Peters, Øye and ECN dynamic inflow models for step time-varying uniform load. It is evident that the Pitt-Peters model predicts the smallest time delay, the Øye and ECN models predict a larger time delay than the Pitt-Peters model, and the FWVR model has the largest time delay among all for both loading and deloading cases. The difference exists in both the start-up and load transient part, but the start-up part is not the designed load case for the two engineering models. The FWVR predicts a larger time delay for the load increasing case than that of the load decreasing case, which implies that the load strength, which determines the strength of the newly shed vortex, also has an impact on the time delay.

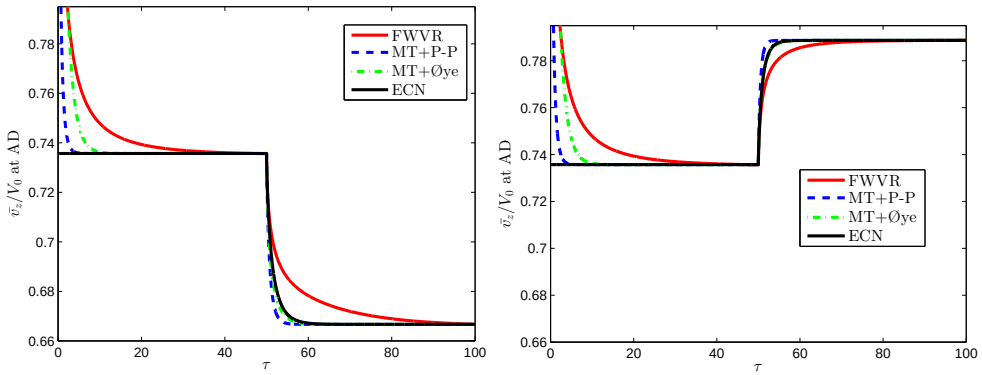

(a) Case II (1)(a)

(b) Case II (1)(b)

Figure 3.12: Comparison of averaged axial velocity at the actuator disc between the FWVR model, the Pitt-Peters, the Øye and ECN model for Case II (1) (a) and II (1) (b).

HARMONICALLY TIME-VARYING LOAD

The results of a harmonically time-varying uniform load are analyzed here, the simulations are presented for k = 0.05, 0.2, 0.5 and 1. Figure 3.13 compares the hysteresis loops of the averaged axial velocity at the actuator disc from the FWVR model, Momentum Theory, Pitt-Peters, Øye and ECN dynamic inflow models for Case II (2). The amplitude difference (difference in amplitude of $\bar{v}_z$ from that of Momentum Theory) and the phase lag are mainly analyzed.

The dynamic $\bar{v}_z$ is plotted versus thrust coefficient C_t at the actuator disc. Momentum Theory can not predict any dynamic effect due to its basis of the static state, however, it is plotted here for comparison. Consistent with Figure 3.12, the Øye model is in great agreement with the ECN model for all the frequencies. As seen for k= 0.05, the amplitude of $\bar{v}_z$ predicted by the Pitt-Peters dynamic inflow model matches with the quasi-steady values from Momentum Theory, but has a small phase lag from Momentum Theory. The Øye and ECN dynamic inflow models predict a larger phase lag and amplitude difference than the Pitt-Peters dynamic inflow model, and the FWVR model predicts an even larger phase lag and amplitude difference than the Øye and ECN dy-

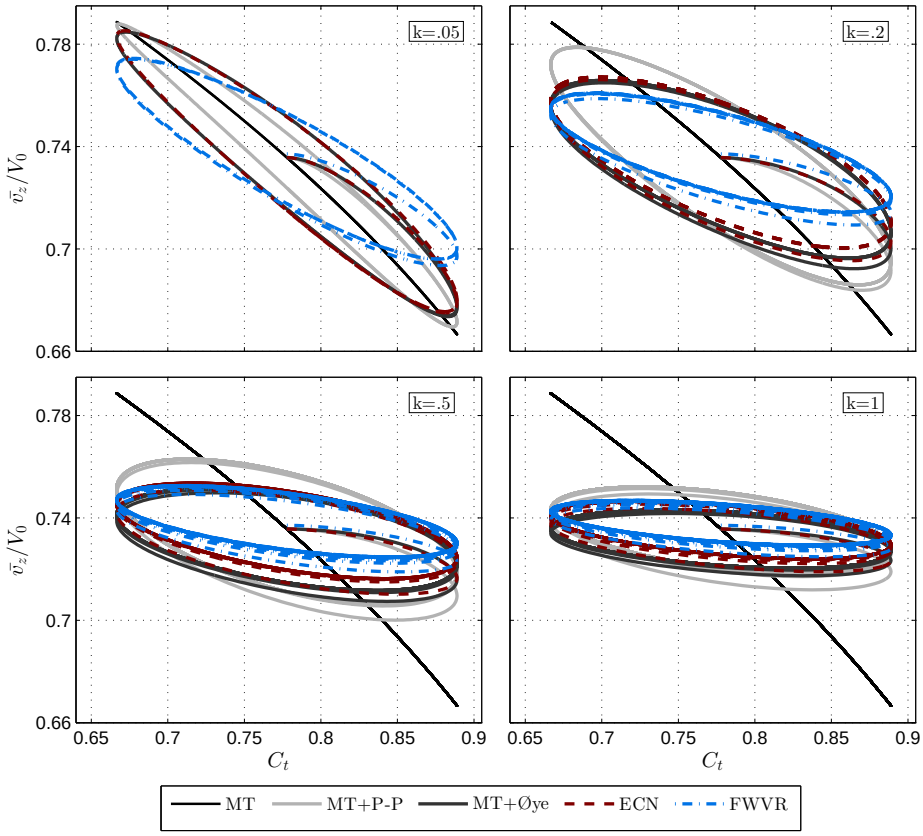

Figure 3.13: Comparison of hysteresis loops of the averaged axial velocity at the actuator disc between Momentum Theory, the FWVR model, Pitt-Peters, Øye and ECN models for Case II (2) — an actuator disc undergoing harmonic thrust oscillations with an amplitude of ΔC_t=1/9 for k = 0.05, 0.2, 0.5 and 1.

namic inflow model. For the larger reduced frequency k=0.2, phase lag and amplitude difference predicted by the three engineering models increase, but there is only a visible increase in amplitude difference from the FWVR model. For k= 0.5, the amplitude difference increases for all the models, and the Pitt-Peters model still predicts an increased phase lag, but the phase lag obtained from the Øye, ECN and the FWVR model decreases compared to k=0.2. For k=1, all the four models predict an increased amplitude difference and a decreased phase lag in $\bar{v}_z$ compared to k=0.5.

In general, the frequency of unsteady load has a significant impact on the dynamic induction. The larger k, the larger amplitude difference compared to Momentum Theory predicted by all the models. The Øye and ECN dynamic inflow models predict a larger amplitude difference than the Pitt-Peters model, and the FWVR model predicts an even larger amplitude difference than the former two. Phase lag predicted by all the models experiences first an increase and then a decrease as k increases, but the maximum point of k is different. The FWVR model predicts a time delay (both amplitude and phase lag) closer to the Øye and ECN model than the Pitt-Peters model. This may be because time constants from the Øye and ECN models are also calibrated using a vortex model, whereas the Pitt-Peters model is initiated for a helicopter based on the 'apparent mass' concept. The difference between the Øye model and the FWVR model might be that the constants of the Øye model were calibrated for a certain type of rotor with certain loads, they need to be tuned for different load cases; while the FWVR model is intrinsically applicable for this generic load case. The difference between the ECN model and the FWVR model might be that the constants of ECN model were derived based on a linearized vortex model with prescribed convection velocity; while the FWVR model takes the wake expansion and the local convection velocity into account .

Figure 3.14 shows the time series of axial velocity v_z and radial velocity v_r at different annuli obtained from the FWVR model at the reduced frequency of 0.2. As seen, the unsteady load has a similar impact on both axial and radial velocity at different radii, but the extent of the effect is different for different radii; the influence increases from root to tip in both v_z and v_r.

Figure 3.15 compares the dynamic loop characteristics of v_z beween the FWVR model, Momentum Theory and the three dynamic-inflow engineering models for different radial positions r/R=0, 0.3, 0.55, 0.6, 0.7, 0.8, 0.85, 0.95 and 0.99, at reduced frequency 0.2. Noticeably, the loop of v_z at different radii from the three dynamic-inflow engineering models is symmetric to the center (C_t=7/9, v_z=0.736), because the dynamic corrections are added to the disc averaged value of Momentum Theory. As the radius is included in equation 2.15, 2.19 and 2.21, it takes into account the variations in time delay at different radii. For the Pitt-Peters dynamic inflow model, both the amplitude difference and the phase lag increase as the radial position moves from root to tip. The axial velocity from the Pitt-Peters dynamic inflow model coincides with Momentum Theory at the root, because the first term of Equation 2.15 goes to zero at root, which represents the dynamic effect.

Contrary to the Pitt-Peters dynamic inflow model, both amplitude difference and phase lag of the Øye and ECN model decrease as the radial position moves outboard. Different from all the three dynamic-inflow engineering models, the center of v_z at different radii from the FWVR model vary with radial positions due to the non-uniform axial

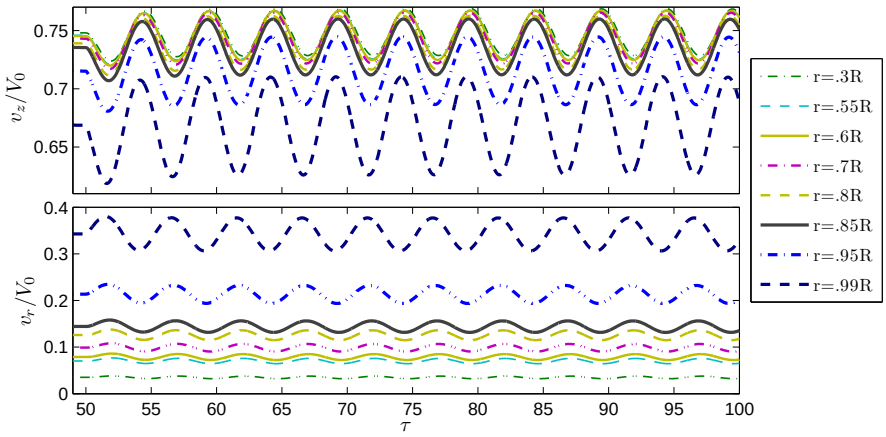

Figure 3.14: The axial (up) and the radial (down) velocity at different radii from the FWVR model at k=0.2 for Case II (2) — an actuator disc undergoing harmonic thrust oscillations with an amplitude of ΔC_t=1/9.

velocity distribution even for the uniform load (see Figure 3.9). The amplitude of v_z predicted by the FWVR model increases as the increase of local radius due to the increasing impact from the tip vorticity. However, there is no discernible variation in phase lag for different positions.

The FWVR model predicts a larger time delay than the three dynamic-inflow engineering models for both the step and harmonically time-varying load of case II. The difference in the predicted velocity between the FWVR model and the dynamic-inflow engineering models indicates that the engineering models needs to be improved or better calibrated for unsteady load effects.

3.4.3. UNSTEADY RADIALLY-VARYING LOAD

In this section, Case III is considered. Figure 3.16 compares hysteresis loops of the dynamic axial velocity v_z at 0.7R (the center of load locally changed region) between the FWVR model, Momentum Theory, the three dynamic-inflow engineering models. The dynamic velocity v_z is plotted against the thrust coefficient at 0.7R. Loops of v_z at the local annulus predicted by the three dynamic-inflow engineering models have a similar pattern as for load Case II (2). The amplitude difference predicted by these models increases as the increase of k. The phase lag first increases and then decreases as k increases. However, the phase lag is very small in the local velocity v_z from the FWVR model for all reduced frequencies, and the amplitude difference from the FWVR model also changes slightly with k. The difference in v_z between the FWVR model and Momentum Theory increases as the increase of thrust coefficient. This implies again that the time delay relates to the thrust strength.

The substantial difference for Case III from Case II (2) is that the FWVR model predicts much smaller phase lag in this unsteady radially-varying load case. This is because the shed vortices at 0.6R and 0.8R are with the same strength but opposite signs (as

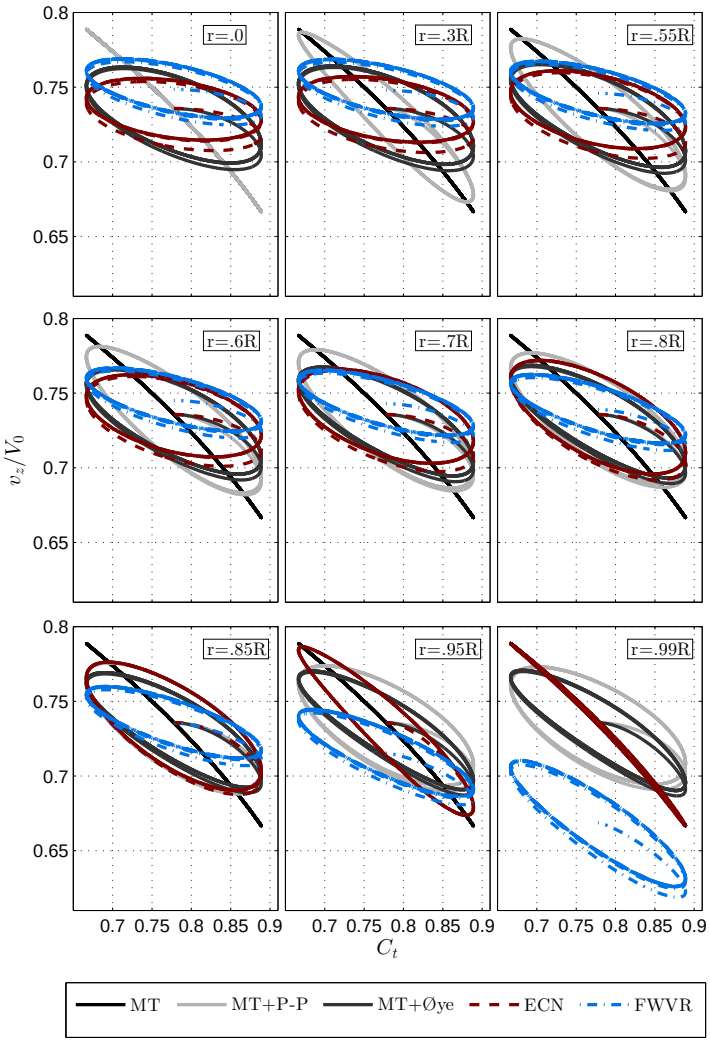

Figure 3.15: Comparison of hysteresis loops of the axial velocity at different radii beween the FWVR model, Momentum Theory, the Pitt-Peters, the Øye and ECN model for Case II (2) for $k = 0.2$.

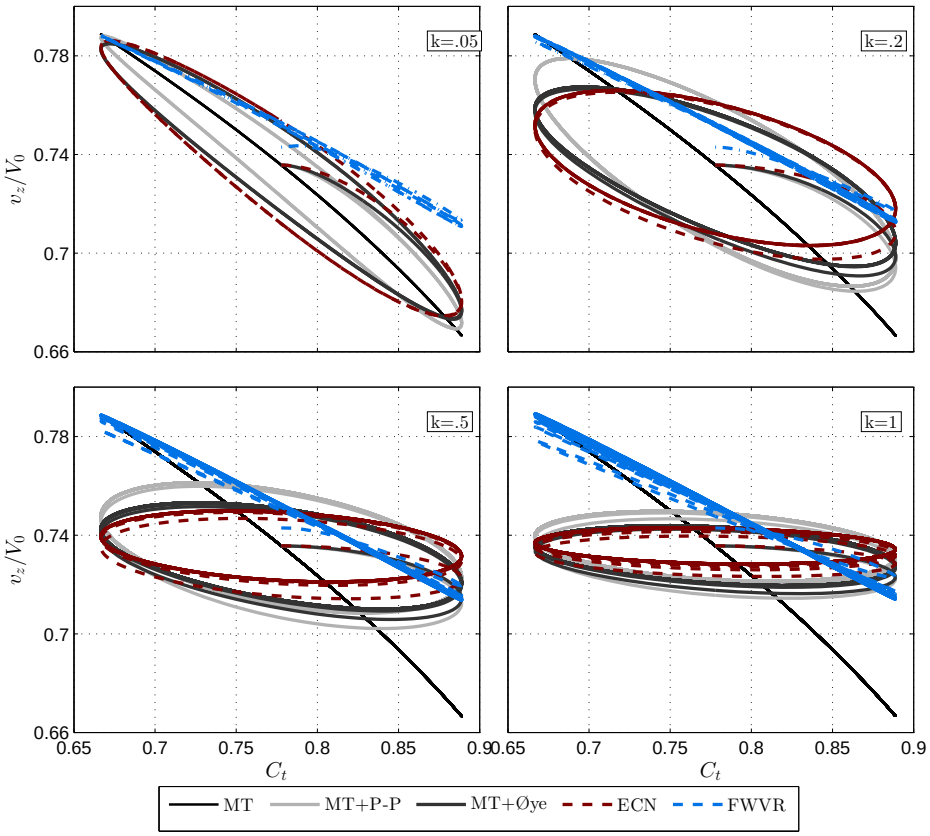

Figure 3.16: Comparison of hysteresis loops of the axial velocity at 0.7R beween the FWVR model, Momentum Theory, the Pitt-Peters, the Øye and ECN model for Case III — an actuator disc undergoing harmonic thrust oscillations in the annulus region 0.6R - 0.8R with an amplitude of ΔC_t=1/9 for k = 0.05, 0.2, 0.5 and 1.

indicated in Figure 3.1), the difference in phase lag induced by them partially cancels out. The main reason behind the difference between the FWVR model and the three dynamic-inflow engineering models for this case is that the engineering models have been developed for an actuator disc with uniform load, but they are extended to radial annuli assuming annuli independent as in BEM, while the FWVR model can inherently account for load radially-varying effects. Therefore, the dynamic inflow models, which are extended to an actuator annulus based on the independent annuli assumption, should be improved for localized unsteady loads.

Figure 3.17 shows v_z and v_r at different radii for k=0.2. The effect on v_z at the region with the time-varying load, 0.6R - 0.8R, is prominent, especially the center of this area, 0.7R. Another phenomenon is that the locally varied unsteady load has more effect on v_z at the outboard part than that at the inboard part, even when they are at the same distance from the load changing area, for example, 0.55R and 0.85R. The trend of v_r is

different from that of v_z. The center, 0.7R, is least affected as shed vortices at 0.6R and 0.8R are in anti-phase but with the same strength, so the radial velocity induced by both shed vortices are partially cancelled out at 0.7R. That v_r at different sides from the center 0.7R changes with opposed phase can be explained by the same reason. Vortices shed at 0.6R dominate the inboard part, while vortices shed at 0.8R dominate the outboard part. The average v_r increases with the increasing local radius, which is consistent with Figure 3.10 (b).

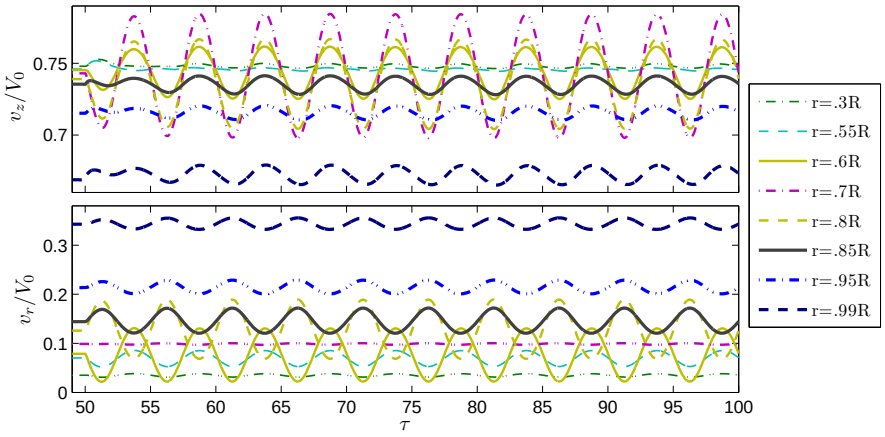

Figure 3.17: The axial (up) and the radial (down) velocity from the FWVR model at different radii at k =0.2 for Case III — an actuator disc undergoing harmonic thrust oscillations in the annulus region 0.6R - 0.8R with an amplitude of ΔC_t=1/9.

Figure 3.18 compares the dynamic loop characteristics of v_z given by the FWVR model, Momentum Theory and the three dynamic-inflow engineering models for different radii for the reduced frequency of 0.2. The locally varied load has an influence on v_z at any radial position calculated by the FWVR model, which has been already known from Figure 3.17. However, the dynamic effects on v_z predicted by the three dynamic-inflow engineering models is in the region restricted to the local area 0.6R - 0.8R, outside this region the velocity predicted by them coincides exactly with Momentum Theory. The difference of v_z at radii outside the load varying area between the FWVR model and Momentum Theory and the three engineering models confirms again that the independent annuli assumption has an impact. Comparing Figure 3.15 with Figure 3.18, it is known that the local unsteady load has a significantly different influence on the dynamic velocity at every annulus compared to the uniform dynamic load. This further emphasizes that the use of independent annuli assumption based dynamic inflow models are insufficient for the induction calculation of localized unsteady load.

3.4.4. AERODYNAMIC WORK ANALYSIS

The impact of the different dynamic induction from different models on the aerodynamic work is discussed in this section. The results are much different from that of Madsen and Rasmussen (2004). In addition to the difference caused by different free wake

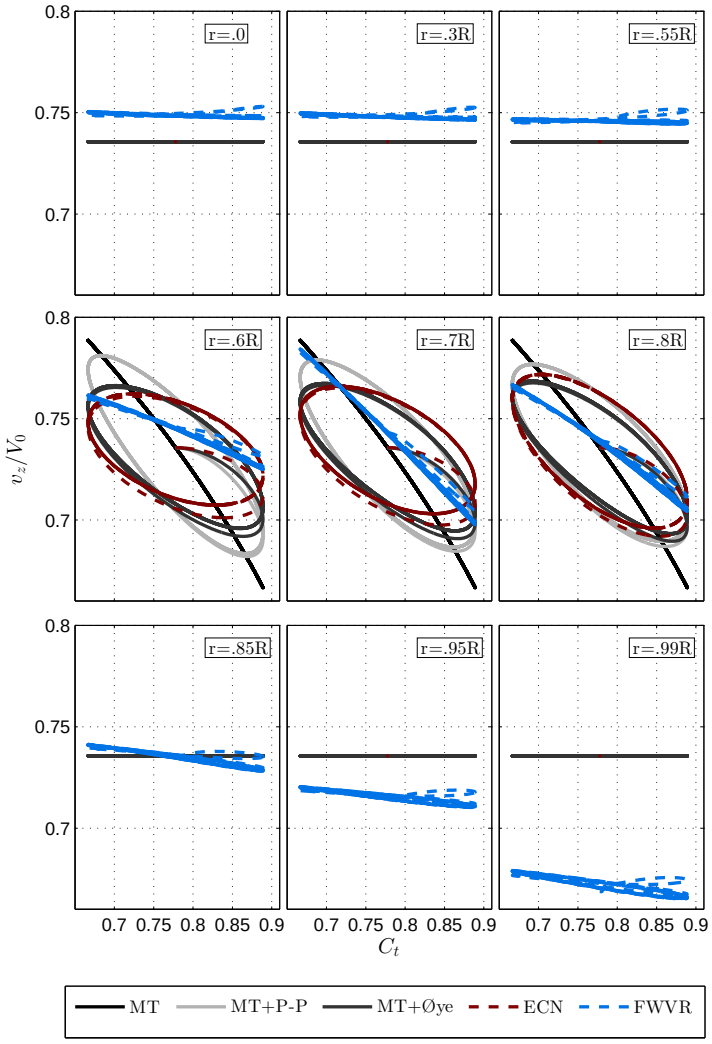

Figure 3.18: Comparison of hysteresis loops of the axial velocity at different radii beween the FWVR model, Momentum Theory, the Pitt-Peters, the Øye and ECN model for Case III for $k = 0.2$.

models, the main reason is that the work is calculated in a different way here. Madsen and Rasmussen (2004) assumed that the harmonic thrust on the blade is caused by a harmonic translation of the rotating blade with an amplitude of 1 meter, and the work is calculated by integrating this load at this translation distance. However, here it starts from the point of view of energy harvesting, no assumption is made between load and disc motion. Under the distributed force on the actuator disc prescribed in Table 3.1, the rate of work done by the force is $\int f v_z dA$. Therefore, the work (W) done on the disc by

the air in one harmonic cycle is given by

$$W = \int_{\Delta T} \int_{A} (f \cdot v_z) dA dt. \tag{3.17}$$

When normalized to the work that can be done on the disc without any induction, a new term, the coefficient of relative work (C_{rw}) is defined here

$$C_{rw} = \frac{W}{\int_{\Delta T} \int_{A} (f \cdot V_0) dA dt}. \tag{3.18}$$

The definition of the denominator has no practical meaning, it is used for nondimensionalization here. Both load Case II (2) and Case III are investigated here. This implies that A is the area of the disc for Case II (2), but the area of the local annulus of 0.6R-0.8R for Case III. In order to obtain a stable induction, integration is done over the third cycle. The results are plotted in Figure 3.19.

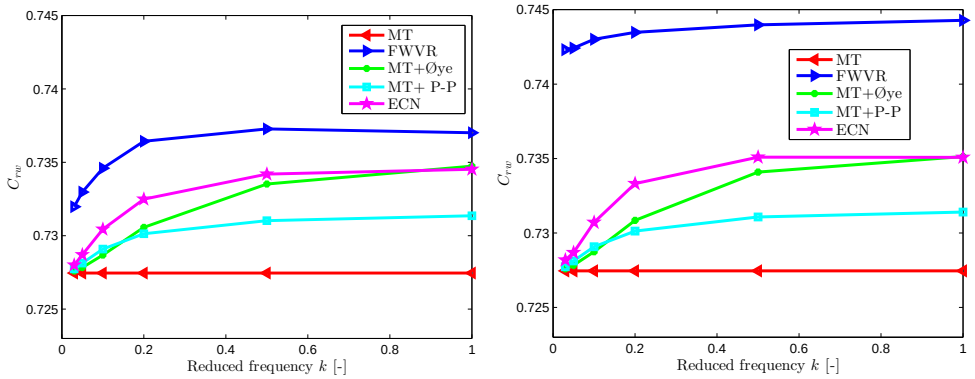

(a) Case II (2) (b) Case III

Figure 3.19: Comparison of relative work of the aerodynamic thrust force from Momentum Theory, the FWVR model, the Pitt-Peters, the Øye and ECN model.

As seen, the three engineering models predict no difference in the two different load cases because they are based on the assumption of annular independence. The Pitt-Peters model predicts higher aerodynamic work than Momentum Theory, and the Øye and ECN models predict even higher aerodynamic work than the Pitt-Peters model at high frequencies for both cases, the results from the Øye and ECN models are in great agreement for low and high frequencies. This observation is consistent with the area formed by the loops and the coordinates in Figure 3.13 and Figure 3.16. C_{rw} from Momentum Theory is at a constant value of 0.7275 for both Case II (2) and Case III for all frequencies, which is 0.2725 lower than that when induction is not considered. This is consistent with the velocity deficit at the actuator disc induced by the cylindrical wake of Momentum Theory (a=0.2643 for C_t= 7/9), the difference of 0.0082 is caused by the non-linear relationship between C_t and a in Momentum theory.

For Case II(2), the FWVR model predicts a higher aerodynamic work than Momentum Theory and the three engineering models. Moreover, for Case III, the FWVR model predicts even higher aerodynamic work. Momentum Theory is based on the steady assumption, it predicts constant aerodynamic work for all frequencies. As expected, when the frequency decreases, the flow field approaches a quasi-steady state, aerodynamic work from the three engineering models and the FWVR model approaches that of Momentum Theory in both load Cases. However, the work from the FWVR model for the smallest considered frequency k=0.03 is still larger than that from Momentum Theory, which means the FWVR model predicts a different threshold value to consider the flow quasi-steady than the engineering models.

The three engineering models, which are extended from an actuator disc to annular-level (based on the annuli independence assumption), predict exactly the same relative aerodynamic work in both Case II (2) and Case III. The higher relative aerodynamic work from the FWVR model in both Case II(2) and Case III shows that the dynamic-inflow engineering models underestimate the energy which can be extracted from the air, especially for radially-varying load case.

3.5. CONCLUSIONS

A free wake model has been developed for the calculation of the induced velocity field of an actuator disc with radially-varying and unsteady loads. The model is composed of free wake vortex rings for the near wake and semi-infinite cylindrical vortex tubes for the far wake. This FWVR model has been applied to three load cases: (I) steady uniform and radially-varying load, (II) two types of unsteady uniform load, and (III) unsteady radially-varying load. Comparison of results between the FWVR model, Momentum Theory and the three dynamic-inflow engineering models of the Pitt-Peters, the Øye and ECN leads to the following main conclusions.

For Case I, the velocity field is predictably most affected at the areas where there is load variation, with an insignificant effect on other radial positions. For Case II, the FWVR model predicts a larger time delay than the three dynamic-inflow engineering models for both step and harmonically time-varying loads. For Case III, the velocity obtained from the three dynamic-inflow engineering models follow a same trend, leading to the same trend in aerodynamic work as for Case II (2). However, the FWVR model predicts significant differences of v_z from Momentum Theory and the three dynamic-inflow engineering models for Case III, which results in even higher relative aerodynamic work. This means that the dynamic-inflow engineering models underestimate the energy which can be extracted from the air, especially for localized unsteady load.

The small difference in predicted velocity between Momentum Theory and the FWVR model in the steady load case proves that Momentum Theory and the independent annuli assumption is acceptable for steady load. The larger time delay from the FWVR model for the unsteady uniform load, and the resulting different aerodynamic work between the FWVR model and the three dynamic-inflow engineering models in the harmonically time-varying load indicates that these engineering models should be improved or better tuned for unsteady load analysis. The significant difference in the dynamic velocity and aerodynamic work between the FWVR model and the three engineering models for the unsteady radially-varying load reveals that the three dynamic-

inflow engineering models, which are derived based on uniform load, are not sufficient for investigation of localized unsteady loads. Improving the existing engineering models or developing more advanced models are needed.

In order to understand the dynamic inflow phenomena better, an experiment of actuator-disc model undergoing unsteady loading are performed in chapter 4.

4

EXPERIMENTAL STUDY OF AN ACTUATOR DISC UNDERGOING UNSTEADY LOAD

Problems worthy of attack prove their worth by fighting back

Paul Erdos (1913-1996)

The main content of this chapter has been published in

Yu, W., Hong, V. W., Ferreira, C., van Kuik, G. A. M.. Experimental analysis on the dynamic wake of an actuator disc undergoing transient loads. Exp Fluids (2017) 58: 149. https://doi.org/10.1007/s00348-017-2432-9.

This chapter aims to study the impact of an unsteady load on the wake of an actuator disc. The load and flow of an actuator disc are measured in the Open Jet Facility wind tunnel of Delft University of Technology, for steady and unsteady cases. The velocity and turbulence profiles are characterized in three regions: the inner wake region, the shear layer region and the region outside the wake. For unsteady load cases, the measured velocity field shows a hysteresis effect in relation to the loading, showing differences between the cases when loading is increased and loading is decreased. The flow field also shows a transient response to the step change in loading, with either an overshoot or undershoot of the velocity in relation to the steady-state velocity. In general, a smaller reduced ramp time results in a faster velocity transient, and in turn a larger amplitude of overshoot or undershoot. Time constants analysis shows that the flow reaches the new steady-state slower for load increase than for load decrease; the time constants outside the wake are generally larger than that inside the wake for a given downstream plane; the time constants of measured velocity in the wake show radial dependence.

The data are relevant for the validation of numerical models for unsteady actuator discs and wind turbines.

4.1. INTRODUCTION

As discussed in chapter 2, a number of experimental studies were conducted focusing on the dynamic load measurements of a wind turbine model under practical situations, such as a pitch angle transient, yaw and wind speed change etc. However, no experimental work using an actuator disc to investigate the unsteady flow field of an open rotor has been reported.

The unsteady wake of a fully loaded actuator disc (or flat plate) undergoing unsteady motion was studied experimentally by Pierides et al. (2013), Yang et al. (2012), and Higuchi and Balligand (1996). Pierides et al. (2013) observed a big overshoot in aerodynamic forces generated during the impulsive rotation of a wall mounted plates in their experiments. The formation process of the vortex ring generated by an impulsively started circular disc was measured by Yang et al. (2012). The vortex ring structure of a disc during an acceleration and a counter-rotating vortex ring structure during a deceleration was visualized by Higuchi and Balligand (1996).

Porous discs have been used by many researchers to physically represent actuator discs experimentally. Different types of porous discs were tried out by Sforza et al. (1981); Pierella and Sætran (2010); Medici (2005); Aubrun et al. (2011); Lignarolo et al. (2014); Muller et al. (2015). Castro (1971) discovered a reverse flow region dominating the wake of a perforated plate at low values of porosity, and the vortex street was not observed for high values of porosity. The wake properties of a wind turbine model and a porous disc model were compared experimentally by Aubrun et al. (2013), which showed indistinguishable difference in their wake after 3D downstream distance. The pressure recovery was shown at 1.5D for both models in a neutral atmospheric boundary layer with a TI=13% at the disc hub for C_t=0.5. A good match in the basic properties, such as coefficient of thrust and energy, field of velocity, pressure and enthalpy was observed between a wind turbine and an actuator disc model using PIV measurements by Lignarolo et al. (2016b), which suggested that the near wake of a wind turbine can be also represented by the near wake of a porous disc. However, the wake was shown not fully expanded at the

distance of 2.2D downstream for the two models with C_t=0.93 in this low turbulence condition. Chamorro and Porté-Agel (2009) found that the boundary-layer turbulence has an important effect on the wake development, which is found to even persist at z/D=15. In addition to the different thrust coefficients, the different boundary-layer turbulence is the other important factor causing the difference in the discoveries of the experiments done by Aubrun et al. (2013) and Lignarolo et al. (2016b). Not only a single turbine was represented by a porous disc, the wind turbine array in a wind farm can also be imitated by an array of porous discs. The mean kinetic energy transport within the wake of an array of rotating wind turbines and an array of static porous discs was compared experimentally by Camp and Cal (2016). The spatio-temporal characteristics of a model wind farm consist of 100 porous discs was studied by Bossuyt et al. (2017).

In addition to the usage of a porous disc model in the aforementioned experiments for steady load cases, it was also used in some unsteady cases. The characteristics of instantaneous thrust of an impulsively started porous surface was studied experimentally in a water tunnel and numerically using a point vortex wake model by Johnson et al. (2013); however, this study did not analyse the wake. Furthermore, the disc had relative motions to the incoming flow in this set-up. The relative motion between the disc and its instantaneous wake results in a temporal impulse exerted by the disc on the fluid. Flow in such situations is different from that in a general dynamic inflow problem. Nevertheless, the measurements of the dynamic wake development of a porous disc under unsteady load are not available.

In this study, a novel approach is used to experimentally investigate the basic problem of wake flow response of an actuator disc undergoing unsteady load by using a disc model with variable porosity. The unsteady load is generated by a ramp type variation of porosity of the disc, at several reduced times of the ramp motion. The unsteady loads on the actuator disc are measured with a load cell. The flow downstream of the disc (in and outside of the wake) is measured at various positions using a hot-wire anemometer. The results create a database for validation of unsteady numerical models, in prediction of the dynamic induction in the near wake (0.5D to 3D) of an actuator disc or a rotor, in order to more accurately predict load and induction on the disc itself under unsteadiness.

4.2. EXPERIMENTAL METHODS

This section provides information on the experimental methods used in this chapter, including the description of the experimental set-up, the wind tunnel, the unsteady actuator disc model, the load and flow measuring techniques, tested load cases and the data analysis method. A photograph and a schematic representation of the set-up is shown in Figure 4.1. The tower is mounted directly on the external OJF Balance which is equipped with six load cells. The hot-wire is mounted on a traverse system, which can traverse axially (z direction) and radially (y direction) the probe to the measuring points.

4.2.1. WIND-TUNNEL AND ACTUATOR DISC MODEL

The experiments are carried out in the low speed closed-circuit Open Jet Facility (OJF) of Delft University of Technology. The OJF wind tunnel has an octagonal cross-section of 2.85 × 2.85 m^2 and a contraction ratio of 3:1, it is free to expand in an area of 13.7 × 6.6

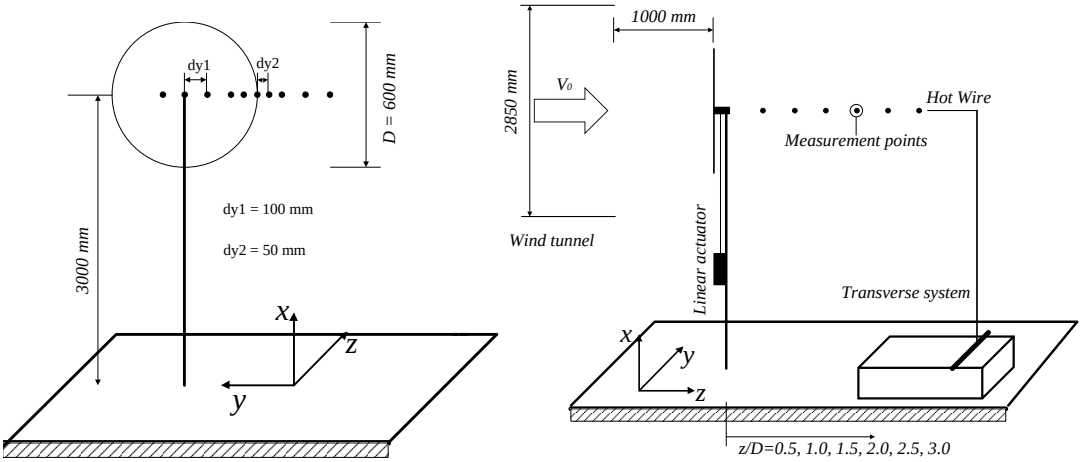

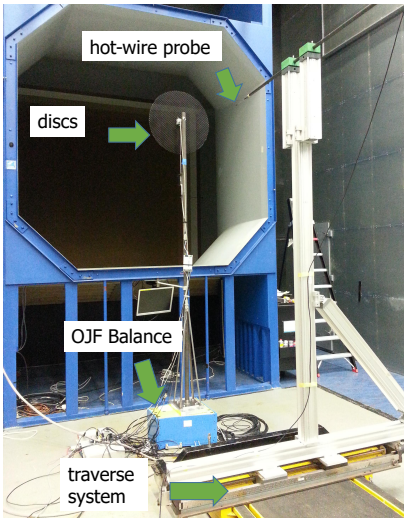

Figure 4.1: Schematic of the set-up (only for reference, not to scale), front view (left),side view (middle) and photograph of the test section with the actuator disc model (right).

× 8.2 m^3. The free stream velocity ranges from 3 m/s to 34 m/s with a flow uniformity of ± 0.5% and a turbulence level of 0.24%, powered by a 500 kW electric motor. The temperature in the test section is maintained at a constant temperature of 20°C by a 350 kW heat exchanger through the experiments.

The purpose of the experiment is to investigate the unsteady load effects: the load on the disc is varied through adjustment of the relative open area (porosity) formed by two identical parallel porous discs. Different types of discs were tried out in Hong (2015) with the aim of reaching the optimal thrust coefficient of a wind turbine around 8/9, while a distinct load change to be achieved with a small displacement of the disc. The final chosen discs are made from 2.0 mm thick aluminium plate with punctured 10×10 mm^2 square holes. Each disc has a diameter of 600 mm, hole-to-hole spacing of 2.0 mm, and porosity of 69.4%. The characteristics are summarized in Table 4.1. The uniform distributed porosity over the disc is aimed for uniform distributed load. The magnitude and rate of porosity change are defined by the displacement and speed of the moving disc, respectively. The gap clearance between the two discs is kept at around 1.7 ‰ D, which is the optimized gap at this set-up for the tested wind speed. Ideally, the smaller the gap, the closer it can represent one single actuator disc model. However, if the two discs are tightly pressed when wind is on, the large friction between the two discs will affect the accuracy of disc displacement. The high and low porosity states of the actuator disc model are shown in Figure 4.2.

Table 4.1: Characteristics of tested porosity disc.

Material	Aluminium plate
Diameter [mm]	600
Hole shape	square
Hole size [mm]	10×10 mm^2
Hole-to-hole space [mm]	2.0
Thickness [mm]	2.0
Porosity [%]	69.4

The nacelle and actuator system is shown in Figure 4.3. As seen, a linear slider is mounted inside the channel-type nacelle. The fixed disc is mounted directly on the top of the nacelle, the moving disc is mounted on the moving rail of the slider. The clearance between the two discs can be adjusted by shims.

The slider is connected to a linear voice coil actuator SMAC LCA31-012-62CS through a rod. The moving disc together with the moving rail of the slider is actuated vertically by the linear actuator. The copper coil rides inside a magnet assembly, in which way the reaction force can be controlled by current flows through the coil. The movement of the disc is controlled by a SMAC LAC-1 controller. The actuator is equipped with a resolution of 0.1 μm, and the sampling intervals of the controller is up to 0.2 ms (5 ms is used in the experiment). The entire nacelle system is mounted to the tower through a TUD-made sensor, which is a uni-axial load cell.

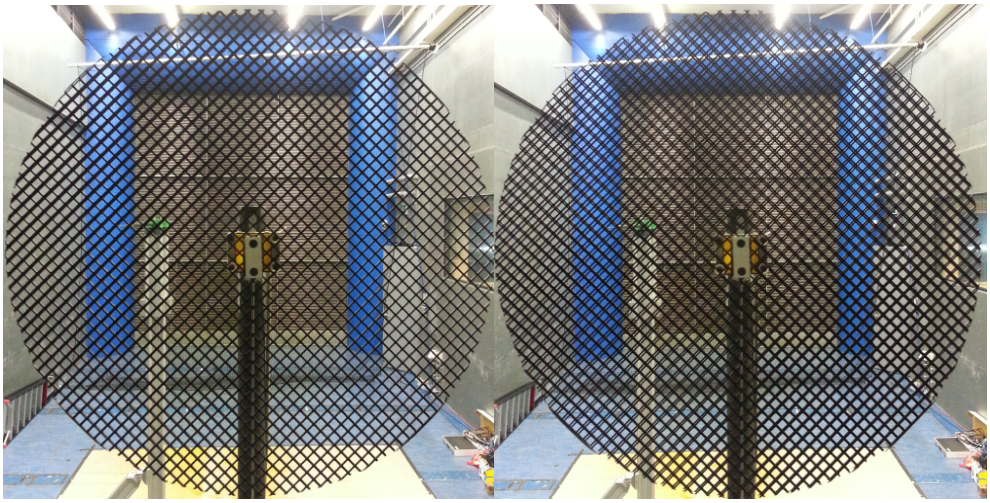

(a) porosity at 69.4% (b) porosity at 44.4%

Figure 4.2: Actuator disc at high and low porosity states.

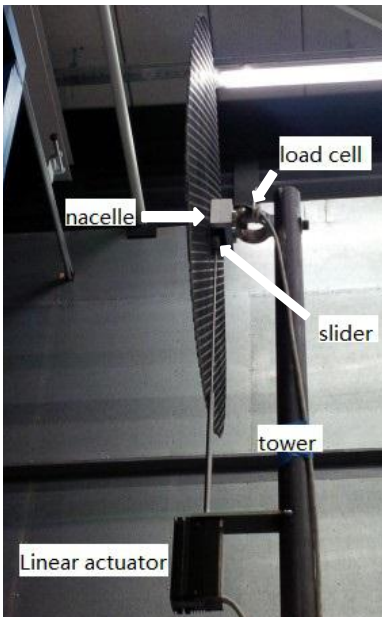

Figure 4.3: Nacelle system and actuator scheme

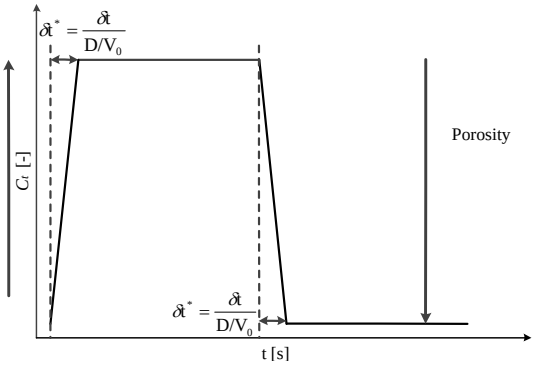

Figure 4.4: Unsteady load profile

4.2.2. TEST CASES AND DATA AVERAGING

The tested wind speed for this experiment is set at 6 m/s, which gives a diameter based Reynolds number of 270680. Knight M. (1926) showed that the aerodynamic thrust of an actuator disc is insensitive to Reynolds number when it is larger than 150000 using tunnel test of three different types of discs. Hoerner (1965) summarized that above diameter-based Reynolds number of 1000, the drag coefficient of discs and other plates is practically constant up to the highest tested Reynolds number of 1×10^7. Besides the consideration of Re number, the upstream velocity is chosen based on a balance of a distinct force change for the given porosity change and an acceptable axial force between the two discs. The control of the actuator motion and data acquisition were synchronized in LabVIEW. The output signals of the hot-wire, the load cell, the OJF balance and the position of motor shaft is sampled at 2kHz.

There are two steady thrust coefficients (C_t) corresponding to the two porosity states in Figure 4.2, henceforth, called C_t^{low} and C_t^{high} accordingly. The velocity aft of the disc under the steady states is measured as a reference. To represent pitching transients of a wind turbine, a ramp change profile is prescribed in all unsteady cases (see Figure 4.4), with δt representing the ramp time. The reduced ramp time (δt^*) is used in this experiment, which is defined by Equation 4.1.

$$\delta t^* = \frac{\delta t}{D/V_0} \tag{4.1}$$

As known from the experiments in project JOULE I and II (Snel and Schepers, 1995; Schepers and Snel, 1995), the time scale in the dynamic inflow process appeared to be on the order of 0.3-0.5$\frac{D}{V_0}$. Therefore, three different reduced ramp times δt^*=0.2, 0.4, 0.8 are tested in this experiment. The steady and unsteady tested cases are summarized in Table 4.2 .

The acquiring period for steady cases is 20 seconds, the mean velocity and thrust is directly time-averaged. For the unsteady experimental cases, unsteady load is varied by dynamically changing the porosity of the disc. Factors as turbulence and signal noise will affect the instantaneous results. To obtain the ensemble average velocity profile,

Table 4.2: Tested steady and unsteady cases.

Cases	number	porosity [%]	thrust	δt^*
Steady cases	SI	69.4	C_t^{low}	-
	SII	44.4	C_t^{high}	-
Unsteady cases	UI	44.4 → 69.4	$C_t^{high} \rightarrow C_t^{low}$	0.2
	UII	44.4 → 69.4	$C_t^{high} \rightarrow C_t^{low}$	0.4
	UIII	44.4 → 69.4	$C_t^{high} \rightarrow C_t^{low}$	0.8

multiple unsteady load cycles for the same measuring point ($\vec{x}$) at the same test conditions are measured consecutively. The instantaneous value is denoted as $u_i(\vec{x},t)$, with a number of experimental cycles at the identical point $u_i^{(n)}(\vec{x},t)$, the ensemble average value $U_i(\vec{x},t)$ is then defined by Equation 4.2, where n is the cycle index and N is the total number of cycles.

$$U_i(\vec{x},t) = \frac{1}{N}\sum_{n=1}^{N} u_i^{(n)}(\vec{x},t). \tag{4.2}$$

For this experiment, N is 10, the reason behind this choice is given in subsection 4.2.5.

4.2.3. LOAD MEASUREMENT AND PROCESSING

Initially, the OJF Balance in Figure 4.1 is used for load measurement. In addition to that, to minimise the influence of the dynamics of the supporting structures, a load cell (as shown in Figure 4.3) is installed at the disc axis, which is capable sensing uni-axial load up to 500 N. The force measured by the load cell is eventually used for all unsteady cases.

Tests, at the absence of any wind and at the designed wind speed of 6 m/s with the actuator activated, are carried out to determine the frequency response of the load cell systems. Figure 4.5a and c presents the thrust coefficient obtained by the load cell and its power spectrum during the unsteady load cycle, while the wind tunnel is off. The measured C_t and its power spectrum with the wind tunnel switched on are shown in Figure 4.5b and d. When the wind tunnel is off and the actuator is activated, the load is purely the inertial force due to the system vibration. From the power spectrum, the natural frequency of the system mechanical vibration is around 5.5 Hz. When the wind is on, Figure 4.5b shows a distinct step change in aerodynamic force. However, the natural frequency is evident in C_t in Figure 4.5b and in its spectrum Figure 4.5d. The high energy at the low frequencies in Figure 4.5d is due to the presence of the two steady states in the signal, which is not relevant.

Based on the system study, a 6th-order Butterworth bandstop filter with a normalized edge frequencies of 4 Hz and 8 Hz is designed to filter out the effect of system vibration, and a cut-off frequency of 10 Hz was applied. The filtered C_t is also shown in Figure 4.5b. As seen, the filtered data captured the trend of the C_t well.

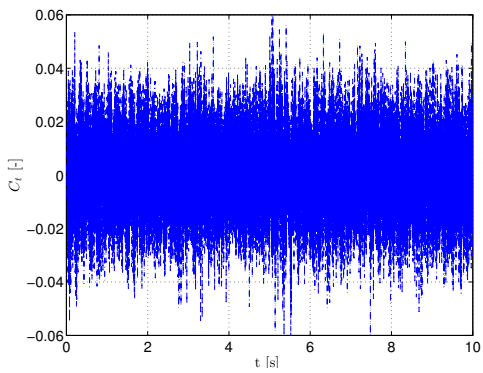

(a) Ensemble average C_t at V_0=0 with actuator on

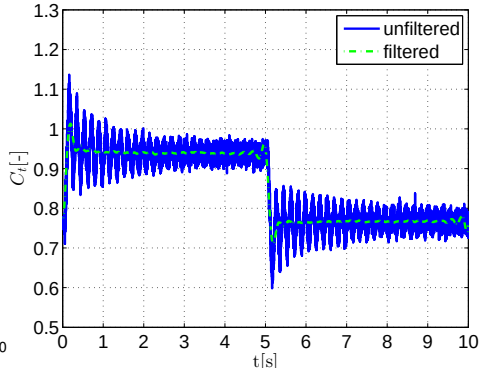

(b) Ensemble average and filtered C_t at V_0=6 m/s with actuator on

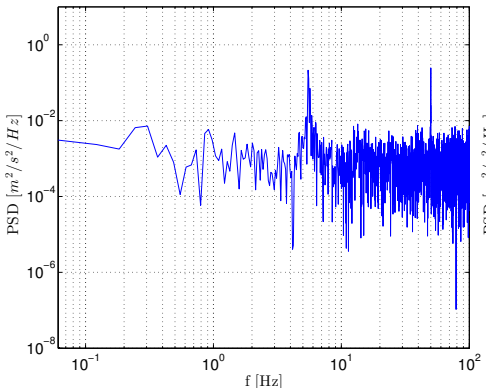

(c) PSD of C_t in (a) at V_0=0 with actuator on

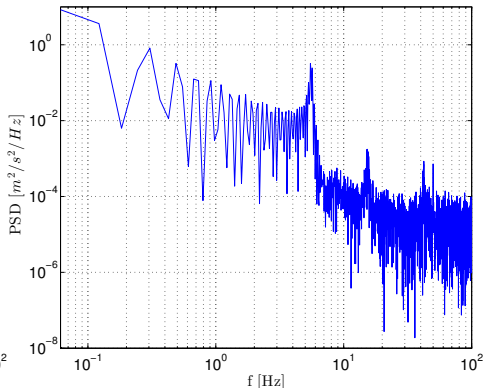

(d) PSD of C_t in (b) at V_0 =6 m/s with actuator on

Figure 4.5: C_t obtained by the load cell signals with actuator on, at wind speed of 0 or 6 m/s, and their power spectrum.

4.2.4. VELOCITY MEASUREMENT

A constant temperature thermal anemometer system of TSI IFA 300 was used to measure the axial velocity. Calibration of the hot-wire anemometer is done at the beginning of each measurement, using a TSI Model 1127 Manual Velocity Calibrator.

As shown in Figure 4.1, the velocity field at planes of 0.5D to 3.0D with an interval of 0.5D is measured. A spatial interval of 0.167D is taken between measurement points in the radial direction. In the region of $y/D = \frac{1}{3} - \frac{2}{3}$, the resolution is increased to 0.083D to lend clarity on the flow field in this high turbulent region. The radial spatial interval of 0.083D is also used in the steady case to obtain the steady spatial velocity profiles.

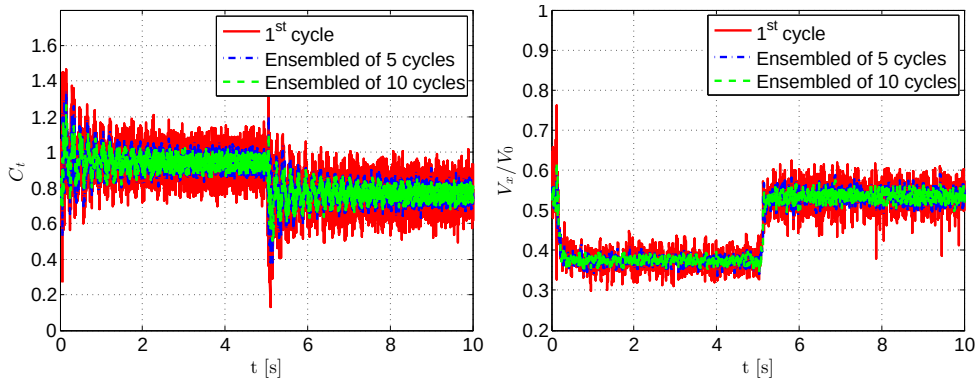

(a) C_t (b) Axial velocity

Figure 4.6: Ensemble average thrust and velocity measured at z/D=0.5, y/D=0.5 of case δt^*=0.2 for different number of cycles.

4.2.5. EXPERIMENTAL UNCERTAINTY

The major uncertainties of these experimental measurements are discussed in this section.

The accuracy of hot-wire traverse system is 0.02mm, resulting in a maximum uncertainty of each traversing distance of 0.4‰. The hot-wire anemometer is calibrated every day during the experimental campaign. The offset errors of the measured points to the fit curves are kept within ± 0.1% for each calibration. The tunnel blockage ratio is 3.5% for the tested model, where no blockage factor correction is needed as suggested by Chen and Liou (2011) and Garner et al. (1966).

All the data shown for the unsteady cases are ensemble average values of 10 full cycles. Figure 4.6 shows the thrust coefficient measured by the load cell and the velocity at location (z/D = 0.5,y/D = 0.5) in the wake measured by the hot-wire anemometer for case δt^* = 0.2, only the first cycle and ensemble average of the first 5 cycles and ensemble average from the 10 cycles are shown. As seen, the more cycles are used, the less noisy will the ensemble average value be. An error of the mean value to number-of-cycles dependency was studied at (z/D=0.5, y/D=0.5), the shear layer region, where the turbulence is most significant. The final 10 cycles is a deliberate value by balancing the accuracy and the needed time, which gives an error less than 0.5% (more details referred to Hong (2015)). The natural frequency will be always present as only ensemble average is applied for thrust in Figure 4.6a.

The steady load is determined by both the load cell and the OJF balance after calibrating them with the entire system. Due to the change in temperature during the continuous measurements in the unsteady cases, a drift in both the load cell and the OJF balance signals is observed, a common problem in a load cell. To compensate the effect of load cell drift, the lower mean value of thrust corresponding to the porosity 69.4% of the unsteady cases is shifted to the measured steady reference value. This process does not have any impact on the velocity and the transient load profiles.

4.3. RESULTS AND DISCUSSION OF STEADY CASES

4.3.1. DISC LOADING

From the OJF balance and the load cell signals, the measured time-averaged steady thrust coefficients are C_t^{low}=0.767 and C_t^{high}=0.933, corresponding to porosity values of 69.4% and 44.4% respectively. The thrust coefficient is defined by Equation 2.9.

4.3.2. VELOCITY MEASUREMENTS

The time averaged radial profiles of axial velocity and turbulent intensity are plotted in Figure 4.7 and 4.8. The subplot (a) and (b) of Figure 4.7 and 4.8 are a comparison of the velocities of each steady case at several downstream planes, (c) is a comparison between the two steady cases at each downstream plane in both figures. From Figure 4.7, the velocity in the region around y/D=0 is lowest under both steady loads. This is caused by the effect of the nacelle and the tower. As expected, the velocity in the wake for C_t^{low} is larger than that for C_t^{high} for the same locations in Figure 4.7c. Additionally, the disc with C_t^{high} has a higher blockage effect on the velocity outside the wake at $y/D > 0.6$. The velocity deficit almost reaches the maximum at 2D for case C_t^{low} but not even at 3D for the case C_t^{high}, which indicates an earlier starting of wake recovery of a lower thrust. This implies a heavier load has a longer wake recovery distance. From Figure 4.7, the axial velocity profiles are not axisymmetric at the hub region. It might be caused by the cable of the load cell, which is bound to the tower only passing one side of the hub (as seen in Figure 4.3). The difference decreases for downstream planes and decreases with higher thrust. From Figure 4.8, the largest turbulence is observed around y/D=0, where the nacelle is. Turbulence decreases as the planes moves downstream from the disc. The second peak is in the shear layer region. Notably, the shear layer of the disc with a lower load persists longer and is relatively stable. The opposite is seen in the higher load case. This can be explained by the higher turbulence intensity and the large pressure gradient in the shear layer of the higher disc load case, which results in an earlier onset of the shear layer breakdown.

4.3.3. DISC LOAD ANALYSIS BY MOMENTUM BALANCE

Figure 4.9 illustrates the control volume of the flow used in this axi-symmetric load case for C_t^{high}, being the stream-tube passing through the actuator disc. The measured axial velocities in the wake field are also plotted by the vector arrows. The radii of the wake estimated from the measured velocity are also marked by the red dot on the stream-tube surface. It is approximated at the radial position where the axial velocity is 99% of the free stream value. The contribution of the lateral force on the stream-tube boundary is zero (Thoma, 1925), so the axial momentum balance gives

$$T = -\left[\rho \int_{A_w} V_w (V_w - V_0) dA_w + \int_{A_w} (p_w - p_0) dA_w\right] \tag{4.3}$$

where the thrust on the disc (T) equals but with opposite sign to the thrust exerted on the flow by the disc, V_0 and V_w represents the velocity of the incoming flow and the velocity in the wake, p_0 and p_w represents the undisturbed pressure and pressure in the wake, the A_w stands for the area of the stream-tube section in the wake where it is examined.

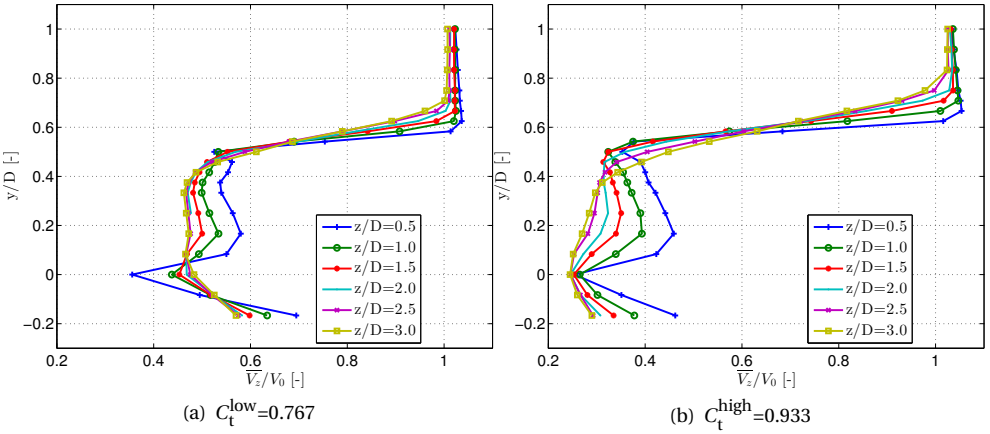

(a) C_t^{low}=0.767 (b) C_t^{high}=0.933

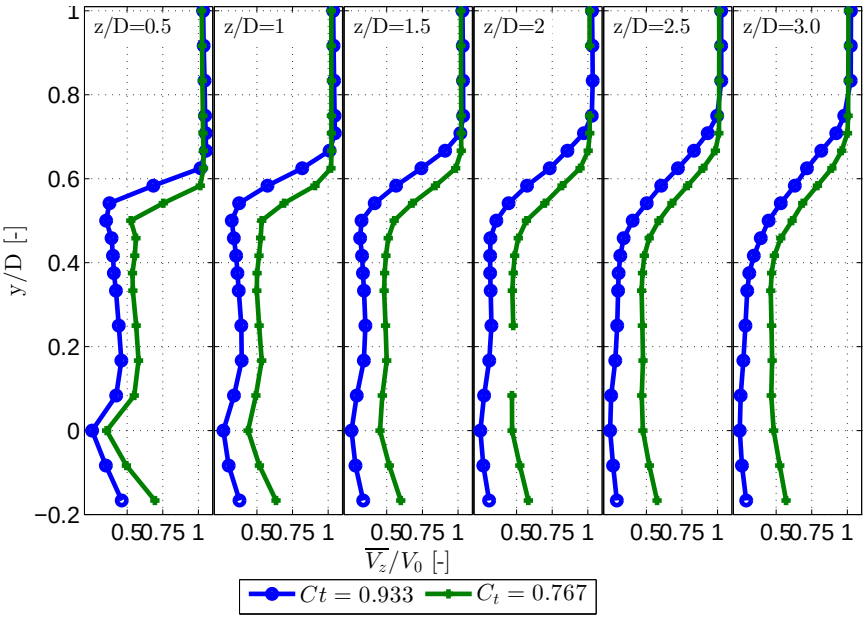

(c) C_t^{low}=0.767 and C_t^{high}=0.933

Figure 4.7: Normalized time-averaged axial velocity at different downstream locations under steady loads.

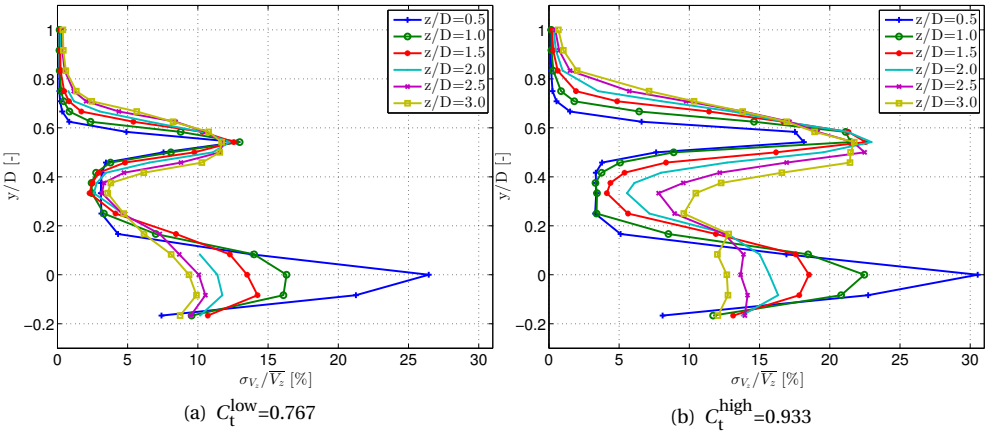

(a) C_t^{low}=0.767 (b) C_t^{high}=0.933

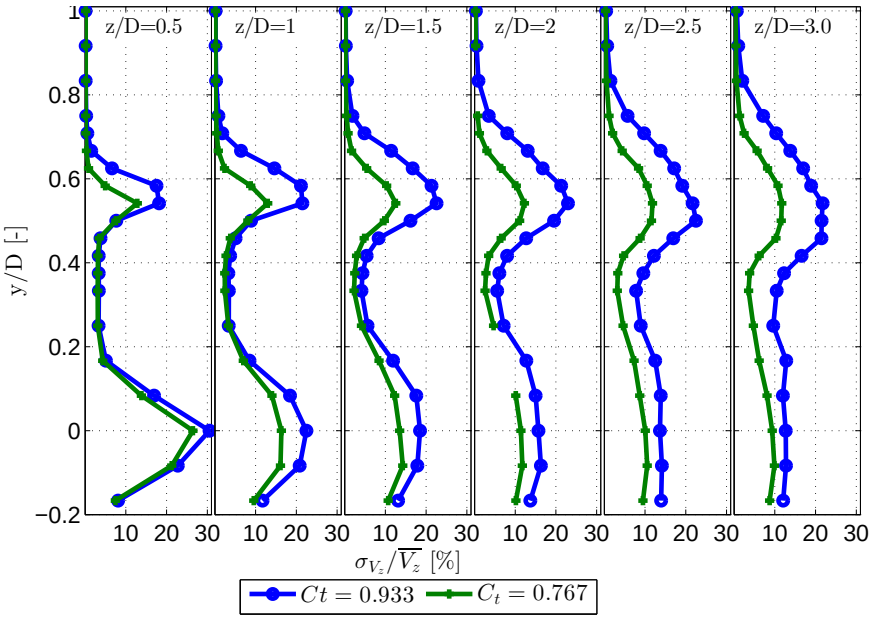

(c) C_t^{low}=0.767 and C_t^{high}=0.933

Figure 4.8: Turbulent intensity of axial velocity at different downstream locations under steady loads.

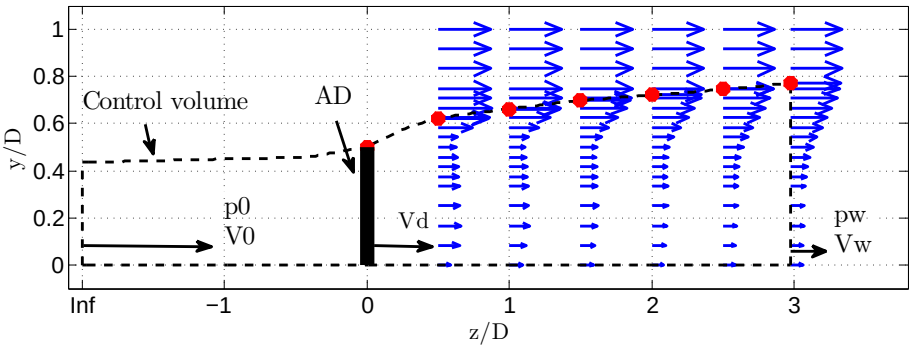

Figure 4.9: Control volume of the momentum balance analysis for C_t^{high}=0.933.

Under the assumption that the wake is fully expanded at the measured furthest plane z/D=3.0, the term $\int_{A_w}(p_w - p_0)dA_w$ goes to zero in Equation 4.3. The thrust coefficient can be calculated by Equation 4.3 and 6.6, yielding C_t=0.856 for the high load case. The same procedure of momentum balance analysis is applied to the low load case, where C_t=0.741 is obtained. The thrust coefficient C_t^{low} and C_t^{high} from the directly measured data are 3.4% and 8.3% higher than the values calculated from the momentum balance analysis. The comparison is summarized in Table 4.3. The relative higher values from the experiments might be due to the assumption of $\int_{A_w}(p_w - p_0)dA_w$=0 at the plane z/D=3.0, it can be also caused by the dissipation. As shown in Figure 4.7, a heavier load has a longer wake recovery distance, which explains that the relative difference is larger in the case C_t^{high} than the case C_t^{low}.

Table 4.3: Comparison of thrust coefficient C_t obtained with the direct measurement and calculated from the momentum balance analysis

Load cases	High load	Low load
C_t from measurement	0.933	0.767
C_t from Momentum Balance analysis	0.856	0.741
Relative Difference (%)	+8.3	+3.4

4.4. RESULTS AND DISCUSSION OF UNSTEADY CASES

In this section, the measured disc displacement and disc load are presented. The velocity at different locations of the case δt^*=0.2 is discussed. Subsequently, the velocities at different downstream locations between the three different unsteady load cases δt^*=0.2, 0.4, 0.8 are compared.

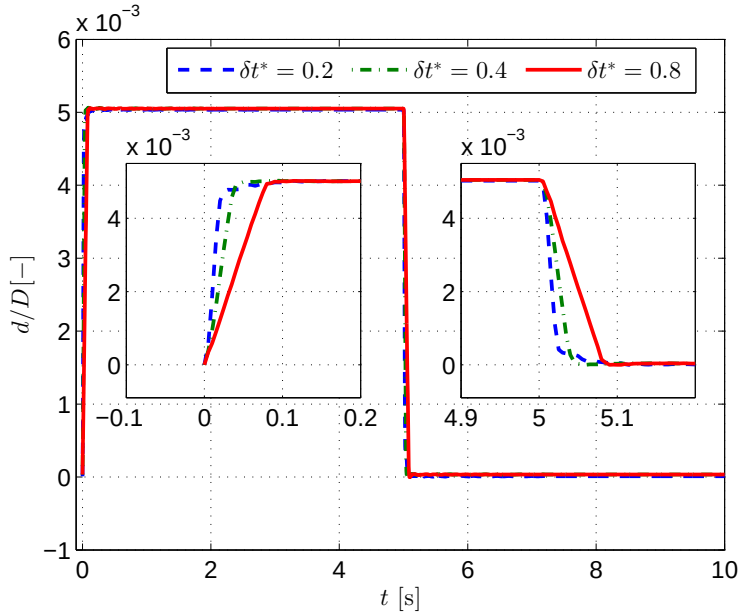

Figure 4.10: Ensemble average disc displacement for case δt^*=0.2, 0.4, 0.8.

4.4.1. DISC DISPLACEMENT

Signals from the encoder of the motor are repeatable during each test case. Figure 4.10 shows the ensemble average disc displacements measured by the encoder, the view of the time period of load increase and decrease are enlarged. It can be seen that the disc displacement is realized according to the design for the two cases of δt^*=0.4 and δt^*=0.8. For the fastest test case δt^*=0.2, the acceleration decreased upon approaching the new steady state due to limited power generated by the actuator.

4.4.2. DISC LOADING

Figure 4.11 gives the ensemble average of the filtered thrust coefficient for the three cases measured by the load cell. As seen, there is an overshoot and undershoot in the measured thrust when load increases and decreases. Consistent with references (Carpenter and Fridovich, 1953; Pierides et al., 2013), a larger reduced ramp time results in a lower thrust overshoot or undershoot. The relatively small amplitude of undershoot and overshoot for the case δt^*=0.2 compared with case δt^*=0.4 is caused by the decreased acceleration when the moving disc reaches the new position as shown in Figure 4.10. The thrust starts to respond before the starting time of porosity change is caused by the filter, which can be seen in Figure 4.5b.

4.4.3. VELOCITY PROFILE FOR UNSTEADY CASE $\delta t^* = 0.2$

The velocity at a number of locations inside and outside the wake is measured (as shown in Figure 4.1), but only three main radial positions which can highlight the characteris-

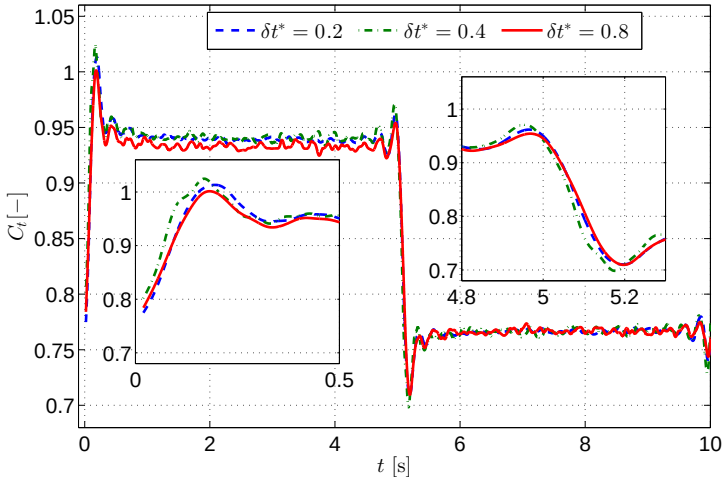

Figure 4.11: Ensemble average of the filtered C_t measured by load cell for cases δt^*=0.2, 0.4, 0.8.

tics of the flow aft of the disc are presented. The three radial locations are at (a) the inner wake, y/D =0.33, (b) the shear layer, y/D= 0.58 and (c) the outer wake, y/D= 0.83. The ensemble average velocity for the six downstream planes z/D=0.5, 1.0, 1.5, 2.0, 2.5, 3.0 at the three radial locations are plotted in Figure 4.12. The mean flow characteristics under steady conditions (i.e. between 3-5 s and 8-10 s of the unsteady cycles) have been discussed in the subsection 4.3.2, the discussion here will focus on the transient behaviour during the load change.

As seen from Figure 4.12, the flow in the shear layer region y/D=0.58 is most turbulent due to the large vorticity in this region. However, due to the smaller order of turbulence when compared to the jump in velocity, the transient changes of flow are still discernible. As expected, the flow in the outer wake y/D=0.83 is the least turbulent because the flow in this region has not passed the disc. Resulting from the effect of holes in the porous discs and the shadow of nacelle and tower, the flow in the inner wake y/D=0.33 is relatively more turbulent than that in the outer region.

Considering the same point in the outer wake region, for example (z/D=3.0, y/D=0.83), the flow is more turbulent for the high thrust than that for the low thrust. This shows the effect of wake expansion, the point (z/D=3.0, y/D=0.83) is outside the shear layer at the low thrust C_t^{low}, but closer to the shear layer at the high thrust C_t^{high} when the wake expansion is larger.

The key observation is the overshoot or undershoot in the flow velocity before it decays to the steady state. The overshoot or undershoot was only observed in load measurement in previous projects (Snel and Schepers, 1995; Schepers and Snel, 1995; Hand et al., 2001), where it was explained by the cause of unsteady airfoil aerodynamics. Airfoil aerodynamics do not play a role in this experiment with disc, it might provide clues on the cause of overshoot or undershoot in thrust. In the inner wake y/D=0.33 and shear layer region y/D=0.58, the amplitude of overshoot or undershoot is larger for load increase than for load decrease. On the contrary, in the outer wake y/D=0.83, the ampli-

tude of overshoot or undershoot is larger for load decrease than for load increase. It is hypothesised that the overshoot or undershoot is caused by the passage of the shed vorticity at the disc edge, which is generated when the thrust changed abruptly. The fact that measurements show the overshoot in velocity having a delay proportional to the downstream distance, suggests a travelling and momentary 'one-time' phenomena that has propagated from the disc upon the sudden load change. This implies the passage of the vorticity. The physical cause of the velocity overshoot or undershoot and the difference at different locations will be further discussed in chapter 5.

4.4.4. COMPARISON OF VELOCITY PROFILE FOR THREE UNSTEADY CASES

This section compares the measured velocity profiles in the wake between the three different cases δt^*=0.2, 0.4, 0.8. Figure 4.13 compares the velocity of the three cases at the radial position y/D = 0.33, 0.83 of the downstream planes z/D = 1.0, 2.0 and 3.0, after load increase and decrease respectively.

First of all, what was observed in subsection 4.4.3 still holds for all the three cases in Figure 4.13. Secondly, although the velocity profiles of the three cases are similar, the effect of speed of load change, the reduced ramp time, can be seen. It can be generally concluded that the smaller the reduced ramp time (the more rapid the load change), the larger the velocity overshoot or undershoot, and the steeper the slope of the transient velocity profiles.

The ensemble average velocity at the radial locations y/D= 0, 0.17, 0.33, 0.42, 0.58, 0.83 of the plane z/D=1.0 are shown in Figure 4.14 for load increase and decrease respectively. What is already discussed in Figure 4.13 is also relevant in Figure 4.14, the speed of load change mainly affects the initial velocity transient profiles. A steeper ramp time results in a faster velocity transient, and in turn a larger amplitude of velocity overshoot or undershoot. The difference between the three cases is less distinct near the region around y/D=0 where the wake effect of the nacelle and tower dominates, and the shear layer region y/D=0.58 where the flow is susceptible to the higher turbulence.

The overshoot or undershoot appears intermittently at different radial locations for the same plane. For instance, in the load increase case in Figure 4.14, there is an undershoot in the velocity at the locations y/D=0.17-0.42, but an overshoot at locations y/D=0.5-0.58. This might be caused by their different relative positions to the convecting vortex, which is shed at the disc edge when the thrust suddenly changed.

The other observation is that the onset time of flow responding to the disturbance from the disc varies between different radial locations of the same plane, which implies that the convection velocity of disturbance varies radially. Additionally, it can be seen that the time the velocity takes to transition from the old steady state to the new steady state also varies radially. The phenomena indicates that the time constant of flow decay in the wake field varies in the radial direction, which will be further discussed in subsection 4.4.5.

4.4.5. TIME CONSTANT FOR DYNAMIC INFLOW DECAY

The time constant of the measured velocity decay is not straightforward due to the velocity fluctuations. The similar approach used in Snel and Schepers (1995) is used, where the velocity profile is approached by an exponential behaviour according to the follow-

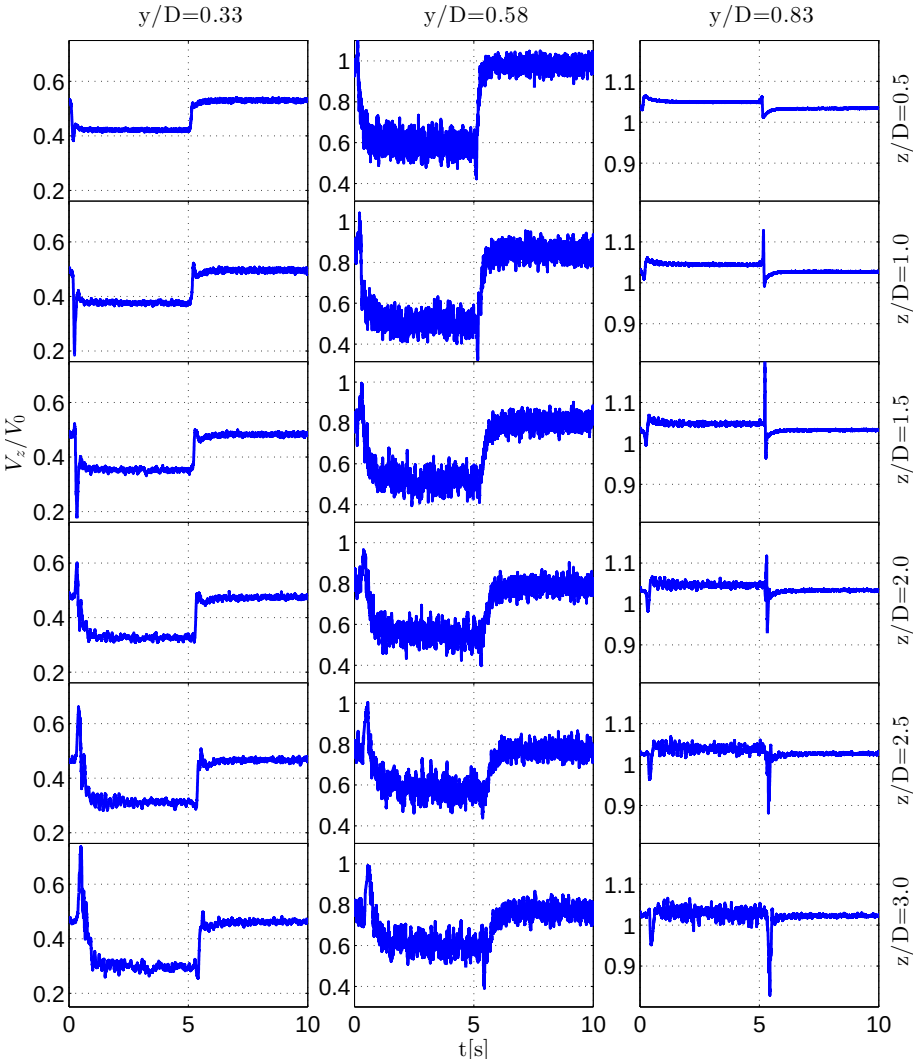

Figure 4.12: Ensemble average velocity at y/D=0.33, 0.58, 0.83 for downstream planes z/D=0.5, 1.0, 1.5, 2.0, 2.5, 3.0 under unsteady load for case δt^*=0.2.

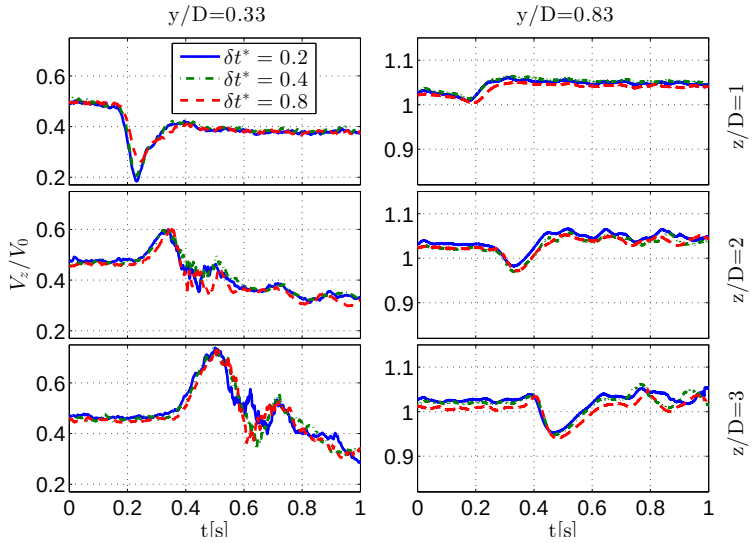

(a) load increase

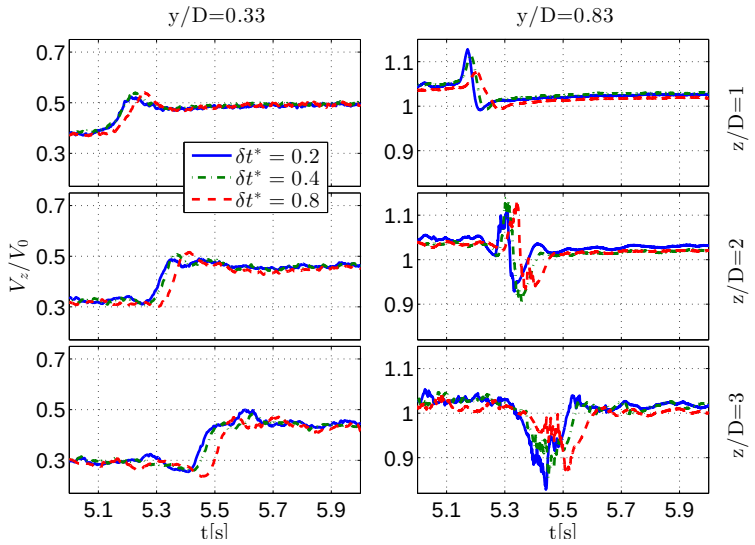

(b) load decrease

Figure 4.13: Ensemble average velocity at different downstream locations under unsteady load for case δt^*=0.2, 0.4, 0.8.

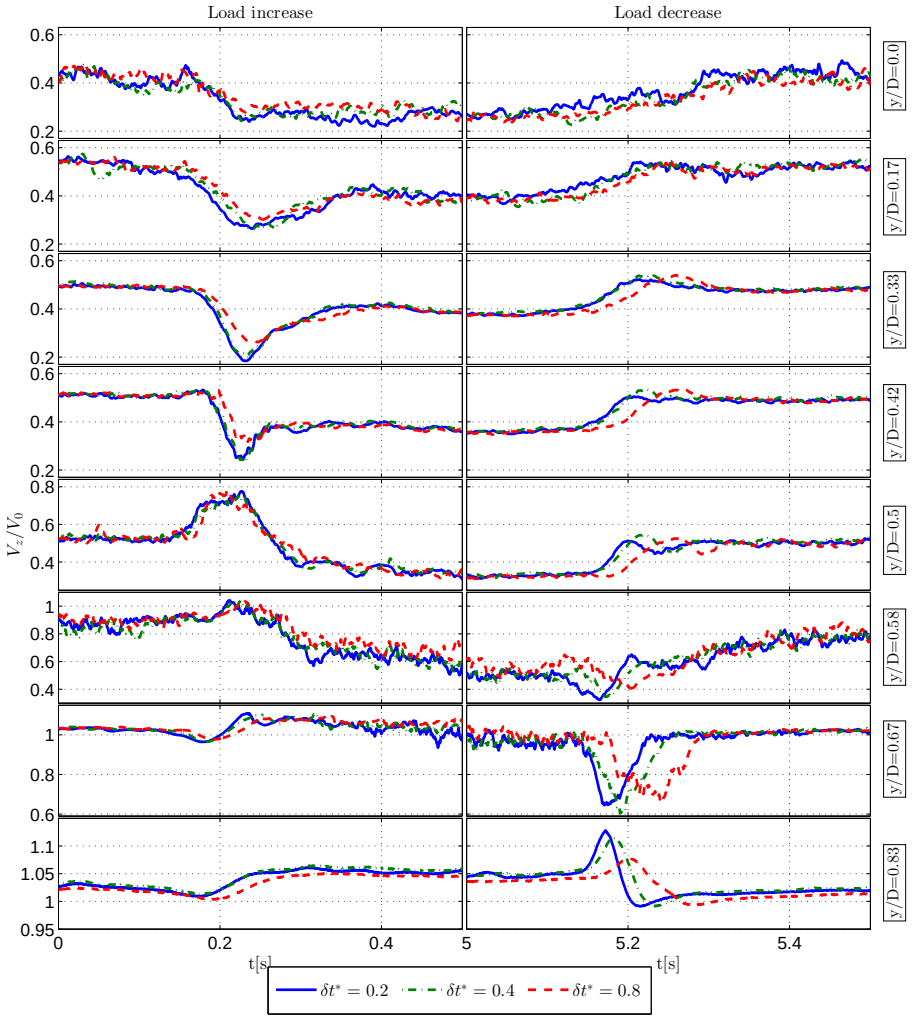

Figure 4.14: Ensemble average velocity at y/D=0, 0.17, 0.33, 0.42, 0.5, 0.67, 0.83 for downstream planes z/D= 1.0 under unsteady load for cases δt^*=0.2, 0.4, 0.8.

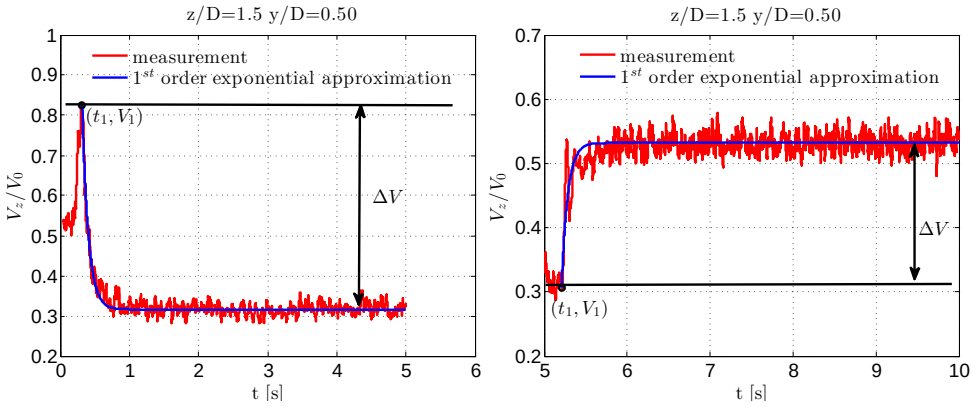

(a) case with overshoot (b) case without overshoot

Figure 4.15: Measured velocity and one order exponential approximation to determine the dynamic inflow time constant.

ing equation

$$V(t) = V_1 + \Delta V * (1 - exp^{-\frac{t-t_1}{\tau}}). \tag{4.4}$$

The determination of V_1, t_1, ΔV are given in Figure 4.15 as an example for two typical different situations of measured wake velocity. For most locations, there is a velocity overshoot, where the peak value and the according peak time are treated as the starting value V_1 and the starting time t_1 of the decay. For the situation where there is no velocity overshoot, the last value before abrupt change is treated as the starting value V_1 and the according time is treated as the starting time t_1.

The mean value of the velocity from 2 seconds after load change to the new load change start (i.e. between 3-5 s and 8-10 s of the unsteady cycle) is treated as the new steady value V_2. Consequently, $\Delta V = V_2 - V_1$.

The fitted curves are also plotted in Figure 4.15.

The dynamic inflow time constants for velocity at all the measured locations are plotted separately for load increase and decrease, for the three cases in Figure 4.16. The following general observations can be drawn from the comparison:

The decay time outside the wake is generally larger than other radial locations for a given downstream plane. The shorter decay time might be caused by the relatively higher turbulence intensity inside the wake, which facilitates momentum mixing and results in the faster attainment of the new equilibrium.

For the same locations, the decay time for load increase is relatively larger than for load decrease. This observation is consistent with the trend of induction change at the actuator disc in chapter 3, where the induction at the actuator disc reaches the new steady values faster in the load decrease case than in the load increase case. This is because the larger disc load results in a larger induction field, which gives a slower convection velocity of the new generated vorticity. This leads to a slower equilibrium of the

new steady state.

The time constants of velocity at y/D = 0-0.17 have been influenced by the hub and tower evidently. For the near downstream planes z/D=0.5, the time constants decrease from y/D=0.33 towards to y/D=0.5 for the load increase cases, decrease from y/D=0.33 towards to y/D=0.67 for the load decrease cases. This direct wake measurement is an important evidence for the same finding by an analytical model in Schepers (2007) that the time constants at the actuator disc plane reduce towards to the edge of the disc. However, Schepers (2007) also showed this finding is not affirmed by the previous load data measured from the NASA Ames Phase VI unsteady aerodynamic experiments (Hand et al., 2001) and numerical simulations from AWSM (van Garrel, 2003), a free wake vortex code.

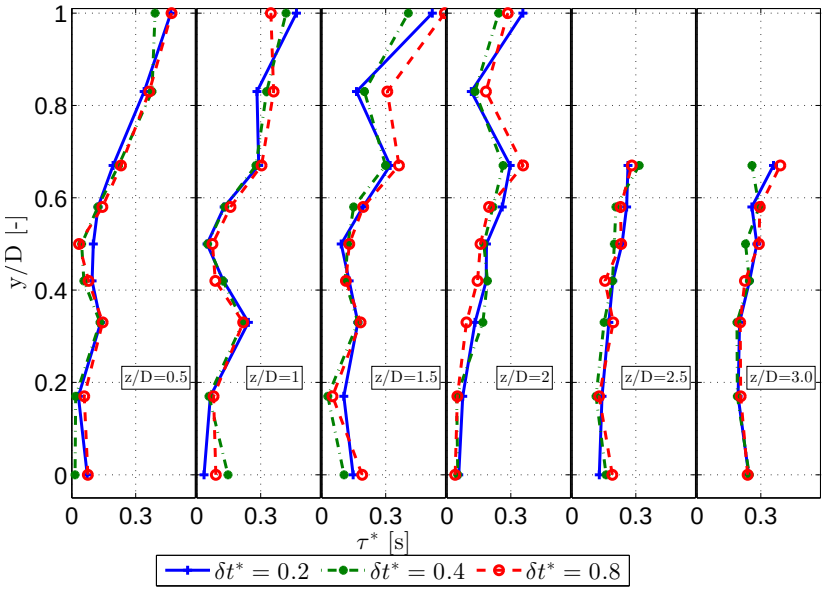

(a) load increase

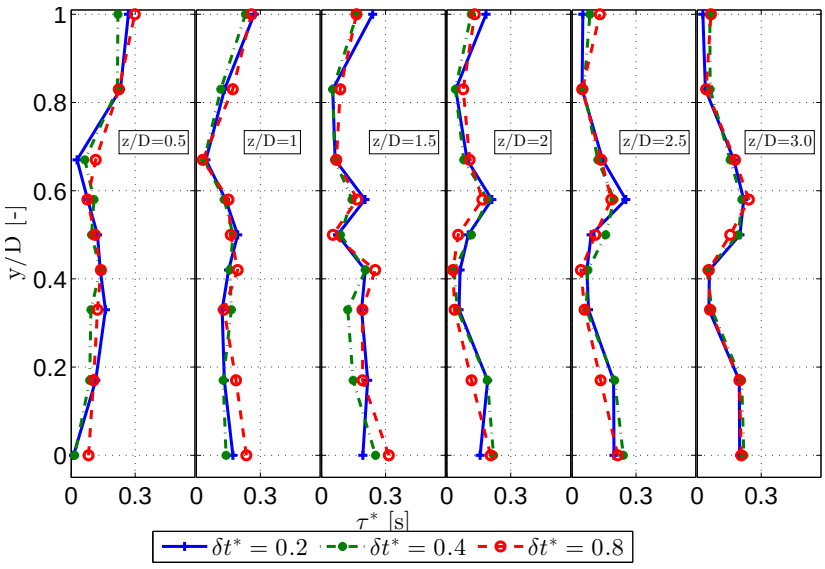

(b) load decrease

Figure 4.16: The dynamic inflow time constant estimated from the measured velocity at different locations for cases δt^*=0.2, 0.4, 0.8.

4.5. INTERPRETATION OF THE RESULTS AND CONCLUSIONS

In this chapter, the flow at locations downstream of an unsteady actuator disc is studied by a hot-wire anemometer. The unsteady load of the actuator disc is invoked by changing the porosity of the actuator formed by two identical metal screens. Flow is measured for three different change rates of porosity.

4.5.1. INTERPRETATION OF THE RESULTS

RESULTS TO BE EXPECTED

The velocity and turbulence profiles are shown to be characterised by three regions, the inner wake region, the shear layer region and the region outside the wake.

Due to different distances from the disc, the flow at different downstream planes responds to the disturbance exerted by the disc successively.

The flow reaches the new steady state slower in the load increase case than the load decrease case due to the larger induction in the wake field of the load increase case.

NEW FINDINGS

The time constants outside the wake are generally larger than other radial locations for a given downstream plane due to the relative higher turbulence intensity inside the wake.

In addition to the transient change of velocity to the new steady state, an overshoot or undershoot in velocity is observed at different locations in the field. A difference in overshoot or undershoot is observed between cases when loading is increased and loading is decreased, also between the different locations in the field where the velocity is measured.

The reduced ramp time is found to have an impact on the wake dynamics, the smaller the reduced ramp time (the faster the load change), the steeper the transient velocity change is and the larger the amplitude of the velocity overshoot or undershoot.

The time constants at the same plane show a radial dependence.

4.5.2. CONCLUSIONS

From the observations and the interpretation of the results, it can be concluded that the convection velocity of the wake and the local turbulence intensity are the key factors determining the total transient time from one steady state to another steady state. The impact of turbulence intensity on the transient time needs to be further quantified for the future work. The shed vorticity plays an important role in the dynamic inflow problem, it determines the overshoot and undershoot of velocity in the wake, the radial dependence of time constants. Better understanding of this by detailed unsteady wake study using a numerical method is done in chapter 5.

5

NUMERICAL STUDY OF AN ACTUATOR DISC UNDERGOING UNSTEADY LOAD

There are no facts, only interpretations.

Friedrich Nietzsche (1844-1900)

The wake development of an actuator disc undergoing transient load is modelled, for the same load cases studied experimentally in chapter 4. The numerical simulation has been performed using the free wake vortex ring model developed in chapter 3. The results of the computation complement previous experimental work while providing information such as the vorticity field and contributions from different vortex elements, which allows the disclosure of the physics behind the observed velocity development in the wake. The velocity at different locations are compared and good agreement is shown between the experimental and numerical results. Consistent with experimental results, velocity overshoot and undershoot are also observed in the numerical results at different measured positions. The wake path from the FWVR model shows that the vortex sheet at the edge of the disc starts gradually rolling up into a vortical ring structure after the load change. The vortex spirals inward in the load increase cases, and spirals outward in the load decrease cases. The decomposed velocity induced by the vorticity shed before and after the load change, and the rolled-up vorticity explain the velocity peaks at different locations downstream. This is mainly caused by the different extent of the rolling-up process and the relative distance of the rolled-up vorticity to the locations in the wake as it traverses. Comparison of the three reduced ramp time cases shows that speed of load change mainly affects the initial velocity transient profile. A steeper ramp time results in a steeper velocity transient slope, and in turn in a larger amplitude of overshoot or undershoot. Decomposing velocity from the different vorticity elements of the three ramp time cases reveals that the difference in transient velocity gradient and amplitude of overshoot and undershoot at the same location is caused by the different extent of rolling-up process. The smaller the reduced ramp time, the quicker the vorticity rolls-up.

5.1. INTRODUCTION

The unsteady wake development of an actuator disc (or a flat plate) undergoing impulsive motion in the flow direction was studied numerically by Koumoutsakos and Shiels (1996); Higuchi and Balligand (1996). Higuchi and Balligand (1996) observed a vortex ring structure in the wake of a disc during an acceleration and a counter-rotating vortex ring structure during a deceleration using a vortex model. Koumoutsakos and Shiels (1996) quantitatively analysed the vorticity and force generated from a flat plate during an impulsively started and uniformly accelerated normal to the free stream with a two-dimensional viscous incompressible model. Both studies showed the formation of vortex ring structures at the edge of the disc or plate shortly after the load change. The ring-like vortical structures increase with time but the spatial position adheres to the body edge. Secondary vortices were also observed at the back of the disc by Koumoutsakos and Shiels (1996) and Higuchi and Balligand (1996).

The wake development of an actuator disc undergoing transient load is investigated experimentally using a disc model with variable porosity in chapter 4. This chapter aims to compare the wake field of an actuator disc undergoing transient load with the wind tunnel measurements from chapter 4 and numerical results from the FWVR model. Induction from different vortex elements — vortex shed before and after the load change and the rolled-up vorticity, is decomposed to explain the physics behind the velocity overshoot and undershoot, to discover the difference between the three reduced ramp

time cases, and the difference between load increase and decrease cases.

This chapter is structured as follows. Section 5.2 recaps the methods used in this chapter, including a brief description of the FWVR model and the experimental test cases. Section 5.3 and 5.4 presents the results and discussions for steady and unsteady load cases, respectively. The wake velocity profiles are compared between the numerical and experimental results, and the key observations in velocity are explained by decomposing the velocity induced by different vorticity elements of the FWVR model for the unsteady cases. Section 5.5 presents the main conclusions.

5.2. METHODS

5.2.1. FREE WAKE VORTEX RING MODEL

The free wake vortex ring model developed in chapter 3 has been used for this study. In this model, the near wake is modelled by dynamic surfaces, consisting of free vortex rings shed from the edge of the actuator disc; the far wake is represented by a semi-infinite cylindrical vortex tube with constant strength and radius. The vortex rings are considered thin, axisymmetric and uniform. In this axisymmetric loaded actuator disc study, vortex rings may expand or contract, their central axis always coinciding with the axis of the actuator disc. The relationship between the strength of the new vortex ring generated during time Δt and the corresponding C_t is given by

$$\Gamma = C_t(\frac{1}{2}V^2)\Delta t. \tag{5.1}$$

A time step of $\Delta\tau$ =0.05 and a cut-off radius of δ =1×10^{-5} were chosen for the simulations. The effect of time step and the cut-off radius are presented in chapter 3.

5.2.2. EXPERIMENTAL CASES

The information on the experimental cases are shortly recalled here, more details can be found in chapter 4.

The load on the disc is varied through adjustment of the relative open area (porosity) formed by two identical parallel porous discs. The velocity field at planes of 0.5D to 3.0D with an interval of 0.5D is measured by a hot-wire anemometer. Figure 5.1 depicts the measurement locations taken during the experiments.

In addition to the two steady cases corresponding to the two steady porosity states, three different reduced ramp times δt^*=0.2, 0.4, 0.8 are tested for the unsteady cases in the experiment. The steady and unsteady tested cases are summarized in Table 4.2.

Figure 5.2 gives the filtered thrust coefficients for the three cases measured by the load cell. As explained in chapter 4, the measured ramp time of both the filtered and unfiltered load signals are not only due to the aerodynamic effect because the existence of the dynamic response of the entire mechanical system. Therefore, the load change profiles are assumed to change at the same reduced ramp time as the porosity change, which are plotted as solid lines in Figure 5.2. These prescribed thrust profiles instead of the directly measured ones serve as input for the numerical simulation of the FWVR model.

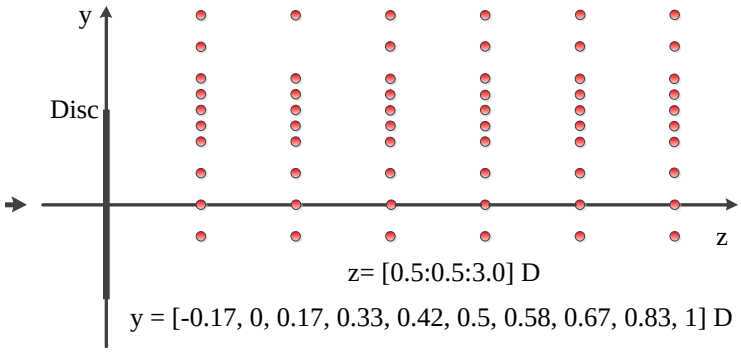

Figure 5.1: Locations of velocity measured downstream the disc.

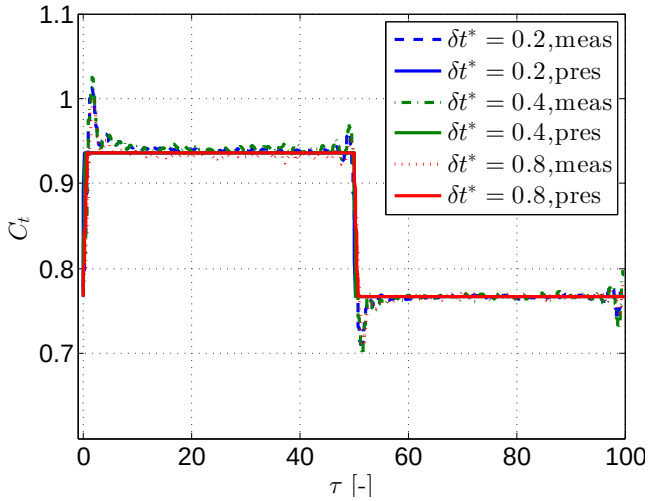

Figure 5.2: The filtered experimental measured thrust (meas) and the prescribed thrust (pres) for the three unsteady cases, the latter serves as input for the simulations.

5.3. RESULTS AND DISCUSSION OF STEADY CASES

Figure 5.3 compares the measured axial velocity profiles with those from the FWVR model at the six downstream planes for the two steady cases. Generally, the steady velocity profiles predicted by the FWVR model track the experimental measurements. At y/D=0, the velocity deficit from the experimental data is larger due to the additional blockage effect from the nacelle in the experiments. The effect from the nacelle decreases as the plane moves downstream, it dissipates at z/D=2. The discrepancy is larger for the shear layer region, which might be caused by two reasons. The first reason is that the viscous dissipation is not modelled in the FWVR model. The other one is that the shear layer region where the vortex elements concentrate is prone to the effects from the vortex, as shown later in Figure 5.4 and Figure 5.5.

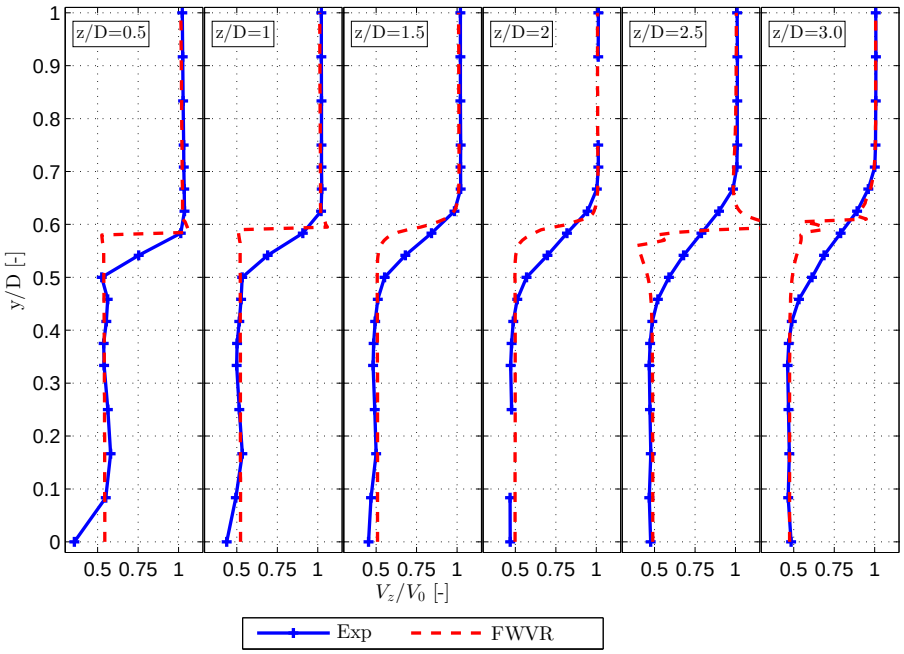

(a) C_t^{low}=0.767

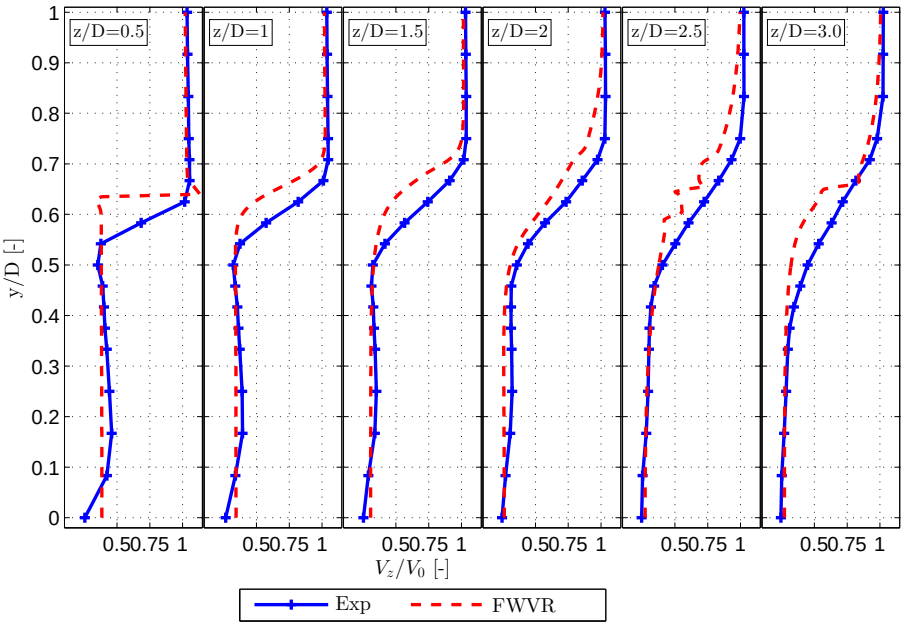

(b) C_t^{high}=0.933

Figure 5.3: Comparison of normalized axial velocity at different downstream locations under steady load between experiments and the FWVR model.

5.4. RESULTS AND DISCUSSION OF UNSTEADY CASES

A number of locations in the wake as shown in Figure 5.1 have been measured. Velocity at 7 locations which highlight the characteristics of the flow downstream the disc is presented. They are located inside the inner wake, outside the wake and in the shear layer of three planes z/D= 1.0, 2.0 and 3.0, which are summarized in Table 5.1.

The comparison of the velocity in the wake under the steady load has been shown in section 5.3. The analysis of flow under unsteady conditions focuses on the transient wake changes instead of comparing the steady state values. Therefore, the velocity is presented in a non-dimensional way using

$$\widetilde{\Delta V_x} = \frac{V_x - V_{x,s1}}{V_{x,s2} - V_{x,s1}}. \tag{5.2}$$

The subscripts $s1$ and $s2$ represent the initial (before load change) and the final steady state (sufficient time after load change). Hereinafter, the self-normalized transient responses from the experimental and numerical results are compared. The times presented in the results are non-dimensionalizing to the dynamic inflow time scale using $\tau = \frac{V_0 t}{D}$.

5.4.1. DYNAMIC WAKE FOR THE LOAD CASE δt^*=0.2

Take the load case δt^*=0.2 as an example, this section compares the velocity at different locations between the numerical and experimental results.

Figure 5.4 shows the development of the wake after load increase. Locations of intersections of the vortex rings with the symmetry plane from the FWVR model are plotted at time τ=0.5, 1, 1.5, 2, 3, 6. The vortices shed before and after the onset of load change from the FWVR model are presented separately by particles with light and dark color. Figure 5.5 shows the wake development after load decrease.

As seen in Figure 5.4, under the interaction of the vorticity shed before and after the load increase, the vortex sheet starts to form an inward knot. As the vorticity accumulates, the knot rolls into a ring-like vortical structure gradually. This is different from the fully loaded disc cases observed in literature, Pierides et al. (2013); Koumoutsakos and Shiels (1996); Yang et al. (2012); Higuchi and Balligand (1996), where the vorticity rolls up at the edge of the disc shortly after the impulsive motion and maintains attached to the disc while growing up into ring-like vortical structures. Remarkably, as shown in Figure 5.5, the new and old vorticity interacts to form an outward knot after the disc load decreased. Eventually, the knot rolls into a big ring-like vortical structure. The roll-up vortical structure moves outwards and is also convected downstream at the same time.

Figure 5.6 shows the velocity development from the experiment and FWVR model at

Position	P1	P2	P3	P4	P5	P6	P7
z/D	1.0	2.0	3.0	1.0	2.0	3.0	2.0
y/D	0.33	0.33	0.33	0.83	0.83	0.83	0.58

Table 5.1: Locations in the wake of the discussed positions.

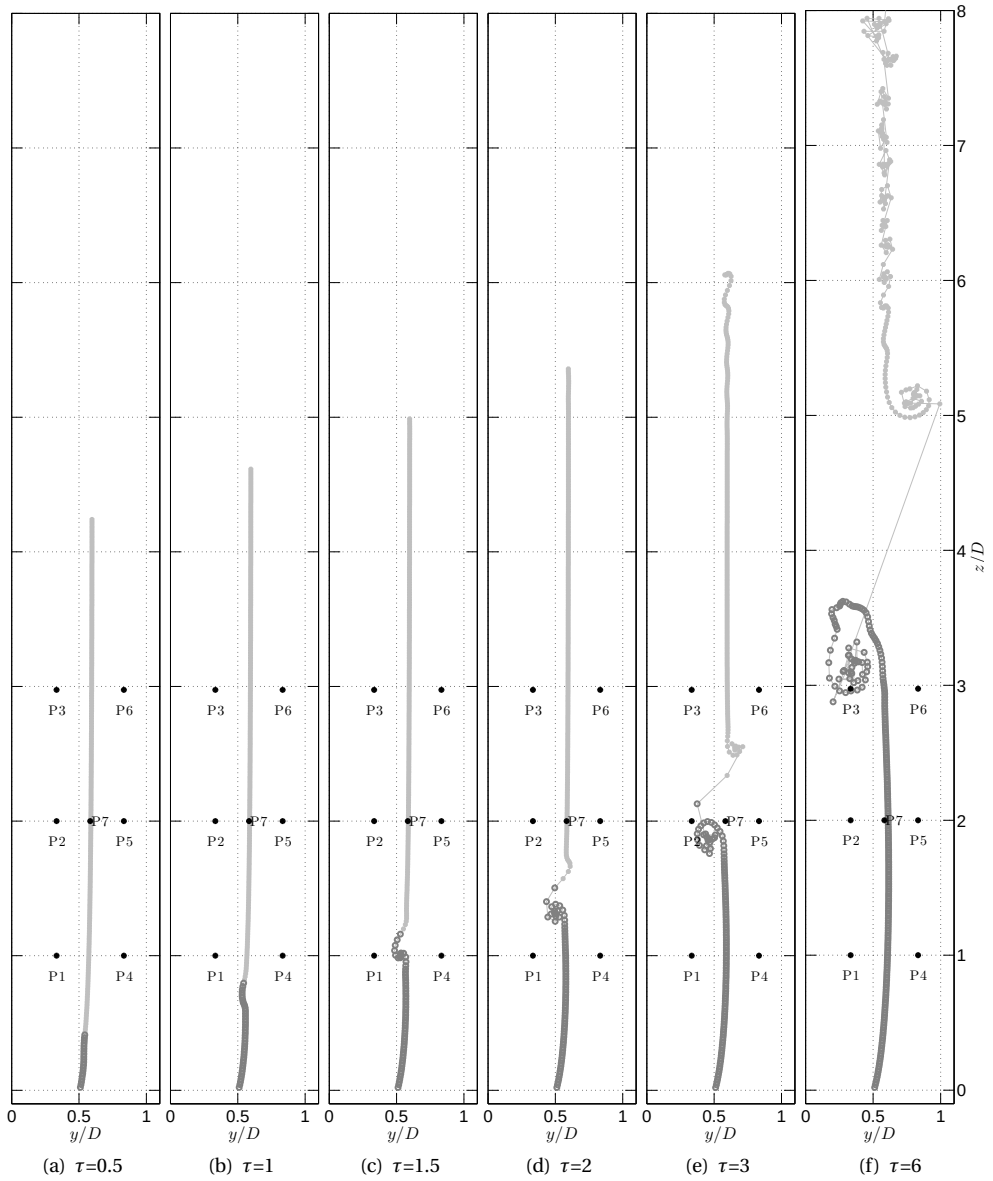

(a) τ=0.5 (b) τ=1 (c) τ=1.5 (d) τ=2 (e) τ=3 (f) τ=6

Figure 5.4: Wake development after load increase calculated by the FWVR model (dark and light particles represent vortices shed after and before load change separately).

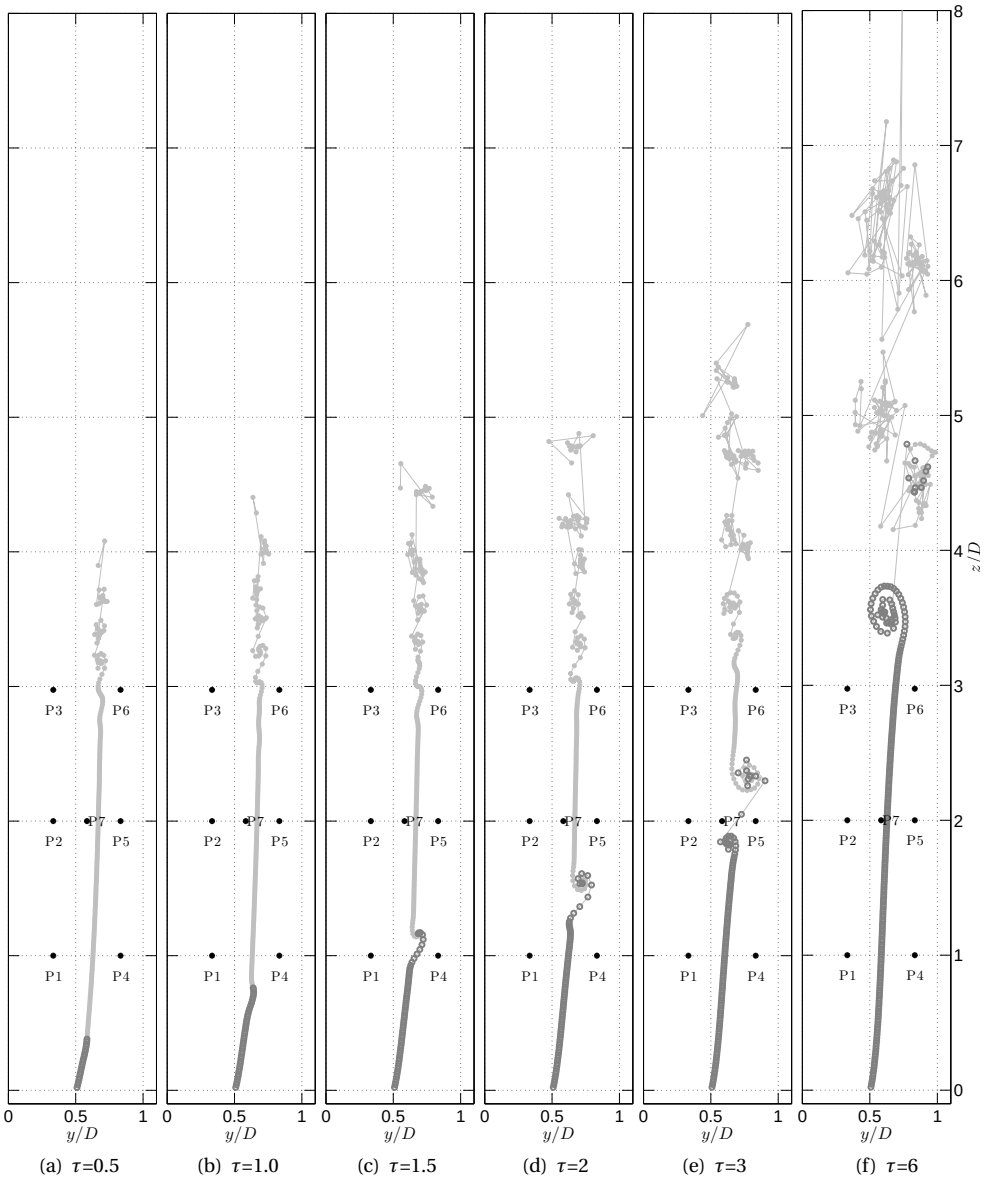

(a) τ=0.5 (b) τ=1.0 (c) τ=1.5 (d) τ=2 (e) τ=3 (f) τ=6

Figure 5.5: Wake development after load decrease calculated by the FWVR model (dark and light particles represent vortices shed after and before load change separately).

P2, P7, P5, after load increase and decrease. The velocity at all the three different radial positions of the same axial plane starts to respond to the load variation at around τ=2 for both load increase and decrease cases. From the experimental results, the turbulence is higher in the shear layer region at P7 in both the load increase and decrease cases. Due to the velocity singularity induced by the vorticity when the observed locations are too close to the vortex element, the result from the FWVR model is highly influenced by the vorticity elements in the shear layer region.

For the load increase case, with the entire vortex system convecting downstream, it can be seen that the velocity decreases eventually to the new steady state of the higher disc load at the inner wake y/D=0.33 and the shear layer y/D=0.58. The eventual decrease of velocity inside the wake corresponds to the higher induction at this higher disc load state. The velocity at the outer wake y/D=0.83 eventually increases to the new steady state. The final increase of velocity is due to the larger blockage effect of the disc at the higher disc load; and vice versa for the load decrease case.

The undershoot and overshoot of the velocity before the new steady state is also observed from the numerical results. This is presumed to be caused by the the rolling-up process of the vortex and its relative positions to the observed positions during its passage, which will be verified in the subsection 5.4.2.

Comparing Figure 5.6a and Figure 5.6b, there is a larger overshoot or undershoot at P2 for the load increase case than that for the load decrease case. On the opposite, there is a larger overshoot or undershoot at P5 for the load decrease case than that for the load increase case, for both experimental and numerical methods. This will be further explained in the subsection 5.4.2.

The velocity development from both methods at the locations P1, P2, P3 after load increase and decrease are presented in Figure 5.7. From Figure 5.7a and 5.7b, the time onset of velocity response at the same radial positions but different planes upon the onset of load change are different - the velocity starts to perturb at τ=1.0 for P1, at around τ=2.0 for P2, at around τ=3.0 for P3. As the flow disturbance convects downstream, the velocity field at locations from the near wake to the far wake starts to respond successively. The comparison of the velocity profiles at these locations between the load increase and decrease cases shows that there is a larger secondary unsteadiness effect in the load increase case than that in the load decrease case; this is true for both experimental and numerical results.

Figure 5.8 presents the velocity development at the P4, P5, P6 after load increase and decrease. As similar as locations at y/D=0.33 on these planes in Figure 5.7, the velocity starts to perturb at around τ=1.0 for P4, at around τ=2.0 for P5, at around τ=3.0 for P6. It shows that the velocity overshoot or undershoot increases as the plane goes further downstream for both load increase and decrease cases for both methods. On the contrary to the velocity at y/D=0.33 in Figure 5.7, the secondary unsteadiness effect is larger in the load decrease case than that in the load increase case at the locations of y/D=0.83; this holds for both methods.

As seen from Figure 5.6–5.8, the numerical model can capture the experimental dynamic velocity profiles at different locations in the field generally well in terms of the secondary velocity unsteadiness and the transient profile which includes the time to start to respond to the disturbance and the time it takes to reach the new steady state; although

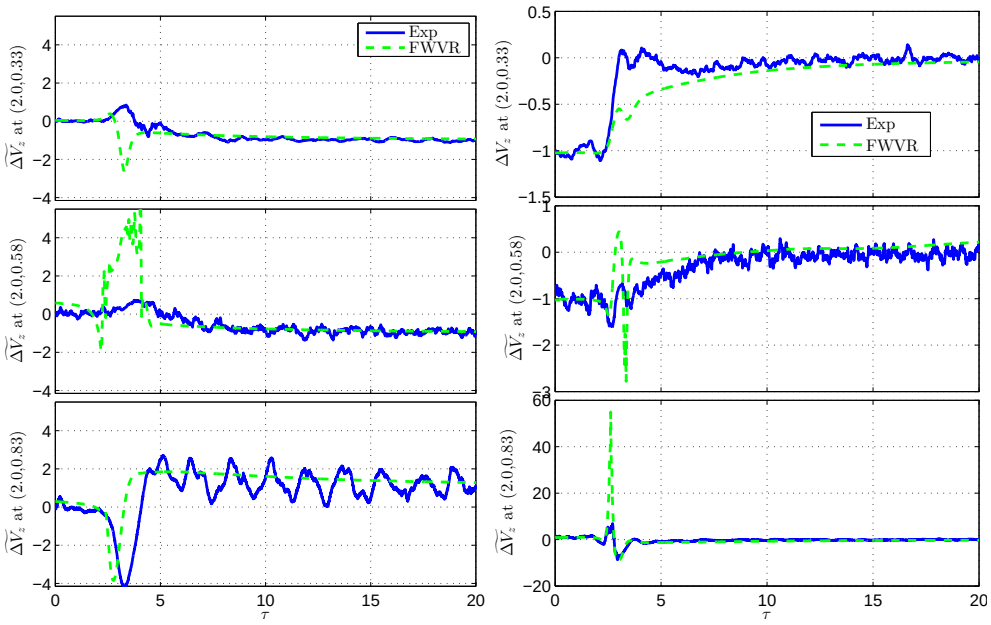

(a) load increase case (b) load decrease case

Figure 5.6: Velocity at P2(z/D=2.0, y/D=0.33), P7(z/D=2.0, y/D=0.58), P5(z/D=2.0, y/D=0.83) from experiment and the FWVR model in load increase and decrease cases.

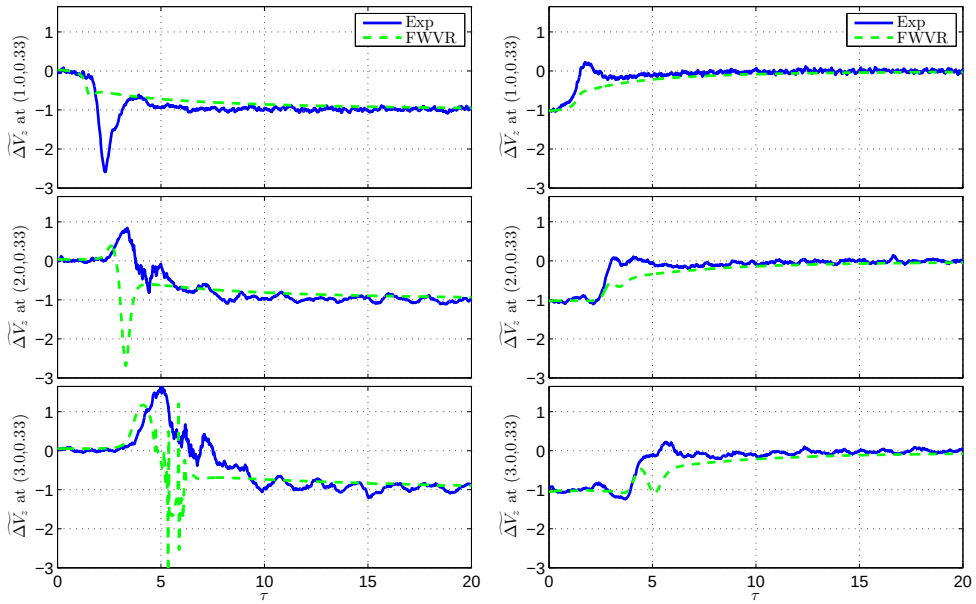

(a) load increase case

(b) load decrease case

Figure 5.7: Velocity at P1(z/D=1.0, y/D=0.33), P2(z/D=2.0, y/D=0.33), P3(z/D=3.0, y/D=0.33) from experiment and the FWVR model in load increase and decrease cases.

there are some local magnitude differences for the overshoots or undershoots.

The difference in overshoot and undershoot between the numerical and experimental results, e.g. the opposite overshoot at P2 in the load increase case in Figure 5.7a, is likely caused by the different extent of vorticity accumulation and the relative distance of the rolled-up vortices to the observation points in the numerical and experimental data. Specifically, the effect of tower and holes of disc mesh is present in the experiment, which is not taken into account in the simulations. The effect of the systematic mechanical vibration is another reason, whose effect is unknown and it can not be totally isolated from the aerodynamic effect in the experiment.

5.4.2. DECOMPOSED VELOCITY ANALYSIS OF CASE $\delta t^* = 0.2$

Section 5.4.1 shows the secondary unsteadiness — velocity overshoot and undershoot in the wake caused by the dynamic load change on the disc, where it is assumed that the abrupt velocity change is caused by the rolling-up process of the vorticity and its subsequent passage downstream.

In this section, the assumption will be verified by decomposing the velocity induced by different vorticity elements from the FWVR model, using case δt^*=0.2 as an example. Figure 5.9b plots the positions of the vortex rings at time τ=1.5, 2.5, 4.0 after load increase. The vorticity shed before and after the onset of load change are separated by

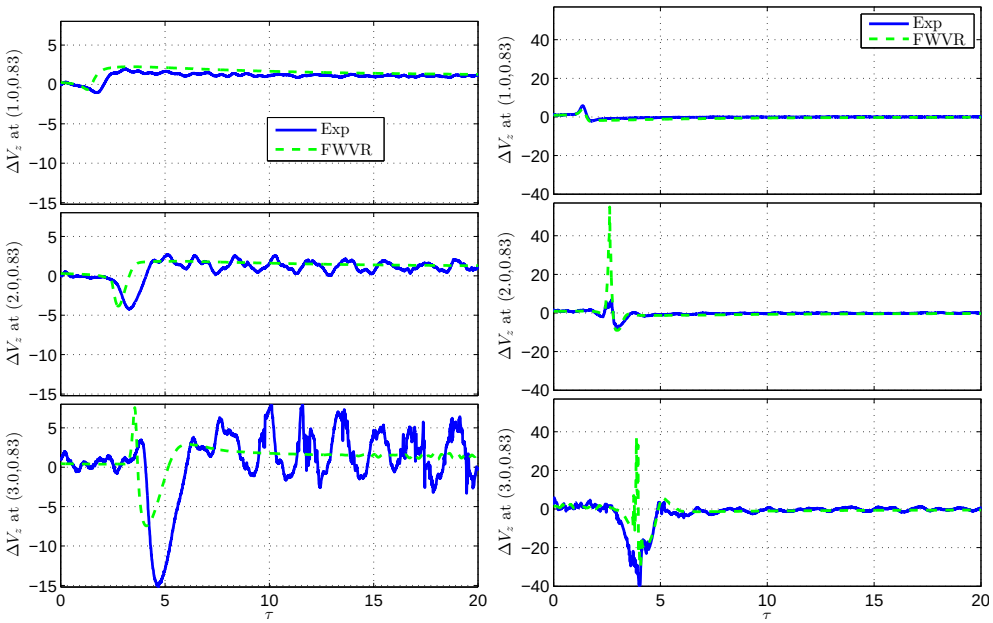

(a) load increase case

(b) load decrease case

Figure 5.8: Velocity at P4(z/D=1.0, y/D=0.83), P5(z/D=2.0, y/D=0.83), P6(z/D=3.0, y/D=0.83) from experiment and the FWVR model in load increase and decrease cases.

the circular mark. The rolled-up vorticity is counted from the first vortex element shed when the load starts to change, with one increment at each side of vorticity shed before and after the load change in every $0.125\tau_0$, as marked with diamonds in Figure 5.9b. The three time points the vorticity plotted in Figure 5.9b are also marked by the vertical dash line accordingly in Figure 5.9a and 5.9c. As seen, these are the time points around when the velocity peaks at these planes. Figure 5.9a and 5.9c shows the velocity induced by the new and old shed vorticity and the rolled-up vorticity and the total at locations P4-P6 and P1-P3, separately, for load increase case. These locations are also marked in Figure 5.9b.

As the rolled-up vorticity is convected downstream, the induced velocity from the rolled-up vorticity at the three planes peaks around τ=1.5, 2.5, 4.0 accordingly for both y/D=0.83 and 0.33 . As the rolled-up vorticity grows as it is being convected, the amplitude of the peak velocity induced by the rolled-up vorticity increases with downstream planes. The increased peak of the velocity induced by the roll-up vorticity results in an increase peak in the total velocity from x/D=1 to x/D=3. This explains the increase amplitude of undershoot when the planes moves downstream in figures 5.6 and 5.7. The further downstream the plane is, the larger extent of accumulation of vortices is, which results in a larger amplitude of velocity undershoot.

As clearly seen from Figure 5.9a and 5.9c, the rolled-up vorticity has a larger effect on the inner wake y/D =0.33 than the outer wake y/D =0.83. This is due to the inward movement of the rolled-up vorticity in the load increase case. The total velocity peaks at the time when the velocity induced by the rolled-up vorticity peaks for Figure 5.9c, this is not the case for P4 and P5 in Figure 5.9a. This explains the larger overshoot or undershoot at P1, P2, P3 in the load increase case than that in the load decrease case in Figure 5.7 for both numerical and experimental results.

The velocity induced by the new shed vorticity at P4 - P6 firstly decreases before increasing to a peak, and then finally decays to a converged value. Despite the new shed vorticity accumulated with time, it starts to roll up before reaching these positions. The roll-up process moves the vorticity away from these positions, resulting in a temporal decrease in induced velocity. Combining the contribution from the old shed vorticity, it results in the undershoot in the total velocity at these locations. The overshoot at P6 is caused by its short distance to part of the rolled-up vorticity as seen in Figure 5.9b.

Figure 5.10b plots the vorticity position of the vortex rings at times τ=1.5, 2.5, 4.0 after load decrease. Figure 5.10a and 5.10c show the velocity induced by the new and old shed vorticity, and the rolled-up vorticity and the total at locations P4-P6 and P1-P3 separately, for load decrease case. The induced velocity from the rolled-up vorticity at the three planes also peaks around τ=1.5, 2.5, 4.0 accordingly for both y/D=0.83 and 0.33 in this load decrease case. The peak amplitude of the velocity induced by the rolled-up vorticity increases with downstream planes with an exception of P6. P6 is sensitive to the vortex elements as it is inside the rolled-up vorticity, as seen in Figure 5.10b. At τ=1.5, the rolling-up process just starts, the peak amplitude of the induced velocity by the rolled-up vorticity at P4 is still low, which results in a slight peak in the total velocity curve. This explains the increase amplitude of overshoot or undershoot when the planes moves downstream in Figure 5.8.

As clearly seen from Figure 5.10b, in this load decrease case, the accumulated rolled-

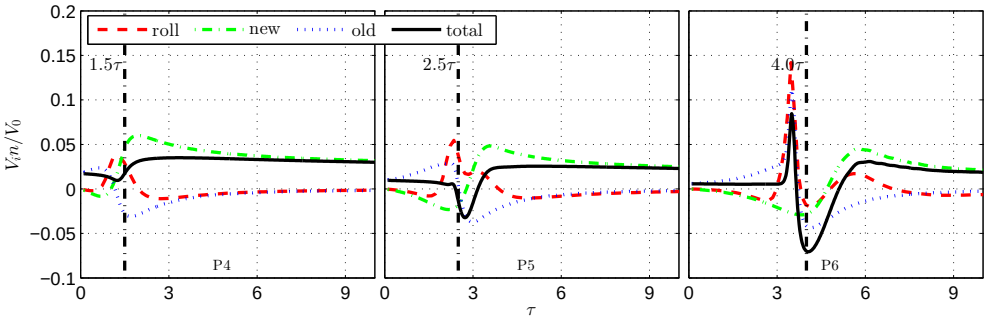

(a) Velocity at P4, P5, P6

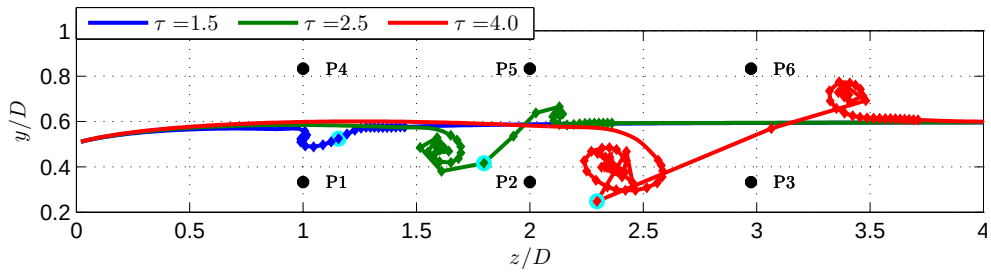

(b) vortex position at time τ=1.5, 2.5, 4.0

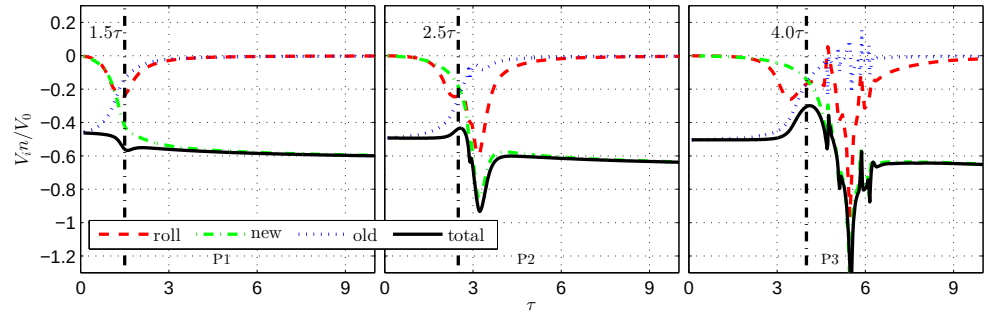

(c) Velocity at P1, P2, P3

Figure 5.9: The velocity induced by the new, the old shed vorticity, the rolled-up vorticity and the total at P1-P6 and wake of the FWVR model at time step τ=1.5, 2.5, 4.0 for load increase of case δt^*=0.2.

up vorticity moves outwards, it moves closer to the locations in the outer wake y/D =0.83. The total velocity peaks at where the velocity induced by the rolled-up vorticity peaks for P4-P6. It is not the case for the locations at y/D =0.33 P1-P3 in Figure 5.10c, as the accumulated rolled-up vorticity moves away from these locations. This explains why the secondary unsteadiness at P4, P5, P6 in the load decrease case is larger than that in the load increase case in Figure 5.8. The reason is the same for that there is no or negligible peak in velocity at P1, P2, P3 for load decrease case in Figure 5.7b.

The decomposed induced velocity at different locations shows that the secondary unsteadiness in velocity is determined by the effect of the passage of accumulated rolled-up vorticity and its relative distance to the observing locations during the process of convecting downstream. It presents as a velocity overshoot or undershoot or nothing under the combined effect. This verifies the hypothesis made in subsection 5.4.1.

5.4.3. THE EFFECT OF REDUCED RAMP TIME

This section compares the wake velocity profiles between the three different cases δt^*=0.2, 0.4, 0.8.

Figure 5.11 compares the velocity of the three reduced ramp time cases between the numerical and experimental results at P1, P2, P3 for load increase and decrease cases, separately. From both Figure 5.11a and 5.11b, it can be seen the smaller the reduced ramp time, the larger the amplitude of velocity overshoot or undershoot, and the steeper slope of the transient velocity. For the experimental results, for all three cases, the difference is larger in the load decrease case than that in the load increase case. This may be caused by the stronger interaction of the rolled-up vorticity with the turbulence caused by the holes in the disc in the load increase case, because the vorticity moving inward results in higher turbulence in the inner wake (referred to Figure 4.8).

Figure 5.12 presents the velocity development at P4, P5, P6 for load increase and decrease cases. The observations in the velocity profile are consistent with those inside the wake, a larger overshoot or undershoot and a steeper slope of velocity transient curve occurs for the smaller reduced ramp time case. This observation is true for both the experimental and the numerical results.

Figures 5.11 and 5.12 show that the numerical model can capture the basic trend of dynamic velocity profiles of the experiments for different reduced ramp time cases apart from some local amplitude difference. The main reasons causing the difference have been discussed in subsection 5.4.1, the turbulence caused by the porous disc, effects of the hub, tower etc.. All these factors will affect the direct cause — the relative distances of rolled-up vorticity to the observed locations in the field during the process of convecting downstream, as discussed in subsection 5.4.2.

5.4.4. DECOMPOSED VELOCITY ANALYSIS OF CASES $\delta t^* = 0.2, 0.4, 0.8$

The difference in transient velocity for different reduced ramp time cases are discussed in subsection 5.4.3. The causes of this difference are further explored by decomposing the velocity induced by different vorticity elements from the FWVR model in this section.

Figure 5.13 presents the decomposed induced velocity from the new and old shed vorticity, the rolled-up vorticity and the total at P2 and P5, and the locations of the vortex rings at τ=2.5 after load increase for the three cases δt^*=0.2, 0.4, 0.8.

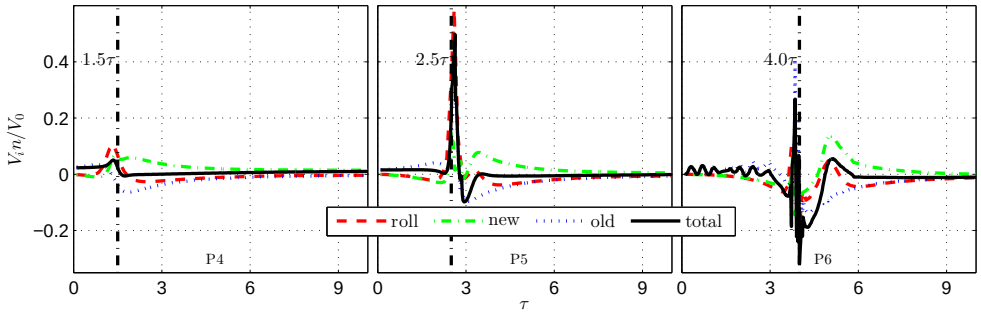

(a) Velocity at P4 (z/D=1, y/D=0.83), P5 (z/D=2,y/D=0.83), P6 (z/D=3, y/D=0.83)

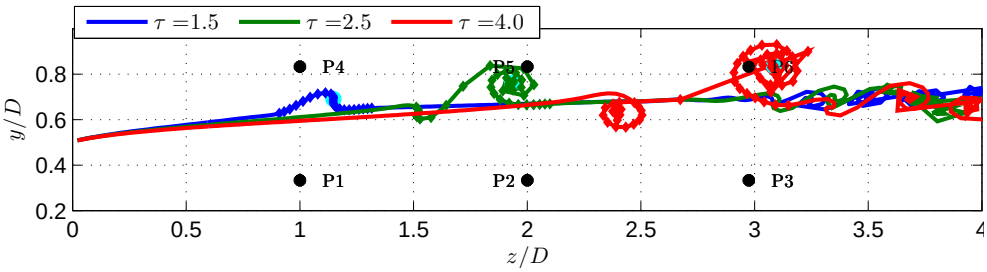

(b) vortex position at time τ=1.5, 2.5, 4.0

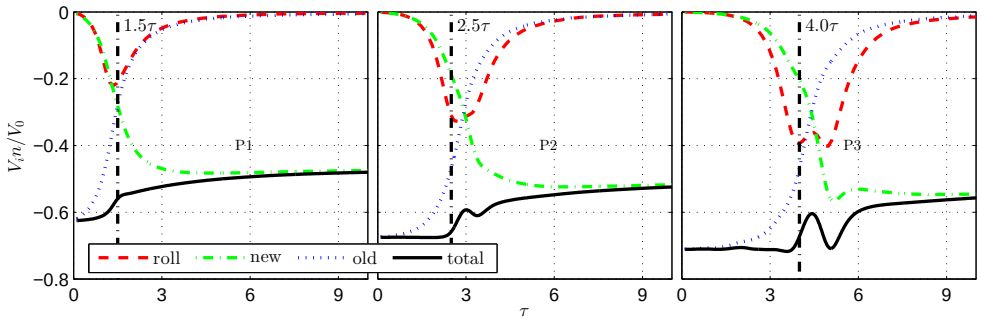

(c) Velocity at P1 (z/D=1, y/D=0.33), P2 (z/D=2, y/D=0.33), P3 (z/D=3, y/D=0.33)

Figure 5.10: The velocity induced by the new, the old shed vorticity, the rolled-up vorticity and the total at P1-P6 and wake of the FWVR model at time step τ=1.5, 2.5, 4.0 for load decrease of case δt^*=0.2.

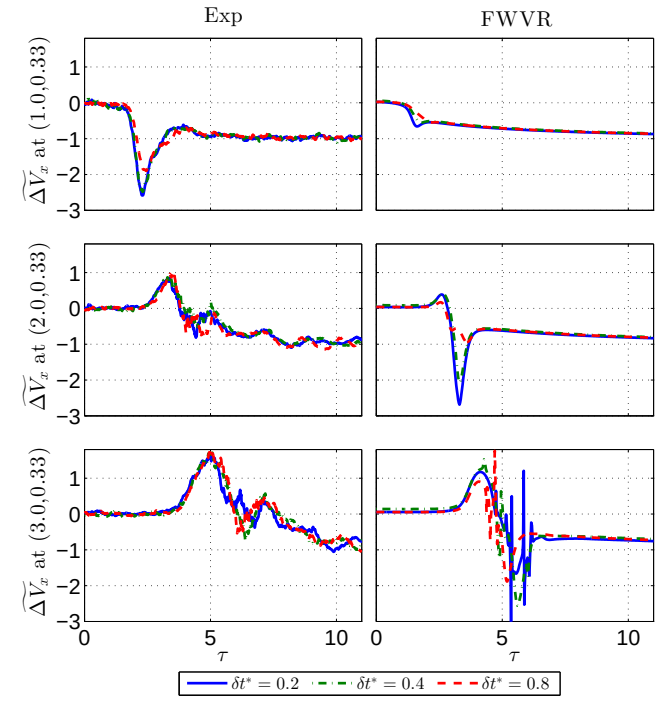

(a) load increase case

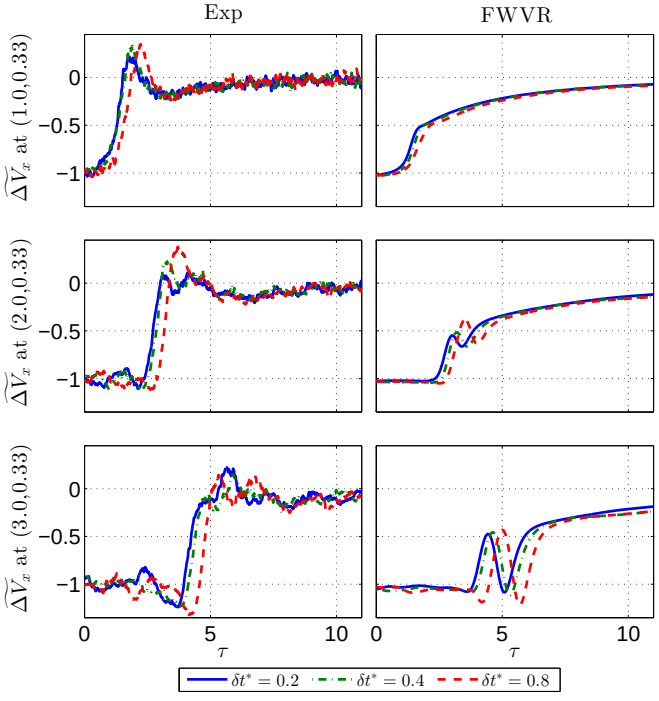

(b) load decrease case

Figure 5.11: Velocity at P1(z/D=1, y/D=0.33),P2(z/D=2, y/D=0.33),P3(z/D=3, y/D=0.33) from experiment and the FWVR model in load increase and decrease cases for δt^*=0.2, 0.4, 0.8.

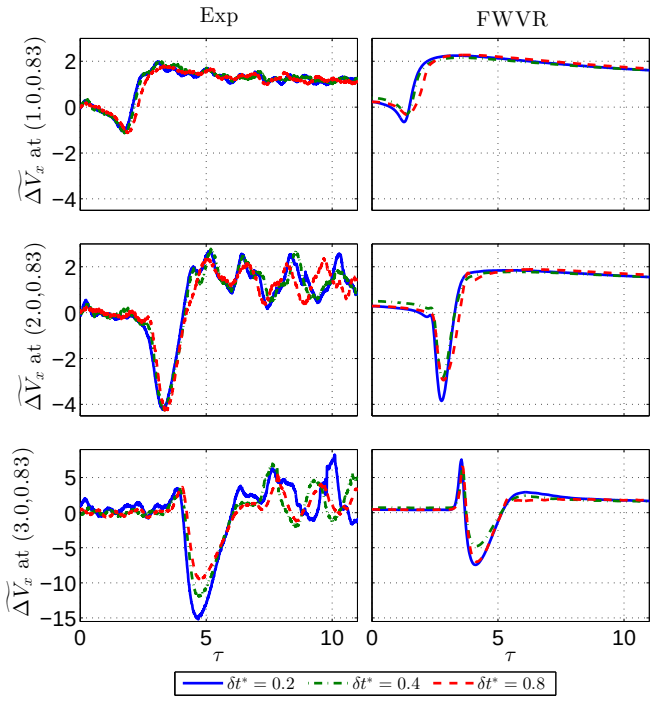

(a) load increase case

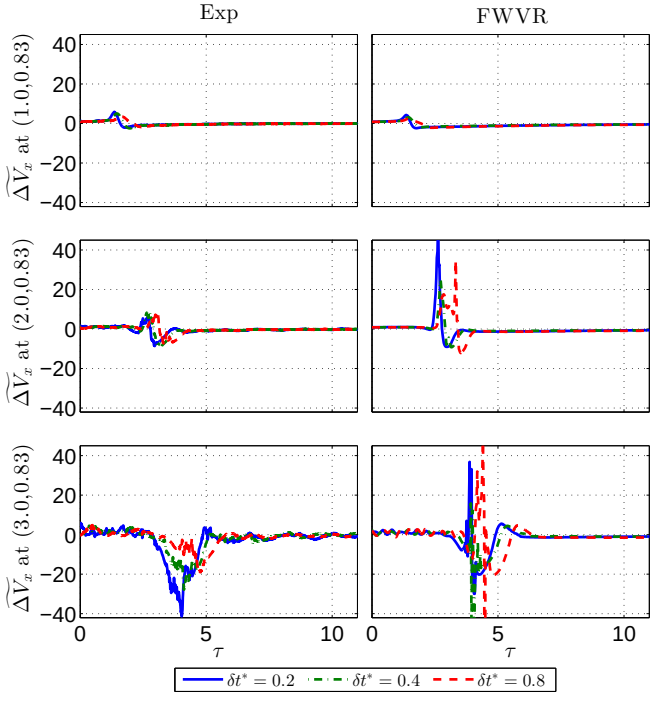

(b) load decrease case

Figure 5.12: Velocity at P4(z/D=1, y/D=0.83),P5(z/D=2, y/D=0.83),P6(z/D=3, y/D=0.83) from experiment and the FWVR model in load increase and decrease cases for δt^*=0.2, 0.4, 0.8.

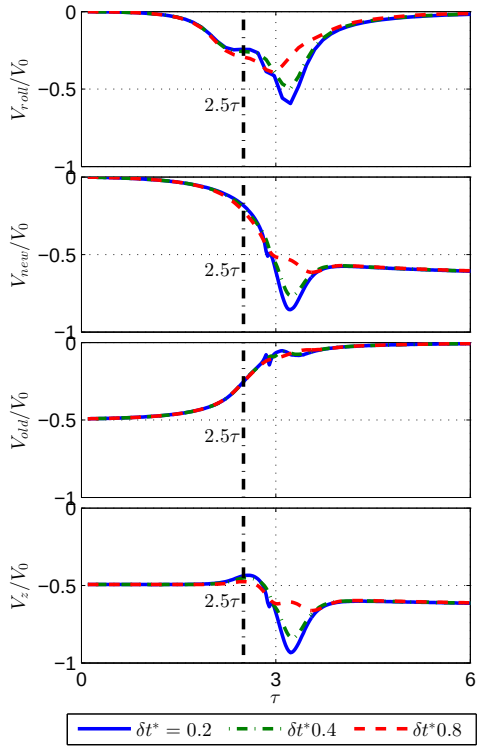

(a) Decomposed induced velocity at P2

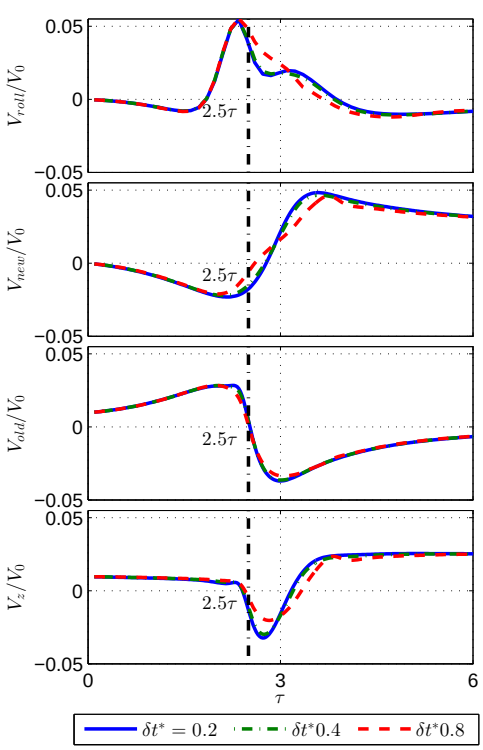

(b) Decomposed induced velocity at P5

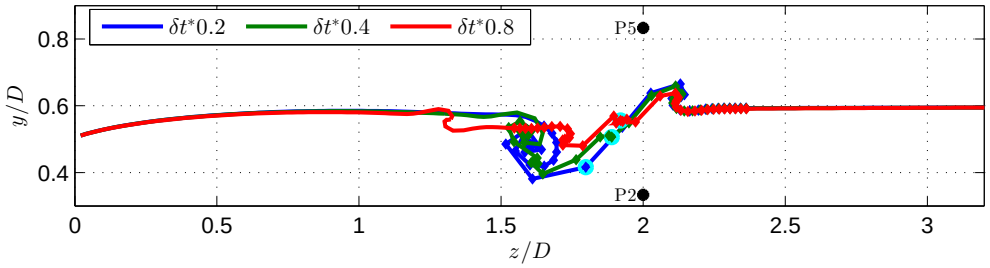

(c) Locations of vortex rings from the FWVR model for δt^*=0.2, 0.4, 0.8 at τ=2.5

Figure 5.13: The velocity induced by the new, the old shed vorticity, the rolled-up vorticity and the total at P2 (z/D=2, y/D=0.33) and P5 (z/D=2, y/D=0.83), and locations of the vortex rings of the FWVR model at τ=2.5 for load increase of cases δt^*=0.2, 0.4, 0.8.

As seen from Figure 5.13c, the smaller the reduced ramp time, the larger extent of the rolling up process at the same time after the load change. In these load increase cases, the rolled-up vorticity moves inward, which is moving towards to P2 but moving away from P5. Under the superposition effect of larger roll-up extent and smaller distance between the rolled-up vorticity to the observed locations, a smaller reduced ramp time resulting in a larger peak of velocity at P2 induced by the rolled-up vorticity. Under the counter effect of larger roll-up extent and larger distance between the rolled-up vorticity to the observed locations, there is no difference in the peak of velocity at P5 induced by the rolled-up vorticity between the three cases. In this load increase case, few vortex elements shed before the load change are involved in the roll-up process, resulting in a slight difference of velocity induced by the vortex shed before load change at both locations. The smaller the reduced ramp time, the larger the amplitude of velocity at P2 and the steeper the slope of velocity at P5 induced by the vortex shed after load change.

Figure 5.14 presents the decomposed induced velocity from the new, old shed vorticity, the rolled-up vorticity and the total at P2 and P5, and the locations of the vortex rings at τ=2.5 after load decrease for the three cases δt^*=0.2, 0.4, 0.8.

It is consistent with the load increase case in Figure 5.13, a smaller reduced ramp time results in a larger extent of the rolling up part in Figure 5.14c. Due to the outward movement of the rolled-up vorticity in this load decrease case, the rolled-up vorticity is moving towards to P5 but moving away from P2. Under the superposition effect of larger roll-up extent and smaller distance between the rolled-up vorticity to the observed locations, a smaller reduced ramp time results in a larger peak of velocity at P5 induced by the rolled-up vorticity. Under the counter effect of larger roll-up extent and larger distance between the rolled-up vorticity to the observed locations, a smaller reduced ramp time resulting in a smaller peak of velocity at P2 induced by the rolled-up vorticity.

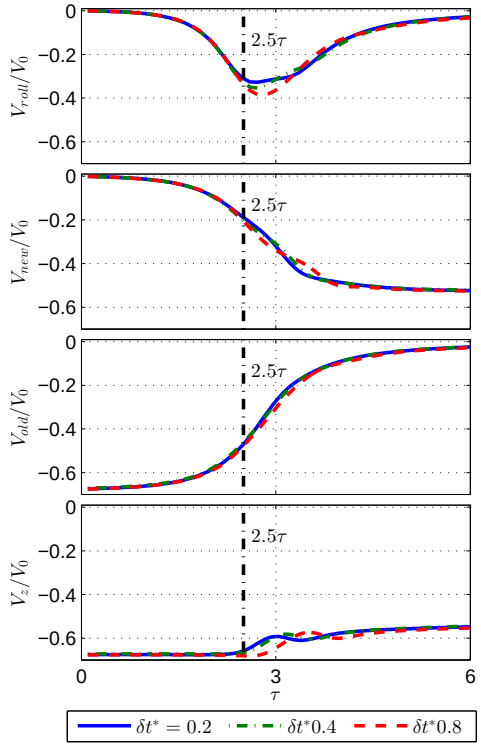

(a) Decomposed induced velocity at P2

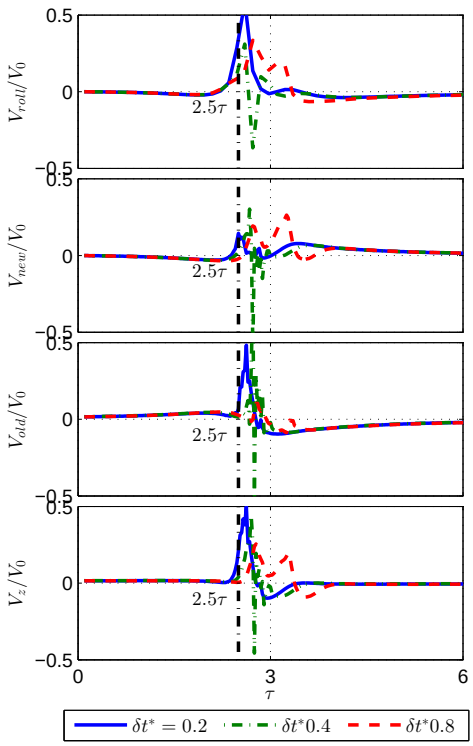

(b) Decomposed induced velocity at P5

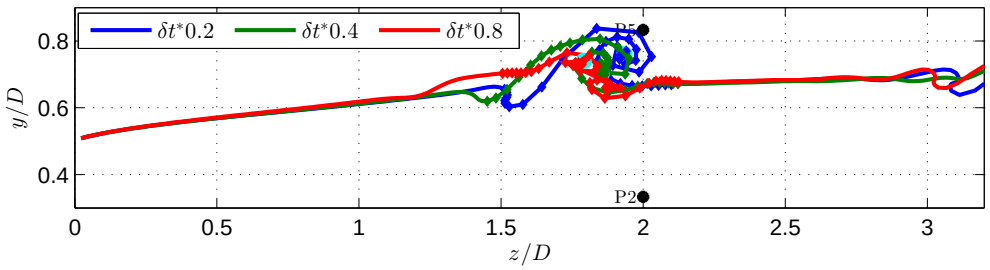

(c) Locations of vortex rings from the FWVR model for δt^*=0.2, 0.4, 0.8 at τ=2.5

Figure 5.14: The velocity induced by the new, the old shed vorticity, the rolled-up vorticity and the total at P2 (z/D=2, y/D=0.33) and P5 (z/D=2, y/D=0.83) and locations of vortex rings of the FWVR model at τ=2.5 for load decrease of cases δt^*=0.2, 0.4, 0.8.

5.5. CONCLUSIONS

The unsteady flow of an actuator disc during transient load with different reduced ramp time has been investigated numerically with a free wake vortex ring model. The secondary unsteadiness — overshoot and undershoot in velocity from the experiments, is also observed in the numerical results. The comparison between the numerical and experimental results show that the free wake vortex model can capture the wake velocity profiles, for the steady radial distributed velocity profile and the transient velocity profiles.

The wake development from the FWVR model shows that the vortex sheet at the edge of the disc rolls up into a vortical ring structure gradually during the convecting downstream process after the disc load change. The vortex spirals inward in the load increase cases, spirals outward in the load decrease cases. This is the main reason which causes the difference in wake velocity between the load increase and decrease cases.

Decomposing the velocity induced by different vortex elements confirms that the extent of the rolling-up process and its relative distance to the observed points are the main reasons causing the difference in velocity transient slope and difference in the amplitude of velocity overshoot and undershoot at the different observed locations.

The effect of ramp time as observed in the experimental results is confirmed with the vortex model. It shows that a smaller reduced ramp time (a faster load change) results in a steeper transient velocity change and in turn a larger amplitude of the velocity overshoot or undershoot. Decomposing the induced velocity from different vorticity elements also reveals that the different velocity profile at the same location in different reduced ramp time cases resulted from the different extent of the rolling up process. A smaller reduced ramp time leads to a larger extent of the rolling up process.

The dynamic wake response of an unsteady actuator disc from the experiment is reproduced by the FWVR model reasonably well. The decomposing velocity from the FWVR model offers much insight into the dynamic wake response.

Based on the performance of the free wake vortex model, a few steps are tried to simplify it for engineering purpose. The first step is to disregard the wake expansion, which is done by extending the linear actuator disc model from steady load to unsteady load in chapter 6.

6

SEMI-ANALYTICAL ACTUATOR DISC SOLUTION FOR UNSTEADY LOAD

Make everything as simple as possible, but not simpler.

Albert Einstein (1879-1955)

The main content of this chapter has been published in

Yu, W., Ferreira, C. S., van Kuik, G., Analytical actuator disk solution for unsteady and/or non-uniform loading. in 34th Wind Energy Symposium, California, January 2016.

This chapter extends the classical steady cylindrical vortex tube model to unsteady flow, while keeping the inherent simplicity of the theory. The three representative load cases investigated in chapter 3: (I) steady uniform and radially-varying , (II) unsteady uniform, and (III) unsteady radially-varying load, are studied using this improved vortex tube model. The results are compared with the free wake vortex ring model developed in chapter 3, and also with the three dynamic-inflow engineering models - the Pitt-Peters, Øye and ECN model for unsteady load cases. Results shows that the vortex tube model has an acceptable prediction of axial and radial induction at the disc for steady load. The predictions of the induction from the vortex tube model are comparable to the Øye engineering model for unsteady uniform load. It has an improved prediction in induction compared with the three dynamic-inflow engineering models for unsteady radially-varying load.

6.1. INTRODUCTION

The most elementary version of the momentum theory is based on uniform axial load in an axi-symmetrical flow. The axial momentum theory is introduced in chapter 2. The axial momentum theory is extended to BEM or stream-tube analysis of radially-varying load based on the assumption of annuli independence.

The application of the actuator disc concept provides a simple wake model, which is introduced in chapter 2. This vortex model gives detailed information of a rotor flow field. It is only valid for an actuator disc with uniform load. The induced velocity field of an actuator disc with radially-varying load can be calculated by using a superposition of a system of coaxial vortex cylinders, it has been applied by Heyson and Katzoff (1956) and Branlard and Gaunaa (2014).

However, the actuator-disc model introduced in chapter 2 is only valid for steady flow. Only a limited amount of work was tried to overcome this limitation of the steady actuator disc model. Chattot (2014) tried to extend the steady actuator disc theory to unsteady flow based on conservation laws, but numerical results showed the formulae can not correctly account for unsteady effects. He subsequently implemented a vortex ring model with a prescribed wake vortex line model for unsteady load calculations. Concurrently, Branlard and Gaunaa (2014) also extended the steady actuator-disc model to unsteady load case, a step change in pitch was studied.

The main purpose of this chapter is to extend the steady vortex tube model of an actuator disc to unsteady flow. The vortex tube model can in principle be applied to unsteady and arbitrarily distributed axi-symmetrical flow of discs representing aircraft propellers or wind turbines. In section 6.2, the existing vortex tube model for steady uniform and radially-varying disc loading and the upgraded vortex tube model for unsteady uniform and radially-varying disc loading is detailed. The results from the vortex tube model are presented in section 6.3. Comparisons of the vortex tube model with the free wake vortex ring model and the three dynamic-inflow engineering models are presented for the three load cases considered in chapter 3: (I) steady uniform and radially-varying load, (II) unsteady uniform load, and (III) unsteady radially-varying load. Conclusions are drawn in section 6.4. The time and velocity presented in the results are non-dimensionalizing using $\tau = \frac{V_0 t}{R}$ and the incoming wind speed V_0, respectively.

6.2. METHODOLOGY

The velocity field of an actuator disc with axial flow has been analytically studied by Conway (1995) and Branlard and Gaunaa (2014). Their analysis consistently decomposes the cylindrical vortex system into two components: (a) a vortex tube with circular vorticity and (b) a vortex system including longitudinal vortices shed from the disc edge and disc center, and the radially distributed bound vorticity on the actuator disc. The first component created axial and radial velocity in the flow field, while the second component determines azimuthal velocity. If the tip speed ratio goes to infinity, the rotation can be neglected, the effect of the second component goes to zero. This scenario is considered in this chapter.

This section begins with the introduction of the existing model for steady uniform and radially-varying load, followed by the extension of the model to unsteady flow. Figure 6.1 shows the assumed vortex system for all the four different load cases: steady uniform load, steady radially-varying load, unsteady uniform load and unsteady radially-varying load.

6.2.1. VORTEX TUBE MODEL FOR STEADY UNIFORM AND RADIALLY-VARYING DISC LOADING

The expression for the axial (u_z) and radial (u_r) velocity field induced by a semi-infinite vortex tube with constant tangential vorticity has been derived by Callaghan and Maslen (1960), Gibson (1974), van Kuik and Lignarolo (2016) and Branlard and Gaunaa (2014). Even though they use different methods, the final format is the same, given as

$$u_z(r,z) = \frac{\gamma}{2}\left[\frac{R_{tube}-r+|R_{tube}-r|}{2|R_{tube}-r|} - \frac{(Z_{tube}-z)}{2\pi\sqrt{rR_{tube}}}\cdot k(K(k^2)+\frac{R_{tube}-r}{R_{tube}+r}\Pi(\alpha^2,k^2))\right] \quad (6.1)$$

$$u_r(r,z) = -\frac{\gamma}{2\pi}\sqrt{\frac{R_{tube}}{r}}\left[\frac{2-k^2}{k}K(k^2)-\frac{2}{k}E(k^2)\right] \quad (6.2)$$

where E,K and Π are respectively the complete elliptic integrals of the first, second and third kind. The two elliptic parameters are given in Equation 6.3 and 6.4

$$k^2 = \frac{4rR_{tube}}{(Z_{tube}-z)^2+(R_{tube}+r)^2} \quad (6.3)$$

$$\alpha^2 = \frac{4rR_{tube}}{(R_{tube}+r)^2} \quad (6.4)$$

where (z,r) are coordinates of an arbitrary point P in the field, Z_{tube} is the starting axial coordinate and R_{tube} is the radius of the semi-infinite vortex tube. The vortex system for steady uniform load is given in Figure 6.1a.

The relationship of the strength of vortex sheet (γ) and the uniform pressure jump (Δp) of an actuator disc has been analyzed by van Kuik (2003). For steady flow, the product of the strength of the vortex sheet and the convection speed of the vortex sheet (v_s) is constant, it is given in Equation 6.5 (van Kuik, 2003).

$$v_s\gamma = \frac{\Delta p}{\rho}. \tag{6.5}$$

The definition of thrust coefficient is

$$C_T = \frac{T}{\rho A V_0^2/2} = \frac{A\Delta p}{\rho A V_0^2/2}. \tag{6.6}$$

Combining Equation 6.5 with Equation 6.6, the relationship between the strength of the vortex sheet and thrust coefficient is given by Equation 6.7.

$$\gamma = \frac{C_t(V_0)^2}{2v_s}. \tag{6.7}$$

If the disc loading is not uniform along the radial direction, vorticity will be shed along the radius instead of only at the edge of the disc as in the uniform load case. Equation 6.7 is thus applied to local annulus, which is separated by the vortex sheet in the radially-varying cases. A system of coaxial vortex cylinders to calculate the flow field induced by radially-varying load has been adopted by Heyson and Katzoff (1956) and Branlard and Gaunaa (2014). The application is the same here. The assumed vortex system is shown in Figure 6.1b. A semi-infinite vortex tube with strength $\tilde{\gamma}_i$ is shed at the radius r_i where there is load variation, where $i = 1,2...k$, $r_1 = R$, $r_k = 0$, $\tilde{\gamma}_i = \gamma_i - \gamma_{i-1}$, $\tilde{\gamma}_1 = \gamma_1$. γ_i is the strength of the vortex tube of the annulus with the local load, which is defined by Equation 6.7. In principle, any circularly symmetrical disc load can be obtained by a superposition of a series of vortex cylinders.

6.2.2. VORTEX TUBE MODEL FOR UNSTEADY UNIFORM AND RADIALLY-VARYING DISC LOADING

In unsteady flow, disturbances can arise from fluctuations in the incoming flow and change of load on the disc resulting from a pitch change or local control actions. For simplification, the incoming flow is assumed to be constant, and only the load variation is addressed here.

In the unsteady load case, the semi-infinite vortex tube is considered as a superposition of a semi-infinite vortex tube with a series of finite vortex tubes. The semi-infinite vortex tube for an unsteady uniform load is illustrated in Figure 6.1c. The series of finite vortex tubes with strength γ_j, extending from z_j to z_{j-1}, are generated at time j^{th}. The semi-infinite vortex tube with strength γ_1 extending from z_1 to infinity is generated before the unsteadiness happens. γ_j and z_j are respectively the strength and the convected distance of the tube shed at the time j^{th}, where $j = 1,2,...n$.

The relationship between the strength of the newly generated vortex surface at disc edge during time Δt and the strength of load on the disc is present in chapter 3, it is given in Equation 6.8.

$$\Delta\Gamma(t) = C_t(t)(V_0^2/2)\Delta t. \tag{6.8}$$

If the newly produced vortex surface has been convected at a velocity of $v_s(t)$, the convected distance of the vortex tube during this Δt is $\Delta s = v_s(t)\Delta t$. The strength of the

newly generated finite vortex tube is given in

$$\gamma(t) = -\frac{\Delta\Gamma(t)}{v_s(t)\Delta t} = \frac{C_t(t)\frac{(V_0)^2}{2}\Delta t}{v_s(t)\Delta t} = \frac{C_t(t)\frac{(V_0)^2}{2}}{v_s(t)}. \tag{6.9}$$

Equation 6.7 and Equation 6.10 are consistent with the equation obtained by Øye (1990), which is the basis of the Øye dynamic inflow model. $v_s = V_0(1-a)$ is used to determine the strength of the new generated vortex tube, where a is the axial induction factor at the disc.

Inputting $v_s = V_0(1-a)$ and $a = \frac{1-\sqrt{1-C_t(t)}}{2}$ into Equation 6.9 yields

$$\gamma(t) = V_0(\sqrt{(1-C_t(t)}-1). \tag{6.10}$$

The strength of the individual finite or semi-infinite vortex tube keeps constant while convecting downstream in this implementation, which means the updating of the vortex surface is determined by the contraction and extension of the tubes.

The induced velocity field by a finite vortex tube extending from z_1 to z_2 can be calculated directly by the analytical equations given by Branlard and Gaunaa (2014). In this chapter, the semi-infinite vortex tube is treated as a superposition of a series of semi-infinite vortex tubes starting at z_j, with strength of $\tilde{\gamma}_j$, where $\tilde{\gamma}_j$=γ_j-$\sum_{j=1}^{j-1}\tilde{\gamma}_j$, $\tilde{\gamma}_1$=γ_1. γ_1 and z_1 is the vortex strength and convected distances of the oldest vortex tube, γ_n and z_n are for the newest vortex tube.

Combining described models for steady radially-varying load and unsteady uniform load, any arbitrary radial radially-varying and unsteady load can be addressed by introducing

$$\tilde{\tilde{\gamma}}_{i,j} = \gamma_{i,j} - \gamma_{i-1,j} \tag{6.11}$$

$$\tilde{\tilde{\gamma}}_{1,j} = \gamma_{1,j} \tag{6.12}$$

$$\tilde{\gamma}_{i,j} = \tilde{\tilde{\gamma}}_{i,j} - \sum_{j=1}^{j-1}\tilde{\gamma}_{i,j} \tag{6.13}$$

$$\tilde{\gamma}_{i,1} = \tilde{\tilde{\gamma}}_{i,1} \tag{6.14}$$

where $\gamma_{i,j}$ is the vortex strength defined by Equation 6.10 for the local annulus with the local load. $\tilde{\gamma}_{i,j}$ and $z_{i,j}$ are respectively the final used vortex strength and position of the vortex tube to calculate the velocity field using Equation 6.1 and 6.2. $\tilde{\tilde{\gamma}}_{i,j}$ is an intermediate variable. The vortex system for unsteady radially-varying load is shown in Figure 6.1d.

The vortex tube model for both steady and unsteady load cases are denoted as VTM for all the following figures and discussions.

6.2.3. THE EFFECT OF CONVECTION VELOCITY

The convecting speed of the vortex tube needs to be determined. The different types of convection velocity and their effect is discussed in this section.

The free stream velocity (V_0) is used in Chattot (2014). A simplified convection velocity is used in Branlard (2015), which is denoted as V_1. For unsteady uniform load in

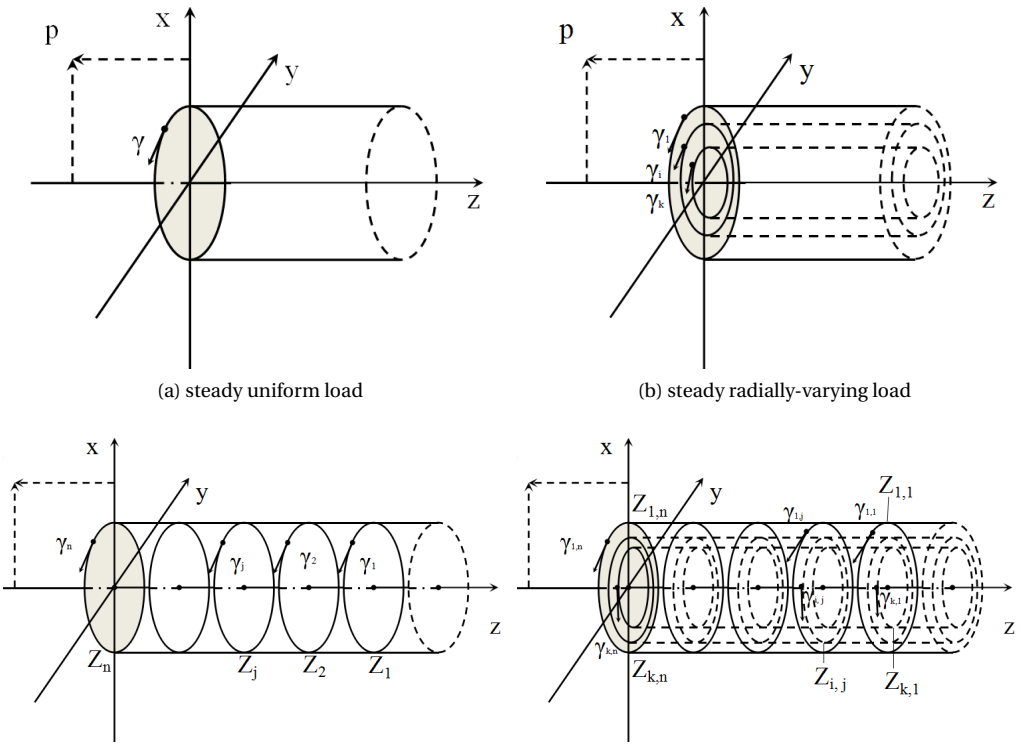

(a) steady uniform load

(b) steady radially-varying load

(c) unsteady uniform load

(d) unsteady radially-varying load

Figure 6.1: Assumed vortex system for the rotor wake.

Figure 6.1c, V_1 for convecting the axial position of j^{th} finite tube is defined by Equation 6.15. For unsteady radially-varying load in Figure 6.1d, V_1 for updating the position of $Z_{i,j}$ is defined by Equation 6.16. The convection velocity used in the Øye model is also considered, which is defined in Equation 6.17. It is the sum of the free stream velocity and the averaged induced velocity at the position (Z_i, R). The average induced velocity at positions of small distance outside and inside the tube $(Z_{i,j}, R_{i,j}+dy)$ and $(Z_{i,j}, R_{i,j}-dy)$ is used for the averaged induced velocity.

$$V_1(j) = V_0(\frac{1+\sqrt{1-C_t(j)}}{2}) \tag{6.15}$$

$$V_1(i,j) = V_0 + \sum_{i=i+1}^{k} \tilde{\gamma}_{i,j} + \tilde{\gamma}_{i,j}/2 \tag{6.16}$$

$$V_2(i,j) = V_0 + \frac{v_x(Z_{i,j}, R_{i,j}+dy) + v_x(Z_{i,j}, R_{i,j}-dy)}{2}. \tag{6.17}$$

Figure 6.2 compares the averaged axial velocity at the actuator disc through a step-increased and a step-decreased load between the VTM with the different convection velocity V_0, V_1 and V_2. It is also compared against results from MT, the FWVR model and the three dynamic-inflow engineering models. There is a local enlarged view inside each figure. As seen, the convection velocity has an important effect. The FWVR model decays slowest among all different models, the Øye and ECN model decays faster than the FWVR model but slower than all the other cases. When V_0 is used, where induction from the wake is not taken into account for the convection velocity, the VTM model decays faster than the other two cases (V_1, V_2) where the induction is considered. When only the induction from the simplified tube system V_1 is considered, the decay is close to the Øye and ECN models. When the the averaged induced velocity at the tube edge V_2 is used, the decay is even faster. Clearly, the larger induction, the slower the vortex tube is convected downstream, the slower the decay of the velocity. When V_1 of the three different convection speeds is used, the VTM model is the closest to the FWVR model. In addition, the calculation of V_1 costs much less time than the computation of V_2. Thus, the V_1 is used through the simulations in this chapter.

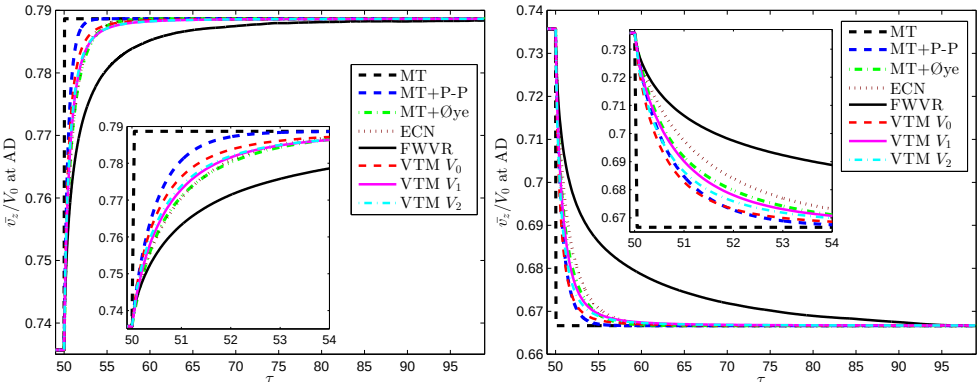

(a) step-decreased load

(b) step-increased load

Figure 6.2: Comparison of averaged axial velocity at the actuator disc between the VTM with different convection velocity, the FWVR model, the Pitt-Peters, Øye, ECN model and MT for a step-decreased and a step-increased load.

6

6.3. RESULTS AND ANALYSIS

6.3.1. STEADY UNIFORM AND RADIALLY-VARYING LOAD

Figure 6.3 compares the radial distribution of axial and radial velocity for steady uniform, radially increased, radially decreased load between the VTM and the FWVR model. As seen, the general trend of both axial and radial velocity from the VTM and the FWVR model matches well for the steady uniform and radially-varying load cases. The main difference between the two models is that the effect of the local variation of load on axial velocity is confined to the local region for the VTM, which is in line with the assumption of independent annuli. This was also shown by Branlard and Gaunaa (2014) with similar method. However, what is not mentioned there is that the effect of the local variation of load on radial velocity is also observed outside the local load varied region of the VTM. This means that the assumption of independent annuli only determines the independence of axial velocity of every annulus, but does not restrict the radial velocity for the VTM. The other difference in the two models is the uniformity of axial velocity along the radius. Excluding the effect of local varied load, the VTM model predicts uniform axial velocity distribution, but the FWVR model predicts a radially-varying axial velocity distribution even for uniform load. This means the VTM, which is extended from the axial momentum theory, inherits the wrong assumption of uniform axial velocity distribution of momentum theory. Instead of the axial velocity, the absolute velocity is found to be constant by van Kuik and Lignarolo (2016). However, the VTM in this study shows that the annuli independence of axial induction at the disc is only satisfied for steady case, where only infinite vortex tubes are shed from the disc. Load case III shows the local time-varying load affects the induction on the entire disc. In this load case, the prediction of the axial and radial induction from the simple VTM is close to the prediction by the more advanced free wake vortex ring model.

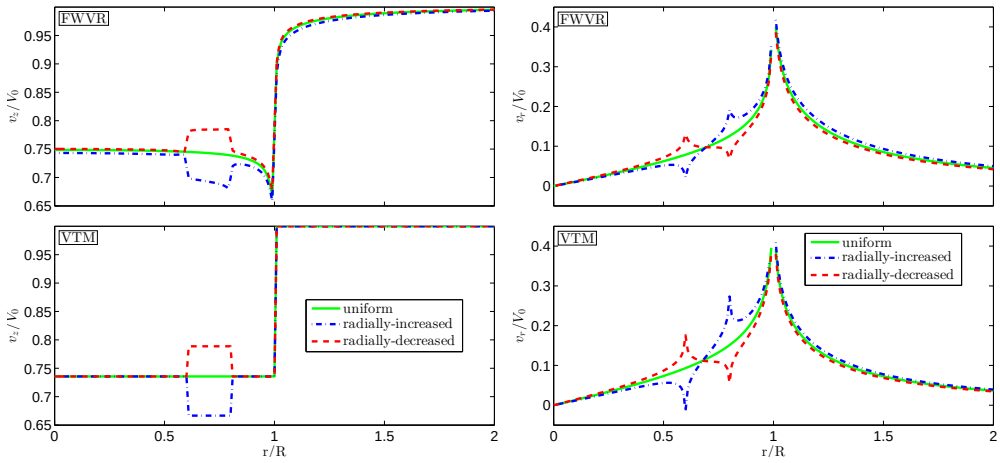

(a) axial velocity (b) radial velocity

Figure 6.3: Comparison of the axial and radial velocity distribution at the actuator disc plane between the VTM and the FWVR model for steady uniform, radially-increased, radially-decreased load.

6.3.2. UNSTEADY UNIFORM LOAD

In this section, the results of harmonically time-varying uniform load are analyzed, the simulations are presented for $k = 0.05, 0.2, 0.5$ and 1.0. Figure 6.4 compares the hysteresis loops of averaged axial velocity $\bar{v}_z$ at the actuator disc predicted by the VTM, the FWVR model, the Pitt-Peters, Øye and ECN dynamic inflow models. Results from MT is plotted as a reference. The amplitude difference — difference in amplitude of $\bar{v}_z$ from that of MT, and the phase lag — width of the hysteresis loop are analyzed.

The comparison of results between the FWVR model and the three dynamic-inflow engineering models is presented in chapter 3. The discussions here mainly focus on the VTM model.

The results show that the axial velocity from the VTM is comparable with the Øye and ECN model in terms of both amplitude difference and phase lag. This similarity in the VTM and the Øye and ECN model may be caused by the fact that the time constants in these two models are also obtained by vortex tube-based model.

Figure 6.5 compares the dynamic loop characteristics of v_z between the VTM, the FWVR model, MT and the three dynamic-inflow engineering models at different radial positions r/R=0, 0.3, 0.55, 0.6, 0.7, 0.8, 0.85, 0.95 and 0.99, at reduced frequency 0.2. It shows the VTM matches well with the Øye model along the radius. Figure 4.2b shows the radial velocity predicted by the VTM and the FWVR model matches, but the values and the phase lag from the VTM are relatively higher for the same radial position. This might be caused by the exclusion of expansion of the VTM. The comparison in this section shows that the axial velocity predicted by the VTM is comparable to the Øye dynamic inflow model.

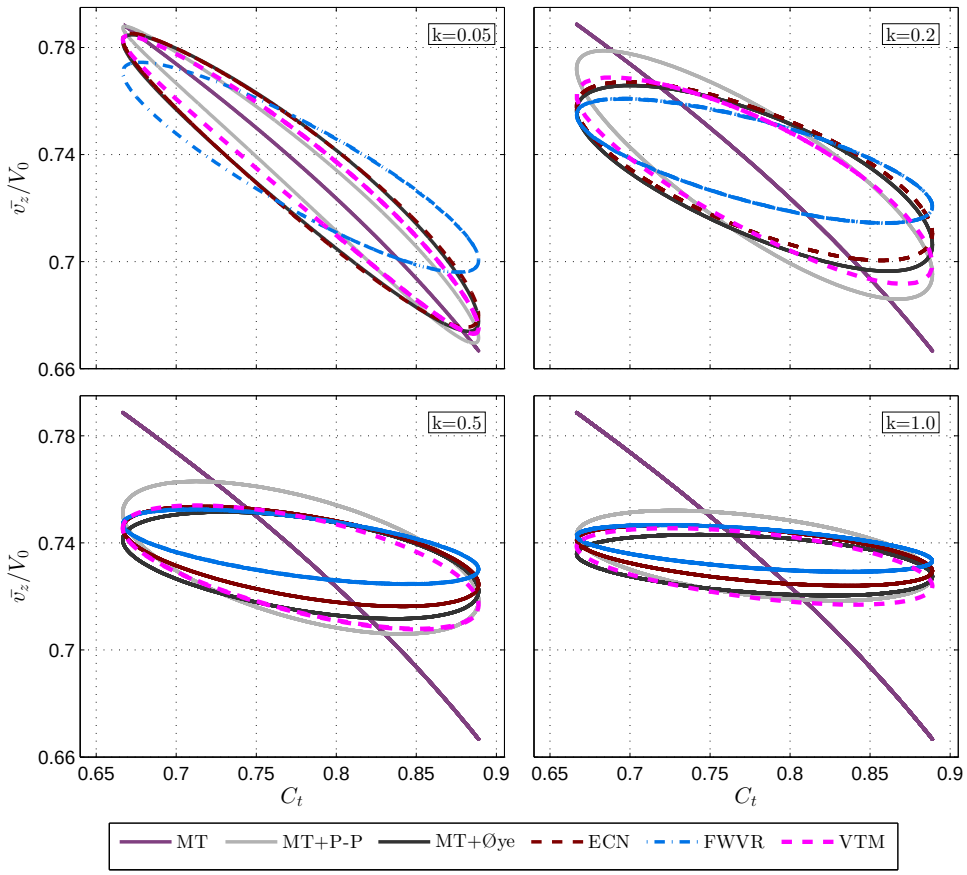

Figure 6.4: Comparison of hysteresis loops of the averaged axial velocity at the actuator disc between the VTM, FWVR model, MT, the Pitt-Peters, Øye and ECN model for unsteady uniform load — an actuator disc undergoing harmonic thrust oscillations with an amplitude of ΔC_t=1/9 for k = 0.05, 0.2, 0.5, 1.0.

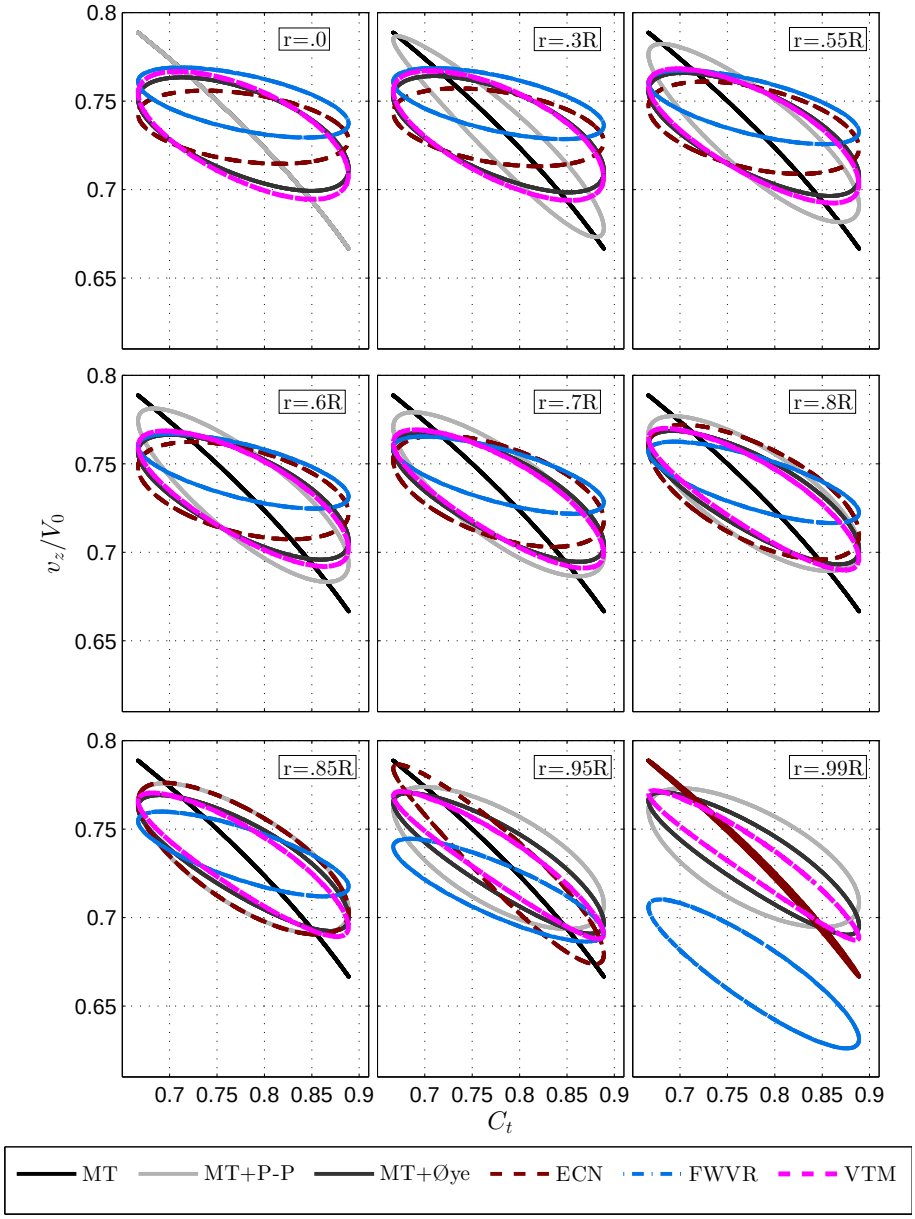

Figure 6.5: Comparison of hysteresis loops of the axial velocity at different radii between the VTM, FWVR model, MT, the Pitt-Peters, Øye and ECN model for unsteady uniform load at $k = 0.2$.

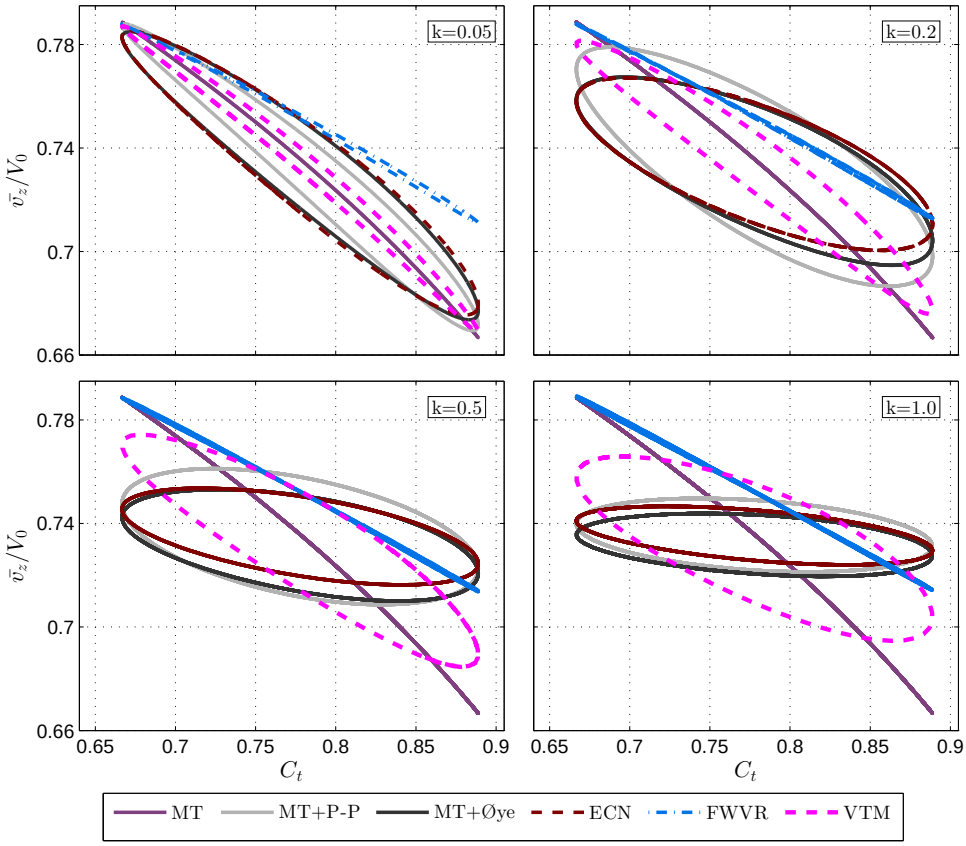

Figure 6.6: Comparison of hysteresis loops of the axial velocity at 0.7R between the VTM, the FWVR model, MT, the Pitt-Peters, the Øye and ECN model for unsteady radially-varying load — an actuator disc undergoing harmonic thrust oscillations in the annulus region 0.6R - 0.8R with an amplitude of ΔC_t=1/9 for k= 0.05, 0.2, 0.5, 1.0.

6.3.3. UNSTEADY RADIALLY-VARYING LOAD

Figure 6.6 compares hysteresis loops of the dynamic axial velocity v_z at 0.7R (the center of the region with a local load variation) between the VTM, the FWVR model, MT and the three dynamic-inflow engineering models. The same reduced frequencies k = 0.05, 0.2, 0.5 and 1.0 are presented. The dynamic velocity v_z at 0.7R is plotted against the local thrust coefficient. The orientation of the VTM loop matches with the FWVR model better than other engineering models for all reduced frequencies. At lower reduced frequency k=0.05, 0.2, the phase lag of the VTM is much smaller than the two engineering models, but a bit larger than the FWVR model. However, the phase lag of the VTM keeps increasing as the reduced frequency increases, while the phase lag of the FWVR model is small for all reduced frequencies.

Figure 6.7 compares the dynamic loop characteristics of v_z between the VTM, the FWVR model, MT and the three dynamic-inflow engineering models at different radial

positions r/R=0, 0.3, 0.55, 0.6, 0.7, 0.8, 0.85, 0.95 and 0.99, at reduced frequency 0.2. As seen from Figure 6.7, the VTM predicts smaller phase delay than the three engineering models, but larger phase delay than the FWVR model inside the load varying region 0.6R-0.8R. The VTM can also reflect the effect of local load variation on the induction of the actuator disc outside the local load varying region, although the loop is different from the FWVR model. This means that, different from the steady radially-varying load case, the local load effect of the VTM does not confine locally for the unsteady radially-varying load. As explained in chapter 3, the negligible effect from the FWVR model in this region in the unsteady radially-varying load cases is because the shed vortices at the two ends of the load locally varied region have opposite signs, so the velocity induced by them cancels out with each other. The linearized vorticity-based VTM model can partly predict this effect, however, the engineering models can not. This is because all the engineering model are derived based on uniform load and are subsequently applied to annuli. However, due to the omission of the wake expansion, the VTM is still different from the FWVR model. The difference is larger for the higher frequencies in Figure 6.6 and is larger near the tip in Figure 6.7. Comparison in this load case shows the VTM has better predictions in axial on the disc for unsteady and radially-varying load than the three dynamic-inflow engineering models. However, there is still some difference between the VTM and the FWVR model.

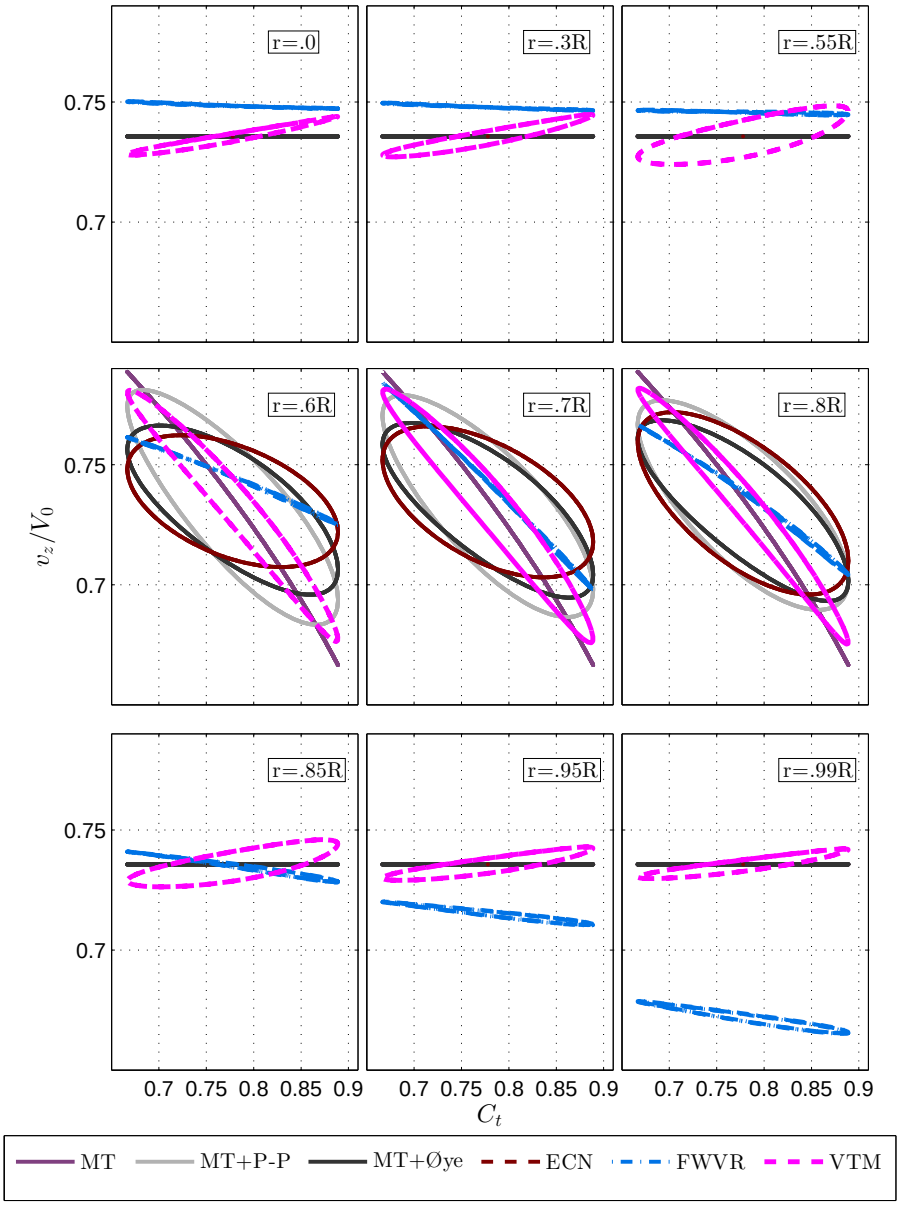

Figure 6.7: Comparison of hysteresis loops of the axial velocity at different radii between the VTM, FWVR model, MT, the Pitt-Peters, Øye and ECN model for unsteady radially-varying load at k = 0.2.

6.4. CONCLUSIONS

The steady vortex tube model is extended to unsteady and radially-varying load. The results from the linear vortex tube model are compared with the high fidelity free wake vortex ring model developed in chapter 3, and the three dynamic-inflow engineering models - Pitt-Peters, Øye and ECN model for the three representative load cases: (I) steady uniform and radially-varying , (II) unsteady uniform, and (III) unsteady radially-varying. The results show that the simple vortex tube model has a reasonable prediction of induction at the disc for the steady load case, when compared to the FWVR model. For unsteady uniform load cases, the induction prediction from VTM is comparable to the engineering model of Øye. In the unsteady radially-varying load case, the VTM has a improved prediction in induction than the three engineering models, it can partly predict the effect of locally-varying loads.

The results from the VTM differ from the FWVR model due to the simplifications of the VTM, especially the linearization. As seen, the improved VTM is an intermediate model between an engineering model and a high fidelity free wake model, in terms of accuracy and computational time. It is faster than the FWVR model. However, the calculation of equations 6.1 and 6.2 of each vortex tube is still too time consuming to apply within an aero-elastic simulations for continuously time varying load. A new engineering model based on both the improved VTM model and the high fidelity FWVR model is proposed in chapter 7.

7

A NEW DYNAMIC-INFLOW ENGINEERING MODEL BASED ON LINEAR AND NONLINEAR ACTUATOR-DISC VORTEX-MODELS

In theory, there is no difference between theory and practice.
But, in practice, there is.

Jan L.A. van de Snepscheut (1953-1994)

The engineering models of Pitt-Peters, Øye and ECN are shown to underestimate the dynamic-inflow effect in chapter 3. The linear and nonlinear actuator-disc based vortex-models show improved prediction of the dynamic-inflow effect in chapters 3, 5 and 6. However, the time-marching vortex-model is too computationally expensive to be integrated within an aero-servo-elastic model directly. A new engineering model is developed using the differential form of the Duhamel's integrals of indicial responses of the actuator-disc type vortex-models. The time constants of the indicial functions are obtained by indicial responses of a linear and a nonlinear actuator-disc model, respectively. The new dynamic-inflow engineering models are verified against the results from the FWVR model and compared against dynamic-inflow engineering models of Pitt-Peters, Øye and ECN, for several load cases.

7.1. INTRODUCTION

Although the high fidelity vortex methods can account for the dynamic-inflow effect of a wind turbine, the Blade Element Momentum (BEM) method with dynamic-inflow engineering models has been proven to give the current highest predictive confidence levels for design purposes (Leishman, 2002).

The widely used dynamic-inflow engineering models of Pitt-Peters, Øye, and ECN are introduced in chapter 2. The Pitt-Peters model was developed based on the concept of 'apparent mass'. It is assumed that the uniform induced velocity of the initial flow field is analogous to the flow field produced by an impermeable disc moved normal to its plane. It was proposed for helicopters, whose operational conditions are different from wind turbines. The engineering models of Øye and ECN are based on vortex-models. The Øye model was verified against limited load cases of certain wind turbines. The ECN model was developed based on a simplified linear actuator-disc model using prescribed convection velocity. A validation, in chapter 3, against numerical results of a free wake model further shows that these three dynamic-inflow engineering models underestimate the dynamic-inflow effect. Pirrung and Madsen (2018) concluded that the time constants for dynamic inflow models can not be directly obtained from forces from measurements or CFD simulations of a wind turbine, on the other hand, the vortex type-model can have better performance.

In this chapter, a new approach is proposed to account for the dynamic-inflow effect, which is similar to the procedure of the development of Wagner's model (Wagner, 1925) for 2-D unsteady airfoil aerodynamic.

The flow decay functions are obtained from a linear and a nonlinear actuator-disc model, separately. In the linear actuator-disc model, the indicial flow field responses of a linear actuator-disc model are obtained by the VTM model developed in chapter 6. In the nonlinear actuator-disc model, the indicial flow field responses of a nonlinear actuator-disc model are obtained by the FWVR model developed in chapter 3.

If the indicial functions are known, the output flow field of any known thrust input can be calculated directly using the Duhamel's integral of the indicial functions. In order to be implemented in a time-marching numerical code (e.g. BEM) to compute the dynamic-inflow effect, the indicial functions are given in an exponential approximation. The coefficients of the exponential equations are found to be a function of radius and a function of baseline thrust. Finally, the model is verified for the induction on the ac-

tuator disc. It is validated against the numerical results from the FWVR model and the engineering models of Pitt-Peters, Øye and ECN for several load cases.

The method to develop the engineering models is introduced in section 7.2, where the indicial functions of a linear and a nonlinear actuator-disc model are obtained; their exponential approximations are given; the Duhamel's integral of the indicial functions are presented. The validation load cases and the quantifying method are given in section 7.3. The verification of the new models for the induction at the actuator disc against the numerical results from the FWVR model and the three engineering models are presented in section 7.4. Conclusions are drawn in section 7.5. The details related to how the relationship between the coefficients of the indicial functions and the radial positions and the baseline thrust is obtained, and the quality of the polynomial representation of the coefficients from the linear and the nonlinear actuator-disc models are demonstrated in Appendix A and B, respectively. Appendix C presents the fully developed wake from the FWVR model for all the verifying cases.

7.2. METHOD

The induced velocity field of an actuator disc with an arbitrarily oscillating load can be calculated from the vortex system in Figure 7.1. The strength the vorticity newly shed into the wake vary with the the varying load. The wake, as a tube surface with varying strength and expansion, extends from the edge of the disc to infinity. The newly shed wake is generated at the edge of the disc and convected downstream by the local velocity.

By applying the equation of velocity induced by a finite vortex cylinder derived by Branlard and Gaunaa (2014), the axial velocity at a position (z_p, r_p) induced by the wake vorticity system can be calculated by the following integral

$$\Phi(z_p, r_p, t) = \int_0^\infty \frac{-\gamma_t(z,t)}{4\pi\sqrt{r_p R(z,t)}} \left[(z-z_p) k \left(K(k^2) + \frac{R(z,t)-r_p}{R(z,t)+r_p} \Pi(k_0^2, k^2) \right) \right]_z^{z+dz} \tag{7.1}$$

where

$$k^2 = \frac{4 r_p R(z,t)}{(z-z_p)^2 + (R(z,t)+r_p)^2} \tag{7.2}$$

$$k_0^2 = \frac{4 r_p R(z,t)}{(R(z,t)+r_p)^2} \tag{7.3}$$

Unsteady aerodynamic forces of an airfoil in potential flow conditions are usually described by the indicial formulations in the time domain, as described by Beddoes (1982) and Leishman (2006). The method is applied to an actuator disc in the potential flow conditions in this chapter. The indicial functions are obtained instead of directly finding an analytical solution for Equation 7.1. The indicial functions of a series of baseline thrust ranging from 0 to 1, with an amplitude of thrust change $\delta C_t = \pm 0.1$, are calculated by a linear actuator-disc model (the VTM developed in chapter 6) and a nonlinear actuator-disc model (the FWVR model developed in chapter 3). The linear actuator-disc model is used to develop the engineering model, because it can act as a benchmark for models developed based on a linear actuator-disc model, e.g. the ECN model.

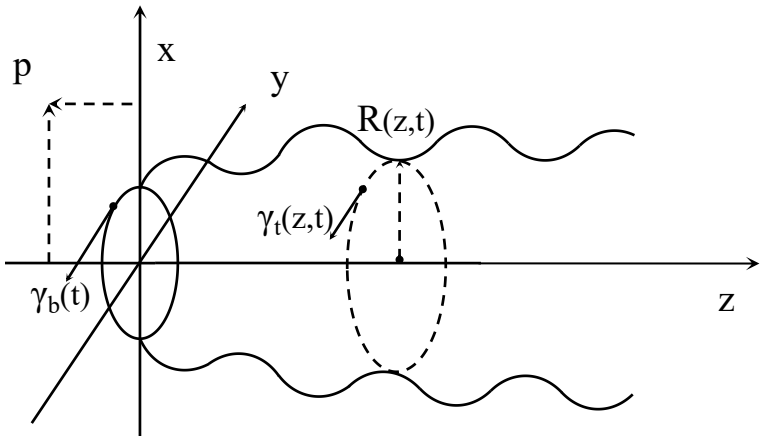

Figure 7.1: Mathematical model of an actuator-disc model with harmonically oscillating load.

The indicial functions of an airfoil are expressed in terms of exponential functions of time for the practical considerations for the implementing in a time marching simulation e.g. the exponential representation of the Wagner's function (Jones, 1939) and the indicial lift functions of an airfoil Beddoes (1982). The indicial response functions of the actuator disc are also chosen to be represented by exponential approximations in this chapter.

Because the induction on the actuator disc is of most interest, only the approximation of the induced velocity at the actuator disc is investigated in this chapter. The induction at other locations can be dealt in the same way. Pirrung and Madsen (2018) suggested that two time constants are necessary for accurate modelling of dynamic inflow effects. The induction at the actuator disc is denoted as $\Phi_d(r_j,t)$, which are approximated by a two term exponential series

$$\Phi_d(r_j,t) = 1-\beta_j e^{\omega_{1j}t} - (1-\beta_j)e^{\omega_{2j}t}. \tag{7.4}$$

where the subscript j represents the radial position.

The coefficients β, ω_1 and ω_2 of Equation 7.4 are obtained by directly fitting the original indicial responses calculated by the actuator-disc models. The fitting error — the difference between the original calculated data and the fitting values is defined by

$$error = 100 * \frac{\Phi_d(r_j,t)_{cal} - \Phi_d(r_j,t)_{fit}}{\Phi_d(r_j,t\rightarrow\infty)_{cal}}. \tag{7.5}$$

where $\Phi_d(r_j,t)_{cal}$ and $\Phi_d(r_j,t)_{fit}$ are the directly calculated and fitted values at the radial position r_j at time t, $\Phi_d(r_j,t\rightarrow\infty)_{cal}$ is the calculated value at steady state.

As an example, figure 7.2 shows the directly calculated values from the VTM model and the exponential approximation of the indicial response of velocity at radial position r/R=0, r/R=0.5, r/R=0.7, r/R=1.0 for baseline C_t=0.4, and the fitting errors. The maximum fitting error for all the radial positions and all considered baseline C_t from the VTM is 3.2%.

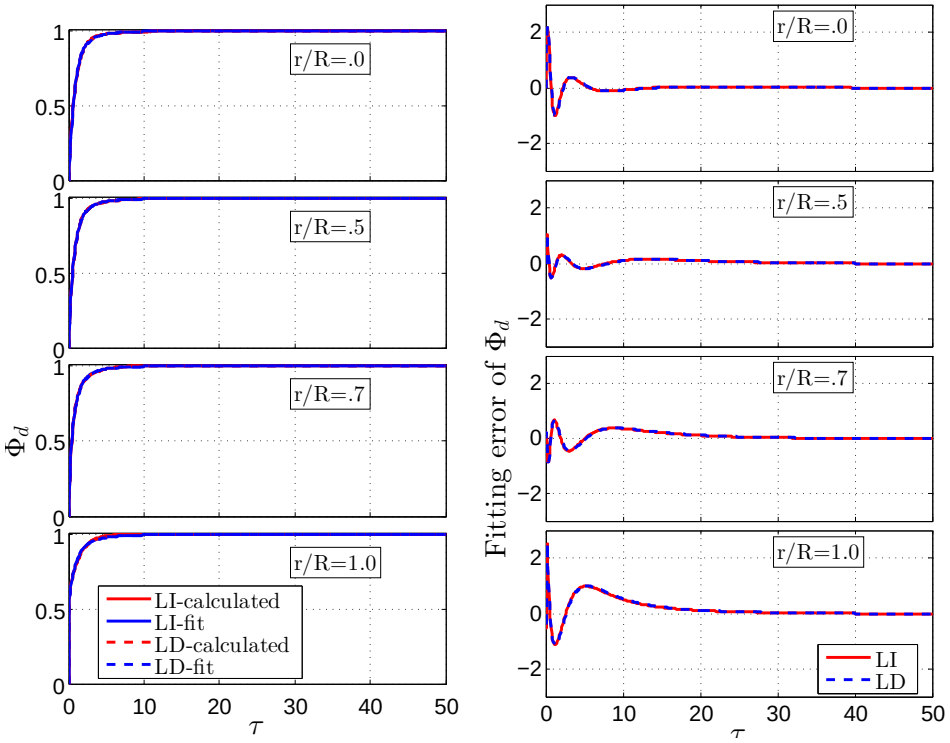

(a) The calculated and fitting curves

(b) The error of fitting curves

Figure 7.2: Φ_d calculated by the VTM and the exponential approximation for baseline C_t=0.4, and the fitting error. LI - load increase case, LD - load decrease case.

As an example, figure 7.3 shows the directly calculated values from the FWVR model and the exponential approximation using Equation 7.4 of the indicial responses of velocity at different radial positions r/R=0, r/R=0.5, r/R=0.7, r/R=1.0 for baseline C_t=0.4, and the fitting error. The maximum fitting error for region $r/R \leq 0.95$ for all considered baseline thrust from the FWVR model is 3.8%. The fitting error increases as the radial position moves outboard. The tip region is highly influenced by the cut-off radius used in the FWVR model, which is not fully captured by the fitting curves, as shown in Figure B.1.

The coefficients β, ω_1 and ω_2 are found to depend on the radial position and the baseline thrust. The radial distributed coefficients are represented by polynomial functions, and the parameters of the polynomials are functions of baseline thrust. The radial distribution of the coefficients and the parameters of the polynomials from the linear and the nonlinear actuator-disc model are presented in subsection 7.2.1 and 7.2.2, separately. The details related to how these parameters are obtained are given in Appendix A and B, separately, for the linear and nonlinear actuator-disc model.

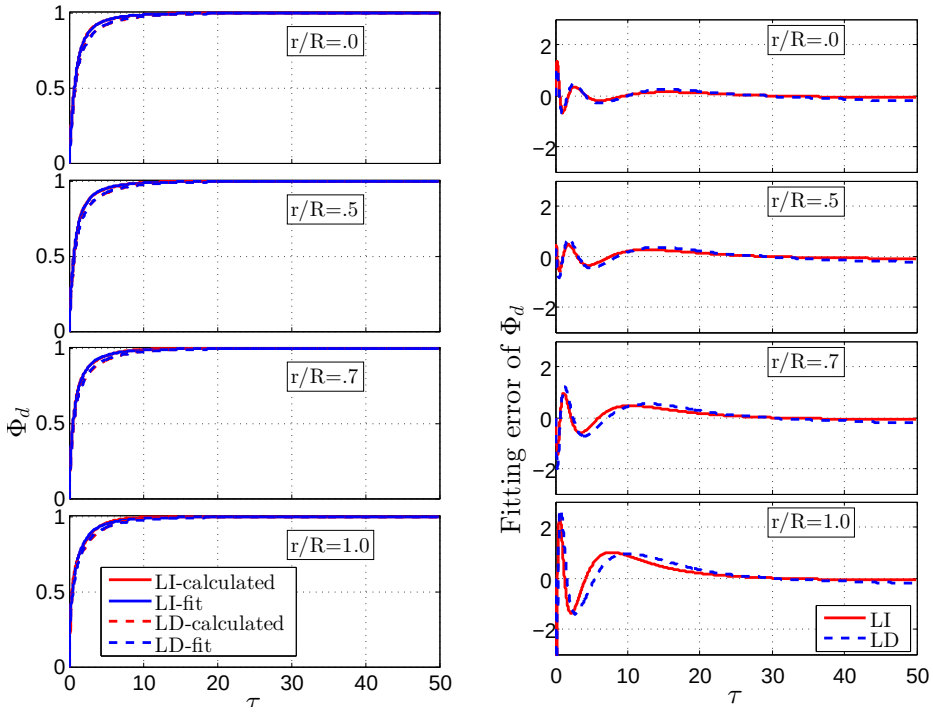

(a) The raw and fitting curves

(b) The error of fitting curves

Figure 7.3: Φ_d calculated by the FWVR and the exponential approximation for baseline C_t=0.4, and the fitting error. LI - load increase case, LD - load decrease case.

7.2.1. COEFFICIENTS OBTAINED BY THE LINEAR ACTUATOR-DISC MODEL

The radial distribution of the coefficients of β, ω_1 and ω_2 obtained by the VTM model are represented by

$$\begin{aligned}\beta(r) &= 1/(a_3 r^3 + a_2 r^2 + a_1 r^1 + a_0 r^0)\\ \omega_1(r) &= 1/(a_3 r^3 + a_2 r^2 + a_1 r^1 + a_0 r^0)\\ \omega_2(r) &= 1/(a_3 r^3 + a_2 r^2 + a_1 r^1 + a_0 r^0)\end{aligned} \quad . \tag{7.6}$$

The parameters a_3, a_2, a_1, a_0 for β, ω_1 and ω_2 are functions of the baseline thrusts, which are given in Table 7.1. More details related to the radial distributed β, ω_1, ω_2, and the relationship between a_3, a_2, a_1, a_0 and the baseline thrust from the VTM are given in Appendix A. The quality of the polynomial representation is also shown in figures A.3 - A.5 in Appendix A.

7.2.2. COEFFICIENTS OBTAINED BY THE NONLINEAR ACTUATOR-DISC MODEL

The radial distribution of the coefficients of β, ω_1 and ω_2 obtained by the FWVR model are represented by

Table 7.1: The parameters for the radial distribution of β, ω_1 and ω_2 obtained from the linear actuator-disc model.

	β	ω_1	ω_2
a_3	38.9	$-3.1C_t - 6.2$	$0.1C_t + 0.1$
a_2	-50.3	$5.0C_t + 9.4$	$0.4C_t + 0.7$
a_1	-2.9	$-0.3C_t - 0.6$	$-0.1C_t - 0.1$
a_0	17.2	$-2.4C_t - 3.8$	$-0.5C_t - 0.7$

$$\begin{aligned} \beta(r) &= a_3 r^3 + a_2 r^2 + a_1 r^1 + a_0 r^0 \\ \omega_1(r) &= a_3 r^3 + a_2 r^2 + a_1 r^1 + a_0 r^0 \\ \omega_2(r) &= 1/(a_3 r^3 + a_2 r^2 + a_1 r^1 + a_0 r^0) \end{aligned} \quad . \tag{7.7}$$

The parameters a_3, a_2, a_1, a_0 for β, ω_1 and ω_2 are functions of the baseline thrusts, which are given in Table 7.2. More details related to the radial distributed β, ω_1, ω_2, and the relationship between a_3, a_2, a_1, a_0 and baseline thrust from the FWVR model are given in Appendix B. The quality of the polynomial representation is also shown in figures B.3 - B.5 in Appendix B.

Table 7.2: The parameters for the radial distribution of β, ω_1 and ω_2 obtained from the nonlinear actuator-disc model.

	β	ω_1	ω_2
a_3	$0.98C_t - 1.09$	$3.45C_t^2 - 5.19C_t + 2.01$	$0.05C_t - 0.60$
a_2	$-2.01C_t + 1.99$	$-4.60C_t^2 + 7.01C_t - 2.81$	$-0.38C_t + 1.6$
a_1	$0.57C_t - 0.34$	$0.06C_t - 0.09$	$0.32C_t - 0.23$
a_0	$0.62C_t - 0.03$	$-0.07C_t - 0.12$	$-0.19C_t - 0.79$

7.2.3. DUHAMEL'S INTEGRAL AND ITS DIFFERENTIAL FORM

BACKGROUND OF DUHAMEL'S INTEGRAL

Duhamel's integral is a way to calculate the response of a linear system to an arbitrary time-varying external perturbation.

If a linear system is initially rest at an equilibrium position, a unit impulse force is applied at $t = \tau$, $\tau \neq 0$. The response of the linear system to the unit impulse can be written as

$$h(t-\tau) = \frac{1}{m\omega_d} e^{-\zeta\omega_n(t-\tau)} sin(\omega_d(t-\tau)), \quad t > \tau \tag{7.8}$$

where m, ζ, ω_n and ω_d represent the inertia, the damping ratio, the undamped natural angular frequency and the damped natural frequency of the linear system. The

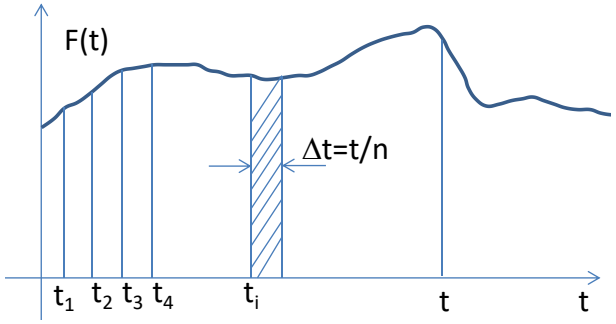

Figure 7.4: Arbitrary excitation force, F(t), split into n impulses.

relationship between the damped and undamped natural frequency is given by $\omega_d = \omega_n\sqrt{1-\zeta^2}$. Further details related to the derivation of the impulse response of a linear system can be found in Inman (2009).

The response of the linear system to an arbitrary applied force, $F(t)$, can be obtained by dividing the exciting force into infinitesimal impulses and adding the individual response of each of these. Figure 7.4 illustrates the arbitrary force, $F(t)$, which has been divided into n time intervals of length Δt. Therefore, the duration of each time increment is $\Delta t = t_n/n$. The response to the impulse at time t_i is given by

$$\Delta x(t_i) = F(t_i)h(t-t_i)\Delta t \tag{7.9}$$

From the linearity of the system, the total response can be calculated by superposition of the series of impulse-responses:

$$x(t_j) = \sum_{i=1}^{j} F(t_i)h(t-t_i)\Delta t \tag{7.10}$$

Forming the sequence of partial sums and finding the limit as $\Delta t \to 0$ ($n \to \infty$) gives

$$x(t) = \int_0^t F(\tau)h(t-\tau)d\tau \tag{7.11}$$

Equation 7.11 is known as Duhamel's integral. Further details can be found in Inman (2009).

APPLICATION OF THE DUHAMEL'S INTEGRAL TO THE ACTUATOR DISC

The application of the Duhamel's integral in this chapter is under the assumption that the induction response of the actuator disc to an arbitrary force can be built up as a superposition of response to a series of step changes in induction. The system response can be determined from the indicial functions of an actuator disc using the Duhamel's integral.

However, figure 7.5 shows the averaged induced velocity at the actuator disc against the thrust obtained from the momentum theory. As seen from Figure 7.5, the induction

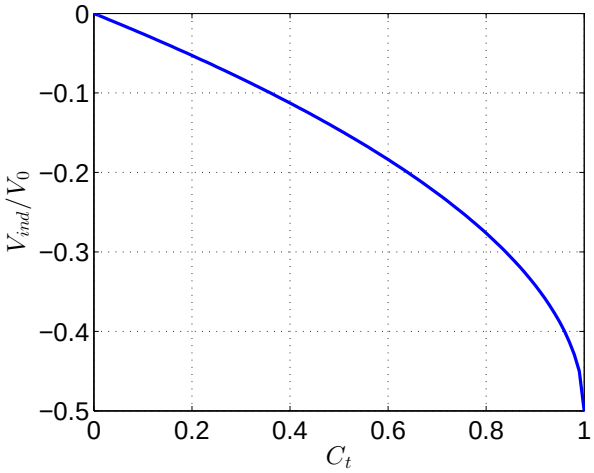

Figure 7.5: Averaged induced velocity at the actuator disc against C_t from the momentum theory

field of an actuator disc is not linear to the thrust, and the nonlinearity increases as the thrust increases.

If the strength of the vortex tube is a general function $\gamma(t)$, $t \geq 0$, since the indicial function $\Phi_d(r,t)$ is known, the induced velocity output at the disc plane $u_d(r,t)$ of the system can be written in terms of Duhamel's integral as :

$$u_d(r,t) = \gamma(0)\Phi_d(r,t) + \int_0^t \frac{d\gamma}{d\sigma}\Phi_d(r,t-\sigma)d\sigma. \tag{7.12}$$

The relationship between the strength of vortex tube $\gamma(t)$ and the thrust C_t is given in Equation 6.10. For any known thrust variation, the entire induction velocity field can be calculated directly by the Duhamel's integral of the indicial functions analytically or numerically henceforth. However, in the practical operations, the thrust variation is usually unknown in advance. It varies based on the wind conditions and control strategy, which is determined based on the performance of the previous step. The Duhamel's integral should be transformed into a differential form, which can be implemented in a time dependent code as BEM.

Substitute Equation 7.4 into Equation 7.12, and let

$$c_{k,j}(t) = \int_0^t \gamma'(\sigma)A_{k,j}e^{\omega_{k,j}(t-\sigma)}d\sigma \tag{7.13}$$

where $k = 1,2$, $A_{1j} = \beta_j$, $A_{2j} = 1-\beta_j$.

Differentiating equation 7.13 with time t gives

$$\dot{c}_{k,j}(t) - \omega_{k,j}c_{k,j}(t) = A_{k,j}\dot{\gamma}(t), k = 1,2. \tag{7.14}$$

Therefore, the final velocity can be represented by

$$u_d(r,t) = \gamma(t) - c_{1,j}(t) - c_{2,j}(t). \tag{7.15}$$

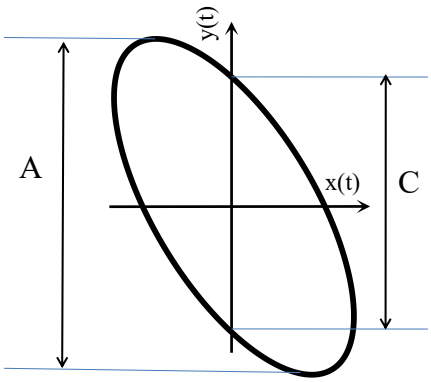

Figure 7.6: Lissajous figure, A - the vertical height, C - the zero crossing height.

7.3. VALIDATION CASES AND QUANTIFYING METHOD

The investigated harmonically time varying load is shown schematically in load case II.2 of Table 3.1. Three different baseline loads of C_t=1/9, C_t=4/9, C_t=7/9 with the harmonically time-varying load are investigated. The amplitude of harmonic load is ΔC_t=1/9. Four different reduced frequencies of k= 0.05, 0.2, 0.5, 1.0 are tested for each case. The studied load cases in this chapter are summarized in Table 7.3.

Table 7.3: The studied load cases.

Baseline C_t	$\frac{2}{9}$	$\frac{4}{9}$	$\frac{7}{9}$
ΔC_t	$\frac{1}{9}$	$\frac{1}{9}$	$\frac{1}{9}$
k	0.05, 0.2, 0.5, 1.0	0.05, 0.2, 0.5, 1.0	0.05, 0.2, 0.5, 1.0

The hysteresis loop in Figure 3.3 is copied here for convenience. As shown in Figure 7.6, the vertical height A represents the velocity amplitude, C is the zero crossing height. The phase difference between the velocity and thrust is

$$\Delta\theta = -[180^\circ - sin^{-1}(C/A)]. \tag{7.16}$$

The phase difference between the velocity and the induction is 180°, the phase difference between the thrust and the induction for the momentum theory is 0°. Therefore, the phase delay between the induction from each model and the induction from momentum theory can be calculated by

$$\Delta\theta = -[180^\circ - sin^{-1}(C/A)] + 180^\circ = sin^{-1}(C/A). \tag{7.17}$$

7.4. RESULTS AND DISCUSSIONS

The new engineering models using coefficients obtained by the indicial responses of both the linear and nonlinear actuator-disc models are validated against the numerical results from the FWVR model for the load cases introduced in section 7.3. They are also compared against the existing engineering models of Pitt-Peters, Øye and ECN. The velocity at the actuator disc center and the radial distribution of velocity are compared between all the models, separately.

In all the following figures and discussions, the names of MT, MT+P-P, MT+Øye, ECN, FWVR, TUD-VT and TUD-VR are used consistently to refer to the different models. Their definitions are given in nomenclature.

7.4.1. VELOCITY AT THE CENTER OF THE ACTUATOR DISC

Figures 7.7 — 7.9 compares the hysteresis loops of the axial velocity at the actuator disc center between the seven models for the baseline C_t=1/9, C_t=4/9 and C_t=7/9, separately. As seen, at the center, the Pitt-Peters model goes to MT because the 'apparent mass' goes to zero for zero area.

From figures 7.7 — 7.9, a larger frequency leads to a larger phase delay and a larger amplitude difference from the steady values. This is because that a higher unsteadiness is for a larger frequency.

For the lowest baseline thrust C_t=1/9 in Figure 7.7, where the dynamic effect is less significant, the induction at the actuator disc center predicted by all the models is in good match with that from the FWVR model. The difference between the ECN model and the FWVR model is larger for medium frequencies of k=0.2, 0.5. The difference between the Øye model and the FWVR model is larger for higher frequencies of k=0.5, 1. The new models of TUD-VT and TUD-VR are in great match with the FWVR model for velocity at the actuator disc center for all the frequencies for this low baseline thrust.

For baseline thrust C_t=4/9 in Figure 7.8, the difference between the ECN, Øye model and FWVR model increases. The TUD-VR is in great match with the FWVR model for velocity at the center for all the frequencies. The difference between the TUD-VT and the FWVR model is larger than that in case of baseline thrust C_t=1/9.

For the highest thrust C_t=7/9 in Figure 7.9, the difference between all the models is even larger. The difference of the TUD-VR model from the FWVR model also increases for this high thrust case.

In order to quantify the results, Figure 7.10 compares the calculated amplitude and phase delay of the velocity at the actuator disc center between the different models. The amplitude is normalized to the amplitude of induction from momentum theory. As seen in Figure 7.10, the amplitude from MT is constant and the phase delay is zero for all frequencies, due to the steady physics. It is consistent with figures 7.7 - 7.9, the TUD-VR model is closest to the FWVR model for all the cases with all frequencies in terms of both phase delay and amplitude of the velocity at the actuator disc center. The discrepancy between the TUD-VR and the FWVR model is slightly larger for the amplitude for baseline C_t=7/9. The phase delay from the TUD-VT also matches well with that from the FWVR model, however, the amplitude difference from that of the FWVR model increases for higher thrust. The larger discrepancy of the model of TUD-VT and TUD-VR from the FWVR model for the higher load case C_t=7/9 is because that the nonlinearity of the ac-

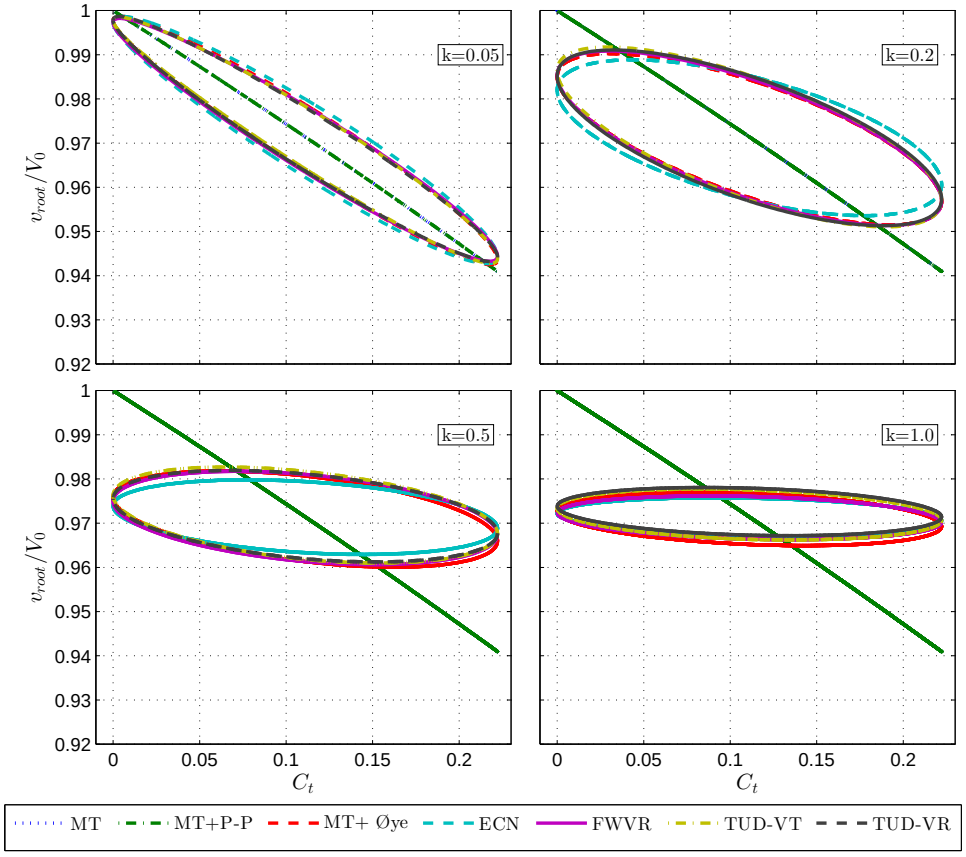

Figure 7.7: Comparison of hysteresis loops of the axial velocity at r/R=0 between the seven models for an actuator disc undergoing harmonic thrust oscillations for baseline C_t=1/9 with an amplitude of ΔC_t=1/9, for k = 0.05, 0.2, 0.5 and 1.

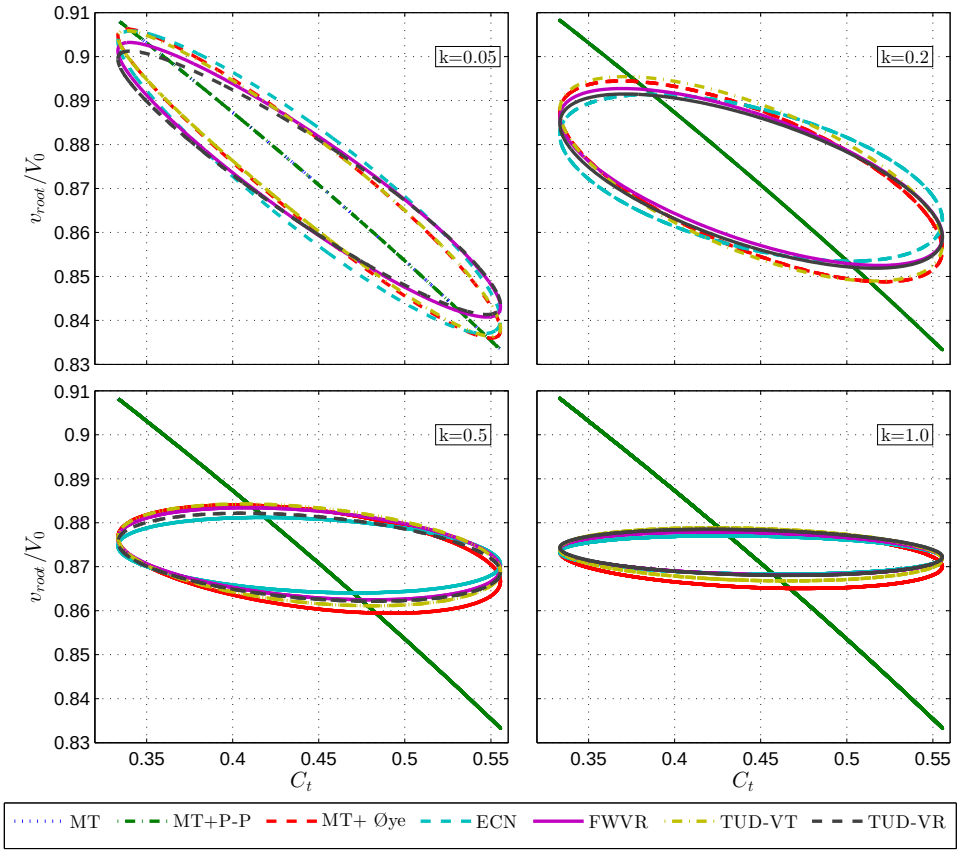

Figure 7.8: Comparison of hysteresis loops of the axial velocity at r/R=0 between the seven models for an actuator disc undergoing harmonic thrust oscillations for baseline C_t=4/9 with an amplitude of ΔC_t=1/9, for k = 0.05, 0.2, 0.5 and 1.

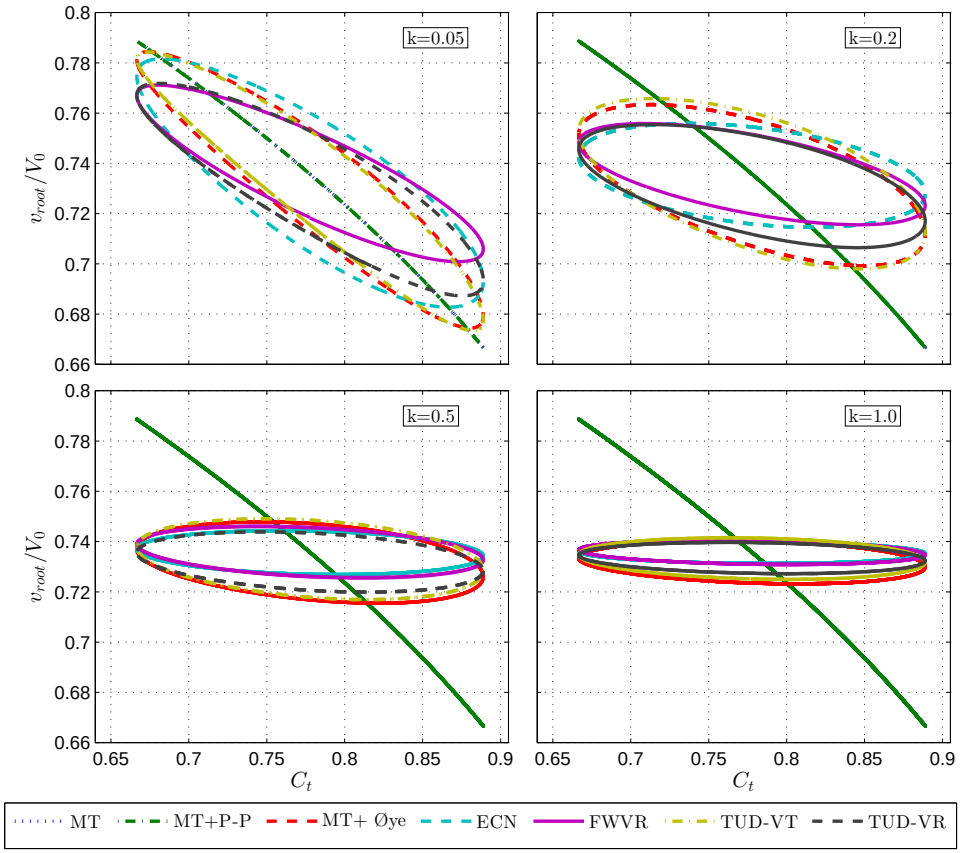

Figure 7.9: Comparison of hysteresis loops of the axial velocity at r/R=0 between the seven models for an actuator disc undergoing harmonic thrust oscillations for baseline C_t=7/9 with an amplitude of ΔC_t=1/9, for k = 0.05, 0.2, 0.5 and 1.

tuator disc system is higher for the higher load as shown in Figure 7.5, which challenges the assumption for Duhamel's integral.

Compared to the FWVR model, the phase delay from the ECN model for all the load cases is overestimated for the velocity at the disc center. The Øye model underestimates the phase delay for higher frequencies for all these load cases and underestimates the amplitude for higher thrust. In general, the model of TUD-VR predicts improved results over all the other models for both the amplitude and phase delay of the velocity at the actuator disc center. The model of TUD-VT predicts better results than the ECN and Øye model for phase delay, but the amplitude is not improved, for the velocity at the actuator disc center.

7.4.2. RADIAL VELOCITY DISTRIBUTION

Only the velocity at the actuator disc center is discussed in subsection 7.4.1, the amplitude and phase delay of the radial distributed velocity on the entire disc from all the models are investigated in this section. Figures 7.11 —7.13 show the radial distribution of the amplitude and phase delay of the velocity at the actuator disc plane between the seven models for frequencies k = 0.05, 0.2, 0.5 and 1, for baseline C_t=1/9, 4/9 and 7/9, separately.

The first observation from figures 7.11 —7.13 is that the distribution of the amplitude and phase delay of the velocity from the Pitt-Peters model is in a reverse trend compared to all the other models. However, this difference can not be detected by evaluating the overall performance in chapter 3, even though it shows that the Pitt-Pters model underestimates the dynamic-inflow effect more than the models of Øye and ECN. This implies the dynamic-inflow model of Pitt-Peters, which is based on the apparent mass theory, can not predict the radial distribution of dynamic-inflow effect correctly. This crucial discrepancy was not explored before because most of the previous research only focused on the overall loads, e.g. the moment at the blade root. The distribution of the dynamic-inflow effect was investigated in limited research(Hand et al., 2001; Schepers, 2007; Pirrung and Madsen, 2018).

The phase delay and amplitude from the ECN model approaches to the steady value at the tip, resulting in a shaper transient in the tip region than other models. The Øye model is close to the TUD-VT model for all load cases, however, the latter has better prediction for the radial distribution of the phase delay and amplitude at the tip region. The TUD-VT model is in good agreement with the FWVR model for the phase delay for most cases, except at the low frequency k=0.05 of the high thrust C_t=7/9. The TUD-VT model is in good agreement with the FWVR model for the amplitude of the lower thrust C_t=1/9, the discrepancy is larger for frequencies k=0.05, 0.2 of C_t=4/9 and even larger for high thrust 7/9. This is because the effect of wake expansion is larger for high thrust, which is not considered in the linear actuator-disc model.

The TUD-VR consistently predicts better results for all the load cases than the existing models of Pitt-Peters, Øye and ECN, even though there is still a discrepancy at the outboard part in terms of both phase delay and amplitude. This is partially caused by the fact that the nonlinearity increases as it moves to the tip due to the existence of the shed vortex at the edge of the disc.

As seen in Equation 7.4, the unsteady flow responses are represented using two terms

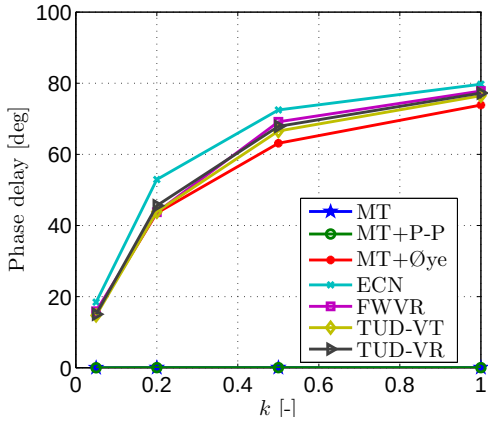

(a) Phase delay for baseline C_t= 1/9, ΔC_t= 1/9

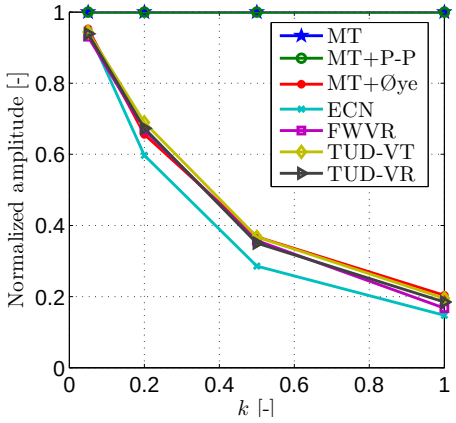

(b) Amplitude of for baseline C_t= 1/9, ΔC_t= 1/9

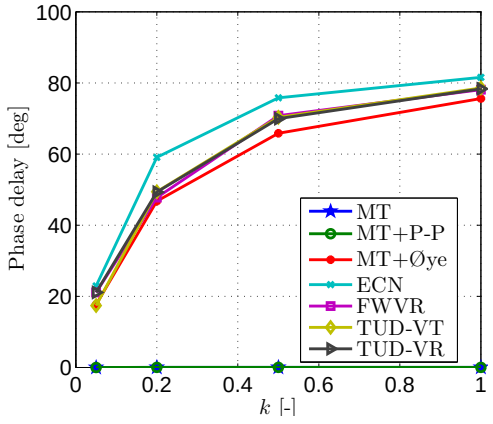

(c) Phase delay for baseline C_t= 4/9, ΔC_t= 1/9

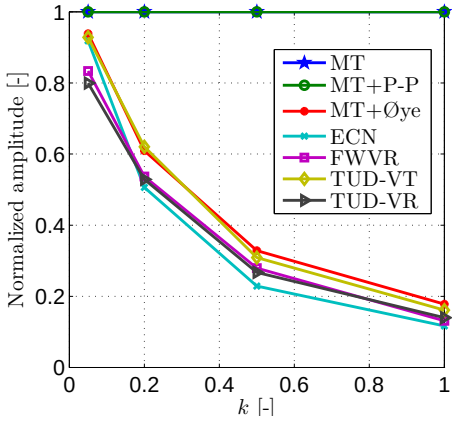

(d) Amplitude for baseline C_t= 4/9, ΔC_t= 1/9

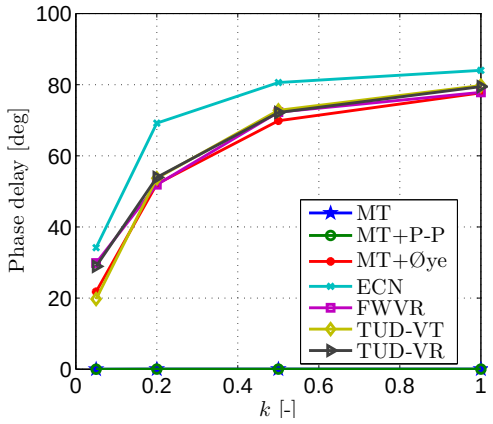

(e) Phase delay for baseline C_t= 7/9, ΔC_t= 1/9

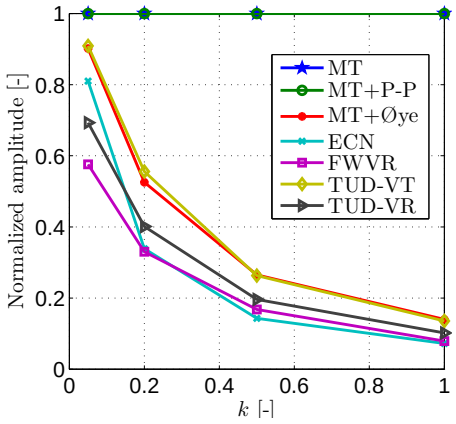

(f) Amplitude for baseline C_t= 7/9, ΔC_t= 1/9

Figure 7.10: The phase delay and amplitude of the velocity at the disc center for baseline C_t=1/9, 4/9, 7/9.

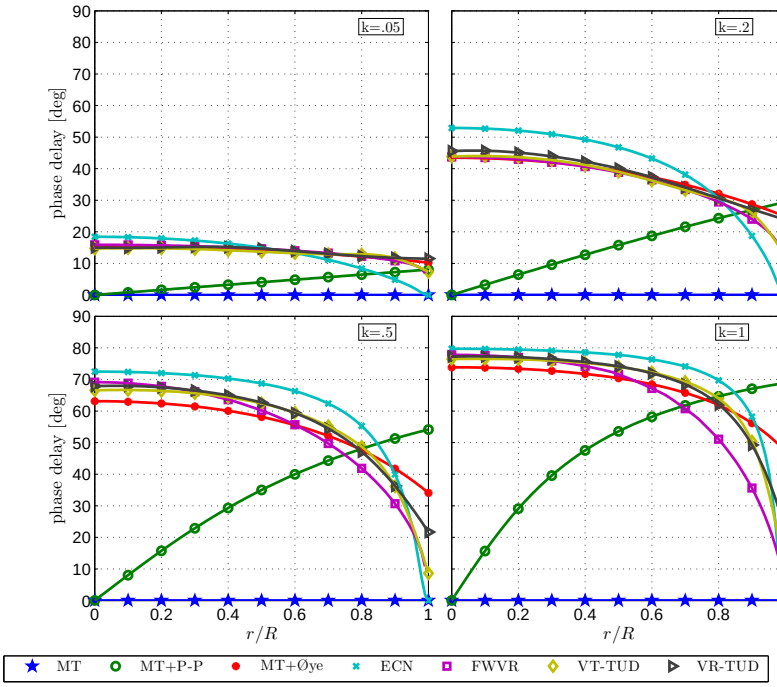

(a) Phase delay

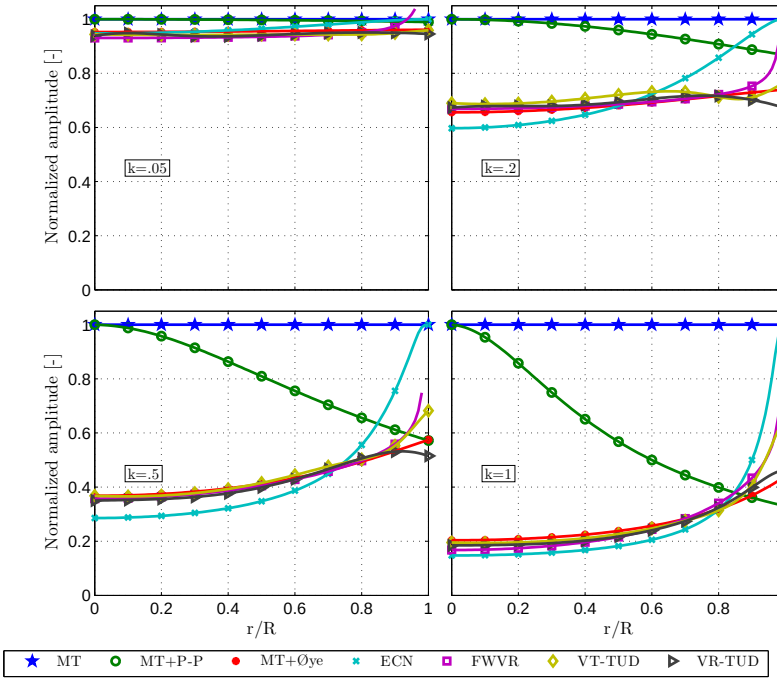

(b) Amplitude

Figure 7.11: Comparison of the radial distribution of the phase delay and amplitude between the seven models for baseline C_t=1/9, for frequencies of k=0.05, 0.2, 0.5, 1.

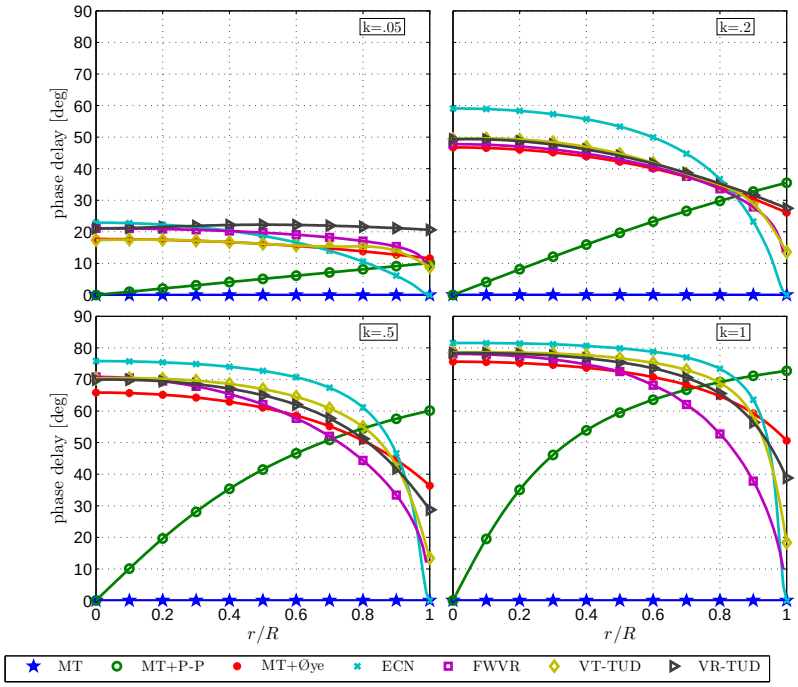

(a) Phase delay

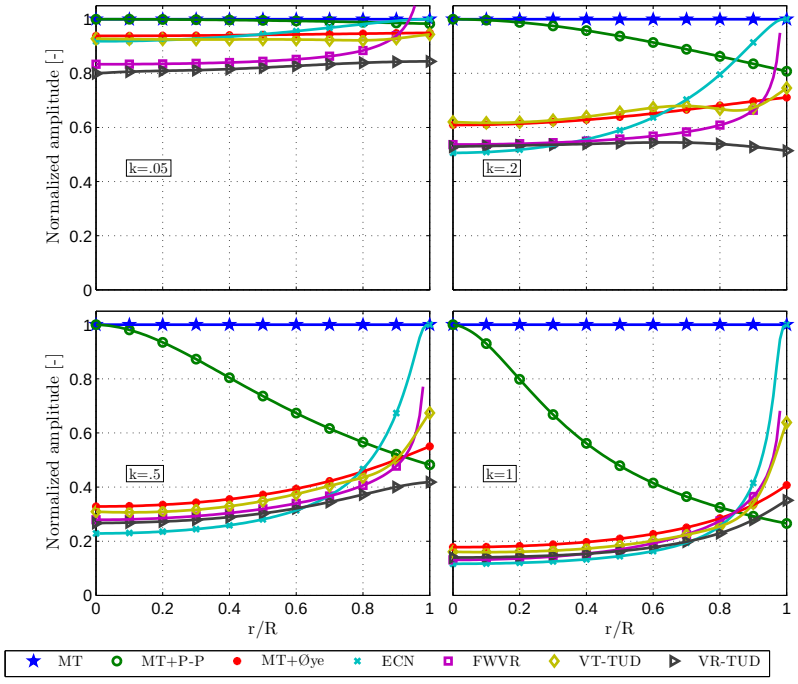

(b) Amplitude

Figure 7.12: Comparison of the radial distribution of the phase delay and amplitude between the seven models for baseline C_t=4/9, for frequencies of k=0.05, 0.2, 0.5, 1.

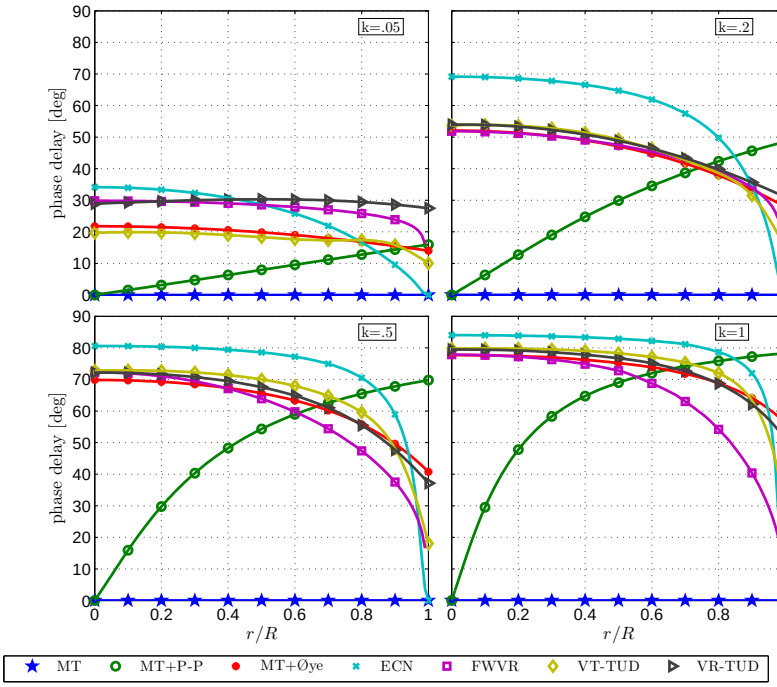

(a) Phase delay

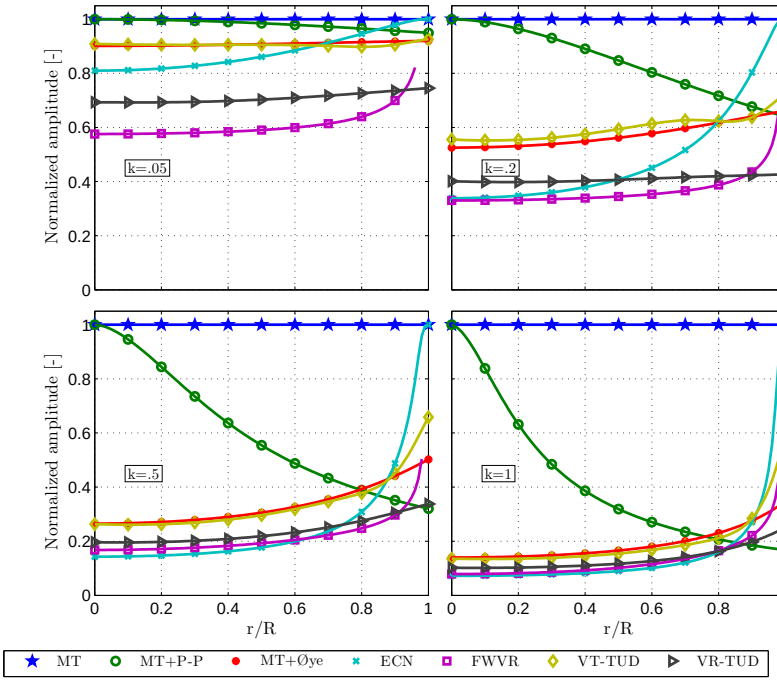

(b) Amplitude

Figure 7.13: Comparison of the radial distribution of the phase delay and amplitude between the seven models for baseline C_t=7/9, for frequencies of k=0.05, 0.2, 0.5, 1.

of exponential series. These two terms embody two speeds of flow decay, a fast decay and a slow decay. Different terms of exponential series are tried in this thesis, it turns out that the two terms of exponential series works better over the others. This might be attributed to the effect of the near wake and far wake. The slow decay represented by ω_1 is determined by the far wake, the fast decay represented by ω_2 is determined by the near wake. This can be confirmed by the fact that the fast decay represented by $\frac{1}{\omega_2}$ in Figure A.1 and B.1 is strongly radial dependent. This is because the newly generated vorticity is shed into the wake from the edge of the disc. The closer the position is to the edge of the disc, the quicker the flow responds to this near wake. The slow decay, as represented by $\frac{1}{\omega_1}$ in Figure A.1 and B.1, is less influenced by the radial position but more affected by the baseline thrust. The baseline thrust determines the far wake, which impact the convection velocity.

As seen from figures 7.11 — 7.13, the phase delay and the amplitude from models of FWVR, TUD-VR, TUD-VT, ECN and Øye show a strong radial dependency, the phase delay and amplitude difference decrease to the tip. The ECN model omits the effect of wake expansion and the far wake, which might explain the sharper radial distribution at the tip region.

7.5. CONCLUSIONS

In this chapter, new dynamic-inflow engineering models are developed based on the indicial responses of a linear actuator-disc model and of a nonlinear actuator-disc model. The differential form of the Duhamel's integral of the new engineering models is readily implemented in time marching code like BEM.

The flow at the actuator disc is shown to decay at two different speeds, a fast one and a slow one, which are caused by the near wake and far wake, respectively. The phase delay and amplitude difference of velocity from all the models (except the MT) shows a strong radial dependency, this is mainly caused by the relative distance to edge of the disc, where the newly generated vorticity shed into the near wake.

The comparisons of the new engineering models of TUD-VT, TUD-VR and existing models of Pitt-Peters, Øye and ECN and the numerical results from the FWVR model shows that the new model based on the indicial responses of the linear actuator-disc model — TUD-VT predicts better results compared with the existing models for phase delay but not amplitude. The model based on the indicial responses of the nonlinear actuator-disc model — TUD-VR consistently predict better results than the other models of Pitt-Peters, Øye, ECN and TUD-VT for all the load cases, even though the distribution at the outboard part still needs improvement. It shows that the Pitt-Peters model, which is based on the "apparent mass", can not predict the dynamic-inflow effect correctly, especially for the radial distribution of the effect.

8

CONCLUSIONS AND RECOMMENDATIONS

This chapter discusses the results presented in the previous ones, in light of the research questions presented in chapter 1. The conclusions are drawn in section 8.1. Section 8.2 proposes topics for future research.

8.1. ANSWER TO THE RESEARCH QUESTIONS

8.1.1. HOW ACCURATE IS BEM WITH CURRENT ENGINEERING MODELS FOR DYNAMIC INFLOW?

BEM is accurate enough for steady load conditions. For unsteady radially-uniform load, BEM with engineering models of Pitt-Peters, Øye and ECN underestimates the averaged induction at the actuator disc and the aerodynamic work. The Pitt-Peters model predicts an inverse radial distribution of phase delay and amplitude of the induction, when compared to the FWVR model. For unsteady radially-varying loads, BEM with the three engineering models is inaccurate.

For steady load cases, BEM is adequate to predict the induction for both radially-uniform and radially-varying loads, with a negligible difference from the free wake vortex models (chapter 3).

For unsteady radially-uniform load, BEM with the models of Pitt-Peters, Øye and ECN underestimates the averaged induction at the actuator disc and the aerodynamic work, compared to the FWVR model (chapter 3). Comparing the models of Øye and ECN, the Pitt-Peters model underestimates the dynamic-inflow effect most. Furthermore, when comparing the radial distribution of the induction field, the Pitt-Peters model shows an inverse trend of phase delay and amplitude from those of the FWVR model and the engineering models of Øye and ECN (chapter 7). This leads to the conclusion that the Pitt-Peters model, which is based on the "apparent mass" concept, is not correct for induction prediction of a wind turbine, especially for considering the radial distribution of the induction.

For unsteady radially-varying load, the dynamic induction and aerodynamic work predicted by the models of Pitt-Peters, Øye and ECN are significantly different from those of the FWVR model. The difference reveals that the three dynamic-inflow engineering models are not accurate for investigation of localized unsteady loads. This is because all the three engineering models are derived based on uniform load and are applied to radially varied load based on the annuli independent assumption, where the effect from the vorticity shed locally is not correctly considered (chapter 3).

8.1.2. HOW DOES THE WAKE FLOW FIELD OF AN UNSTEADY ACTUATOR DISC DEVELOP?

The experimental and numerical results show that the flow field aft the disc possess a transient response to the step change in loading, with either an overshoot or undershoot of the velocity in relation to the steady-state velocity. The time constants of flow decay is influenced by the local turbulence intensity and thrust increase or decrease. A smaller reduced ramp time results in a faster velocity transient, and in turn a larger amplitude of overshoot or undershoot. Decomposing the velocity induced by the vorticity shed before and after the load change, and the rolled-up vorticity, confirms that the extent of the rolling-up process and its relative distance to the observed points are the main

reasons which cause the difference in velocity transient slope and in the amplitude of velocity overshoot and undershoot and in the different reduced ramp time cases.

The experimental and numerical results show that the flow field aft the disc shows a transient response to the step change in loading. The experiment shows that the flow aft an unsteady actuator disc can be characterised by three regions, the inner wake region, the shear layer region and the region outside the wake. The time constants of velocity decay differ for these different regions. The time constants outside the wake are generally larger than that inside the wake for a given downstream plane (chapter 4). The experimental results show the flow reaches the new steady state slower in the load increase case than the load decrease case (chapter 4). This confirms the numerical results from chapter 3.

In addition to the transient change of velocity to the new steady state, an overshoot or undershoot in velocity is observed at different locations in the flow field from both experimental and numerical results. A difference in overshoot or undershoot is observed between cases when loading is increased and loading is decreased, also between the different locations in the field where the velocity is examined (chapter 4). Furthermore, the numerical results from the FWVR model show that the vortex sheet at the edge of the disc rolls up into a vortical ring structure gradually during the convecting downstream process after the disc load change. Decomposing the velocity induced by the vorticity shed before and after the load change, and the rolled-up vorticity, confirms that the extent of the rolling-up process and its relative distance to the observed points are the main reasons which cause the difference in velocity transient slope and in the amplitude of velocity overshoot and undershoot (chapter 5).

The reduced ramp time of load change is found to have an impact on the wake dynamics. A smaller reduced ramp time (a faster load change) results in a steeper transient velocity change and a larger amplitude of the velocity overshoot or undershoot (chapter 4 and 5). Decomposing the velocity induced by different vortex elements reveals that the difference in velocity profile between the three reduced ramp time cases is caused by the different extent of the rolling up process. A smaller reduced ramp time leads to a quicker rolling up process (chapter 5).

8.1.3. HOW TO IMPROVE THE ENGINEERING MODEL FOR DYNAMIC INFLOW?

The Pitt-Peters model does not predict the dynamic-inflow effect correctly. The models of Øye and ECN are shown to underestimate the dynamic-inflow effect. Based on the more physically representative performance of the free wake vortex model in chapter 3 - 5, two steps are carried out to obtain an engineering model for radially-uniform load using free wake models.

The first step is to investigate the performance of a linear free wake vortex model in chapter 6. Subsequently, chapter 7 tries to obtain the time constants of flow decay functions directly from the free wake vortex models. Both linear and nonlinear actuator-disc based vortex-models are used for this purpose. The effect from the strength of thrust is also investigated in the systematic study when developing the new engineering models in chapter 7.

Results from the new model shows that the new engineering model based on the

linear actuator-disc model (TUD-VT) has improved prediction over current engineering models for phase delay but not for amplitude of velocity distribution on the actuator disc. The new engineering model based on the nonlinear actuator disc model (TUD-VR) shows improved prediction over engineering models of Øye and ECN for both phase delay and amplitude of velocity distribution on the actuator disc, even though there is still room for improvement, especially at the outboard part.

8.2. RECOMMENDATIONS

Based on the achievement of this work, some enhancement and extension to current work are proposed as follows.

8.2.1. LOAD CASES

UNSTEADY RADIALLY VARIED LOAD

As shown in chapter 3, all the current dynamic-inflow engineering models provide inaccurate results for unsteady radially varied load. This type of load is relevant especially for control of distributed aerodynamic devices, such as trailing edge flaps or vortex generator. There are limited experimental and numerical data related to this type of load cases. For future work, similar actuator-disc concept based experiments conducted in chapter 4 can be designed to study the radially varied load. The time constants of flow decay for the locally varied load need to be studied systematically. Based on that knowledge, the engineering models developed in chapter 7 can be extended to the radially varied load cases.

THE EFFECT OF NUMBER OF BLADES

This study confines within actuator disc, where infinite number of blades are assumed. All the engineering models including the new developed one in this thesis are also based on actuator disc. The effect of finite number of blades on the dynamic inflow needs to be investigated.

8.2.2. INFLOW CONDITIONS

AXIS-ASYMMETRICAL FLOW

All the experimental and numerical work in this thesis focuses on axis-symmetrical flow. Extending it to axis-symmetrical flow, eg. rotor in yaw or in shear inflow, is of interest.

THE EFFECT OF TURBULENCE

The turbulence intensity is shown to affect the flow decay in chapter 4, this needs to be investigated further.

DYNAMIC INFLOW CONDITIONS

Only the dynamic wake caused by the load variation is studied in this thesis, which can be resulted from a pitch action or a rotor-thrust change. The effect of the change of inflow condition is not considered. Limited research looked into the effect of the changing of inflow conditions on the dynamic wake, it needs further investigation.

8.2.3. EXPERIMENTAL METHOD

The use of flow measurement particle image velocimetry (PIV) can provide more detailed information for the purpose of this research. The non-intrusive measurement can offer flow response closer to the disc, which can be used to directly validate the engineering models. The data obtained through PIV can provide more information about the velocity and vorticity field, which can be used to validate the numerical results directly.

BIBLIOGRAPHY

Abramowitz, M. and Stegun, I. *Handbook of mathematical functions with formulas, graphs, and mathematical tables*. 1972.

Al-Khazali, H. and Askari, M. Geometrical and graphical representations analysis of Lissajous figures in rotor dynamic system. *IOSR Journal of Engineering*, 2(5):971–978, 2012.

Amer, K. B. Theory of Helicopter Damping in Pitch or Roll and Comparison with Flight Measurements. Technical report, Washington, 1950.

Aubrun, S., Loyer, S., Espana, G., Hayden, P., and Hancock, P. Experimental study on the wind turbine wake meandering with the help of a non-rotating simplified model and of a rotating model. In *49th AIAA Aerospace Sciences Meeeting including the New Horizons Forum and Aerospace Exposition*, pages 1–6, Florida, 2011.

Aubrun, S., Loyer, S., Hancock, P. E., and Hayden, P. Wind turbine wake properties: Comparison between a non-rotating simplified wind turbine model and a rotating model. *Journal of Wind Engineering and Industrial Aerodynamics*, 120:1–8, 2013.

Baldacchino, D. *Horizontal Axis Wind Turbine (HAWT) wake stability investigations*. Msc thesis, Delft University of Technology, 2012.

Bareiss, R. and Wagner, S. The free wake / hybrid wake code ROVLM - A tool for aerodynamic analysis of wind turbines. In *European Community Wind Energy Conference*, Lübeck-Travemünde, 1993.

Beddoes, T. Practical computation of unsteady lift. In *Eight European Rotorcraft Forum*, AIX-EN-PROVENCE, 1982.

Bossuyt, J., Howland, M., Meneveau, C., and Meyers, J. Measurement of unsteady loading and power output variability in a micro wind farm model in a wind tunnel. *Experiments in Fluids*, 58(1), 2017.

Branlard, E. *Analysis of wind turbine aerodynamics and aeroelasticity using vortex-based methods*. PhD thesis, Technical University of Denmark, 2015.

Branlard, E. and Gaunaa, M. Cylindrical vortex wake model : right cylinder. *Wind Energy*, 18(11):1973–1987, 2014.

Branlard, E. *Wind Turbine Aerodynamics and Vorticity-Based Methods*. Springer International Publishing AG, 2017.

Burton, T., Sharpe, D., Jenkins, N., and Bossanyi, E. *Wind energy handbook*. John Wiley & Sons, Ltd, 2001.

Callaghan, E. and Maslen, S. The magnetic field of a finite solenoid. Technical report, National Aeronautics and Space Admnistration,Lews Research Center, Ohio, 1960.

Camp, E. and Cal, R. Mean kinetic energy transport and event classification in a model wind turbine array versus an array of porous disks: Energy budget and octant analysis. *Physical Review Fluids*, 1(4):044404, 2016.

Carpenter, P. and Fridovich, B. Effect of a rapid blade-pitch increase on the thrust and induced-velocity response of a full-scale helicopter rotor. Technical Report November, National Advisory Committee for Aeronautics, Washington, 1953.

Castro, I. Wake characteristics of two-dimensional perforated plates normal to an airstream. *Journal of Fluid Mechanics*, 46:599–609, 1971.

Chamorro, L. and Porté-Agel, F. A wind-tunnel investigation of wind-turbine wakes: Boundary-Layer turbulence effects. *Boundary-Layer Meteorology*, 132(1):129–149, 2009.

Chattot, J.-J. Actuator Disk Theory—Steady and Unsteady Models. *Journal of Solar Energy Engineering*, 136(3):1–10, 2014.

Chen, T. Y. and Liou, L. R. Blockage corrections in wind tunnel tests of small horizontal-axis wind turbines. *Experimental Thermal and Fluid Science*, 35(3):565–569, 2011.

Clark D.R., L. A. The free wake analysis—a method for prediction of helicopter rotor hovering performance. *Journal of the American Helicopter Society*, 15:3–11, 1970.

Conway, J. T. Analytical solutions for the actuator disk with variable radial distribution of load. *Journal of Fluid Mechanics*, 297(-1):327, 1995.

Conway, J. Exact actuator disk solutions for non-uniform heavy loading and slipstream contraction. *Journal of Fluid Mechanics*, 365:235–267, 1998.

Cottet, G. H. and Koumoutsakos, P. *Vortex Methods: Theory and Practice*. Cambridge University Press, 2000.

Crews, S. and Hohenemser, K. An Unsteady Wake Model for a Hingeless Rotor. *Journal of Aircraft*, 10:758–760, 1973.

Ferreira, C. S. *The near wake of the VAWT: 2D and 3D views of the VAWT aerodynamics*. PhD thesis, Delft University of Technology, 2009.

Froude, R. E. On the part played in propulsion by differences of fluid pressure. *Transactions of the Institute of Naval Architects*, 30:390–405, 1889.

Gaonkar, G. H. and Peters, D. A. Review of dynamic inflow modeling for rotorcraft flight dynamics. *VERTICA*, 12(3):213–242, 1986.

Garner, H. C., Rogers, E., Acum, W., and Maskell, E. Subsonic wind tunnel wall corrections. *AGARDograph, AG-109*, 1966.

Gibson, I. On the velocity induced by a semi-infinite vortex cylinder: with extension to the short solenoid. *Aeronautical Journal*, 78(762):262–268, 1974.

Hand, M., Simms, D., Fingersh, L., Jager, D., Cotrell, J., Schreck, S., and Larwood, S. Unsteady Aerodynamics Experiment Phase VI : Wind Tunnel Test Configurations and Available Data Campaigns. Technical Report December, National Renewable Energy Laboratory, Colorado, 2001.

Hansen, A. and Butterfield, C. Aerodynamics of horizontal-axis wind turbines. *Annual Review of Fluid Mechanics*, 25:115–149, 1993.

Hansen, M., Hansen, A., Larsen, T., Øye, S., Soresen, P., and Fugisang, P. Control design for a pitch-regulated, variable speed wind turbine. Technical report, Roskilde, 2005.

Henriksen, L. C., Hansen, M. H., and Poulsen, N. K. A simple dynamic inflow model and its effect on the performance of free mean wind speed estimation. *Wind Energy*, 16: 1213–1224, 2013.

Heyson, H. and Katzoff, S. Induced velocities near a lifting rotor with nonuniform disk loading. Technical report, National Advisory Committee for Aeronautics, 1956.

Higuchi, H. and Balligand, H. Numerical and experimental investigations of the flow over a disk undergoing unsteady motion. *Journal of Fluids and Structures*, 10:705–719, 1996.

Hoerner, S. F. *Fluid-Dynamic Drag: theoretical,experimental and statistical information*. S. F. Hoerner, New York, 1965.

Hong, V. W. *Analysis of an Actuator Disc under Unsteady Loading*. Msc thesis, Delft University of Technology, 2015.

Huyer, S., Simms, D., and Robinson, M. Unsteady aerodynamics associated with a horizontal axis wind turbine. *Am. Inst. Aeronaut. Astronaut. J.*, 34(7):1410–1419, 1996.

Inman, D. J. *Engineering vibrations,third edition*. Pearson Education, Inc. Third edition, Upper saddle river, 2009.

Jeng, D. and Keith, T. Aerodynamic Analysis of a Horizontal Axis Wind Turbine by use of Helical Vortex Theory. Technical report, University of Toledo, Toledo, 1982.

Johnson, P., Wojcik, A., Drake, K., and Eames, I. Impulsively started planar actuator surfaces in high-Reynolds-number steady flow. *Journal of Fluid Mechanics*, 733:302–324, 2013.

Jones, R. The unsteady lift of a wing of finite aspect ratio. Technical report, National Advisory Committee for Aeronautics, 1939.

Joukowsky, N. Vortex Theory of Screw Propeller, I. *Trudy Otdeleniya Fizicheskikh Nauk Obshchestva Lubitelei Estestvoznaniya*, 16(1):1–31, 1912.

Joukowsky, N. Vortex Theory of Screw Propeller, II. *Trudy Otdeleniya Fizicheskikh Nauk Obshchestva Lubitelei Estestvoznaniya*, 17(1):1–33, 1914.

Joukowsky, N. Vortex Theory of Screw Propeller, III. *Trudy Otdeleniya Fizicheskikh Nauk Obshchestva Lubitelei Estestvoznaniya*, 17(2):1–23, 1915.

Joukowsky, N. Vortex Theory of Screw Propeller, IV. *Trudy Avia Raschetno-Ispytatelnogo Byuro*, 3(2):1–97, 1918.

Knight M. Wind tunnel standardization disk drag. Technical report, National Advisory Committee for Aeronautics,Langley Aeronautical Laboratory, Washington, 1926.

Koumoutsakos, P. and Shiels, D. Simulations of the viscous flow normal to an impulsively started and uniformly accelerated flat plate. *Journal of Fluid Mechanics*, 328:177–227, 1996.

Laino, D. J. and Hansen, A. USER'S GUIDE to the Wind Turbine Aerodynamics Computer Software AeroDyn. Technical report, Windward Engineering, Salt Lake City, 2002.

Larsen, T. J. and Hansen, A. M. How 2 HAWC2, the user's manual. Technical report, Risø National Laboratory, Roskilde, 2007.

Leishman, J. Challenges in modelling the unsteady aerodynamics of wind turbines. *Wind Energy*, 5(2-3):85–132, 2002.

Leishman, J. *Principles of Helicopter Aerodynamics*. Cambridge University Press, second edi edition, 2006.

Leishman, J., Bhagwat, M. J., and Baga, A. Free-Vortex Filament Methods for the Analysis of Helicopter Rotor Wakes. *Journal of Aircraft*, 39(5):759–775, 2002.

Lewis, R. *Vortex Element Methods for Fluid Dynamic analysis of Engineering Systems*. Cambridge University Press, New York, 1991.

Lignarolo, L., Ragni, D., Ferreira, C., and van Bussel, G. Kinetic energy entrainment in wind turbine and actuator disc wakes: an experimental analysis. *Journal of Physics: Conference Series*, 524(Torque):1–10, 2014.

Lignarolo, L., Mehta, D., Stevens, R., Yilmaz, A., van Kuik, G., Andersen, S. J., Meneveau, C., Ferreira, C., Ragni, D., Meyers, J., van Bussel, G., and Holierhoek, J. Validation of four LES and a vortex model against stereo-PIV measurements in the near wake of an actuator disc and a wind turbine. *Renewable Energy*, 94:510–523, 2016a.

Lignarolo, L., Ragni, D., Ferreira, C., and van Bussel, G. Experimental comparison of a wind-turbine and of an actuator-disc near wake. *Journal of Renewable and Sustainable Energy*, 8:1–27, 2016b.

Lindenburg, C. PHATAS Release "NOV-2003" and "APR-2005" USER'S MANUAL. Technical report, Energy research Centre of the Netherlands, 2005.

Madsen, H. and Rasmussen, F. A near wake model for trailing vorticity compared with the blade element momentum theory. *Wind Energy*, 7(4):325–341, 2004.

Madsen, H. A., Bak, C., Paulsen, U. S., Gaunaa, Mac, Fuglsang, P., Romblad, J., Olesen, N. A., Enevoldsen, P., Laursen, J., and Jensen, L. The DAN-AERO MW Experiments Final report. Technical report, 2010.

Mangler, K. and Squire, H. The induced field of a rotor. *Reports Memoranda No. 2642*, Royal Aircraft Establishment, 1950.

Medici, D. *Experimental Studies of Wind Turbine Wakes - Power Optimisation and Meandering*. PhD thesis, Royal Institute of Technology, 2005.

Micallef, D. *3D flows near a HAWT rotor : A dissection of blade and wake contributions*. PhD thesis, Delft University of Technology, 2012.

Mikkelsen, R. *Actuator disc methods applied to wind turbines*. PhD thesis, Technical University of Denmark, 2003.

Muller, Y.-A., Aubrun, S., and Masson, C. Determination of real-time predictors of the wind turbine wake meandering. *Experiments in Fluids*, 56(3):1–11, 2015.

Øye, S. Unsteady wake effects caused by pitch-anlge changegs. In *Proceedings of the First IEA Symposium on the aerodynamics of wind turbines*, London, 1986.

Øye, S. A simple vortex model of a turbine rotor. In *Proceedings of the third IEA symposium on the aerodynamics of wind turbines*, pages 1–15, Harwell, 1990.

Øye, S. Tjæreborg wind turbine (Esbjerg): First dynamic inflow measurement. Technical Report VK-189, Technical University of Denmark, Lyngby, 1991a.

Øye, S. Tjæreborg wind turbine, 4. dynamic inflow measurement. Technical report, Technical University of Denmark, Lyngby, 1991b.

Paxton, F. Solid angle calculation for a circular disk. *The review of Scientific instruments*, 30(4):254–258, 1959.

Peters, D. A. Hingeless rotor frequency response with unsteady inflow. In *Proceedings of the American Helicopter Society Dynamics Specialists' Meeting*, California, 1974.

Peters, D. How Dynamic Inflow Survives in the Competitive World of Rotorcraft Aerodynamics. *Journal of the American Helicopter Society*, 54(1):011001, 2009.

Pierella, F. and Sætran, L. Effect of initial conditions on flow past grids of finite extension. In *17th Australasian Fluid Mechanics Conference*, number December, Auckland, 2010.

Pierides, A., Elzawawy, A., and Andreopoulos, Y. Transient force generation during impulsive rotation of wall-mounted panels. *Journal of Fluid Mechanics*, 721:403–437, 2013.

Pirrung, G. R. and Madsen, H. A. Dynamic inflow effects in measurements and high fidelity computations. *Wind Energy Science*, pages 1–10, 2018.

Pitt, D. *Rotor dynamic inflow derivatives and time constants from various inflow models*. PhD thesis, Washington University, 1980.

Pitt, D. and Peters, D. Theoretical prediction of dynamic-inflow derivatives. *Vertica*, 5(1): 21–34, 1981.

Qiu, Y. X., Wang, X., Kang, S., Zhao, M., and Liang, J. Predictions of unsteady HAWT aerodynamics in yawing and pitching using the free vortex method. *Renewable Energy*, pages 1–14, 2014.

Rajagopalan, K. P. C., R Ganesh and Rickerl, T. L. The free wake analysis—a method for prediction of helicopter rotor hovering performance. *Journal of Propulsion and Power*, 6(5):645–653, 1990.

Rankine, W. J. M. *On the mechanical principles of the action of propellers*. Trans Inst Naval Archit, 1865.

Sanderse, B., van der Pijl, S., and Koren, B. Review of computational fluid dynamics for wind turbine wake aerodynamics. *Wind Energy*, 14:799–819, 2011.

Schepers, J. G., Boorsma, K., Cho, T., Schaffarczyk, P., Jeromin, A., Shen, W. Z., Lutz, T., Meister, K., Stoevesandt, B., Schreck, S., Micallef, D., Pereira, R., Sant, T., Madsen, H., and Sørensen, N. Final report of IEA Task 29 , Mexnext (Phase 1): Analysis of Mexico wind tunnel measurements. Technical report, Energy Research Center of the Netherlands, Petten, 2012.

Schepers, J. IEA Annex XX : Dynamic Inflow effects at fast pitching steps on a wind turbine placed in the NASA-Ames wind tunnel. Technical report, Energy Research Center of the Netherlands, Petten, 2007.

Schepers, J. *Engineering models in wind energy aerodynamics*. PhD thesis, Delft University of Technology, 2012.

Schepers, J. and Snel, H. Dynamic inflow: yawed conditions and partial span pitch control. Technical report, Energy Research Center of the Netherlands, Petten, 1995.

Schepers, J. and Snel, H. Model experiments in controlled conditions. Technical report, Energy Research Center of the Netherlands, 2009.

Schepers, J., Boorsma, K., Gomez-Iradi, S., Schaffarczyk, P., Madsen, H. A., Sørensen, N. N., Shen, W. Z., Lutz, T., Schulz, C., Herraez, I., and Schreck, S. Final report of IEA Task 29, Mexnext (Phase 2). Technical report, Energy Research Center of the Netherlands, Petten, 2014.

Sforza, P., Sheerin, P., and Smorto, M. Three-Dimensional Wakes of Simulated Wind Turbines. *AIAA Journal*, 19(9):1101–1107, 1981.

Shen, W. Z., Zhang, J. H., and Sorensen, J. N. Actuator surface model for wind turbine flow computations. In *Proceedings of European Wind Energy Conference and Exhibition*, 2007.

Shen, W. Z., Zhang, J. H., and Sørensen, J. N. The Actuator Surface Model: A New Navier–Stokes Based Model for Rotor Computations. *Journal of Solar Energy Engineering*, 131(1), 2009.

Sissingh, G. J. The Effect of Induced Velocity Variation on Helicopter Rotor Damping in Pitch or Roll. Technical report, Aeronautical Research Council, 1952.

Snel, H. Review of the present status of rotor aerodynamics. *Wind Energy*, 1:46–69, 1998.

Snel, H. and Schepers, J. Joint investigation of dynamic inflow effects and implemention of an engineering method. Technical report, Energy Research Center of the Netherlands, 1995.

Sørensen, J. N. *General Momentum Theory for Horizontal Axis Wind Turbines*, volume 4. Springer International Publishing, Lyngby, 2016.

Sørensen, J. N. and Shen, W. Z. Numerical Modeling of Wind Turbine Wakes. *Journal of Fluids Engineering*, 124(2):393, 2002.

Sørensen, J. and Kock, C. A model for unsteady rotor aerodynamics. *Journal of Wind Engineering and Industrial Aerodynamics*, 58:259–275, 1995.

Sørensen, J. and Mikkelsen, R. On the validity of the blade element momentum method. In *European Wind Energy Conference*, Copenhagen, 2001.

Sørensen, J. and Myken, A. Unsteady actuator disc model for horizontal axis wind turbines. *Journal of Wind Engineering and Industrial Aerodynamics*, 39(1-3):139–149, jan 1992.

Suzuki, A. *Application of dynamic inflow theory to wind turbine rotors*. PhD thesis, The University of Utah, 2000.

Thoma, D. Grundsatzliches zur einfachen Strahltheorie der Schraube. *Zeitschrift für Flugtechnik und Motorluftschiffahrt*, 16:206–208, 1925.

Troldborg, N., Bak, C., Madsen, H., and Skrzypinski, W. DANAERO MW : Final Report. Technical report, Technical University of Denmark, 2013.

van Engelen, T. G. and van der Hooft, E. L. DYNAMIC INFLOW COMPENSATION FOR PITCH CONTROLLED WIND TURBINES. In *European Wind Energy Conference*, London, 2004.

van Garrel, A. Development of a Wind Turbine Aerodynamics Simulation Module. Technical report, Energy Research Center of the Netherlands, 2003.

van Kuik, G. The edge singularity of an actuator disc with a constant normal load. In *22nd AIAA/ASME Wind Energy Symposium*, Reno, USA, 2003.

van Kuik, G. and Lignarolo, L. Potential flow solutions for energy extracting actuator disc flows. *Wind Energy*, 19:1391–1406, 2016.

van Kuik, G., Sørensen, J., and Okulov, V. Rotor theories by Professor Joukowsky: Momentum theories. *Progress in Aerospace Sciences*, 73:1–18, 2015.

Voutsinas, S. G. Vortex methods in aeronautics: how to make things work. *International Journal of Computational Fluid Dynamics*, 20(1):3–18, 2006.

Wagner, H. A. Über die Entstehung des dynamischen Auftriebes von Tragflügeln. *Zeitschrift für angewandte Mathematik und Mechanik*, 5(1):17–35, 1925.

Wilson, R. and Lissaman, P. Applied Aerodynamics of Wind Power Machines. Technical report, Oregon State University, California, 1974.

Yang, A., Jia, L., and Yin, X. Formation process of the vortex ring generated by an impulsively started circular disc. *Journal of Fluid Mechanics*, 713:61–85, 2012.

Yoon, S. and Heister, S. Analytical formulas for the velocity field induced by an infinitely thin vortex ring. *Int. J. Numer. Meth.Fluids*, 44:665–672, 2004.

Appendices

A

INDICIAL RESPONSES OF A LINEAR ACTUATOR-DISC MODEL

In this section, the process of obtaining the radial distribution of the coefficients for the indicial functions from the linear actuator-disc model is presented.

The radial distribution of the coefficients β, ω_1 and ω_2 are represented by polynomials in Equation 7.6. The directly fitted and the polynomial representation of the radial distribution of the coefficients of β, $\frac{1}{\omega_1}$ and $\frac{1}{\omega_2}$ of different baseline thrust from the VTM are shown in Figure A.1. As seen, the radial distributed coefficients of β, $\frac{1}{\omega_1}$ and $\frac{1}{\omega_2}$ can be well represented by the polynomials.

The parameters of the polynomials in Equation 7.6 for β, ω_1 and ω_2 are plotted against the baseline C_t in Figure A.2. As seen from Figure A.1 and Figure A.2, the difference for the distributed coefficients between load increase and load decrease cases obtained by the linear VTM is small. Therefore, the averaged value of the load increase and decrease cases are used. As seen from Figure A.2 (a), the distribution of β obtained by the VTM is independent from the C_t, only small difference exists at the high thrust side. The parameters of a_3, a_2, a_1, a_0 for ω_1 and ω_2 against C_t are represented by a first degree polynomial. These final used first degree polynomials are also plotted in Figure A.2. The final used parameters are given in Table 7.1.

Figures A.3 — A.5 show the phase delay and amplitude of the radial distributed velocity using coefficients obtained by the VTM with different simplifications for baseline thrust 1/9, 4/9, 7/9, separately. Specifically, the directly fitted coefficients from the indicial responses of the VTM and the polynomial representation of the coefficients. As seen, results using the polynomial represented coefficients are in good match with the results using the directly fitted ones, this shows the good quality of the polynomial representation of the coefficients.

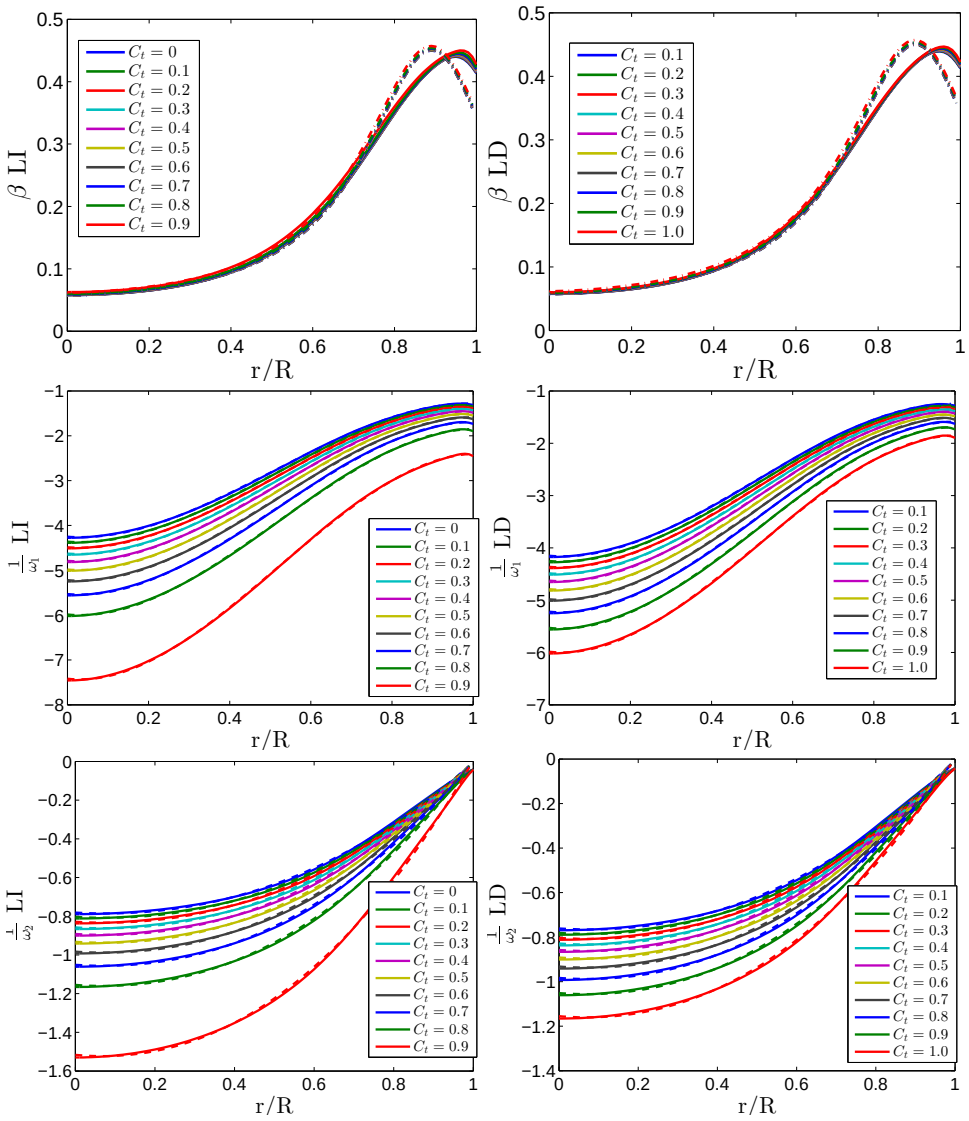

Figure A.1: The radial distribution of β, $\frac{1}{\omega_1}$ and $\frac{1}{\omega_2}$ of the indicial responses of different baseline C_t from the VTM for load increase and decrease cases. Solid lines: directly fitted coefficients; dashed lines: the polynomial approximation of the radial distribution of coefficients.

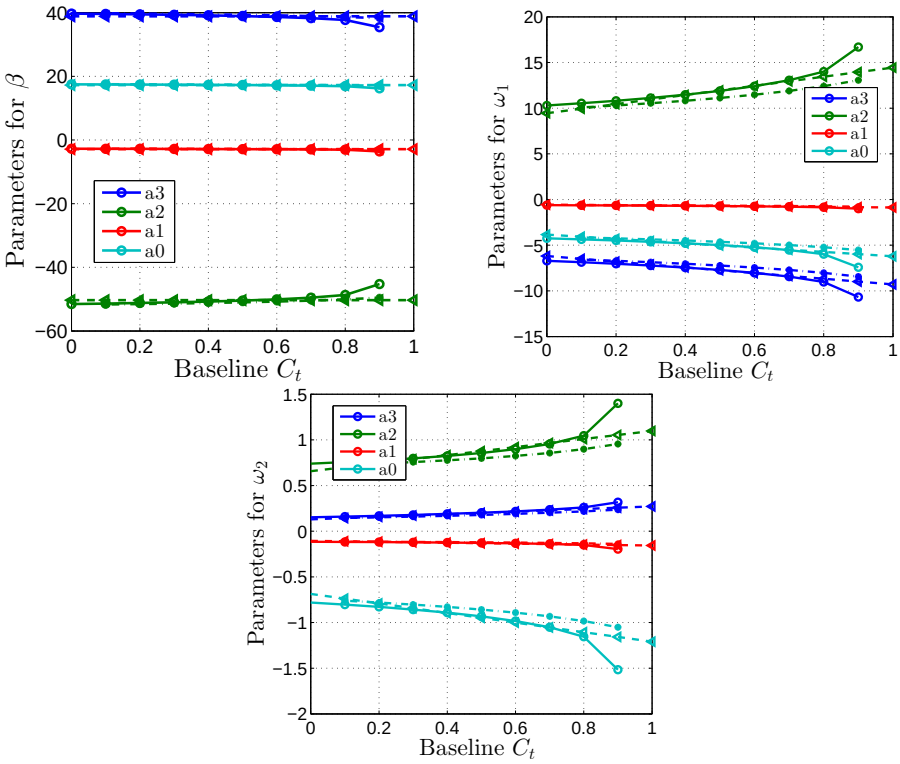

Figure A.2: The parameters of a_3, a_2, a_1, a_0 for β, ω_1 and ω_2 against C_t from the VTM. Solid line: load increase; dot-dashed line: load decrease; dashed line: representation of the average values between load increase and decrease case.

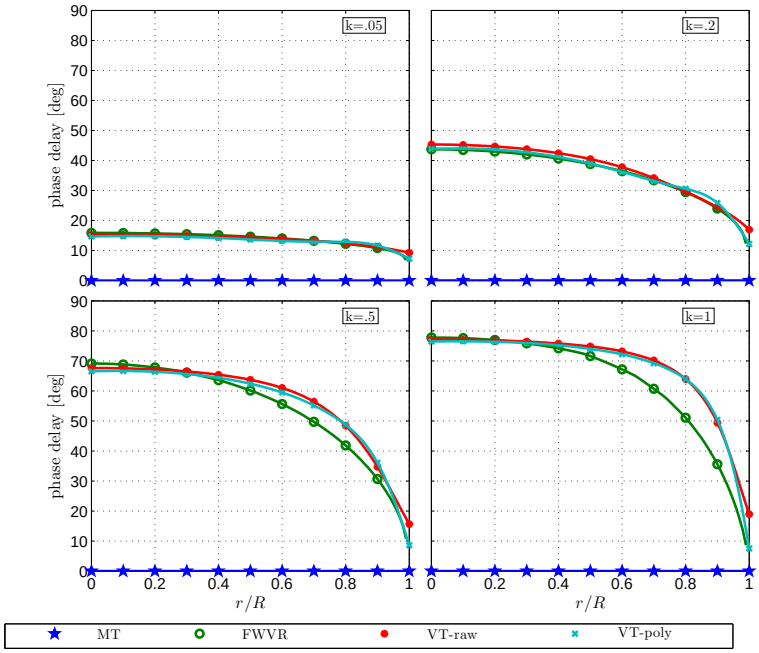

(a) Phase delay for baseline C_t= 1/9, ΔC_t= 1/9

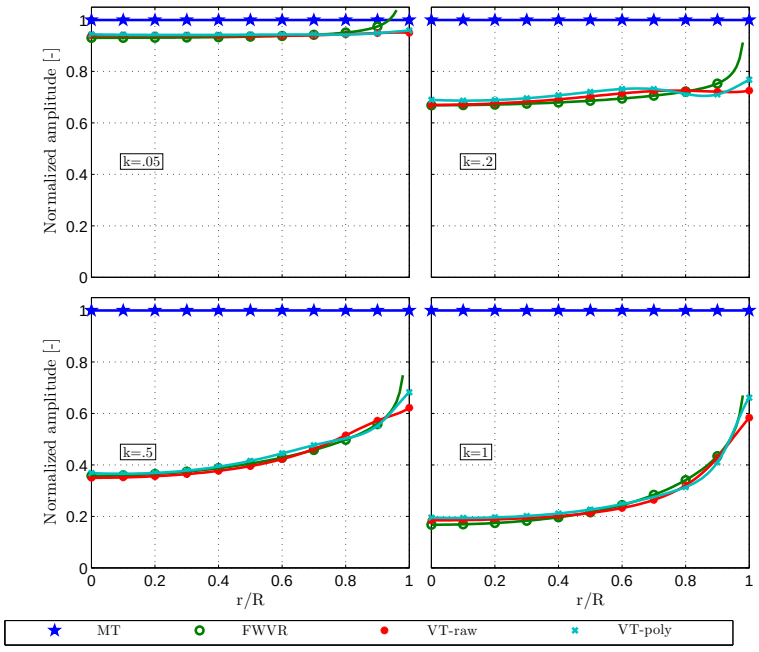

(b) Amplitude for baseline C_t= 1/9, ΔC_t= 1/9

Figure A.3: Comparison of the radial distribution of the phase delay and amplitude of the velocity using coefficients obtained by the VTM with different simplifications for baseline C_t=1/9 for frequencies of k=0.05, 0.2, 0.5, 1. VT-raw, VT-poly represent results using coefficients from the directly fitted coefficients from the indicial responses, the polynomial represented coefficients from the indicial responses of the linear actuator-disc model, separately.

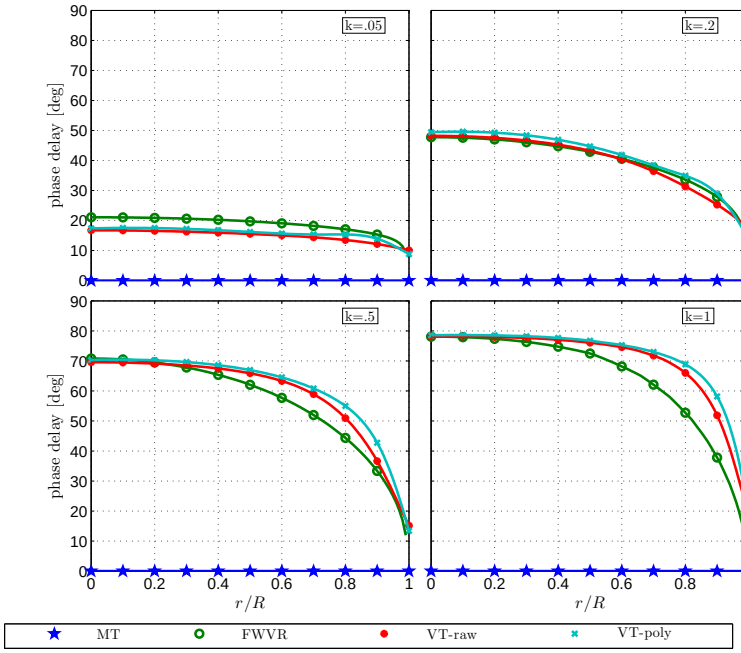

(a) Phase delay for baseline C_t= 4/9, ΔC_t= 1/9

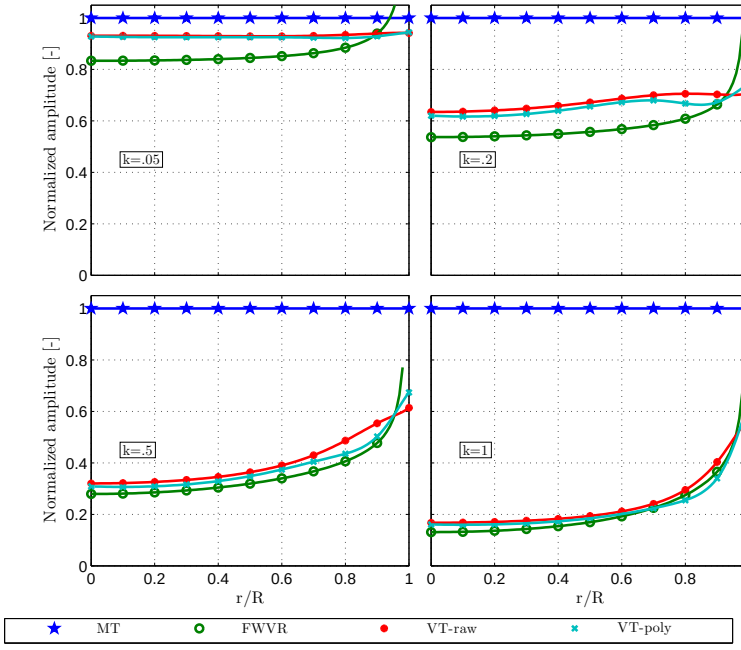

(b) Amplitude for baseline C_t= 4/9, ΔC_t= 1/9

Figure A.4: Comparison of the radial distribution of the phase delay and amplitude of the velocity using coefficients obtained by the VTM with different simplifications for baseline C_t=4/9 for frequencies of k=0.05, 0.2, 0.5, 1. VT-raw, VT-poly represent results using coefficients from the directly fitted coefficients from the indicial responses, the polynomial represented coefficients from the indicial responses of the linear actuator-disc model, separately.

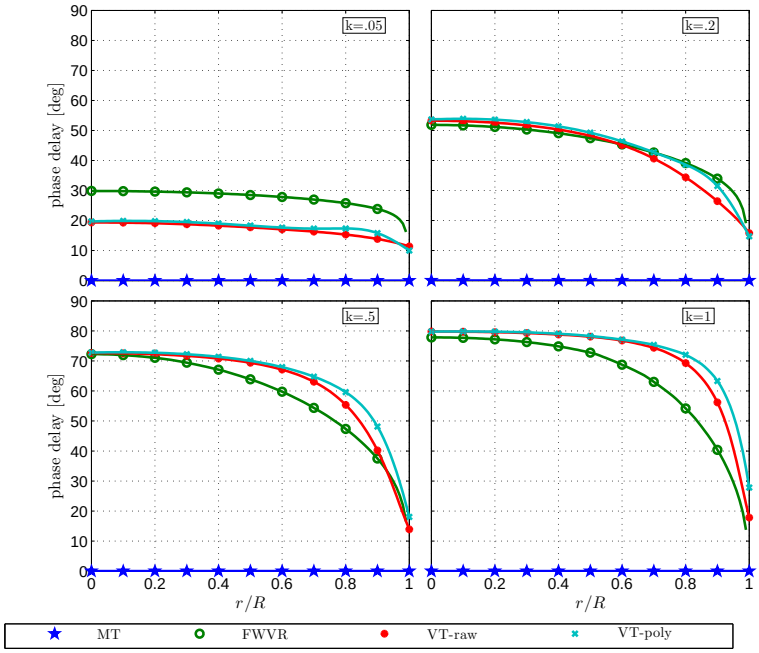

(a) Phase delay for baseline C_t= 7/9, ΔC_t= 1/9

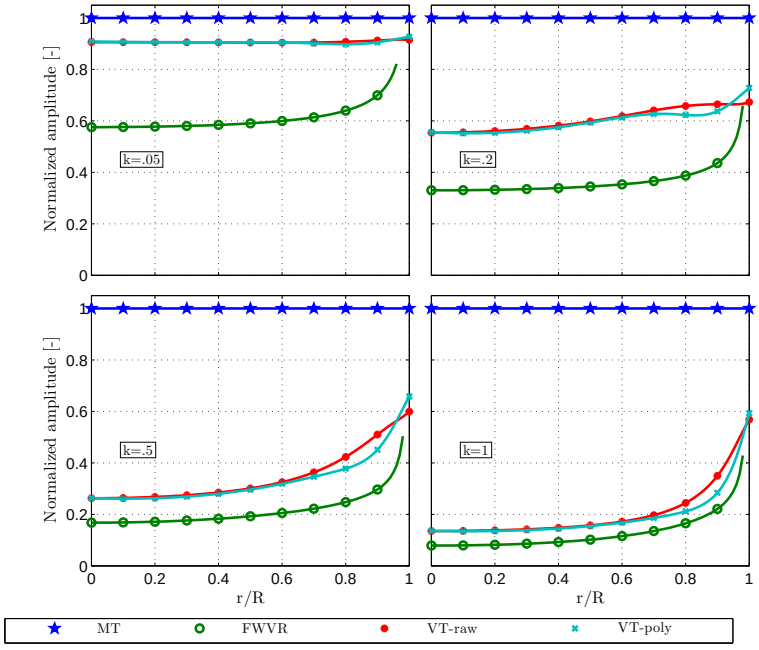

(b) Amplitude for baseline C_t= 7/9, ΔC_t= 1/9

Figure A.5: Comparison of the radial distribution of the phase delay and amplitude of the velocity using coefficients obtained by the VTM with different simplifications for baseline C_t=7/9 for frequencies of k=0.05, 0.2, 0.5, 1. VT-raw, VT-poly represent results using coefficients from the directly fitted coefficients from the indicial responses, the polynomial represented coefficients from the indicial responses of the linear actuator-disc model, separately.

B

INDICIAL RESPONSES OF A NONLINEAR ACTUATOR-DISC MODEL

In this section, the process of obtaining the radial distribution of the coefficients for the indicial functions from the nonlinear actuator-disc model is presented.

The radial distribution of the coefficients β, ω_1 and ω_2 are represented by polynomials in Equation 7.7. The directly fitted and the polynomial representation of the radial distribution of the coefficients of β, $\frac{1}{\omega_1}$ and $\frac{1}{\omega_2}$ of different baseline thrust from the FWVR are shown in Figure B.1. As seen, the values obtained by the FWVR model are strongly affected by the cut-off radius used in the tip region, which is not fully captured by the polynomial representation. Excluding the region $r/R > 0.95$, the radial distributed coefficients can be well represented by the polynomial. As seen from Figure A.1, the baseline thrust has negligible impact on the coefficient β for the VTM. For the FWVR model in Figure B.1, β and $\frac{1}{\omega_1}$ are highly influenced by the baseline thrust, but the thrust has a slight impact on the $\frac{1}{\omega_2}$.

The parameters for β, ω_1 and ω_2 from the FWVR model are plotted against the baseline C_t in Figure B.2. As seen from Figure A.2 and Figure B.2, the difference for the distributed coefficients between load increase and decrease load cases obtained by the nonlinear FWVR model is larger than that from the linear VTM. The parameters of a_3, a_2, a_1, a_0 for ω_1 and ω_2 against C_t are also obtained based on the averaged value between the load increase and decrease cases for the final use. These final used values are also plotted in Figure B.2 and given in Table 7.2.

Figures B.3 — B.5 show the phase delay and amplitude of the radial distributed velocity using the directly fitted coefficients obtained by the FWVR model and the polynomial representation of the coefficients. As seen, the directly fitted coefficients is influenced by the cut-off radius used in the model, also as indicated in Figure B.1. Results using the polynomial represented coefficients are in good match with the results using the directly fitted coefficients except the tip region, as the tip effect is not fully considered in the polynomial representation. The good agreement of results using the directly fitted and polynomial representation of the coefficients within the region $r/R \leq 0.95$ justifies the use of the polynomial representation of the coefficients.

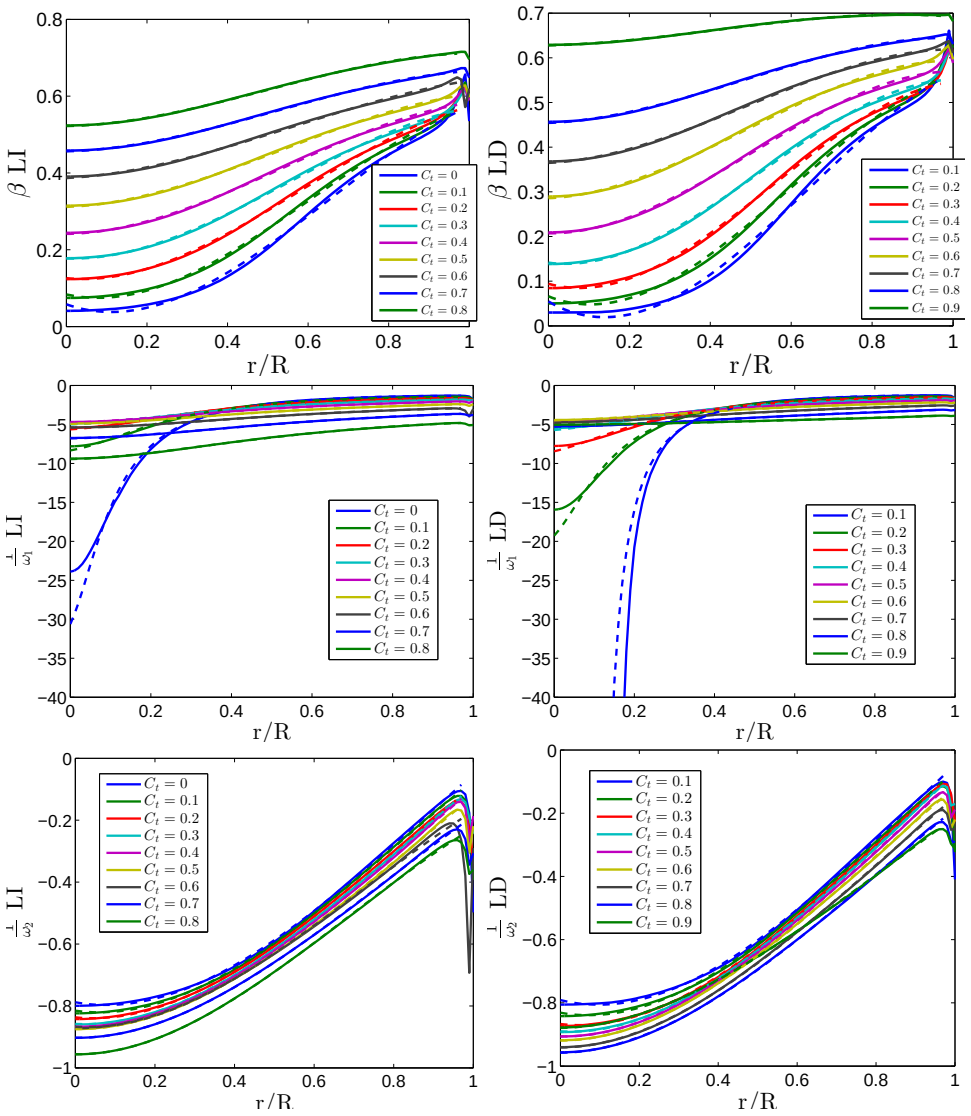

Figure B.1: The radial distribution of β, $\frac{1}{\omega_1}$ and $\frac{1}{\omega_2}$ of the indicial responses of different baseline C_t from the FWVR. Solid line: directly fitted coefficients; dashed line: the polynomial approximation of the radial distribution of coefficients.

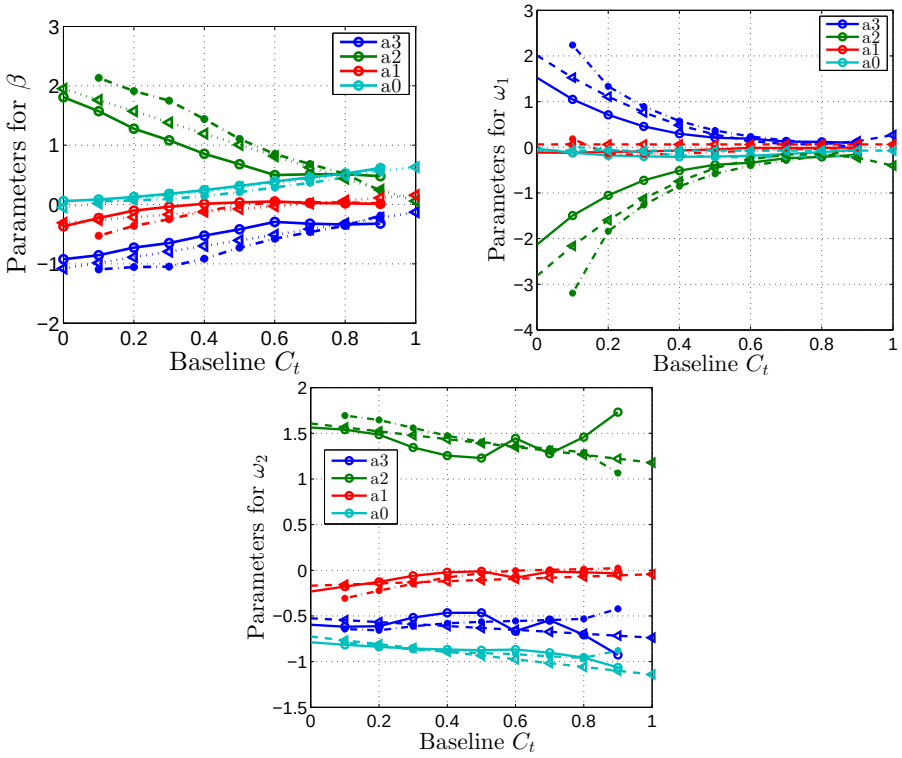

Figure B.2: The parameters of a_3, a_2, a_1, a_0 for β,ω_1 and ω_2 against C_t from the FWVR model. Solid line: load increase; dot-dashed line: load decrease; dashed line: representation of the average values between load increase and decrease case.

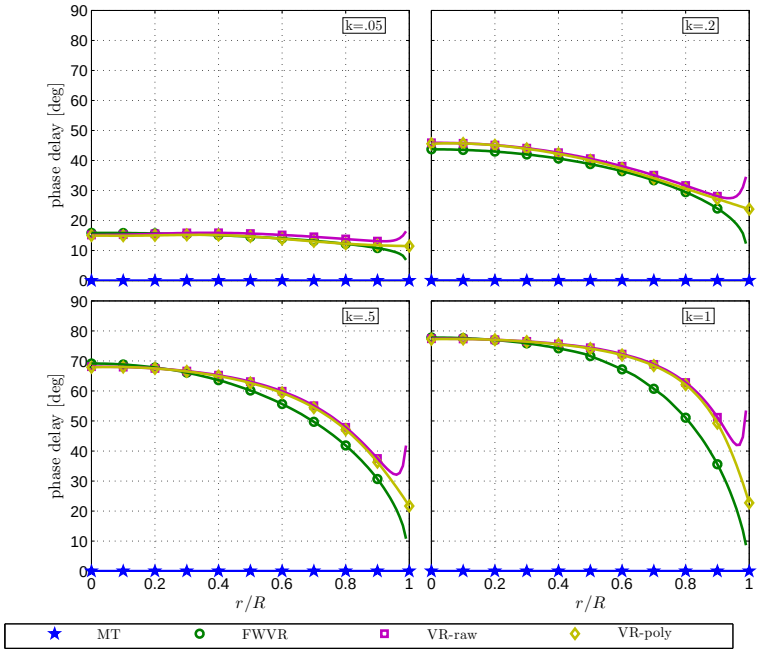

(a) Phase delay for baseline C_t= 1/9, ΔC_t= 1/9

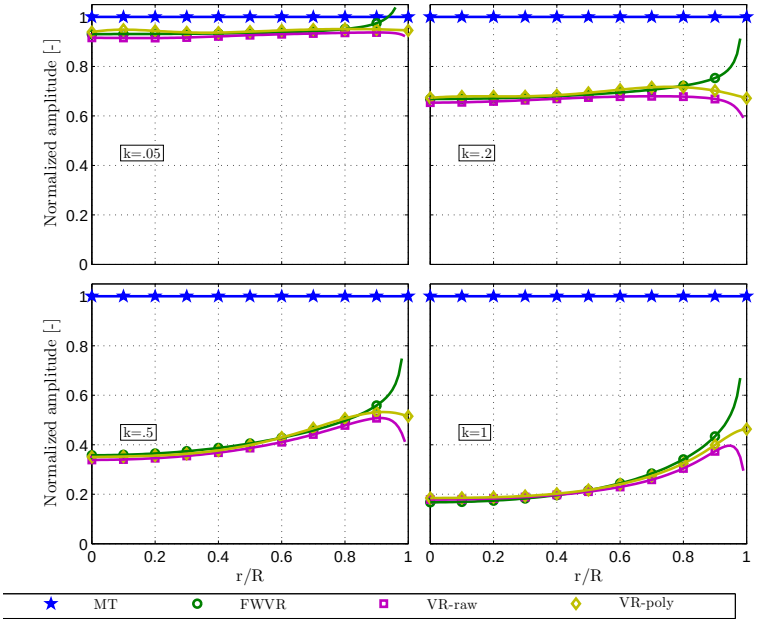

(b) Amplitude for baseline C_t= 1/9, ΔC_t= 1/9

Figure B.3: Comparison of the radial distribution of the phase delay and amplitude of the velocity using coefficients obtained by the FWVR model with different simplifications for baseline C_t=1/9 for frequencies of k=0.05, 0.2, 0.5, 1. VR-raw, VR-poly represent results using the directly fitted coefficients, the polynomial represented coefficients from the indicial responses of the nonlinear actuator-disc model, separately.

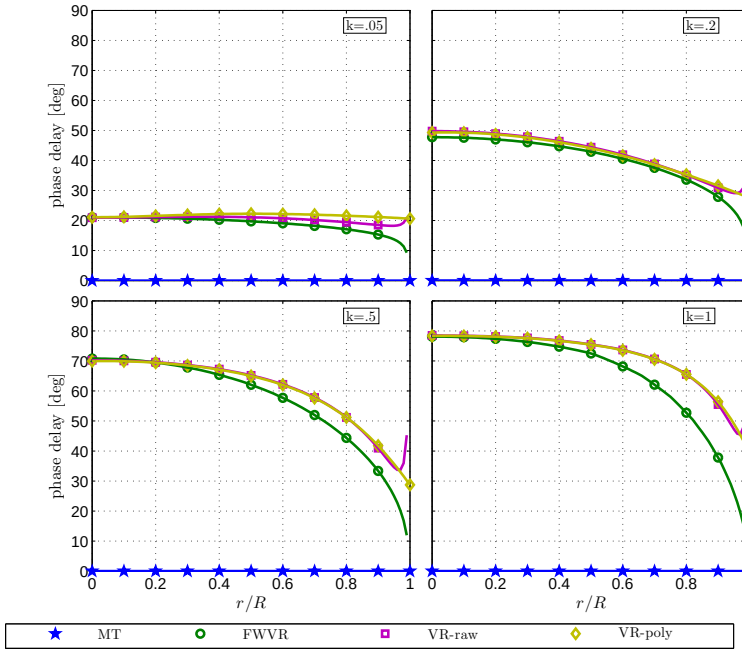

(a) Phase delay for baseline C_t= 4/9, ΔC_t= 1/9

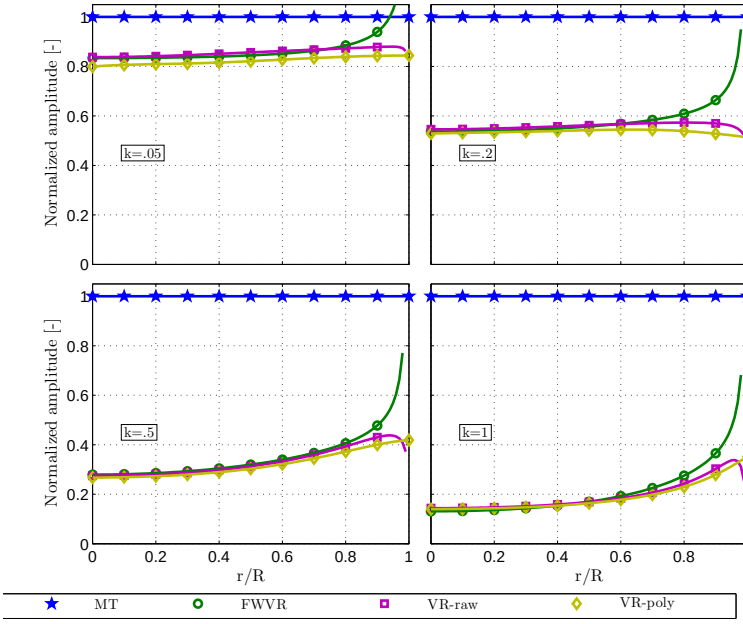

(b) Amplitude for baseline C_t= 4/9, ΔC_t= 1/9

Figure B.4: Comparison of the radial distribution of the phase delay and amplitude of the velocity using coefficients obtained by the FWVR model with different simplifications for baseline C_t=4/9 for frequencies of k=0.05, 0.2, 0.5, 1. VR-raw, VR-poly represent results using the directly fitted coefficients, the polynomial represented coefficients from the indicial responses of the nonlinear actuator-disc model, separately.

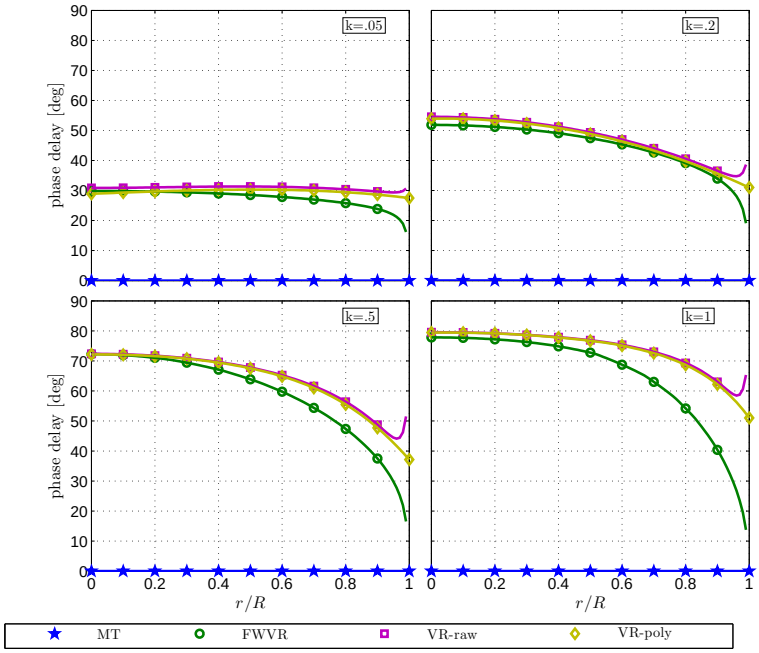

(a) Phase delay for baseline C_t= 7/9, ΔC_t= 1/9

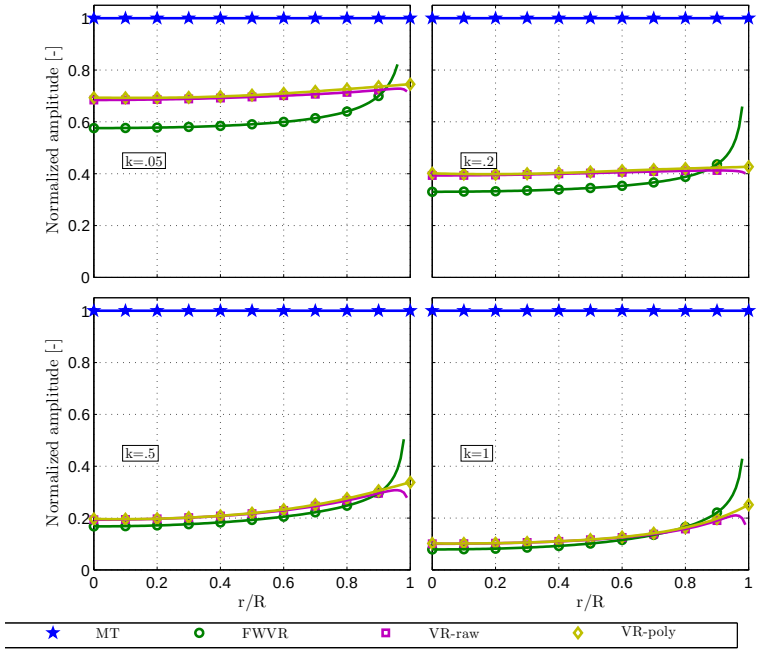

(b) Amplitude for baseline C_t= 7/9, ΔC_t= 1/9

Figure B.5: Comparison of the radial distribution of the phase delay and amplitude of the velocity using coefficients obtained by the FWVR model with different simplifications for baseline C_t=7/9 for frequencies of k=0.05, 0.2, 0.5, 1. VR-raw, VR-poly represent results using the directly fitted coefficients, the polynomial represented coefficients from the indicial responses of the nonlinear actuator-disc model, separately.

C

WAKE FROM THE FWVR MODEL

Figure C.1 — C.3 shows the location of the vortex rings of the fully developed near wake obtained by the FWVR model for baseline C_t= 1/9, 4/9, 7/9, separately, for frequencies k=0.05, 0.2, 0.5, 1. As expected, the wake expansion pattern shows the same frequency as the load variation. As seen, the larger the thrust, the earlier the instability of the wake happens, which is consistent with chapter 3. Due to the interaction with the wake instability, the wake expansion pattern is less discernible for higher thrust.

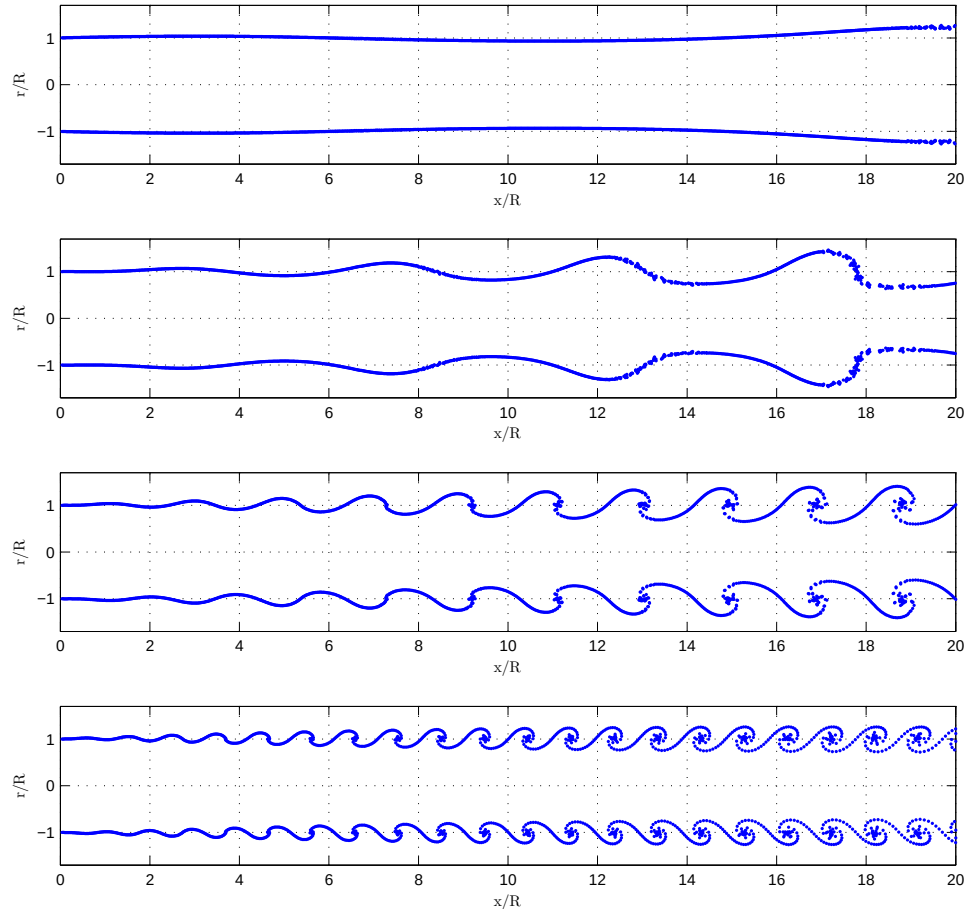

Figure C.1: Location of vortex rings in the fully developed near wake for baseline C_t=1/9 with frequencies k=0.05, 0.2, 0.5, 1. Points represent intersections of the rings with the symmetry plane.

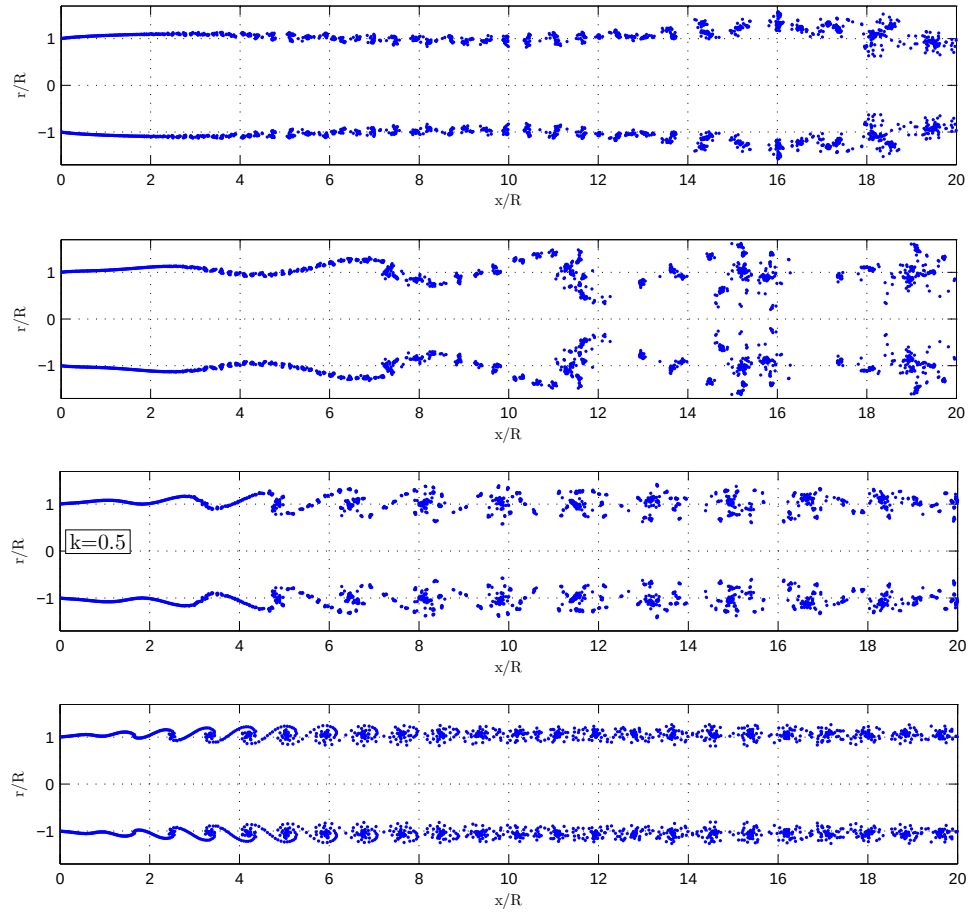

Figure C.2: Location of vortex rings in the fully developed near wake for baseline C_t=4/9 with frequencies k=0.05, 0.2, 0.5, 1. Points represent intersections of the rings with the symmetry plane.

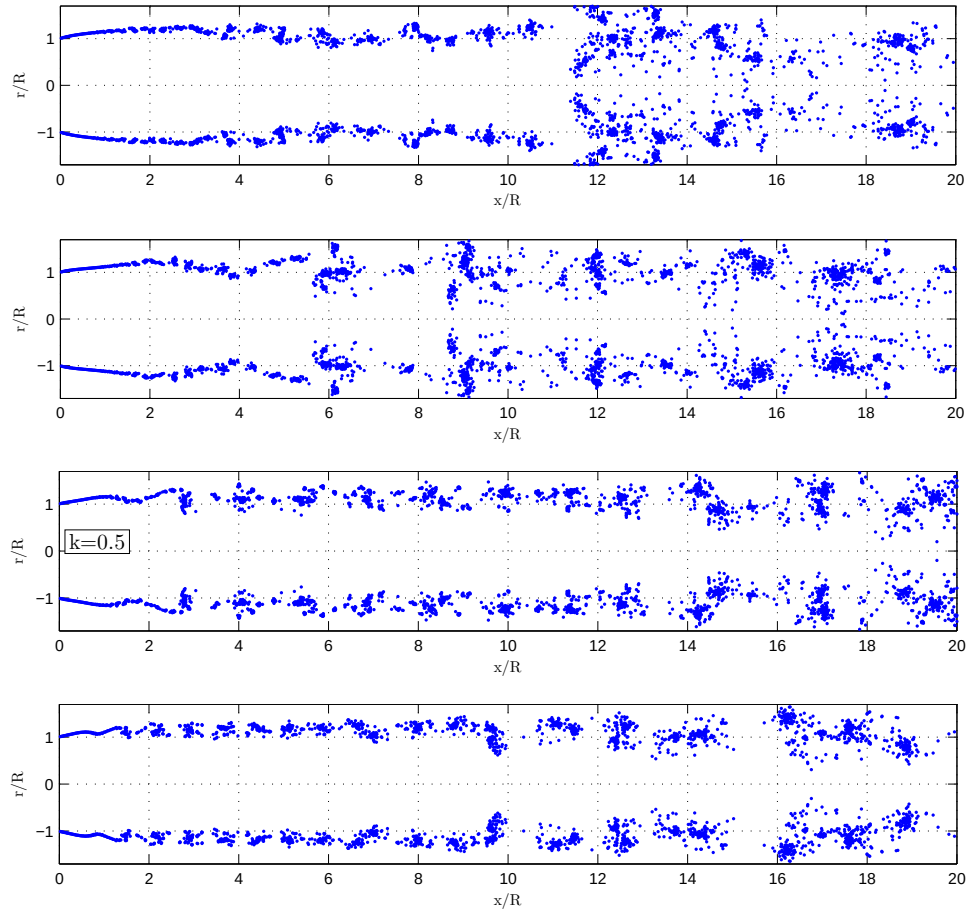

Figure C.3: Location of vortex rings in the fully developed near wake for baseline C_t=7/9 with frequencies k=0.05, 0.2, 0.5, 1. Points represent intersections of the rings with the symmetry plane.

ACKNOWLEDGEMENTS

The course to pursue a PhD is a journey of exploration. It's my pleasure to take this chance to thank all the people who made my journey enriching and fascinating.

Fist and foremost, I would like to express my great gratitude to my supervisors, Gijs and Carlos, for their support, guidance and endless help. Gijs, I remembered the countless chat we had in your office, during conferences and at other occasions, which not only lights up the path of my research, but also the road of my life. Carlos, I remembered the moments you helped me in debugging, the days you were around in the lab... I feel so proud and lucky to be the last Phd student that Gijs promoted and the first one that Carlos promoted (It's a fact in our heart). Thank you.

I would also like to thank Lars and Gerard Schepers, who provided valuable advice during my progress meetings in the first two years and the last two years, respectively. Thanks also go to Lars, Sachin, Thijs and others for sharing knowledge during the 'smart rotor meetings'.

I am grateful to Gerard for all his support, and the same to Sylvia for her excellent professional work on daily issues.

I want to extend my gratitude to other lovely colleagues in the Wind Energy Group, especially the three gentlemen in my office, Daniel, Rene and Ashim. Thank you guys for your accompaniment and all the unforgettable memories we had. Special thanks go to Daniel for his help during the tunnel test. I would also like to thank Gael, Jaco, Tom, Delphine, Bruce, Navi, Vinite, Sebastian and Sebastian, Mikko, Carlos, Lorenzo, Giuseppe, Ricardo, Maarten, Uwe for all the laughs and your kind help. Of course, thanks also go to my Chinese friends in Delft, Ye, Zi, Duo, Juan, Jing, Jinglang for all the happy moments.

The experimental work in the OJF would not succeed without the help from Nico, Stefan, Peters, Frits and the staff at DEMO, Ed and Rob. Special thanks go to Marios, Jacopo and Theo for their kind help in teaching me to use the hot-wire equipment. Big thanks also go to Daniele, Francesco, Shuanghou, Qingqing and Giuseppe Caridi for their kind help in teaching me to use the PIV facilities during the two campaigns.

I would like to thank my master student, Vincent, for his hard work and dedication during the experiments.

I wish to thank the committee members of my thesis for their careful reading and comments to help me improve it into this final version.

I owe my special thanks to my parents and my brother for their endless love and their support whenever I need.

Last but not the least, my deepest gratitude goes to my husband, Zhen. Thank you for accompanying and growing up together with me for the past years' master and phd programmes. Thank you for travelling hundreds of miles every day to live with me. I believe our love will deepen in the cooperated research on bringing up the product of our love - Eva.

LIST OF PUBLICATIONS

JOURNAL PUBLICATIONS

- W. Yu, V.W. Hong, C. Ferreira, G.A.M. van Kuik, Experimental analysis on the dynamic wake of an actuator disc undergoing transient loads. Experiments in Fluids 2017, 58: 149.

- W. Yu, C. Ferreira, G.A.M. van Kuik, D. Baldacchino, Verifying the Blade Element Momentum method in unsteady, radially varied, axisymmetric loading using a vortex ring model, Wind Energy 2016, 20(2), 269-288.

- M.M. Zhang, W. Yu, J.Z. Xu, Aerodynamic physics of smart load control for wind turbine due to extreme wind shear, Renewable Energy 2014, 70, 204-210.

- W. Yu, M.M. Zhang, J.Z. Xu, Effect of smart rotor control using deformable trailing edge flap on load reduction under normal and extreme turbulence, energies 2012, 5, 3608-3626.

CONFERENCE PROCEEDINGS

- W. Yu, V. Hong, C. Ferreira, G.A.M. van Kuik, Validation of engineering dynamic inflow models by experimental and numerical approaches, Journal of Physics: Conference series, 753 (2016) 022024.

- W. Yu, C. Ferreira, G.A.M. van Kuik, Analytical actuator disk solution for unsteady and/or non-uniform loading, Proceedings of the 34th wind energy symposium, AIAA SciTech Forum, California, 2016.

- W. Yu, V. Hong, C. Ferreira, G.A.M. van Kuik, Experimental and numerical analysis of the dynamic wake effects of an actuator disc undergoing transient loads, Proceedings of the 12th EAWE PhD seminar on wind energy in Europe, Lyngby (Denmark), 2016.

- G.A.M van Kuik, W. Yu, S. Sarmast, S. Ivanell. Comaprison of actuator disc and Joukowsky rotor flows, to explore the need for a tip correction, Journal of Physics: Conference series 625 (2015)012013.

- W. Yu, C. Ferreira, G.A.M. van Kuik. Is blade element momentum theory (BEM) enough for smart rotor design, Proceedings of the 10th EAWE PhD seminar on wind energy in Europe, Orleans (France), 2014.

IN SUBMISSION

- W. Yu, C. Ferreira, G.A.M. van Kuik. Numerical investigation of an actuator disc undergoing unsteady load. To be submitted.
- W. Yu, C. Ferreira, G.A.M. van Kuik, G. Schepers. A new dynamic-inflow engineering model based on linear and nonlinear actuator-disc vortex-models. Wind Energy, Under Review

CURRICULUM VITÆ

Wei YU

26-2-1987 Born in Hubei, China.

EDUCATION

09/2013 – present — Ph.D. Researcher in Wind Energy

Thesis: the wake of an unsteady actuator disc
Faculty of Aerospace Engineering
Delft University of Technology, Delft, the Netherlands.

09/2010 – 07/2013 — Master of Science in Wind Energy

Thesis:Investigation on smart load control for large-scale wind turbines using deformable trailing edge flap (with honour)
University of Chinese Academy of Sciences, Beijing, China.

09/2006 – 07/2010 — Bachelor of Science in Thermal Energy and Power Engineering

Final project: Investigation on flow field inside a four-cavity exhaust system of a GP-type car (with honour)
Wuhan University of Technology, Hubei, China.